Molecular transport through atomic-scale apertures and capillaries.

A thesis submitted to the University of Manchester for the degree of

Doctor of Philosophy

in the Faculty of Science and Engineering

SIDRA A DAR

Department of Physics and Astronomy

2022

Blank Page

List of Contents

List of Figures

List of Tables

Blank page

Abstract

It has been an aspiring goal to mimic biological channels like trans-membrane protein channels or aquaporin to achieve the ultimate size to make use of the exotic properties of these channels. Some efforts have been recognised to create a structure with dimensions approaching the size of small ions and water molecules but precise control on geometry and surface roughness makes it challenging to produce capillaries at this spatial scale.

I have fabricated graphene and other 2D materials (h-BN and MoS_2) based capillaries with heights ranging from a single atomic layer of graphene to a few layers (up to several tens of nanometers) by following nanofabrication protocols developed by Radha et al (Nature 2016). This fabrication method provides insight on removing the atomic layers through micromechanical cleavage and restacking these 2D layers through van der Waals heterostructures with no loss in atomic continuity. Such 2D capillaries use high-quality layered crystals (graphite, h-BN and MoS_2) and basal planes of these 2D crystals act as walls (top and bottom). These novel atomic-scale capillaries are employed to study the interaction of molecules (gas, water and ions) inside these conduits for permeation and separation based on size exclusion. In the case of gas permeation, our results demonstrate that the frictionless surface of graphene induces enhanced gas flow and shows a 2-3 order difference compared to classical Knudsen flow. I have also checked the selectivity of different gases as compared to helium gas but no selectivity was found.

Atomic-scale vacancies are demonstrated in monolayer tungsten disulfide (WS_2) as the ultimate atomic limit of the pores, created by focused ion beam irradiation. The permeability of helium through this aperture validate Knudsen descriptions to quantify the relation between atomic-scale vacancies and gas flow. Atomic-scale vacancies proved to be mechanically robust and showed fast helium flow.

Using angstrom scale capillaries, the response of ions flow under mechanical and electrical (pressure and voltage) forces are measured to explore water and ions transport coupling. Ionic motion in these ultimate scale conduits is affected by the channel walls and hydration shells of ions and transport strongly depends on wall

material (graphite and h-BN). Ionic flow is driven by pressure and applied electric force reveals a transistor-like electrohydrodynamic effect under such confinement i.e. slight increase (in fraction) in voltage significantly enhances the measured pressure-driven ionic transport up to 20 times.

Overall, the nanofluidic structures in this thesis will provide a unique platform to study molecular transport at the ultimate atomic scale. The device structures used and the results of this thesis will help further 2D materials use to study the dynamics of molecules for their detection and separation.

Declaration

The University of Manchester

Candidate Name: Sidra Abbas Dar

Faculty: Science and Engineering

Thesis Title: Molecular transport through atomic-scale apertures and capillaries.

Declaration to be completed by the candidate:

No portion of this work referred to in this thesis has been submitted in support of an application for another degree or qualification of this or any other university or other institute of learning.

Copyright Statement

Acknowledgements

All praises for Allah the Most Gracious and the Most Merciful. I am deeply grateful and humble to Him for blessing me with this opportunity of my academic career. I am thankful to the University of Engineering & Technology Lahore, Pakistan for supporting my PhD studies by awarding me a scholarship under the faculty development programme. Sincere thanks go to Prof. Dr M. Shahid Rafique, Prof. Dr M. Zafar Noon and Prof. Dr Aneela Anwar for their wise guidance and assistance in this regard.

I want to express my deep gratitude to Prof. Radha Boya my PhD supervisor for accepting me as her student, giving me a chance to work in her research group and world-class labs. I have learnt a lot from her, she has always been supportive, encouraging and kind to give her expert opinion regarding any problem I have faced during my studies.

Sincere thanks go to Dr Ashok Keerthi for his help and guidance during my studies. I will like to extend my gratitude to all my group members and especially Abdul-ghani Ismail, Yi You, Gautham Solleti, Gangiah Matella (late), Ankit Bhardwaj, Ravalika Sajja and Rongrong.

Many thanks to everyone in the School of Physics and Astronomy who helped me with my learning during PhD time. Also, to staff in National Graphene Institute who support students in a practical and fine working environment especially, Dr Lee Hague, Dr Alexander Zhukhov for their help and sharing their experimental skills in the cleanroom.

Finally and most importantly, I would like to thank my family: my parents, my mother-in-law and my siblings whose constant support, help and prayers are always with me without any condition throughout this tenure. All my sisters Naila Dar, Shumaila Dar Uzma Dar, Saima Dar, Iqra Dar and my brother Adnan Dar were constantly there for my moral support. Their love and support keep me going through all the thicks and thins during my PhD. Deepest gratitude for my mother and mother in law whose help and support make it possible for me to work in the labs without any worry for home and kids. Without their help, it would be so difficult to make this PhD happen.

Further, I am thankful to my husband Mansoor Abdullah for helping me at every step of my life and also for my studies. His patience and support were admirable and the efforts in this regard are tremendous. I must appreciate my kids Muhammed Musa

Abdullah, Muhammad Ibrahim Abdullah and my daughter Zainab Abdullah for their love which was a continuous source of energy and happiness for me.

Last but not the least my Abbu Jan Mr Muhammad Abbas Dar whose motivation and encouragement got me to where I am today. He has always been supportive, kind and encouraging, he is truly a mentor and role model for me. I dedicate this thesis to my Abbu Jan whose vision and persistent encouragement made this PHD happen.

Sidra A Dar.

Manchester, 08 August 2021

Blank Page

Chapter 1

Introduction

1.1 Nanofluidics and emergence of carbon nanofluidics

Nanofluidics is the study of fluid (water, ion and gas) flow at nanoscale where one of the dimensions of the structure is within 1-100nm (1-4). Nanofluidics is fascinating because atoms or molecules of fluids interact and assemble into conduits that possess a unique combination of physical, mechanical and electrochemical properties i.e., superfast flows, selectivity, asymmetric ion transport, slippage over smooth surfaces and nonlinear electro-kinetic transport under such confinement (2, 4, 5). The surface properties of the channel walls and steric forces play a significant role in determining the mass transport when the size of the structure goes down to the nanoscale regime (3, 4). In this scale, molecular interactions and physical phenomena are distinct from the continuum regime because of the large surface-to-volume ratios found in nanochannels (6, 7). This field has a wide range of applications and the most important applications include molecular separation (8) and seawater desalination (9, 10). In these applications, sufficiently small-sized pores sieve molecules for molecular filtration and push the salt and large particles away permeating the water molecules. Salt passage critically depends on pore diameter and water permeability of this material is several orders of magnitude higher than the conventional reverse osmosis membranes.

Individual molecules detection in nanopores has enabled the detectable changes in ionic pore current (blockades in ionic pore current) and developed as an analytical tool that leads to the application of DNA sequencing (11, 12) and biomedical analysis (13, 14).

Ion conduction between channels with an applied voltage or applied pressure produces a voltage difference and this ion current and potential can be coupled to an electrical resistor to produce electrical current and the hydrostatic energy can be converted to electrical power which is used for nanofluidic energy conversion (15-17).

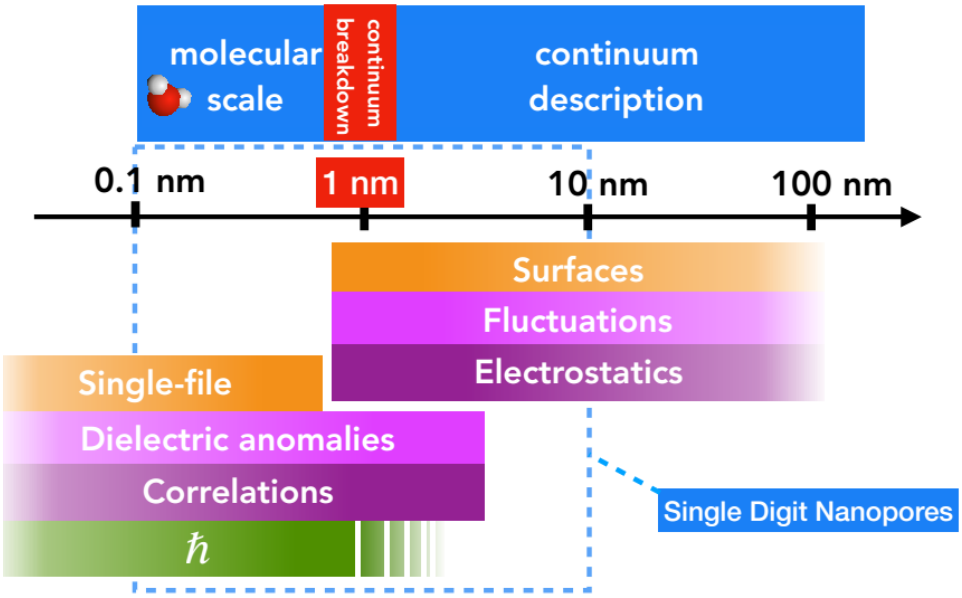

Figure1.1: An overview of nanofluidic length scales. Description of the different length scales and effects arising in such confinement. Continuum description is valid from 1nm to 100nm, 1 nm is the breakdown limit for continuum description and molecular scale confinement starts from there and goes down to molecular size. Single file pores are below 1nm and single-digit nanopores are below 10nm constrictions. Image is taken from (18).

Nanofluidics has recognised development in fabrication technology to a point where new systems are designed to mimic biological nanopores at their length scale. This ultimate step in scale reduction has been reached to explore new properties emerging in molecular scale confinement as continuum limit (18).

The ultimate scale for observing specific effects is set by the molecular size of the fluid and confinement i.e., 1 nm or below where Navier-Strokes equations are still valid. At the molecular scale, biological systems emerge giving huge permeability and perfect selectivity of aquaporin as compared to potassium channels or mechano-sensitive piezo channels. Below 1 nm confinement, fluid dynamics change due to reduced viscosity, thermal fluctuations (due to confining wall and fluid and arise as noise in ionic current measurements) and inter-particle correlations. Fluid changes its form from bulk-like disordered structure to layered structuring (in nanoconfined solid-liquid interfaces, attractive interactions between solids and liquids results in molecular layering i.e., hexagon and pentagon and single-chain) due to confined (below 1nm)

surfaces and pressure come into play as well (18). At this length scale where the size of the nanopore is comparable to gases and ions size atom-wall collisions, ion-wall and ion-water friction play an important role and needs to be taken into account (18).

Nanofluidics transport has significant importance in our daily life and life processes. Transmembrane protein and ion channels serve as biological nanofluidic conduits which transport water, proton and ions in a rapid, efficient and selective way across these cellular membranes (19-21). Nanofluidic channels in these biological membranes are composed of narrow hydrophobic pores like aquaporins which are extremely permeable to water and perfectly selective for other species. To understand the mechanism and function of these hydrophobic nanochannels, carbon nanotubes (CNTs) have been used to clarify the physics of rapid liquid flow and selectivity (22, 23) as they are also hydrophobic.

Carbon nanofluidics studies fluid behaviour and its manipulation inside nanoscale conduits made of carbon materials. These conduits are sp^2 bonded carbon which includes graphene-based membranes i.e. graphene nanopores (GNPs) and graphene oxide (GO) membranes and carbon nanotubes (24-28). Carbon nanofluidics has gained a lot of interest and a lot of work has been done over the years because of various unique transport properties such as fast water transport in carbon nanofluidic structures (29-32). It is due to a very small potential barrier for water molecules within hydrophobic graphitic nanochannels which thus leads to an ultrafast transport of water molecules. Ultrahigh gas permeability and selectivity have been observed in carbon nanofluidic systems (30, 33-36) where the conduits are a few nanometers (nm) to tens of nanometers, and gas flux has exceeded the flux predicted by the Knudsen diffusion model. Precise and ultrafast ion sieving (37, 38) and ultrafast mass transport (36, 39-43) has been observed in graphene-based nanofluidics with the incorporation of nanopores.

The structure of these carbon conduits (CNTs, GO membranes and GNPs) consist of numerous parallel conduits which significantly increase the mass flow rate and ionic conductance. The emergence of mass transport measurements allowed researchers to determine the mass transport in nanoscale conduit down to the molecular level. Apart from these carbon nanostructures single carbon nanotube (24, 44) and single graphene nanopores (14, 45) has been studied for the fundamental understanding of

the transport mechanism inside carbon nanofluidic conduits for the development of better carbon nanofluidic membranes.

All of the unique and remarkable transport properties of carbon nanofluidics has been raised due to the atomically smooth surfaces and hydrophobic graphitic nature of these nanoscale conduits. Also, the minimum possible thickness of graphene-based nanomaterials high mechanical strength, large aspect ratio and chemical robustness makes these materials a good candidate for a diverse range of technological applications in areas including water purification/desalination (46-48), oil extraction or separation (49, 50) and energy storage/conversion (51-53).

1.2 Nanofluidic Systems

For utilising such exceptional properties of the nano-confinement, various nanofluidic structures have been developed over the years. Experimental and computational studies have been done for nanofluidic transport and selectivity of the nanofluidic species i.e. (gas, water and ions) through various nanochannels and membranes made using different materials and designs. In these systems, the minimum dimension of the system is defined as pores, membranes, channels diameter and distance between the laminates etc. which act as a membrane for fluid transport.

Membranes for molecular separation act as a much simpler and more efficient method as compared to traditional chemical separation processes. The perfect membrane for mass transport should be as thin as possible to maximize flux, mechanically robust to prevent fracture and leakage, and have well-defined pore sizes and geometry to achieve selectivity and chemical inertness to prevent any reaction.

Different nanofluidic systems have various unique properties which are due to the design, structure and material used in those systems. Here I will present some of the nanofluidic structures and discuss their characteristic features, merits and demerits, their fundamental properties and applications. Comparison of all these systems has helped me to design a unique state of the art nanofluidic structure by utilising the properties of already developed structures and overcoming their drawbacks to improve the design, structure and reliability of nanofluidic systems.

Nanofluidic structures can be categorized as natural and artificial nanostructures. Amongst natural nanoporous materials shale rocks, zeolites, silica, activated charcoal and cell membrane are widely used. Artificial nanopores include solid-state and graphene nanopores, nano spaces in graphene oxide sheets, metal-organic frameworks and carbon nanotubes.

Shale is a sedimentary rock composed of a mixture of clay minerals and organic matter. Shale matrix has usually had a broad range of poorly connected nano- and micro-pore systems (figure 1.2). Pore size distribution in shale matrix is associated with clay minerals and organic matter. (54, 55). Zeolites can be synthesised from shale rock, volcanic ash (56). Zeolite is a crystalline aluminosilicate and is found most common in sedimentary rocks. The different chemical combination of aluminium, silicon and oxygen makes a three-dimensional framework with well-defined voids and pores of molecular dimensions which are accessible for ion exchange, permittivity and selectivity. Activated charcoal is used to filter out heavy poisonous metal ions and organic molecules from water and air by adsorption.

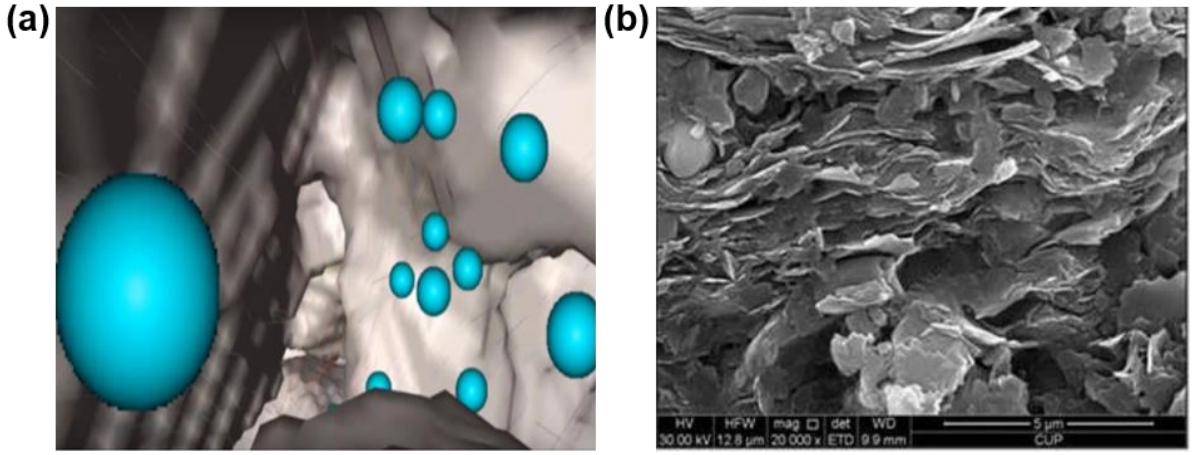

Figure 1. 2: Natural nanoporous cavities. (a) A still taken from a simulation of atoms travelling in the natural nanoporous media. Blue spheres are representing the particle injected in the rock (porous media) for the air flux experiment. Image is taken from(57). (b) SEM image of shale rock, scale bar is 5 µm. Image is taken from (58).

The walls of our cells are also nanoporous membranes used for selective transport of water and ions with a lot of added complexities. Ion channels in the cell membrane regulate different physiological functions in our body and selectively permit certain

proteins and ions to travel into and out of the cell. Aquaporins are the protein channels that only facilitate water transport and block other ions and molecules (figure1.3).

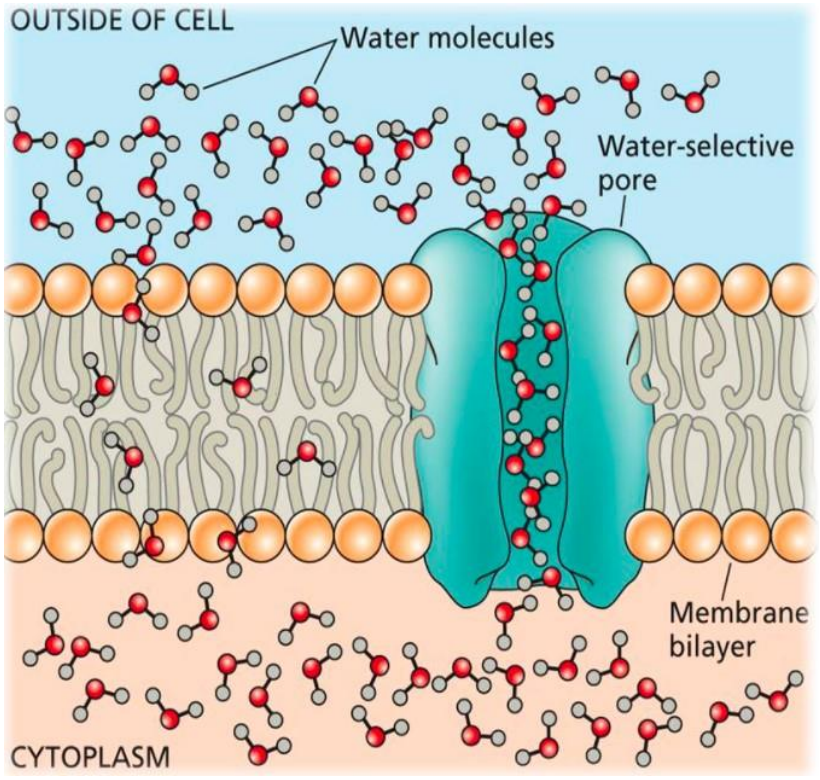

Figure 1.3: Aquaporin-water selective pores. Protein channels in the membrane of biological cells for the transport of water between cells. Water molecules are selectively transported from the pores called aquaporin. Image is taken from (59).

All of these nanoporous materials can be used for nanofluidic studies but their complex geometries and non-uniform wall roughness, mechanical and chemical instability in case of biological pores hinder their use in different applications.

1.2.1 General methods for making nanochannels

Fabrication of nanostructures is usually pursued through two paths. One is the top-down approach and the other one is a bottom-up approach. The Top-down (6, 45, 60, 61) approach is to miniaturize the larger structures with nanofabrication using nanolithography and etching. The top-down approach is good for producing long-range order with precise control of structures size. The bottom-up approach is of

building complex molecular structures atom by atom using chemical synthesis, where chemical and physical forces act at the nanoscale to grow basic units to larger structures. It has many advantages for scalable synthesis has limited control on the pore size for the whole assembly.

The top-down approach uses conventional lithography materials to create nanochannels by lithography on silicon, glass and SiN (6, 60) however it is difficult to reach very small channel dimensions main reason is the surface roughness. Surface roughness dominates if you go below 2 nm and it's quite hard with conventional materials because the surface roughness dominates in that scale. On the other hand with the bottom-up method like carbon nanotube which itself act as a fluidic conduit and reach very dimensions however it is difficult to integrate thousands of tubes with diameter control.

There are a lot of existing systems that can reach nanoscale and angstrom scale dimensions which can be categorized in terms of dimensionality, the first and foremost important structure is the simplest zero-dimensional nanopores. These pores are punched through either a 2D material or a simple conventional membrane type materials. Solid-state nanopores are artificially drilled holes in (silicon oxide, silicon nitride and graphene) membranes. Holes are usually drilled by focused Ion beam (FIB) (62-65), e-beam (66, 67), chemical, laser and ultraviolet (UV) etching (68-71). These nanopores have a very short length with nm resolution. Solid-state nanopores are usually stable, chemically robust and size tuneable than biological pores.

Precise dimensions of the nanopore are difficult to achieve because of pore opening (enlarge) and shrinkage observed by a few groups reported in the literature (72-75). Pore opening and shrinkage depends on many factors such as ion intensity, type of the ion, the intensity of the beam, temperature and thickness of the membrane also play a deterministic role. Precise control on size and number density of nanopores (10, 45, 48, 61) is sometimes difficult to achieve due to the thin nature of graphene membranes and small pores often get blocked. Graphene nanopores (GNPs) fabrication is complex, time-consuming and a rigorous process with many failure modes, and has been developed rapidly over the past decade. Nanopores made in Si_3N_4 (76), graphene (77) and MoS_2 (78) are shown in figure 1.4.

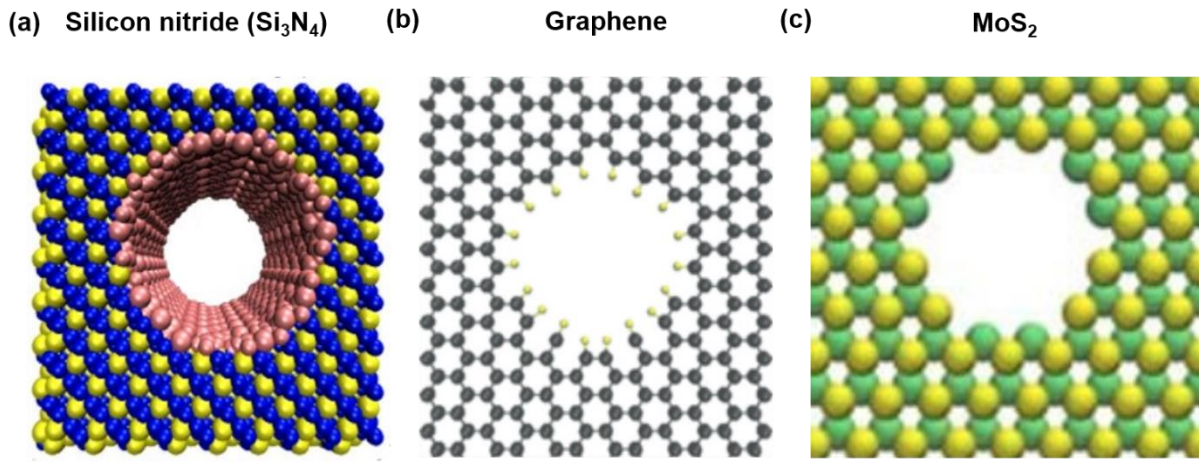

Figure 1.4: Solid-state nanopores. (a) Nanopores in Si_3N_4, (b) in graphene and (c) in MoS_2 by molecular dynamic simulation. In (a) Yellow spheres are Si atoms and blue spheres are N atoms. The pink colour inside the pore is due to the surface charge that appeared during pore creation. To maintain charge neutrality partial charge of Si was adjusted. The pore size is 3.5 nm. 6 Å graphene nanopore created in (b), grey spheres is carbon atoms. In (c) yellow and lime spheres are sulphur and molybdenum atoms respectively. Image (a) is taken from (76) (b) from (77) and (c) from (78).

Another very well-known system is nanotubes which can be categorised as one dimensional system. Carbon nanotubes have been studied for more than two decades and they have been used to study the flow of molecules.

Carbon nanotube (CNT) incorporated membranes typically have a single wall and multi wall tubes of nanometer and sub-nanometer size. Single wall nanotubes have well-defined geometry and sub-nm to angstrom scale resolution. Fast mass transport has been observed through such carbon nanotube membranes (79-81). Individual CNTs are also fabricated but, fabrication of individual nanochannels are challenging in terms of efficiency and the calculation of fluid flux in nanochannels requires very large sampling (82). Schematic and SEM image of carbon nanotube is shown in figure 1.5.

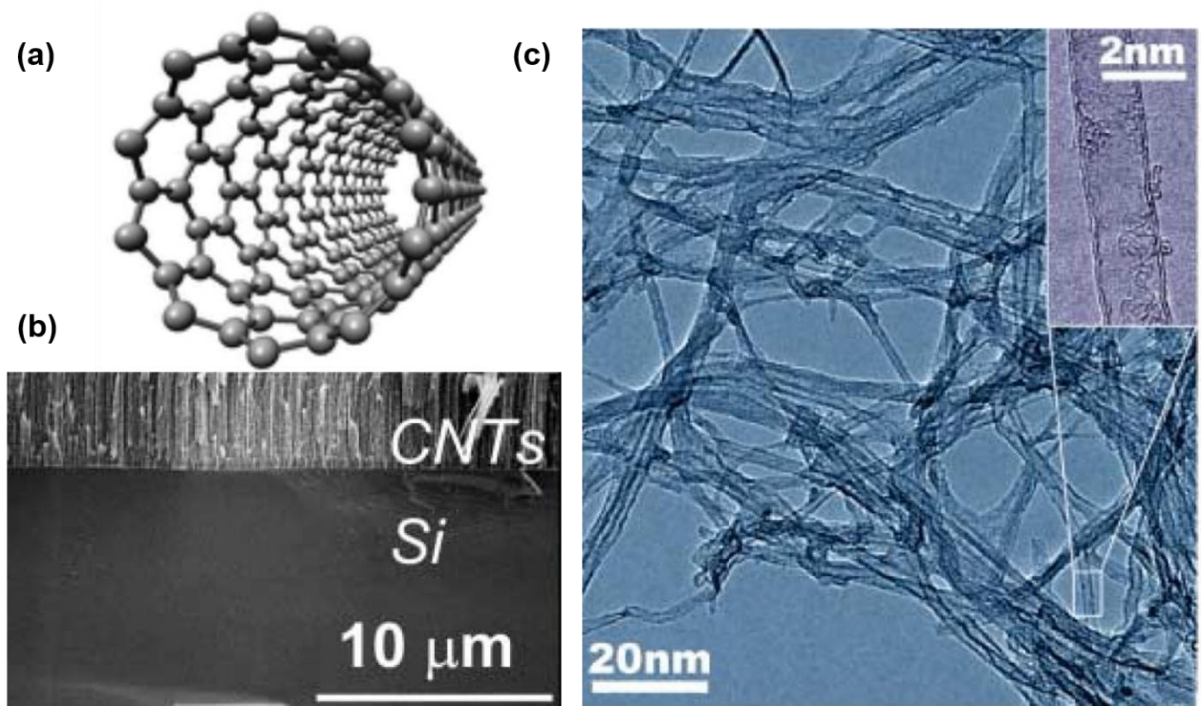

Figure 1.5: Carbon nanotube nanofluidic conduits. (a) Schematic of single-wall carbon nanotube. (b) Cross-section of the as-grown double wall carbon nanotube. (c)TEM image of as grown carbon nanotube showing two concentric graphitic walls. The majority of the CNT are double walls as shown in the high-resolution inset. Image (a) is taken from (83) and (b-c) from(30).

Carbon nanotubes suffer from non-uniform dimensions amongst numerous tubes and are difficult to integrate. Multiwall nanotubes suffers from blockages because of the migration of the catalyst particle in the interior of the tubes reported in (79, 84, 85) due to their unique structure (bamboo type) and these blockages can reduce the active membrane pore density which make it difficult to precisely calculate the flow.

A recent system that has two dimensions is two-dimensional graphene oxide and related laminates where the layers of 2D materials are stacked against each other and the space between these layered materials is used as a capillary.

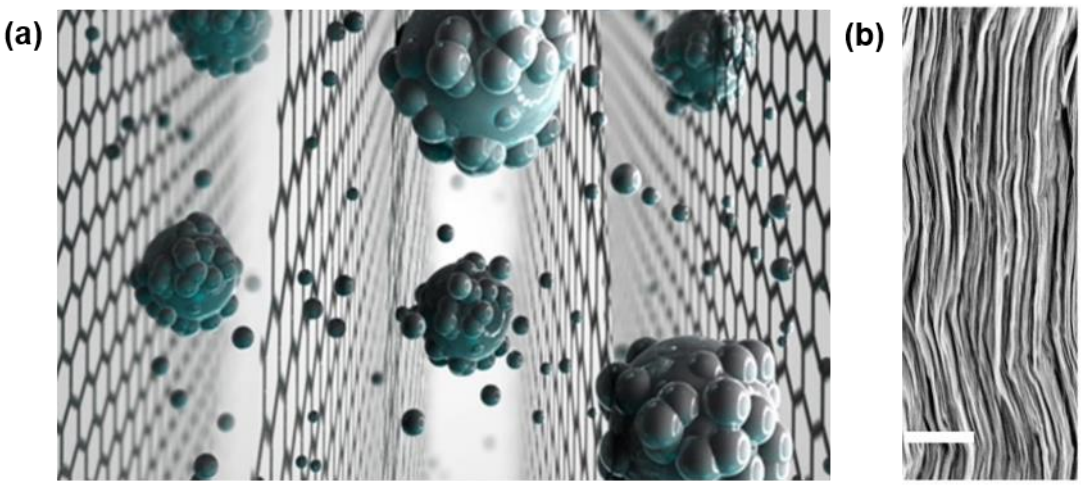

Figure 1.6: Size selective sieving in graphene oxide (GO) membranes. Common salts dissolve in water and form a water layer around salts ions which is called hydration shell. (a) Blue coloured balls are the salt ions with a hydration shell around them. GO sieves block the salt ions and permeate water molecules. Smaller balls are water molecules that can pass through the interlayer spacing in the GO membrane which acts like sieves. (b) Scanning electron microscopy image of 100 µm thick GO laminates embedded in epoxy with interlayer spacing ≈ 6.4 to 9.8 Å. Scale bar, 1 µm. Image (a) is taken from (86) and (b) from (41).

Graphene oxide (GO) membranes (figure 1.6) are the derivatives of graphene with oxygen-containing functional groups. Due to their relatively easy synthesis process, they have gained significant interest over the last few years. These membranes have a laminar structure with numerous interlayers which act as parallel conduits of nm and sub-nm size. These have the advantage of being easily scalable for commercial use and can desalinate water(41). Swelling of pores in water and irregular distribution of oxygen groups observed in (87, 88) limits the control on the size of the pores in GO membranes.

The major advantage of the top-down approach is controlled patterning and no assembly step is needed as in the case of integrated circuits. Using top-down methods, fluidic nanochannels were fabricated by using standard lithography and etching process (60) to study ion transport (figure 1.7). Here 2 nm high channels are prepared on silicon with 60 µm deep microchannel and encapsulated with an oxide layer and anodic bonding. Fluid wall interaction in these channels suggested that ion transport is dominated by the surface charge.

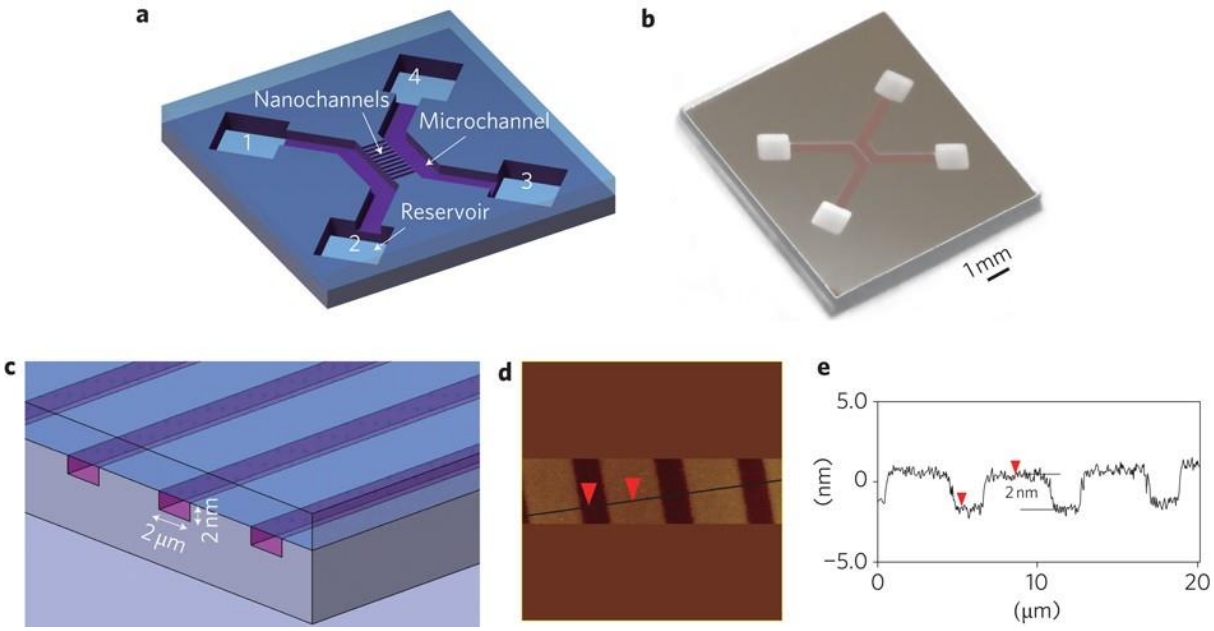

Figure 1.7: Top-down lithography and etching method to prepare nanochannels. a) Schematic of a 2 nm high nanochannels device, with microchannels and reservoirs prepared by top down fabrication method on silicon die. b) Bonded nanochannel device with a transparent Pyrex die on top. The microchannels are 1cm long, 500 µm wide, 60 µm deep and the reservoirs are 2×2 mm^2 through-holes. The pink colour of the microchannel/nanochannel comes from a 500nm thick thermal oxide layer. c) Cross-section schematic of three nanochannels. d-e) AFM image and analysis of nanochannels after surface oxidization. Image is taken from (60).

Surface roughness is incorporated during nanofabrication and lithography of silicon which makes it challenging to make pores/channels at atomic resolution. To overcome the surface roughness 2D materials are ideal building blocks compared to conventional silicon-based materials.

All of these systems have their benefits but none of these systems even come close to the sophistication of protein and biological channels (89, 90) for their mechanosensitivity. To mimic those channels by reducing the channel size down to atomic scale for ultra-sensitive mechanical response under external stimuli.

1.2.2 Challenges with nanofluidic systems

All of these nanofluidics structures have their advantages and disadvantages. Numerous parallel conduits (1D and 2D) significantly increase the conductance which consequently permits one to study physical phenomena arising from the enhanced flow. Apart from enhanced flows due to numerous parallel conduits (30-32, 91) there is a huge variation of results amongst these systems which has opened a debate on the fundamental physics because of this variation of experimental results. These are owing due to the huge differences in the pore size and the total quantities of these membranes which are completely based on the statistical estimation. Inaccuracy of estimation is further magnified when various individual channels aggregate and their integration lead towards inaccuracies in the results. The exact estimation of the size/diameter, cross-sectional geometry and number density of open conduits is challenging which limit their application. On the other hand, another factor limiting the utilization of carbon nanotubes is the difficulty to integrate the membrane structures into lab-on-chip systems. Also, they have leaks and avoiding those leaks is a difficult task.

Despite careful fabrication, several nanofluidic structures (0D, 1D and 2D) are limited by imprecision in cross-sectional geometry (non-uniformity of these pores in size and density) and the presence of oxide and ionic groups which occur as defects. Controlled fabrication of uniform defect-free sub-nanometer pores and the control on interlayers distance is very difficult to attain at the same level and is one of the major current obstacles found in the membranes discussed.

Fundamental restrictions imposed by top-down and bottom-up approaches and lack of robust method to fabricate nanofluidics systems with well-defined pore size and geometry over the whole assembly for numerous channels has been the limiting factor to calculate the flow with precision and instil some complexities.

To avoid the complexities arising from the statistical estimation of these conduits and overcome the challenges associated with the individual systems we have devised a state of the art atomics scale structure. The structure will utilise the properties of graphene and has numerous parallel conduits with precise control on the size, cross-sectional geometry and length and defect-free with no surface roughness.

1.3 Matter transport studies through nanofluidic systems

Ions and molecules are the building blocks of matter. Interaction of ions and molecules in confinements down to nanoscale provide more insights into the fundamentals of physics, chemistry, materials and life sciences. Nanofluids in such confinements behave radically different from their bulk counterparts and the surfaces and interfaces exert vital influence on the transport and interactive behaviours of ions and molecules.

Understanding molecular transport (gas, ions and water) through such confined atomic-scale tight spaces is very important as novel properties have shown to emerge in fluids confined at the sub-nanometer scale. Gas transport through such confined spaces plays a major role in the design of gas extraction and separation techniques (92) and indicated a trade-off between permeation and selectivity. Permeability which provides the amount of flow rate and selectivity which provide the quality of separation are the important parameters for determining the membranes quality and their application.

In extremely small structures the mean free path of gas is much larger than the minimum dimension of the system where the gas dynamics are dominated by the molecular collisions with the wall of the structure rather than the intermolecular collisions (93). This is known as the free molecular regime and gas flux in this regime is described using the Knudsen equation which will be discussed in detail in section (2.5).

Graphene and graphene oxide membranes are studied for gas permeance governed by the Knudsen mechanism of diffusion (33, 94) and reported to decrease with the molecular weight of the gases as expected. Selectivity of these membranes to He was in good agreement with theoretical Knudsen selectivity. Gas permeation is usually inversely proportional to the membrane thickness for conventional membranes but for these membranes, permeation decreases exponentially with membrane thickness.

Gas transport properties through such small structures have been studied by various groups and found marked differences in the permeation of the gases through the nanoconduits (29, 30, 33).

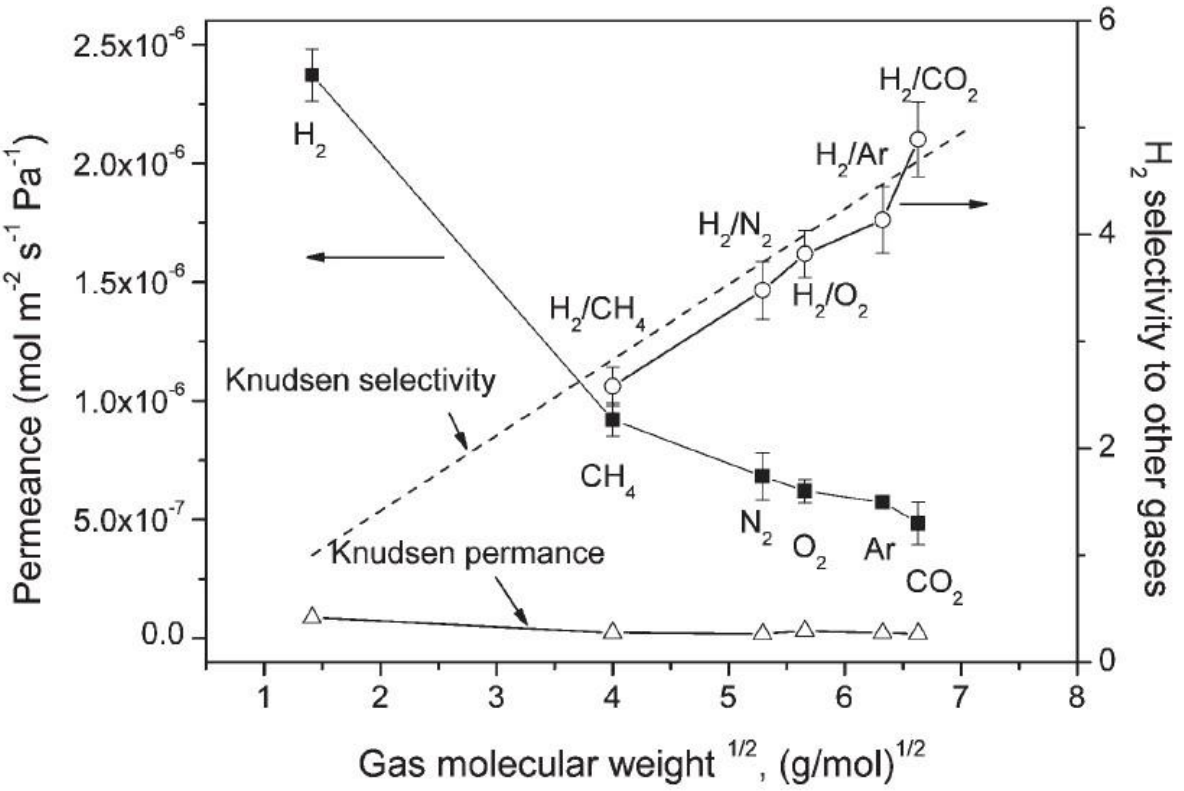

Figure 1.8: Single-gas permeance and selectivity. Single-gas permeance of different gases and selectivity of H_2 over other gases for carbon nanotube membrane as a function of molecular weight. Image is taken from (95).

Vertically-aligned carbon nanotube membranes were measured for the gas permeation (95-98) and compared the fluxes were with the Knudsen diffusion model. Very high permeation fluxes were reported as a contrast to the predicted from the Knudsen diffusion model. It was claimed that high permeation fluxes were due to the inherent smooth and frictionless nature of the interior of the nanotube but there is huge variation in the flux amongst different systems.

To find out a relation between gas flux and nanofluidic structure a comparative gas transport study has been done in (99) which is presented in figure 1.9 (a) to show the permeance of nitrogen molecules through carbon nanotubes (CNTs), as measured by different groups.

The permeance is the flow rate per unit cross-sectional area for a unit pressure difference applied across the membrane. The CNT diameters of the different groups differ as shown along the x-axis. The figure also shows the permeance of reference

membranes of a polycarbonate composite with pore diameters shown. The Enhancement Factor plotted in figure 1.8 (b) is given by

$$\text{Enhancement Factor} = \frac{\text{experimental permeance}}{\text{Knudsen model permeance}} \qquad (1.1)$$

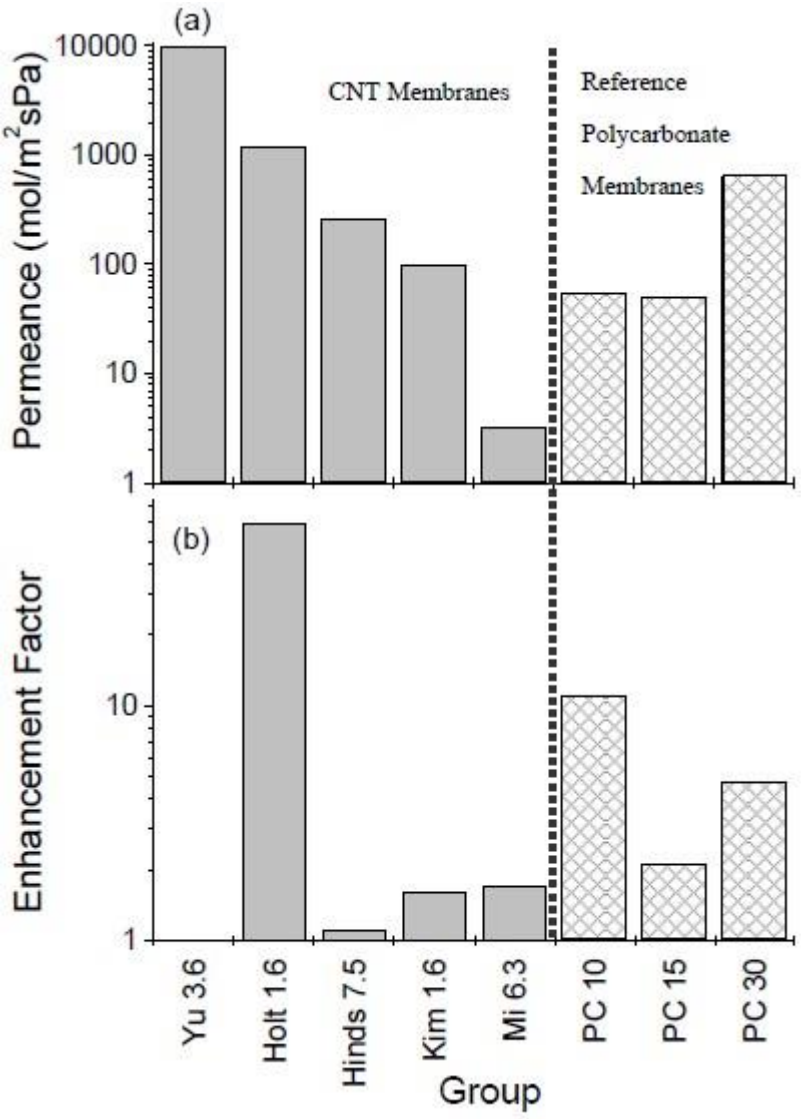

Figure 1.9: Permeance and enhancement over Knudsen theory. (a) Permeance, (b) enhancement of nitrogen gas through different CNT membranes fabricated by various groups. CNT diameter mentioned (in nm) after the name of the group, along the x-axis. Polycarbonate membranes are presented with hatched bars with corresponding pore sizes. Image is taken from (99).

Polycarbonate composite membranes with pore diameters are presented as reference membranes shown with hatched bars with corresponding pore sizes. The enhancement factor allows a direct comparison between the different studies as it normalises for membrane thickness, CNT number and cross-sectional area.

The enhancement of 1-2 over the Knudsen estimate is consistent for all studies except Holt et. al. (30). This is a reasonable agreement with the Knudsen model. The large disparity in Holt 1.6 is attributed to the large density of open CNTs along with the specular nature of molecular reflections off the smooth walls of the 1.6 nm diameter CNTs (99).

Silicon nanochannels (SiNCs) are fabricated in (100) by electrochemically etching from the surface of silicon along the <100> direction.
The etching leaves the surface roughness on the nm scale but an amorphous layer of native silicon dioxide that forms on it provides surface roughness in the picometer range. Gas transport through these channels is measured as a function of relaxation time for equilibration between two chambers at different pressures connected via these nanochannels. Relaxation time plots reveal the diffusion rate to be similar to theoretically expected estimates with no enhancement as seen in CNTs.

Selectivity of gases with different molecular size through nanoscale conduits also provide an insight into the properties of the gas flow. Selectivity of different nonhydrocarbon gases (H_2, He, Ne, N_2, O_2, Ar, CO_2 and Xe) and hydrocarbon gases (CH_4, C_2H_6, C_3H_6, C_4H_6, C_4H_8) studied in (30) through carbon nanotube as a function of molecular weight presented in figure 1.10. Gas selectivity here is measured as permeability of the gas (measured) relative to He. Selectivity of nonhydrocarbon gases follows the inverse square root mass scaling except hydrocarbon gases which is due to preferential interaction of hydrocarbons with nanotubes sidewalls (30).

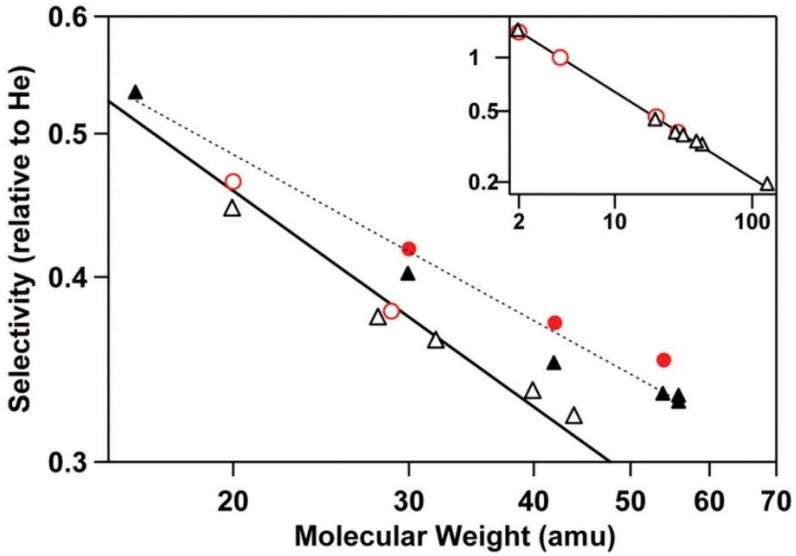

Figure 1.10: Gas selectivity of different gases. Sub-2 nm double-wall nanotube and multiwall nanotube membranes are denoted as triangles and circles respectively. Open symbols denote nonhydrocarbon gases (H_2, He, Ne, N_2, O_2, Ar, CO_2 and Xe), solid symbols denote hydrocarbon gases (CH_4, C_2H_6, C_3H_6, C_4H_6, C_4H_8). The solid line is a power-law fit of the nonhydrocarbon gas selectivity data and represents a scaling predicted by the Knudsen diffusion model (exponent of –0.49 T 0.01). The dashed line is a power-law fit of the hydrocarbon gas data, showing a deviation from the Knudsen model (exponent of-0.37 T 0.02). The full mass range of the nonhydrocarbon gas data is presented in the inset which is in agreement with the Knudsen model scaling. Image is taken from (30).

This enhancement of flow with respect to theoretical results in the case of CNTs and the lack of it in the case of silicon nanochannels point to the difference of gas molecules interaction amongst two materials. The difference in surface roughness of graphene and silicon dioxide leads to different interactions and hence different gas flux. However, the lack of consistency and precision in the results require more rigorous experimental proof from multiple nanochannels whose dimensions can be uniformly and precisely controlled when fabricated to have a systematic investigation through the channels.

Nanofluidic systems have reached a stage where they can mimic the biological channels in terms of their functionality because of the advancement in fabrication techniques to reach the dimension of sub-nanometre. A pressure-sensitive response has been observed for biological mechanosensitive ion channels (101-103) which is very essential for understanding the cellular mechanisms. In response to chemical and

mechanical stimuli, these channels regulate the transport of ions through the cell membrane.

To observe such response in artificial channels most experimental studies done are in carbon nanotubes which have been restricted to electric forces (44, 104, 105). Carbon nanotubes (106) has been explored with ionic transport in these channels using mechanical pressure and electrical voltage forces to mimic the exotic behaviour of biological channels and observed an ionic conductance that depends quadratically on applied pressure. Here a micrometre-long carbon nanotube with radii of ~2 nm embedded in a membrane separating two electrolyte reservoirs has been used to study the coupling between pressure-driven fluid flow and ion transport.

Effects of range of forces i.e., electric field, pressure drop and chemical gradient on fluid transport through the single-channel carbon nanotubes (CNTs) (106) and boron nitride nanotubes (BNNTs) (107) have been explored at the nanoscale.

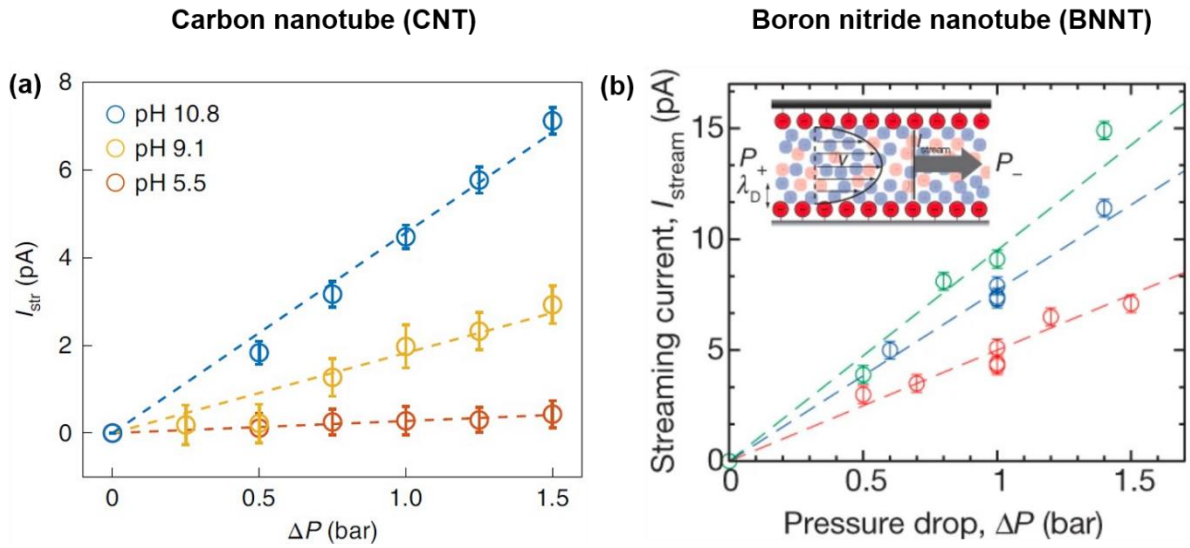

Figure 1.11: Streaming current for CNT and BNNT under different PH values. (a) Streaming current as a function of the pressure gradient Δ*P* for different pH values and 1M salt concentration. (b) Streaming current induced by a pressure drop for BNNT for pH 7 (red), 8.5 (blue) and 10 (green) for salt concentration 10^{-2}M. (a-b) The dashed line represents the best linear fit for each pH value. Error bars represent the standard error over five experimental values. Streaming current is measured without an applied voltage bias (Δ*V* = 0) and ΔP = P_+ - P_- pressure drop. Inset in (b) shows pressure-driven streaming current direction. Image (a) is taken from (106) and (b) from (107).

The response of the confined fluid to a pressure drop across these tubes was measured as streaming current to assess how ion transport through the tube interior is affected by the pressure difference between two sides of the membrane. Nanotube exhibits linear ion transport behaviour under pressure difference with no applied external voltage. Streaming current I_{str} varies linearly with pressure gradient ΔP and the slope increases with pH in both systems. The sign of the current is due to the excess transport of positive charges. Figure 1.11 shows the constant value reached by the ionic current which is measured as I_{str} and plotted as a function of applied pressure Δ*P* for carbon and born nitride nanotubes.

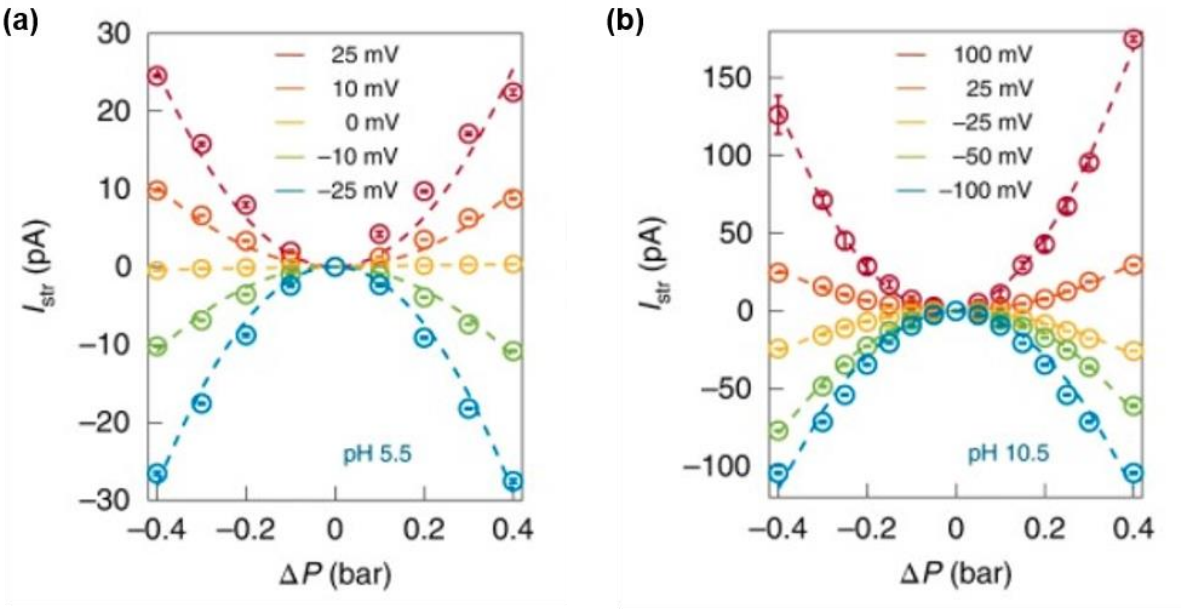

Figure 1.12: Streaming current as a function of applied bias. (a) streaming current as function of pressure drop and applied bias -25V to 25V with PH 5.5 and at *c* = 1 M. (b) streaming current as function of pressure drop and applied bias of -100V to 100 V with PH 10.5 and at *c* = 1 M. The dashed line represents the best parabolic fit for each applied bias. Image is taken from (106).

Under an external driving potential, its current response has a quadratic dependence with an applied pressure which is the as like a membrane potential for ion channels. This result emphasizes that narrow CNTs display mechanosensitive ionic conduction i.e., conductance that is tuned by the mechanical pressure.

This pressure-sensitive ionic response depends on the driving electrical potential and matches the behaviour of mechanically activated currents of biological ion channels (102, 103, 108).

1.4 Scope of the work

Membranes are widely used for nanofluidics (gas and ions) for the permeation and separation process. Membranes present a trade-off between permeability i.e., how fast molecules pass through a membrane and selectivity i.e., to what extent certain molecules are separated from the rest.

Biological membranes and ion channels are highly permeable, highly selective and can regulate ion/molecule transport across the cell membranes. The pressure-sensitive response has been observed for biological mechanosensitive ion channels (101, 102) which is very essential for understanding the cell mechanisms, these channels have concise constrictions of the angstrom scale dimensions.

Taking inspiration from biological channels in the cell membrane artificial nanochannels and nanopores can be constructed to modulate the interactions of molecules and ions inside these channels under a range of forces to probe the fundamental properties.

Several systems have been developed which can achieve nanometer-sized conduits and molecular transport has been observed inside the channel, but a clear understanding of the interaction between channel and molecules and how it affects the flow under different forces to mimic mechano-transduction. For that reason, angstrom scale capillary devices are designed to explore the interaction of gas and ions at the channel wall interface to probe surface-induced properties under electrical field and pressure gradient to mimic the biological channels.

The objective of this study is to fabricate multiple atomic-scale channels of graphene which we call capillaries with different wall materials (graphene, h-BN and MoS_2) by utilising all the properties of graphene i.e. high mechanical strength, chemical inertness, thermal stability and atomic flatness. Atomic-scale capillaries are designed with precise control on channel height by selecting different atomic layers of graphene with great flexibility, cross-sectional geometry and length precisely defined by

lithography and etching to investigate the fundamental transport of gas molecules and ions transport mechanism under electric, chemical and mechanical forces inside these capillaries.

These angstrom scale capillaries will explore the physical interactions between graphene and molecules of fluid near it depending on the flow rate. Fundamentals that are involved in the interaction of molecules of gas at the sub-nanometer scale will be probed for the applications of gas permeation and selectivity. Ion transport under electric and mechanical forces will provide the route for exploring and mimicking the mechanosensitive ion channels.

Chapter 2, will introduce the theoretical background of the 2D materials used along with their atomic structure and the applications in different areas of science will also be discussed. Different production methods for 2D materials will be reviewed. Then I will proceed to present van der Waals structures for the fabrication of devices through different layers to measure mass transport.

Gas transport in such confined spaces is characterised by Knudsen description where the gas molecules are not colliding with each other but only with the confined wall which is discussed in detail in section 2.5. Water and ions transport in such confined conduits and coupling of these fluids under different forces for different materials will be discussed later in the thesis.

In Chapter 3, I will discuss the fabrication techniques and tools used for the fabrication of graphene capillary devices for nanofluidics transport. I will discuss how the geometry of graphene atomic-scale capillaries can be precisely controlled by selecting different layers of graphene used and through e-beam lithography and etching. The step by step process for making the atomic scale capillaries structure is of significant importance and will be discussed in detail.

In chapter 4 gas transport studies through the fabricated capillaries will be studied using a helium leak detector and the impact of channel height affecting the transport phenomena under nanoscale confinement will be discussed. The flow of different gases (hydrogen, deuterium, oxygen, argon, nitrogen, carbon dioxide, methane, butane, isobutane and xenon) as compared to helium will be analysed using a residual gas analyser.

Chapter 5 of this thesis is the study of gas flow through atomic-scale apertures. Atomic-scale apertures made in the WS_2 membrane will be studied for helium gas flows.

Chapter 6 of this thesis is related to molecular streaming and its voltage control in angstrom-scale channels. The use of external voltage and pressure for the ionic current under confinement for different 2D materials will be discussed in this chapter.

The work presented in Chapter 5 and Chapter 6 has been published and for a better presentation of the results, the original papers are attached in each of these chapters.

A summary of the work presented in the thesis is provided in chapter 7. This chapter will include the conclusions of the thesis and an outlook of the future work based on our study.

Chapter 2

Graphene and 2D materials beyond graphene

In this chapter, properties of graphene and other two-dimensional (2D) materials, such as hexagonal boron nitride (h-BN) and molybdenum disulphide (MoS_2) are discussed. Starting with the carbon allotropes, introduction to atomic orbitals and properties of graphene and other 2D materials (h-BN and MoS_2) are reviewed. Production methods, van der Waals heterostructures for stacking different layers of 2D materials for device fabrication and then mass transport properties of nanostructures are also presented here.

2.1 Carbon and its allotropes

Carbon plays an important role in fundamental research being the most abundant element on the earth. Over the years, various carbon-based materials with different physical properties have been discovered based on their symmetry and dimension. Carbon compounds present different characteristics in different structures due to highly flexible molecular chains(109).

Isolation of graphene from bulk graphite by K.S. Novoselov and A.K. Geim in 2004 is one of the most important scientific works of this century. Graphene, which more than 70 years ago was thought of as a ‘state that could not exist’ has brought about tremendous results in the scientific community (110). The first 2D single-layer carbon atoms were isolated from graphite by mechanical exfoliation (111) and proved that single-layer carbon atoms could exist freely without a monocrystal base. Later it was proved that graphene could also exist perfectly well on the membranes (112) and in liquid suspension as well (113).

In graphite, all carbon atoms form a covalent bond and it is a planar allotrope of carbon. The carbon atoms are hexagonally arranged to form a honeycomb lattice structure in graphene. It is a building block of all other graphitic materials such as fullerenes,

carbon nanotube and graphene. From the basic understanding of carbon atoms, they have been divided into different dimensions (D) such as OD, 1D, 2D and 3D. Fullerenes are spherical molecules containing carbon atoms arranged in pentagonal and hexagonal lattices and are a wrapped form of graphene. Fullerenes are considered as zero-dimensional (OD) (figure 2.1a). In carbon nanotubes, hexagonal lattices are rolled in cylindrical tubes with carbon atoms in one-dimensional (1D) and is a rolled form of graphene (figure 2.1b). Graphene has a single layer of carbon atoms packed in a honeycomb structure, with a two-dimensional (2D) hexagonal lattice (figure 2.1c). Graphite (3D) is stacks of graphene with several layers (figure 2.1d) (110).

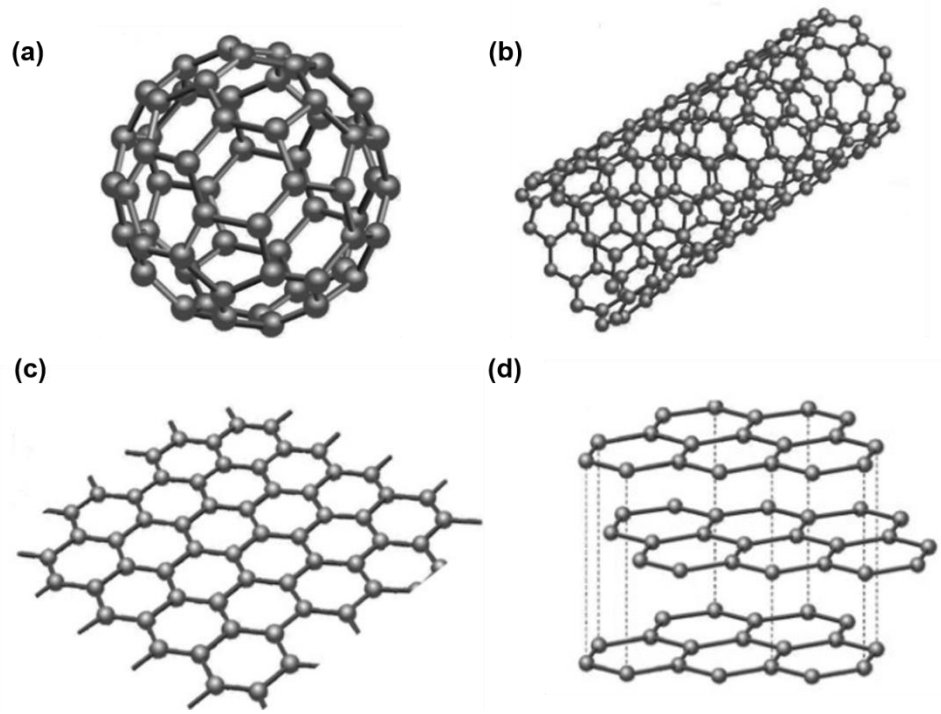

Figure 2.1: Structure of graphene, graphite, carbon nanotube and fullerene. (a) Fullerenes with carbon atoms pack in pentagonal and hexagonal lattices (0D). (b) Graphene/hexagonal lattice rolled into cylinders as nanotube (1D). (c) Graphene with carbon atoms in a hexagonal lattice (2D). (d) Stacks of graphene with several layers as graphite 3D. Image is taken from (109).

Graphene is characterized by various excellent properties, such as exceptional mechanical strength, chemical inertness, high electrical and thermal conductivity, the thinnest material ever discovered and impermeable to many gases. All these versatile

properties combined in graphene have proved it to be this century breakthrough material. The fact that high-quality, clean graphene (114) can be obtained simply and economically in a laboratory has accelerated research on graphene and other 2D materials, including the development of nanopores.

2.2 Atomic orbitals of graphene

The remarkable properties of graphene, particularly its electronic properties and mechanical strength are due to its unique electronic band structure and hybridization. Carbon is an exceptional material and it makes different types of bonds (single, double and triple) to create versatile compounds. To understand the carbon bonds formed in graphite, the electronic configuration of carbon atoms in their ground state, excited state and its hybridization are discussed here.

Carbon has four unpaired electrons to form four covalent bonds with other elements. The electronic configuration of the carbon atom in its ground state is expressed as $1s^2 2s^2 2p^2$ and four valence electrons available for bonding are $2s^2 2p^2$. When one electron jumps from the 2s to the 2p orbital, the unpaired electrons are made available to create electronic structure $1s^2\ 2s^1\ 2px^1\ 2py^1\ 2pz^1$. Due to bond formation, the energy of the system decreases and in turn reconfiguration of valance electrons takes place which is referred to as hybridization. When hybridization takes place one electron from 2s orbital jumped into one of the 2p orbitals, and a combination of these orbitals create three new hybrid orbitals (115). The 2*s* and 2px, 2py orbitals hybridize to form sp^2 hybrid orbitals with one electron filled in each orbital. Three newly formed hybrid orbitals have trigonal planar geometry with an angle of 120° and provide energy stability and elastic strength to the graphene honeycomb structure. Figure 2.2 is presenting the orbital hybridization and bonding process of graphene.

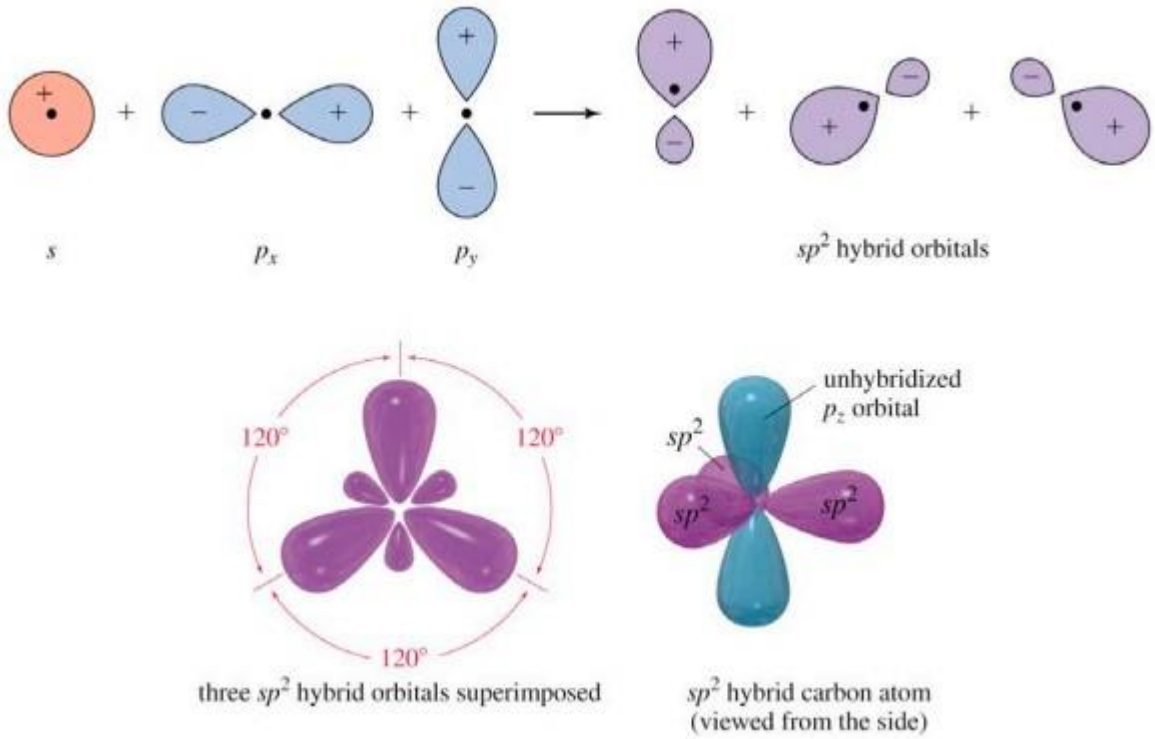

Figure 2.2: Orbital hybridization and bonding process of graphene. sp^2 hybridized orbitals. One 2s orbital and two 2px and 2py orbitals hybridize to sp^2 orbitals, with trigonal planar geometry with an orbital angle of 120°. sp^2 hybrid orbitals overlap to form $\boldsymbol{\sigma}$ bond, remaining 2pz orbital overlap to form $\boldsymbol{\pi}$ bond and is perpendicular to the planar structure. Image is taken from (116).

The three sp^2 hybrid orbitals form a $\boldsymbol{\sigma}$ covalent bond with their nearest neighbour carbon atoms 1.42 Å apart in honeycomb hexagonal lattice structure. Left behind 2pz orbital, which is not involved in hybridization remains unpaired and is responsible for the high charge carrier conduction of graphene. The 2pz orbital is located perpendicular to the plane formed by three sp^2 hybridised $\boldsymbol{\sigma}$ bonds and forms delocalised π bonds in layers with adjacent paralleled neighbours. In graphite, layers of sp^2 hybridized carbon atoms are stacked together to form a hexagonal lattice. There is a week interaction between the layers which makes graphite easier to exfoliate (115).

2.3 Graphene preparation

Graphene can be made with many different techniques. Mechanical exfoliation was the principal method to produce all the flakes needed to fabricate capillary devices in this study.

2.3.1 Mechanical exfoliation of graphene

High-quality monolayer graphene is produced by mechanical exfoliation using scotch tape (111). This method provides a clean and defects free structure on the substrate (117, 118). Bulk graphite is repeatedly peeled off on the scotch tape surface by applying normal force or sheer force on the graphite layers (119). This repeated peeling process would separate the graphite layer and become thinner by exposing fewer layers or a single layer of graphene in the process

Thin graphite on the adhesive tape is then transferred to the substrate by sticking this tape onto the substrate. The tape is then removed from the substrate mechanically to get the different layers of graphene on the substrate. Normal force and shear forces which are responsible for the fragmentation of the bulk crystal to thin crystal is shown in figure 2.3. Step by step process for the exfoliation of 2D flakes onto the substrate of choice is shown in figure 2.4 below.

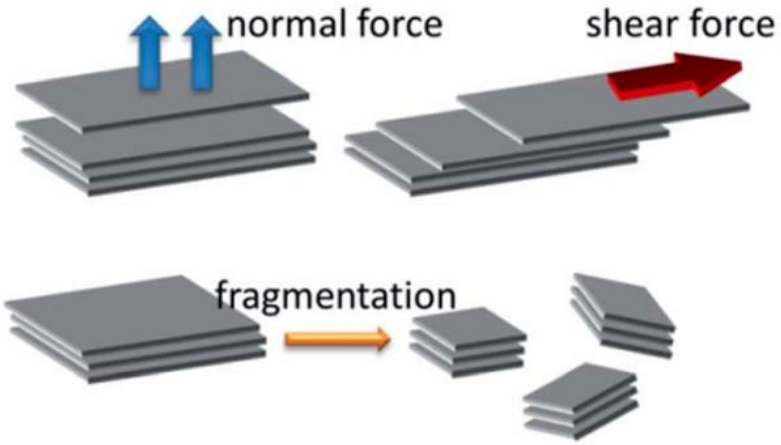

Figure 2.3: Exfoliation process of 2D materials. Mechanical exfoliation route in graphite exfoliation results from normal force, shear force or fragmentation. Image is taken from (119).

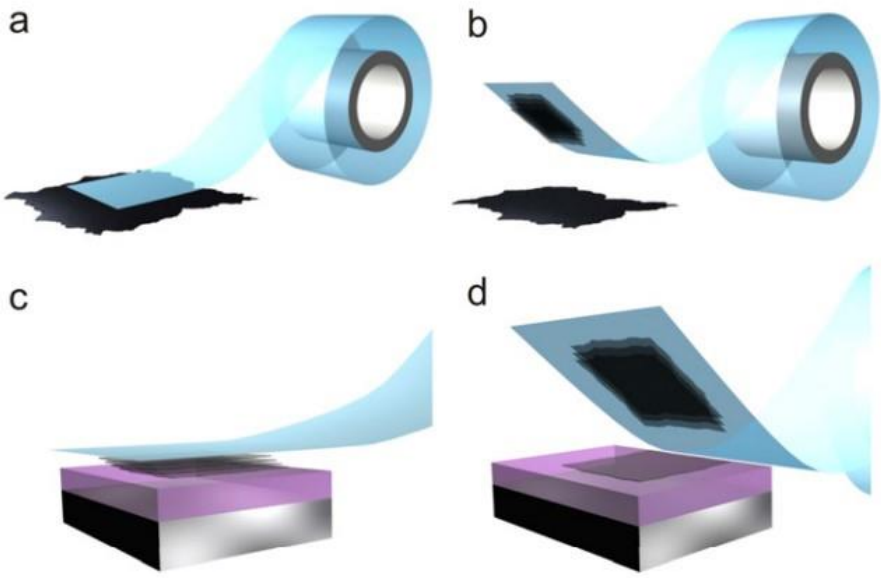

Figure 2. 4: Exfoliation of 2D crystals by tape. (a) Adhesive tape is pressed against a 2D crystal. (b) Tape is peeled a few times to crystal attach few layers to the tape. (c) The tape with thin crystals of layered material is pressed against the substrate. (d) Upon peeling off, the bottom layer of the crystal is left on the substrate. Image is taken from (120).

2.3.2 Other methods of producing graphene

Mechanical exfoliation is the principal method of producing clean, high quality and defect-free graphene flakes but it is time-consuming, low yield and not suitable for

large scale and mass production. In recent years several other methods have been reported to produce graphene for different research and application purposes.

The chemical vapour deposition (CVD) method has attracted a great deal of attention and is perhaps the most studied method of producing large scale graphene(121). In CVD, graphene is grown by thermal decomposition of hydrocarbons using carbon compounds (CH_4, C_2H_2, etc.) as a carbon source at elevated temperatures (up to 1000 °C) (122). Hydrocarbons thermally decompose to carbon radicals and grow uniformly with fewer grain boundaries on the catalytic substrates i.e. copper foil or other metal substrates (Ni, Pt, Pd, Rh etc). Carbon atoms segregate on the surface of the bulk metal to grow graphene.

Ni, Cu and Ni-Cu alloy have received more attention as a graphene substrate material (123-125). Thin Cu films yield (typically) single-layer graphene growth because of its low carbon solubility and Ni typically yield few-layer graphene, whereas the Cu-Ni alloy thin films yield high-quality single layer and bilayer graphene separately. The difference in their carbon solubility (9,000 at. (Atomic) ppm at 900°C in Ni or 7.4 at. ppm at 1,020°C in Cu) leads to produce multilayer thick graphene on Ni and monolayer graphene on Cu (126). Deposition temperature, cooling rate and growth environment are important deterministic parameters for the thickness and quality of the graphene obtained through CVD (127).

Epitaxial growth of graphene is another way to get large-area graphene layers. It involves thermal decomposition of silicon carbide (SiC) (128, 129) at high temperature and low pressure where silicon carbide (SiC) substrate reduces to graphene. CVD graphene on copper provides high-quality graphene in large sizes (30 inches) (122, 130, 131) as compared to reduced graphene oxide or graphene epitaxially grown on silicon carbide.

Liquid-phase exfoliation (LPE) is a key method of producing thin flakes in large quantities involving the exfoliation of graphite(132) or other 2D layered materials(133) with the assistance of sonication in solvents(134). It offers upscale production and good quality at a reasonable cost but few-layer graphene produced is usually small with average lateral dimensions of <1 μm. It is important to choose a suitable liquid whose surface tension enables graphite crystallites to extend into a larger surface area (132). Liquid exfoliation is a promising method in conductive ink and ink printable

electronic circuit applications. Figure 2.5 is presenting the schematic comparison of different routes for the production of graphene.

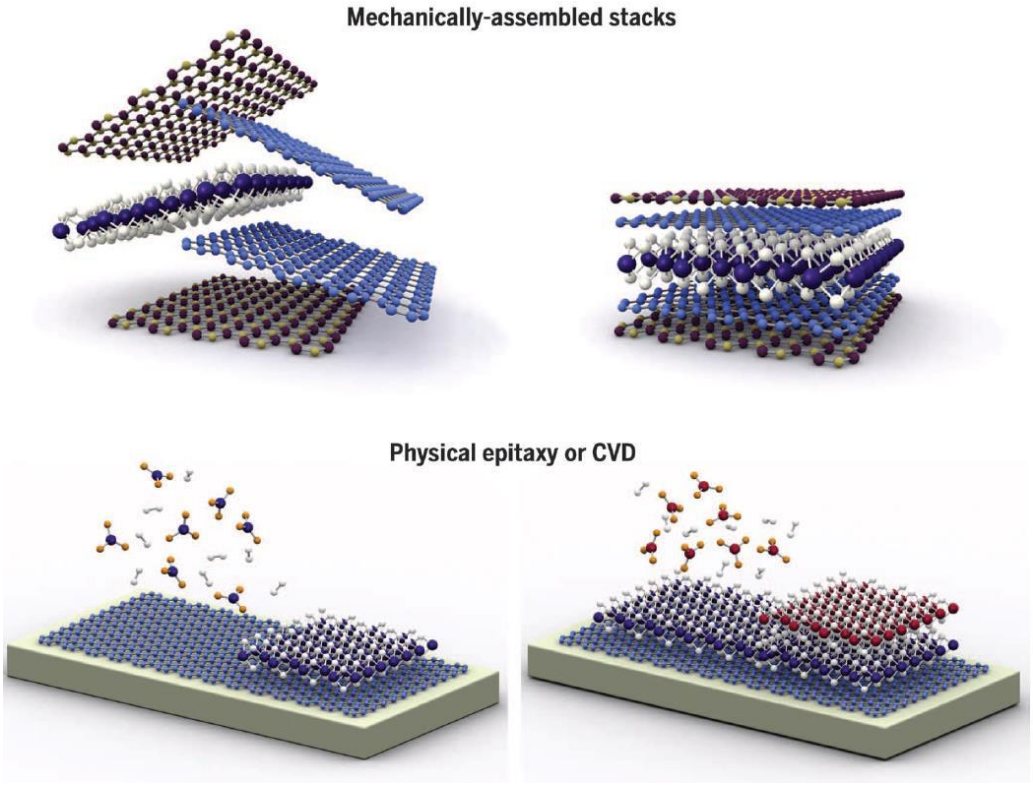

Figure 2.5: Schematic comparison of different routes for production of graphene i.e., mechanically-assembled stacks and physical epitaxy or CVD method. Image is taken from (121).

There is another method to produce large scale graphene by chemically modifying graphite. In this method, graphite is chemically converted to graphite oxide and then dispersion and exfoliation of graphite oxide are done in the liquid phase to produce sheets of graphene oxide (GO). GO is reduced by thermal annealing or chemical reducing agents to produce graphene (135, 136). This method provides a high yield of graphene but the reduction of oxide leave behind structural defects which need to be tailored before using it for different applications. (137, 138). In the context of nanofluidics, as discussed in chapter 1, GO sheets can be assembled into 2D-laminate membranes with channel size < 1 nm.

2.4 2D materials beyond graphene

There are plenty of 2D materials apart from graphene which can be mechanically exfoliated down to a single layer. In fact number of atomic layers stacked up in these materials also have van-der-Waals forces in between the layers. These van-der-Waals forces are weak enough to enable different layers to isolate into two-dimensional individual sheets.

Among different layered materials, graphene and hexagonal boron nitride (h-BN) are the simplest layered materials with atomically thin hexagonal sheets. Other layered materials i.e. transition metal dichalcogenides (TMDs) have more complicated crystal structures. In this section, we discuss the fundamentals and electronic properties of hexagonal boron nitride (h-BN) and molybdenum disulfide (MoS_2).

2.4.1 Hexagonal boron nitride

Boron nitride (BN) is a chemical compound of boron (B) and nitrogen (N) that doesn't exist naturally and has a similar crystal structure and properties to carbon. BN polymorphs have four different crystalline structures i.e. hexagonal BN (h-BN), rhombohedral BN (rBN), cubic BN (cBN) and wurtzite BN (wBN) (139). Hexagonal BN (h-BN) perfectly parallels the crystalline structure to graphene and possess similar physical properties. The other three polymorphs have a parallel with a carbon allotrope, e.g. rBN with rhombohedral graphite, cBN with diamond, wBN with lonsdaleite (wurtzite diamond) (139).

h-BN is an insulating isomorph of graphite and has a layered honeycomb-like crystal lattice. One boron and one nitrogen atom in its unit cell occupy the A and B sub-lattices in the Bernal structure(140). h-BN has AA' AA' stacking (figure 2.6 a) with the same atoms from different layers exactly aligned on top of each other.

Boron and nitrogen atoms in each lattice are bonded together by strong covalent σ bonds and form sp^2 hybridisation of atom orbitals in the layered structure but interatomic bond (π bond) between two successive hexagonal layers is weak (139). Both atoms (B and N) in the h-BN crystal have different electronegativity. The electronegativity of the N atom is higher, which makes the π electron locate mostly

near the N atom. P_z orbital in B atoms are vacant and in N are occupied by paired electrons. This makes h-BN a perfect insulator and white in colour (139). h-BN is considered the most appealing substrate to improve the quality of graphene devices because it has an atomically flat surface, be able to synthesise free from impurities, dangling bonds and charge traps (140, 141).

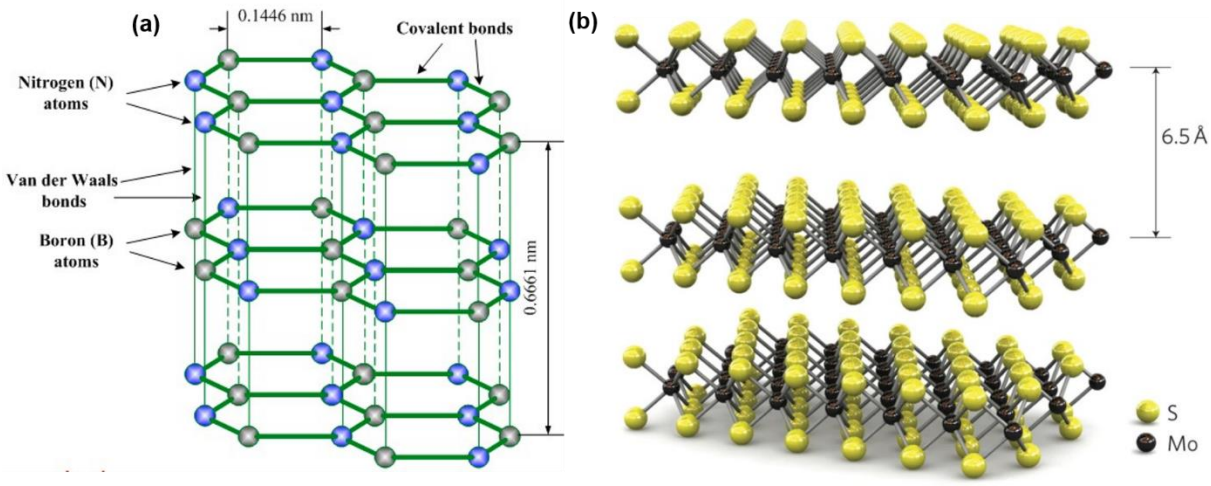

Figure 2.6: Lattice structures of h-BN and MoS_2. In a) h-BN lattice, nitrogen atoms are in blue and boron atoms are in grey colour. The B and N atoms are combined with covalent bonds. (b) MoS_2 lattice, M represents transition metal (Mo), X represents chalcogen (S). The distance between layers in (a) is 3.4 Å in (b) is 6.5 Å. In (a-b) layers are held together with van der Waals forces. Image (a) is taken from (142) and (b) from (143).

2.4.2 Molybdenum disulphide

Molybdenum disulphide is from the group of transition metal dichalcogenides (TMDCs) which have the formula MX_2 (M represents transition metal and X represents chalcogen) (121). TMDCs have a wide range of electronic properties (from insulating to semiconducting). The transition metal of TMDCs comes from the IV (Ti, Zr etc.), V (V, Nb etc.) and VI (Cr, Mo, W etc.) groups; the chalcogen elements are S, Se or Te (144). In TMDCs each monolayer consists of three layers of stacked atoms and also have a hexagonal structure(121). The transition metal atoms packed in between two layers of chalcogen atoms with the form X-M-X (figure 2.6b)

Analogous to graphene and other 2D materials, TMDCs can also be produced by mechanical exfoliation of the bulk crystal. Some other promising techniques include liquid-phase exfoliation (144, 145), CVD growth on a metal substrate (146, 147) and epitaxial growth on gold (Au) substrates(148) and two-step thermolysis process (149).

In the context of nanofluidics, TMDC can host apertures, which are nanometers to as narrow as a few atoms wide. These apertures on monolayer tungsten disulfide (WS_2) membranes permits the gas flows as the ultimate atomic limit of the pores (150), which will be discussed in chapter five.

2.5 Van der Waals heterostructures

Since the discovery of graphene, a lot of research has been done on the studies of freestanding graphene or substrate supported graphene to get their remarkable properties and probably has passed their zenith. A combination of individual stacked layers form the van der Waals heterostructures and could potentially provide unique properties from their original counterparts. Van der Waals heterostructures using various 2D materials provide the way to the discovery of new intrinsic properties of graphene and 2D materials and help design different structures for a range of properties and applications. Recent developments in the technology of van der Waals heterostructures have led to the observation of new physical phenomena, and realization of functional devices for applications of biosensing (151, 152), solar cells (153, 154), photodetector (155, 156) and gas sensing (157).

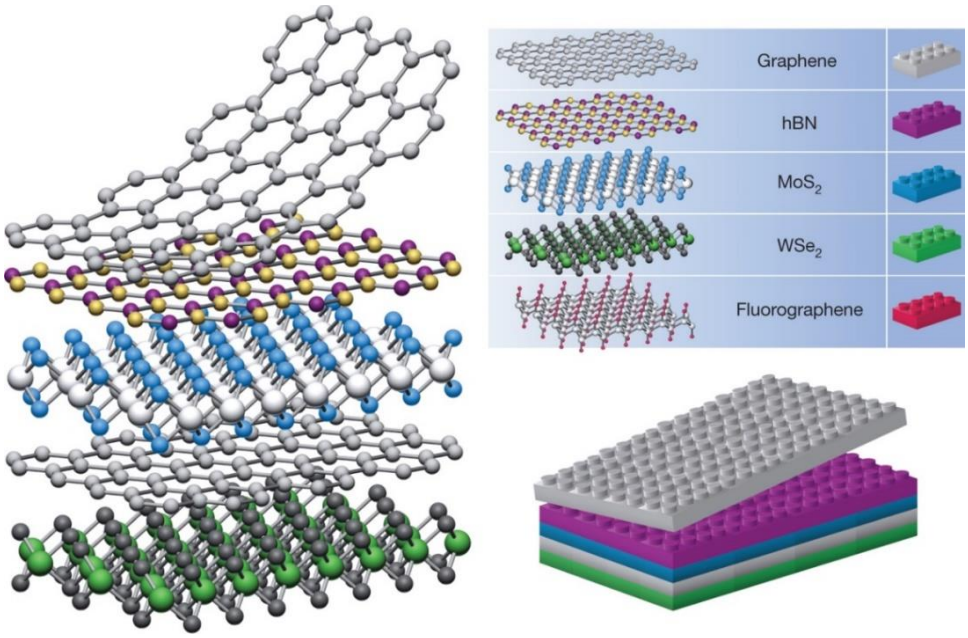

Figure 2.7: Building van der Waals heterostructures. 2D layers of various crystals arranged in form of lego-blocks on top of each other for the construction of Van der Waals heterostructures. Image is taken from (158).

van der Waals heterostructures can be assembled using the analogy of atomically thin lego-blocks (figure 2.7). Before the construction of van der Waals heterostructures, a few factors need to take into account i.e. structure of the material, thermal and chemical stability in bulk form. Materials that have an anisotropic structure in their bulk form can only be used for constructing such heterostructures because they have weak interlayer van der Waals bonds in the z-direction. Also, the thermal stability of bulk form is a very important factor as the melting point of the material decreases with its thickness. Chemical stability also needs to be considered before because the majority of the available 2D materials decompose and oxidize in the air or they need to exfoliate in an inert atmosphere before encapsulation with h-BN or graphene (159).

Most of the two-dimensional heterostructures are composed of stacking individual flakes of different materials on top of each other. This method provides individual layers of two-dimensional materials with outstanding qualities but it is a time-consuming process. Alternative techniques have also been developed for mass production such as synthesis of large-area crystals grown by CVD (160), direct growth

of heterostructures by CVD or physical epitaxy (161-163) etc. Apart from the new physicochemical properties arising from the fabrication of van der Waals heterostructures which combine the physics of various atomically thin materials, this has paved the way for engineering new systems at the atomic level.

For fabrication of the van der Waals heterostructures, two main approaches are followed which are top-down (164) and bottom-up (161, 162, 165). In a top-down approach various mechanically exfoliated layered crystals are stacked on top of each other. These crystals are stacked one above the other by the transfer of individual layers through different transfer techniques i.e. dry transfers (166) and wet transfers The bottom-up-up method involves either the direct synthesis of different two-dimensional crystals in a particular sequence or the direct growth of individual two-dimensional layers, followed by the transfer process. Heterostructures obtained through these two approaches usually requires different transfer techniques; dry transfer for mechanically exfoliated crystals and wet transfer for the synthesized ones.

Practical nanochannels with graphene walls with angstrom scale precise dimensions are fabricated using van der Waal heterostructures to study the molecular transport (gas and ions) will be discussed in detail in the next chapter in this thesis.

Before we discuss the device structure, we shall discuss the properties and the phenomenon involved for fluid flow studies (gas and ion transport) as the bedrock on which our study builds, and they will be referred to as we go along.

2.6 Mass transport properties

Transport of gaseous molecules will be studied to probe the nature of molecule wall interactions, permeation and selectivity of the gases through the atomic scale channels. Ions transport through the fabricated channels will be studied in the electrolyte reservoir between these channels to see the coupling of ions and water molecules at the solid-liquid interface. The ion transport through the channels is affected by the pressure gradient and potential difference between the two sides of the channels.

In addition to gas transport in angstrom scale channels, ion transport is a good model system to probe the roles of surface charges, flow type and surface friction in the

transport. The well-defined geometry and clean interior of the channels made with 2D materials promote fluid flow that renders new functionalities to nanofluidic devices.

Fundamental understanding of fluid transport at sub continuum regime (< 1nm) requires mass (gas and ion) transport dynamics to be characterised through these ultimately small structures. The properties associated with the gas flow inside these small structures have been characterised by the Knudsen equation which will be discussed in the next section.

2.6.1. Knudsen diffusion for gas flow measurements

The flow rate (Q) of gases in long channels (cross-sectional radius R) much smaller than the length L, due to a pressure difference ∆P across it is described by applying mass and momentum conservation, to obtain Poiseuille's law:

$$Q = \Delta P \pi R^4 / 8 \mu L, \tag{2.1}$$

where the gas is treated as a bulk material because bulk properties like viscosity μ play a significant role due to frequent intermolecular interactions. In the case of nanochannels, Poiseuille's law is invalid as the gas molecules are separated by distances greater than the cross-sectional dimension of the channel and thus not in the bulk state.

The dynamics of the gas transport within nanostructures are significantly different from those in larger dimension systems. At room temperature and ambient pressure, most gases have their mean free path around 100 nm. So depending on the exact value of the mean free path and the dimension of the structure, the transport of gas molecules could be governed by their collisions with the walls of the structure or that with each other. Depending on which factor supersedes, different regimes of flow are defined.

In 1909 Knudsen put forward a molecular theory to describe the mass flow rate as,

$$Q = \alpha \left[A \Delta P \sqrt{M / 2\pi R T} \right], \tag{2.2}$$

Where A is the cross-sectional area of the nanochannel and M is the molecular mass of the gaseous molecule (167). The part in the square brackets is the flow rate of molecules into the channel and α is the transmission coefficient of the channel that describes the fraction of molecules that pass through the channel without loss in energy and momentum. Knudsen derived this transmission coefficient for different channel geometries by assuming diffuse reflections at the channel walls.

In the Knudsen diffusion regime, molecules bounce back and forth between the walls of the medium without colliding with each other. The driving force for Knudsen diffusion is the partial pressure gradient, which is equivalent to the total pressure gradient in a single gas system (168). Due to the relative absence of inter-atomic collisions inside nanoconduits atomic-scale capillaries are good experimental setups to study atom-surface interactions in isolation. Knudsen and Smoluchowski has modelled the flow through such nanochannels, with the atom-wall collisions treated as purely diffuse reflections, and formulated equations that described the flow rate of gases through channels of different geometries.

Ionic transport under pressure gradient also characterises the atom surface interaction. If the transport is performed under different forces i.e., voltage and chemical gradient different materials show different responses which will be discussed in chapter 6 of this thesis. Ionic streaming is characterised using streaming current which will be discussed in the next section

2.6.2. Ionic streaming measurements

In liquid environments, transport in nanofluidic conduits that are larger than molecules or ions size is dependent on differences in species diffusivity, steric effects, chemical affinity and electrostatic interactions, including surface charge (169-171).

The interaction of fluid species within the conduits at sub continuum (< 1nm) range can be probed through ions flow under different forces. Ions transport under potential difference provides the electric currents. Streaming current provides the coupling of ions and water under forces (pressure and voltage).

A streaming current is an electric current that originates when an electrolyte is driven by a pressure gradient through a channel. Streaming current is proportional to the

pressure change, changes with the channel height and with salt concentration. Streaming current studies the surface charge phenomena and potential arises due to electro-kinetic fluid in confined conduits because of the large surface to volume ratio. It is sensitive to the polarity of surface charge and reverses the direction upon changing the positively or negatively charged channel surface. Streaming current is suggested to provide a simple and effective way of converting hydrostatic pressure gradients into electrical energy (172-174).

To quantify streaming current, the ionic current is measured versus time while increasing pressure in discrete steps by a pressure pump (figure 2.8a). Each pressure increment last for a few seconds (15 sec) with the delay between two successive increments to measure the ionic streaming current. Current overshoots with a pressure gradient, saturate to a constant value and then drop on pressure removal (figure 2.8b). The streaming current is defined as the difference between the saturation value reached by the ionic current while pressure was applied and its value when the pressure was released. Figure 2.8b shows ionic current measurement as a function of time with no bias voltage applied. The pressure-driven component of the ionic current I, defined as the streaming current I_{str} is equal to (106, 107),

$$I_{\mathrm{str}} = I(\Delta \mathrm{P}, \Delta \mathrm{V}) - I(\Delta \mathrm{P} = 0, \Delta \mathrm{V}) \tag{2.3}$$

Streaming current results from the transport of ions carried by a pressure-induced flow which is explained in figure 2.8b.

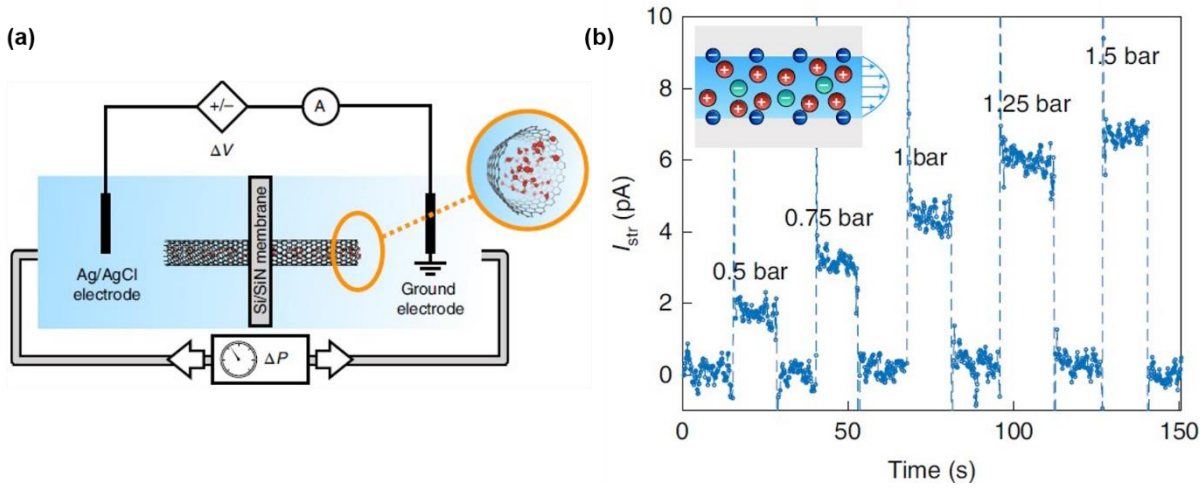

Figure 2.8: Experimental set-up and streaming current (pressure-driven current). (a) Schematic of the nanofluidic transport cell under pressure gradient for

streaming current measurements through a 2nm single CNT membrane. Membrane is immersed between two potassium chloride (KCl) filled reservoirs connected to a pressure controller to execute a pressure gradient in both directions for ionic transport measurements. (b) The ionic current is measured as a function of time for the salt concentration of 1M and pH 10.8 without a bias voltage ($\Delta V = 0$) for a range of pressures which is called streaming current. The current overshoots when the pressure is applied and then saturates to a steady-state value and drops to zero upon pressure release. A schematic of the streaming current through a CNT is shown in the inset. Image is taken from(106).

Carbon nanotubes are well studied to explore different physical and electrochemical phenomena arising in nanoconduits (106, 107, 172) described in terms of streaming current in figure 2.8 b.

Of vital importance to this study is how the pressure, mean free path and the dimension of the nanostructure affects the interaction of mass species (gas, water and ions) with the surface of the nanofluidic conduits. This study will also probe the nature of the interaction of fluids in the angstrom-scale dimension.

To check the response of our channels under voltage and pressure difference for streaming currents and behaviour of fluid–ion dynamics across the channels is studied through the capillary devices and detailed discussion of the results will be presented in chapter 6 of this thesis.

Detailed fabrication procedures and tools used will be discussed in detail in the next chapter.

Chapter 3

Device fabrication and experimental techniques

In this chapter, experimental procedures for assembling 2D materials to fabricate atomic-scale capillary devices will be reviewed. I will go through the tools and techniques used to define the geometry and structure of the channels. In addition, the processes to carry out device fabrication i.e. photolithography, reactive ion etching (RIE) which is dry etching and KOH (potassium hydroxide) wet etching for drilling through-holes on SiN_x/Si substrate will be discussed in detail. Electron beam (e-beam) lithography and etching for defining the channels in the graphene crystal will be discussed. The flake transfer methods used during the fabrication process will be reviewed as well.

3.1 Flake preparation

Graphene and other 2D materials (MoS_2 and h-BN) can be exfoliated with mechanical cleavage on SiO_2/Si. Graphene exfoliation is done by cleaving single-crystal natural graphite. Silicon oxide covered wafer (SiO_2/Si) provides better reflection and hence provide easy identification of graphene and other 2D flakes with an optical microscope. Graphene absorbs only a small amount of light and the oxidised Si layer provides an extra reflection layer and enhances the contrast for single layer-graphene (175).

The wafers used for exfoliation of 2D materials for this work are commercially available with the thickness of oxide layer i.e., 70nm, 90 nm and 290 nm. The thickness of the oxide layer is very important to allow flakes to be visible under an optical microscope. Most of the time, 290 nm wafers were used owing to the fact they give the best contrast needed for flake identification. Different nitto® tape types (BT-130E-SL, BT-150E-KL, BT-50E-FR, BT-150E-CM and 1009R-6.0) are used which give good-sized flakes and leave less tape residue. Depending upon the material (graphite, h-BN and MoS_2) being exfoliated, different tapes were used. The yield and quality of flakes vary for different tapes and materials. BT-130E-SL, BT-150E-CM are good for h-BN and are low tack

tapes. BT-150E-KL, BT-50E-FR, 1009R-6.0 are high tack tapes and good for exfoliating graphene and MoS_2 but not good for h-BN.

Tape used for exfoliation	Type of the tape	Observations
BT-130E-SL	Low tack	Very good for hBN flakes, good for graphene, not good for MoS_2
BT-150E-CM	Low tack	Very good for hBN, not good for graphene and MoS_2
BT-150E-KL	High tack	Very good for graphene, good for hBN and MoS_2
BT-50E-FR	High tack	Very good for graphene, good for MoS_2, not good for hBN
1009R-6.0	High tack	Very good for graphene and MoS_2, not good for hBN

Table 3.1: Comparison of different nitto tapes. Different nitto tapes used for the exfoliation of 2D (graphene, h-BN and MoS_2) materials.

Here, producing good flakes means leaving less tape residue and yielding flakes of larger lateral dimension (more than 10 microns) and a high number density of flakes on the wafer. On an average few flakes (typically, 3 to 10) of lateral size, 50µm can be obtained in a 2x2 inch size wafer. For graphene flakes' exfoliation with high tack tape, on average 2-3 thin flakes (monolayer to 5 layers) of lateral size, 30-50µm are obtained but with low tack tapes, small size flakes (< 20 µm) are obtained with tape residue. Some of the images of flakes obtained through these tapes have been presented below in figure 3.1.

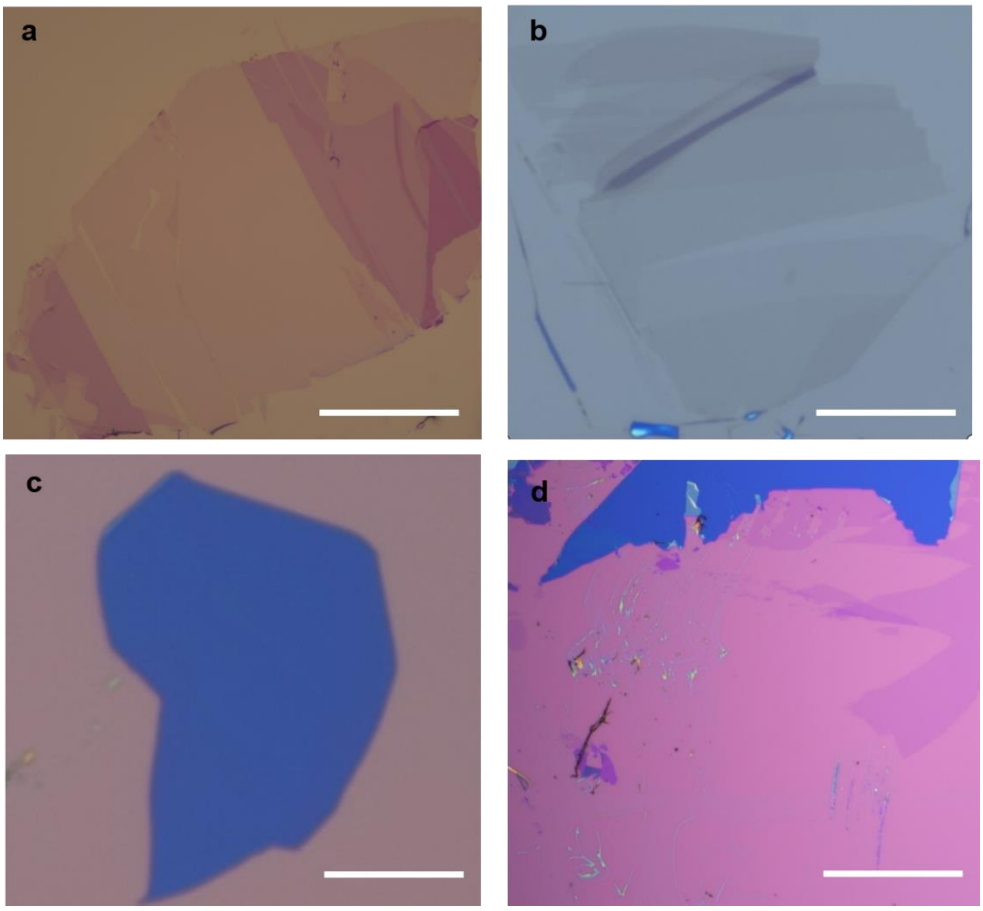

Figure 3.1: Flakes obtained with different Nitto tape. (a) is the graphene flake (b) is h-BN flake (c) is MoS_2 flake and (d) is the graphene flake with tape residue. Scale bar in (a-d) is 20 µm.

Good flakes with no tap residue and better yield are shown in figure 3.1 (a-c). Figure 3.1d is the image where tape residue is present on the substrate and the lateral size of the flake is small as compared to graphene flake in figure 3.1a.

Before the exfoliation of 2D flakes on an oxidized silicon substrate, wafers are cut into a suitable size (typically $2cm^2$) and subsequently cleaned with acetone and isopropanol (IPA) in an ultrasonic bath for 10 minutes each, followed by blowing them dry with filtered nitrogen. This cleaning step enables to remove the particles and chemicals adsorbed on the wafer surface. Soon after cleaning the wafers, SiO_2/Si substrate is exposed to oxygen plasma at low pressure for plasma cleaning for 10 minutes. Oxygen plasma reacts with hydrocarbons and contaminants adsorbed on the surface to clean and remove them. Sometimes heating is also done at 110 °C for 10

minutes on a hot plate for better yield as heating also promotes the flake adhesion to the substrate. The process of making flakes as described in figure 3.2 below.

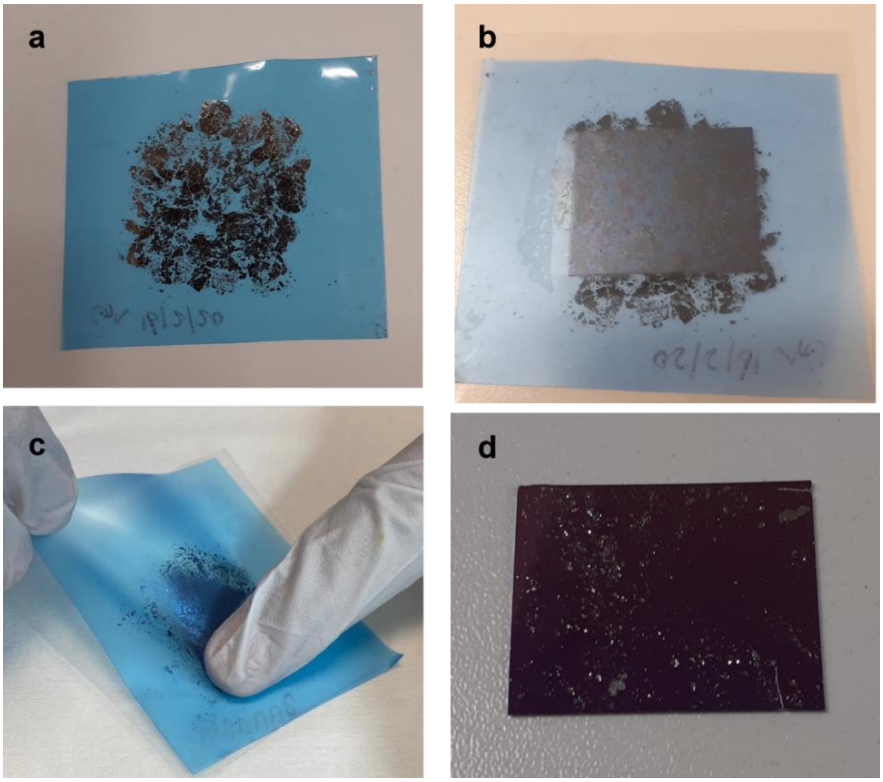

Figure 3.2: Procedure of making graphene flakes. (a) Graphite on a sticky tape pressed and repetitively peeled on the tape to separate the layers of graphite to get thinner graphite flakes. (b) Thin graphite crystals are pressed on a cleaned and plasma-treated substrate as soon as the substrate is removed from oxygen plasma treatment. (c) Tape removed with low angle exfoliation to get the thinner flakes. (d) After tape removal, graphite and thin graphene flakes on the substrate are ready to search.

3.1.1 Images of 2D material flakes on SiO_2

After tape removal, the SiO_2 substrate has different flake thicknesses and is ready (figure 3.2 d) for search and identification under an optical microscope.

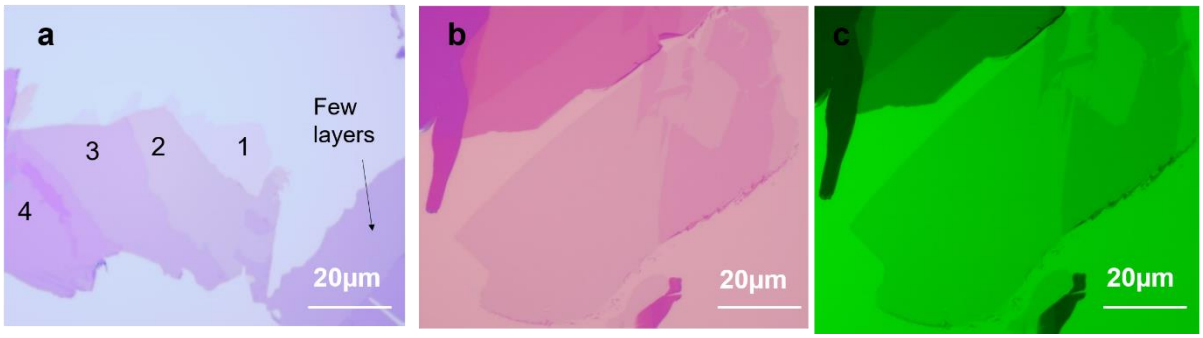

Figure 3.3: Optical images of mechanically exfoliated flakes. (a) Optical image of mono, bi, tri and four-layer graphene thin flakes combined with few layers graphene. (b) Monolayer flake to be used as nanochannels. (c) The same flake in (b) is seen through an optical filter of wavelength 520 nm, for enhanced contrast. All flakes are on 290 nm SiO_2 substrate. The scale bar is 20µm for all images.

Mechanically exfoliated graphene flakes on SiO_2/Si substrate are presented in (figure 3.3) from monolayer to few layers giving different contrast (figure 3.3a) and monolayer flake with the optical filter of 520 nm is also presented (figure 3.3c). Graphene exfoliation was done using high tack tape.

Hexagonal boron nitride (h-BN) crystal was peeled on the tape (water-soluble or low tack) and flakes were exfoliated on 90nm and 290 nm silicon oxide coated silicon wafers. 90nm silicon dioxide gives the best contrast for thin layers of BN and hence helps in searching the flake. MoS_2 flakes were prepared on the 290 nm SiO_2/Si substrate using both low tack and high tack tapes and gave good yield with low residue. MoS_2 flakes were exfoliated the same way as for graphite and h-BN exfoliation.

We have used the graphene flakes from monolayer to a few layers as spacers to define channels through e-beam lithography and etching which will be discussed later in this thesis. Graphite, MoS_2 and h-BN flakes are used as bottom and top materials in this thesis.

Identification of the thicknesses of graphene accurately is very important and usually done by optical microscopy as it is a simple and quick method for the identification of flakes.

3.1.2 Mechanical exfoliation of 2D materials on polymer

Graphene, h-BN and MoS_2 flakes are also prepared on the double-layer polymer substrate with the PMMA/PMGI (Polymethyl methacrylate/ Polymethylglutarimide) polymers. Thin flakes are easy to produce and observe with this method owing to better reflection due to added polymer layer and the lateral size of single-layer MoS_2 produced on the resists substrate (typically 50 μm) is generally larger than produced on the SiO_2/Si substrate.

PMMA used was (950 K molecular weight, 8% w/v in anisole). For bilayer polymer coating, PMGI is spin-coated on a plain silicon wafer or 290 nm SiO_2/Si wafer. This double layer polymer-coated flakes are used in a dry transfer technique which will be discussed later in this chapter in the transfer of flake section 3.5.2. Typical spin-coating speed is 4000 rpm and 7000 rpm with an acceleration of 1000m/s^2 for PMGI and PMMA respectively. PMMA/PMGI dual layer is baked on a hotplate for 5 minutes at 130 °C after each spin coating. After PMGI coating and baking, the substrate is cooled down before PMMA coating. A thin 2D crystal on a piece of adhesive tape is pressed onto the polymer layer and subsequently peeled off with a low angle peeling method to get the flakes (figure 3.4).

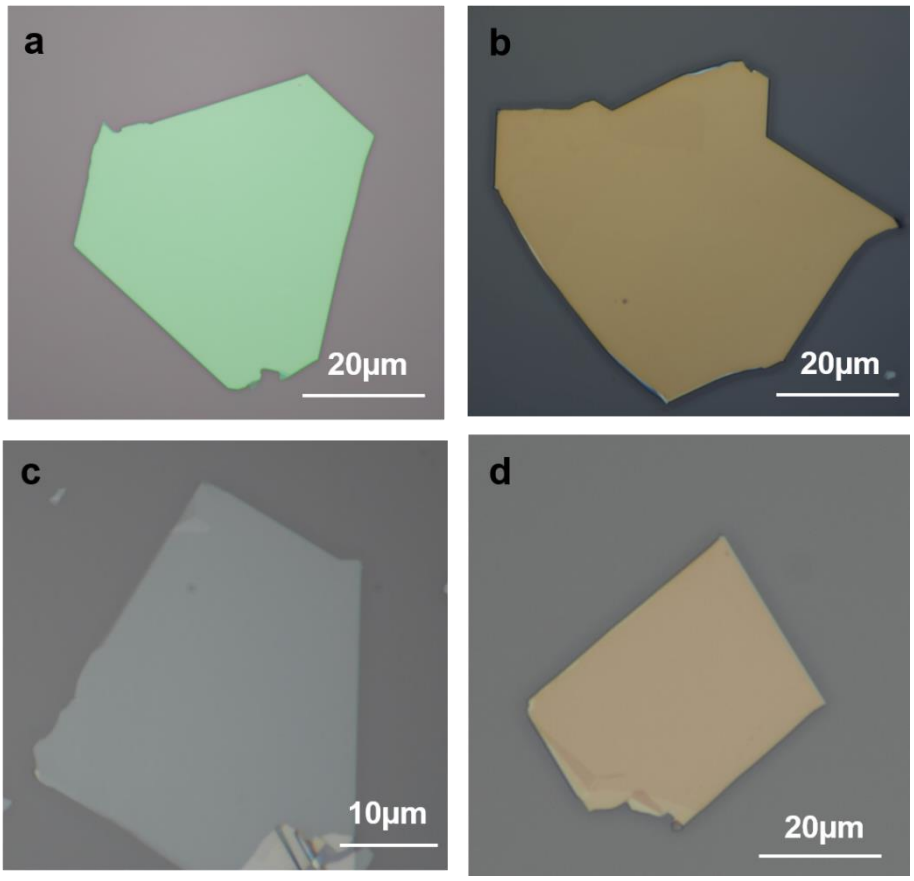

Figure 3.4: Optical images of mechanically exfoliated flakes with bilayer polymer. (a) Mos_2 flake serves as bottom (b) Mos_2 flake more than 100 nm in thickness serves as top. (c) h-BN bottom flake relatively thin as compared to top flakes (d) Thick h-BN flake serves as top. Bottom flakes are thin as compared to top flakes. All flakes are on PMGI/PMMA dual polymer layer.

3.2 Identification of 2D materials-characterization techniques

After the exfoliation and micromechanical cleavage, 2D flakes are searched and identified using different identification instruments amongst which optical microscope, atomic force microscope (AFM) and Raman spectroscopy are utilised for the work done in this thesis.

3.2.1 Optical microscope

An optical microscope is a primary technique for quick observation and identification of 2D flakes of different materials (graphene, h-BN and MoS_2).

By adjusting the exposure time and gain in the optical microscope, monolayer and thin layer flakes can be distinguished (figure 3.3a). The variation in the flake colour in the bright field help determine the thickness of the flakes. Different colour filters also aid in determining the layers and quality of graphene flakes (figure 3.3c). Apart from the thin graphene flakes, thick flakes of different thicknesses used for the bottom and tops are also identified depending on the colour contrast. Figure 3.5 presents bottom and top flakes used for making capillary devices of different materials (graphite, h-BN and MoS_2) on SiO_2/Si substrate. Thick flakes more than 100 nm in thickness are selected to serve as the top and bottom flakes are chosen to have thickness around 15-20nm. Bottom flakes are relatively thin as compared to top flakes. An optical microscope gives a different contrast for different flake thicknesses but exact thickness could be determined by atomic force microscopy.

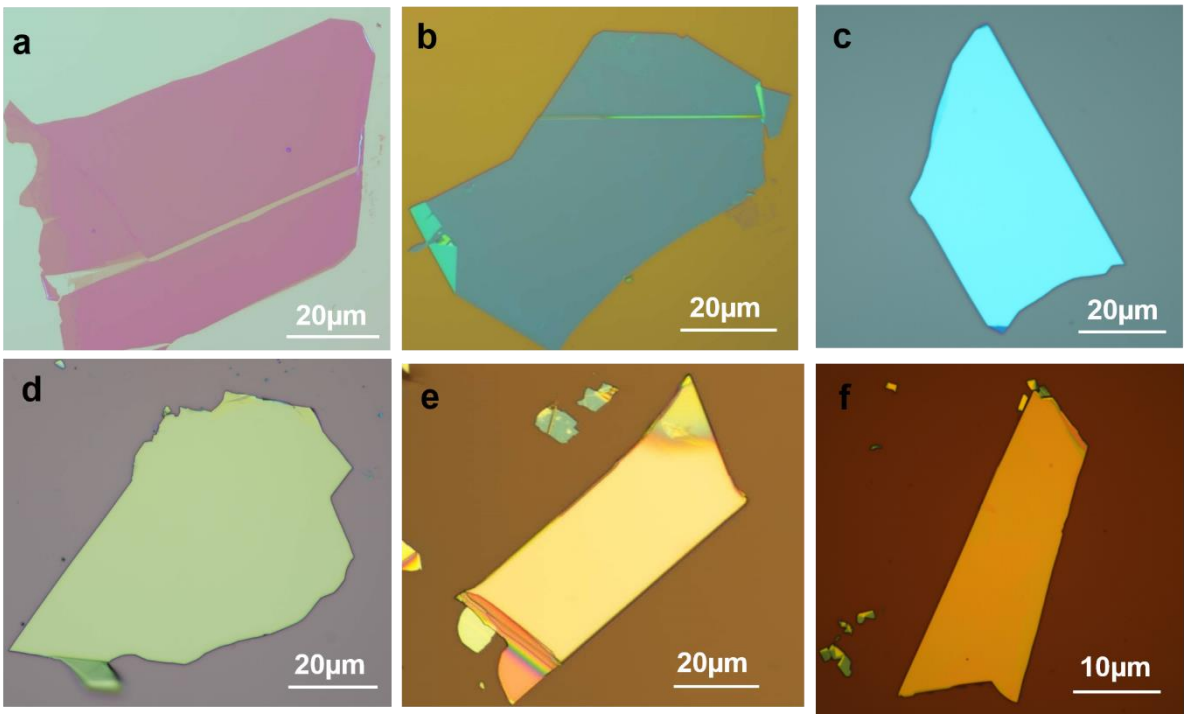

Figure 3. 5: Optical images of 2D materials used as bottom and top: (a-c) Flakes of graphite, h-BN and MoS_2 respectively serves as bottom. (d-f) Relatively thick flakes of graphite, h-BN and MoS_2 respectively more than 100 nm in thickness and serve as top layers for capillary devices. Graphite and MoS_2 are exfoliated on 290nm SiO_2/Si

and hBN on a 90nm SiO_2/Si nm silicon oxide wafer. Top and bottom flakes serve as walls for graphene capillary devices.

As exposure time, illumination intensity is not constant amongst different microscopes, this identification method is sometimes insensitive to determine the exact thickness of graphene layers so other methods are also used for verification of layer thickness.

3.2.2 Atomic force microscopy (AFM)

AFM is a high-resolution microscope that generates images by mechanically scanning a sharp tip (cantilever) over the sample surface. The sharp tip on the end of the cantilever raster scans over the surface, bending the cantilever and changing the amount of laser light reflected into the photodiode. The approach aims to measure the electrostatic force between the surface and the tip by recording the level of sensitivity of cantilever motion to present topographies in high resolution (176). AFM is capable of imaging insulators as well as conductors on the atomic scale.

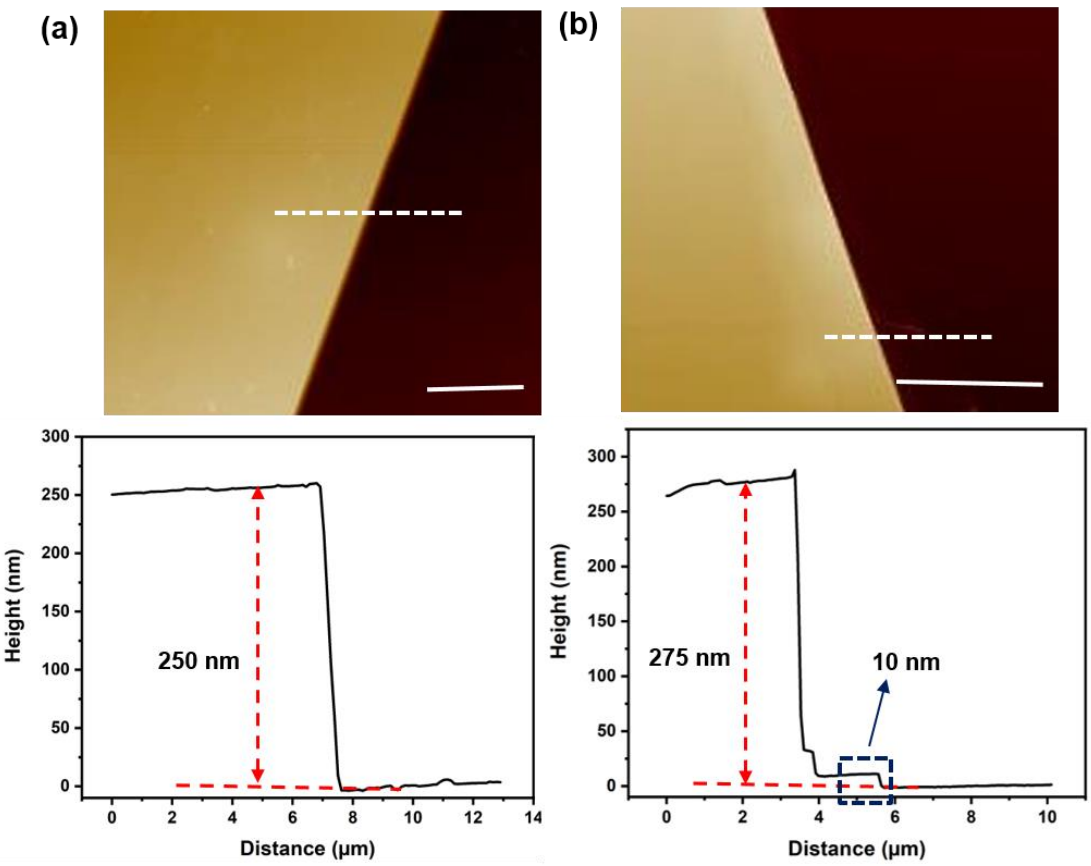

Figure 3.6: AFM images of h-BN and graphite flake for thickness measurement. AFM image and its respective height profile of thick (a) hBN and (b) graphite flake. Thin edge is present in graphite flake shown in blue colour box giving 10 nm thickness. Height profile is taken along the dotted line. Scale bar in (a) and (b) is equal to 5 μm.

The clear identification of the graphene layers is very important and for this reason, an atomic force microscope (AFM) was used to distinguish between graphene single layer and its few layers. AFM was also done to measure the step height (figure 3.6) of the flakes of different 2D materials from the substrate for the thicker flakes. Exact flakes thickness measurement is very crucial for top flakes to avoid sagging of the thin graphene flakes (called spacers) into nanochannels.

Thick flakes usually have undesired thin edges (figure 3.6 b) which often block the channels. Top flakes (less than 100nm) sag into the lithographically designed spacer and channels and affect the efficiency of the device so AFM measurements are very important to avoid the sagging and hence blocking of channels. AFM measurements were also used regularly for checking the height and width of the spacer/channels made with the electron beam lithography and etching and also for checking the cleanliness of the channels which will be discussed in detail later in this thesis.

3.2.3 Raman spectroscopy

Apart from AFM, Raman spectroscopy is widely used as a quick characterization technique to distinguish between single and few layers of graphene. Raman spectroscopy of graphene and graphite consists of two main peaks for the identification of graphene layers.

The G band appearing at 1580 cm^{-1} originates from in-plane vibration of sp^2 carbon atoms and the 2D or G' band at 2670 cm^{-1} originates from a two phonon double resonance Raman process, it is closely related to the band structure of graphene layers. The 2D band becomes broader and blue shifted when the graphene thickness increases from single layer graphene to multilayer graphene. D band is appearing at 1350 cm^{-1} and is for disorder band which is not present here is evidence of clean defect-free graphene flakes used for the devices. D-band is usually not present in pristine graphene monolayer on SiO_2 substrates (177).

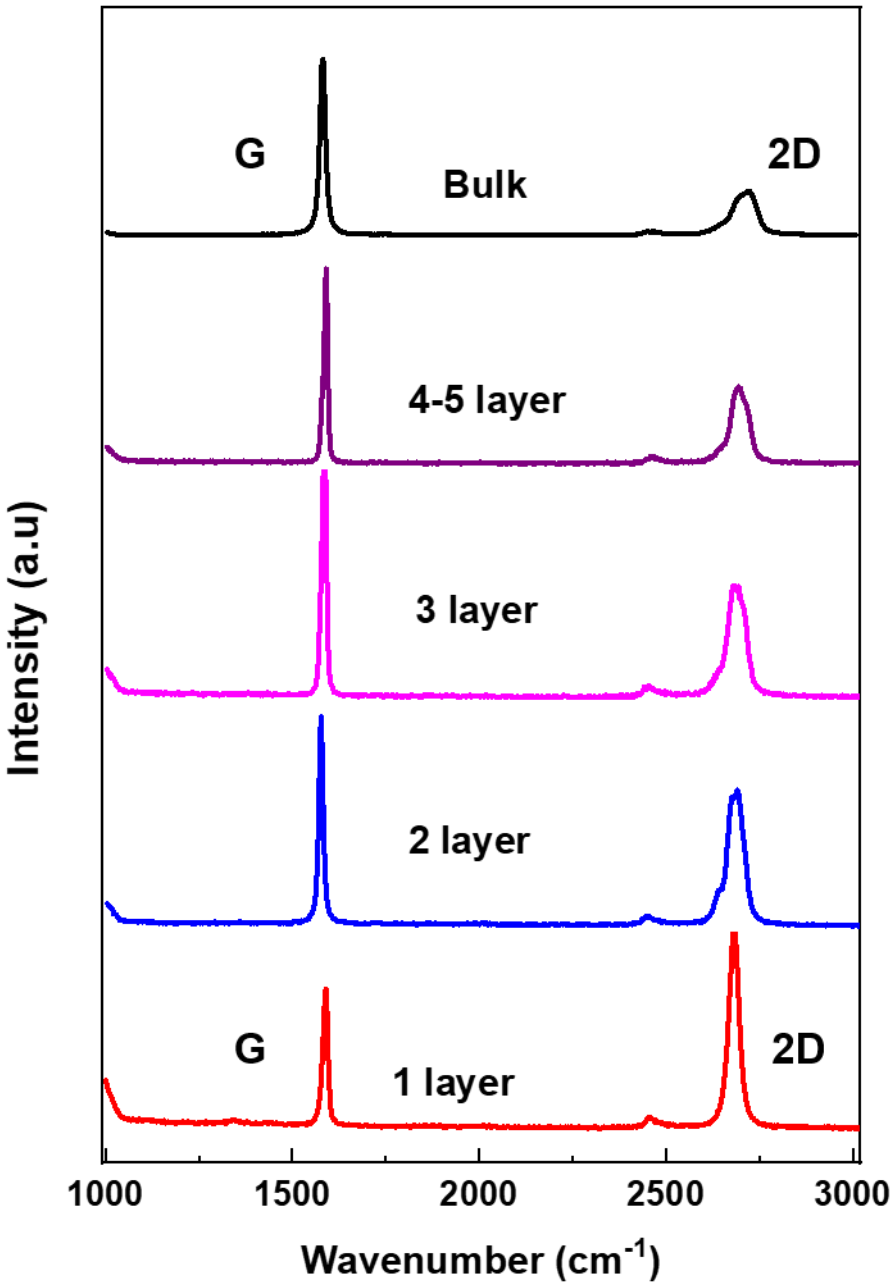

Figure 3. 7: Raman spectroscopy of graphene. Raman spectra of monolayer to few layer graphene and bulk graphite. Evolution of the Raman spectra at 532 nm with the number of layers. G peak appearing at 1580 cm^{-1} and 2D or G' band at 2670 cm^{-1}.

Raman spectroscopy of monolayer to few layer graphene and graphite (bulk) on SiO_2 substrate is shown in figure 3.7. The relative height of G and 2D peaks is a way to distinguish thin graphene flakes. Another feature from graphene Raman spectra is that G-band intensity increases almost linearly as the layer increases, and the shape (intensity) and position of 2D-band change from single to few layers. The position of

bilayer and few layer graphene 2D peak is upshifted compared to a single layer, which is illustrated nicely by Zhenhua et al; (177) Therefore, Raman spectroscopy can be successfully used to quickly identify single layer graphene to its bilayer and a few layers.

3.3 Techniques used for the fabrication of capillary device

To investigate the transport of different nanofluidic species (gas and ions) we have designed the structure with the possibility of the fluid going in and out through 2D materials capillary device. Channels are designed on the 2D flakes of graphite (ranging from monolayer to few layers graphene) through E-beam lithography and etching and encapsulated between different walls of 2D materials through van der Wall assembly to make capillaries. The final device has to have a substrate with a through-hole so that capillaries can be accessed by the nanofluids to go in and out of the capillaries for conductance or permeance measurements. The detailed procedure of fabricating the device is presented below.

3.4 Making an aperture in SiN_x membranes

For defining a hole through a substrate, photolithography with the combination of reactive ion etching (RIE) and KOH wet etching was used. This process drills a hole of specific size and shape which is usually a rectangular hole (3x25 μm^2) straight through the substrate. This is done in two steps, in the first step photolithography and a combination of etching is done to get the SiN_x membrane. The second step involves a similar procedure for defining an aperture in the SiN_x membrane. Double-sided polished 500 nm SiN_x coated on a 500 µm silicon substrate was used for this process. A detailed description of the process is presented here.

3.4.1 Photolithography

Photolithography is a patterning technique that is used to transfer a geometric pattern from a photomask to a light-sensitive polymer which is called a photoresist. There are two types of photolithographic resists: positive tone resists and negative tone resists. Upon light exposure, photoresist reacts with light to change their chemical composition by increasing or decreasing their solubility in an exposed area, which later dissolves in a basic aqueous developer. Positive tone photoresist selectively exposed to light through a mask, chemically reacts with the light to change its composition. The exposed part then can be dissolved in a solvent (MF-319) to provide a pattern onto the substrate (178).

Photolithography was earlier dependent on photomasks to transfer pre-designed patterns. Now a days a focused laser beam is used to define patterns by shining laser light directly onto photoresist with a software designed pattern and usually called maskless photolithography. This photolithography technique provides quick and accurate exposure with sub-micron resolution.

Microtech Laser Writer (LW405B+ with a 405nm GaN diode laser) was used for doing photolithography of double-sided polished 500 nm SiN_x/Si wafer. The resolution of the LW405B+ is 500nm.

A layer of photoresist S1813 (positive photoresist) is spin coated on the SiN_x/Si with a spin speed of 3000 rpm using the acceleration of 1000 m/s^2 for 60 seconds and subsequently heated for 1 minute at 110 °C on the hot plate. The photoresist is spin coated on both sides of the wafer. On one side it serves the purpose to expose laser light to define a pattern and on the other side resist is spin-coated to avoid any scratches from spin coater, laser writer chuck or any other surface. This step is important because after photolithography and KOH etching SiN_x membrane will appear on the other side which will then be used for stacking all the layers for fabricating a device.

To start the process, a square pattern of 800x800 μm^2 is designed with the laser writer compatible software (Clewin). The focused laser beam is aligned on the substrate to expose the substrate with photoresist under conditions d-step 1, filter 3% and dose 254 mJ/cm to pattern the design to get the required membrane size (after RIE and

KOH). After this exposure substrate is developed in MF-319 photoresist developer for 1 minute to remove the photoresist from the exposed region on the substrate as described in figure 3.8. To stop further development, the substrate is thoroughly rinsed in de-ionized water for 1 minute. Lithography is done in two steps first for making a SiN_x membrane (100x100 μm^2) in SiN_x/Si substrate with successive etching (first dry etching through reactive ion etching (RIE) and then wet KOH etching) and in the second step, a rectangular aperture of (3x25μm^2) is drilled in the SiN_x membrane through second photolithography and etching step which will be discussed later in the thesis.

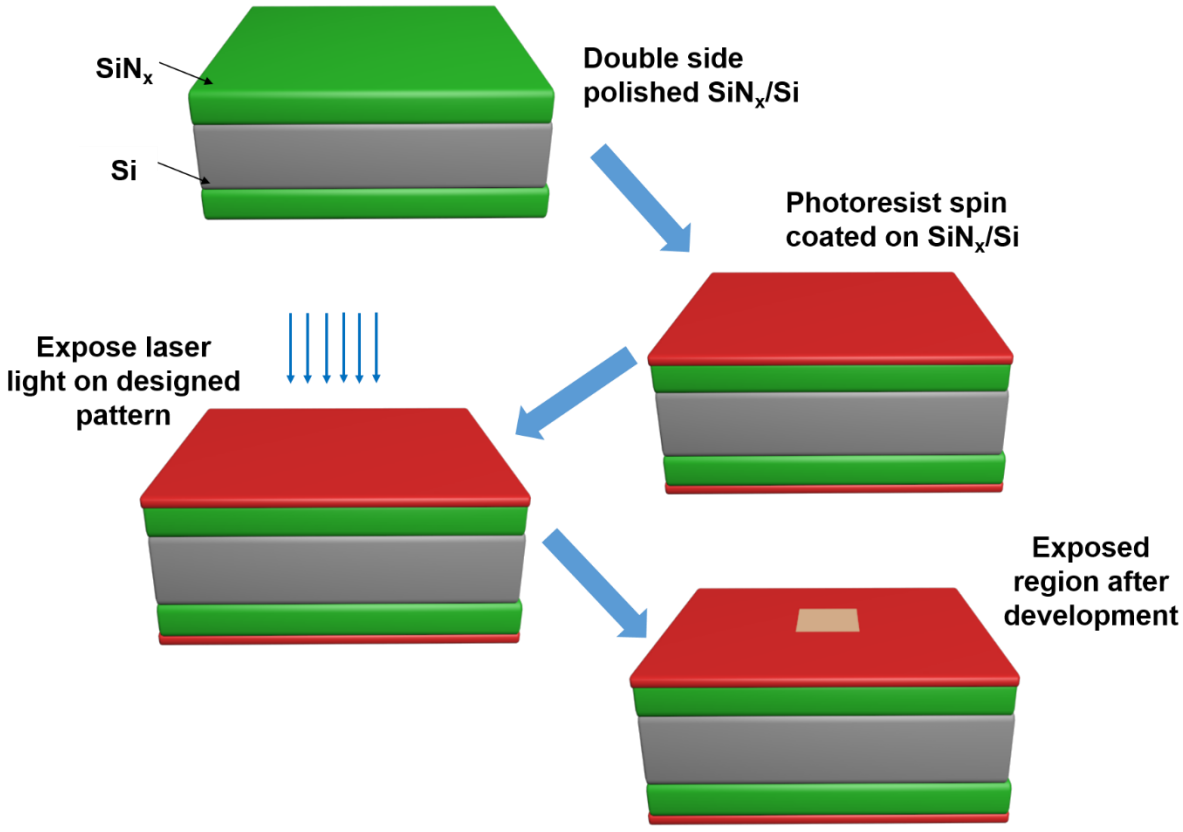

Figure 3.8: Process of photolithography. A detailed step by step process for carrying out photolithography is explained. First, double side polished SiN_x/Si is spin coated with photoresist from both sides. Laser light is exposed on a predefined pattern and developed for subsequent etching of SiN_x and Si for making a SiN_x membrane.

3.4.2 Reactive ion etching (Dry etching)

Reactive ion etching (RIE) is an etching technique used frequently in micro-fabrication processes using plasma of different gases to remove materials deposited on a target wafer. It is a very useful technique and has been developed very rapidly because of the etch directionality irrespective of crystal orientation which is lacking in wet etching. It also transfers the lithographically defined patterns into the underlying layer and is a clean process that is compatible with vacuum processes (179).

RIE of SiN_x is a plasma-assisted etching technique that uses fluorine gas plasma to etch the target substrate. Electromagnetic fields dissociate and ionise relatively stable gas molecules to form chemically reactive molecular and ionic species which then react with the solids to be etched and form the volatile products. Suitable feed gas sulphur hexafluoride (SF_6) is used in glow discharge to dissociate/ionise the gas phase etching environment to neutrals, electrons, photons, radicals (F^*), positive (SF^{+5}) and negative (F^-) ions. Radicals diffuse through the bulk plasma and ions are driven by the DC bias to the wafer surface for etching the SiN_x which follows the reaction.

$$Si_3N_4\,(s) + 3\,SF_6 \Rightarrow 3\,SiF_4\,(g) + 3\,SF_2\,(g) + 2\,N_2\,(g). \qquad (3.1)$$

Plasma lab 100-ICP 65 model RIE is used to etch the SiN_x layer with the recipe (mixture of and SF_6 and CHF_3 gases in the ratio of 60:15, RF 30 kHz and ICP 600 W). The etching rate of the silicon nitride recipe using SF_6 and CHF_3 chemistry which I had used for this work is 3 nm per sec. It usually takes 2.5 to 3 minutes, to completely remove a 500 nm thick silicon nitride layer. SiN_x was etched using an unexposed S1813 photoresist as an etching mask. Upon complete etching, Si was exposed from underneath and the shiny silver colour square was visible which can be seen with the eye without any microscope. After this etching step, the S1813 photoresist is removed by dipping the samples in acetone and subsequently in IPA for 2-3 minutes. Substrates should be cleaned and resist needed to be removed completely from both sides for doing further KOH wet etching for etching of silicon. The whole procedure is illustrated in figure 3.9 below.

Reactive ion etching was also done for etching different 2D materials such as graphene, h-BN and MoS_2 during fabrication.

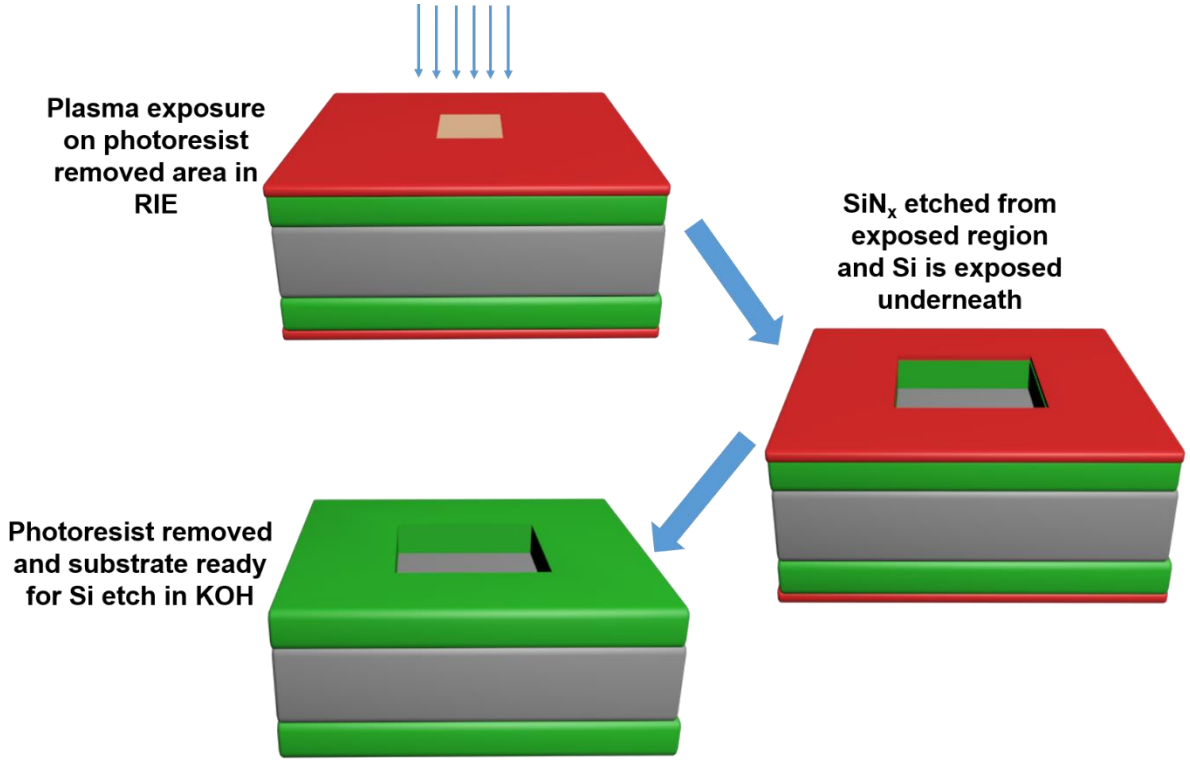

Figure 3.9: Process of etching of SiN_x. Step by step process for etching SiN_x in RIE (reactive ion etching) is presented here. Plasma is exposed to etch away SiN_x from the laser exposed area with photoresist as mask. SiN_x is etched away and bare Si is exposed on plasma exposure. The photoresist is removed for subsequent etching of Si in KOH for making a SiN_x membrane.

3.4.3 KOH etching (wet etching)

KOH wet etching is used for etching Si, by dissolving it in an aqueous etching solution to create the free-standing SiN membranes. There are a lot of chemical reagents available for etching, however, it is important to use the etchant which is etching selectively and has a high selectivity ratio without affecting the mask and underlying material. Selectivity is the ratio of the etching rate of target vs the etching rate of mask in the same etchant.

Usually, the etch rate through KOH is higher as compared to RIE, however, it is dependent on the concentration of the reactant diffusing to the target, surface reaction and products diffusing away from the target surface. By increasing the reaction

temperature or changing the concentration of the etchant these factors are influenced and can speed up the process.

KOH in DI water is an alkaline solution and highly corrosive which is used for etching of the silicon substrate following the chemical reaction below.

$$Si + 2OH^- + 2H_2O \Rightarrow Si(OH)_4^{2-} + 2H_2(g). \quad (3.2)$$

Silicon was etched in 30% weight percentage KOH water solution at 80 ^oC in this study and etch rate along <100> was 1.2 µm/minute and took around 8 hours to etch away 525 µm Si. All the silicon is etched through the exposed Si and a membrane of 500 nm SiN_x is left behind on the other side of the substrate. This can be verified by passing light through the hole and by looking under the microscope. Light can pass through the thin SiN_x membrane if all the silicon is etched away completely if not any silicon remaining will absorb the light. The SiN_x membrane after etching of Si appeared on the backside of the wafer is approximately 100x100 μm^2. The detailed process of etching of Si through SiN_x mask is demonstrated in figure 3.10 below.

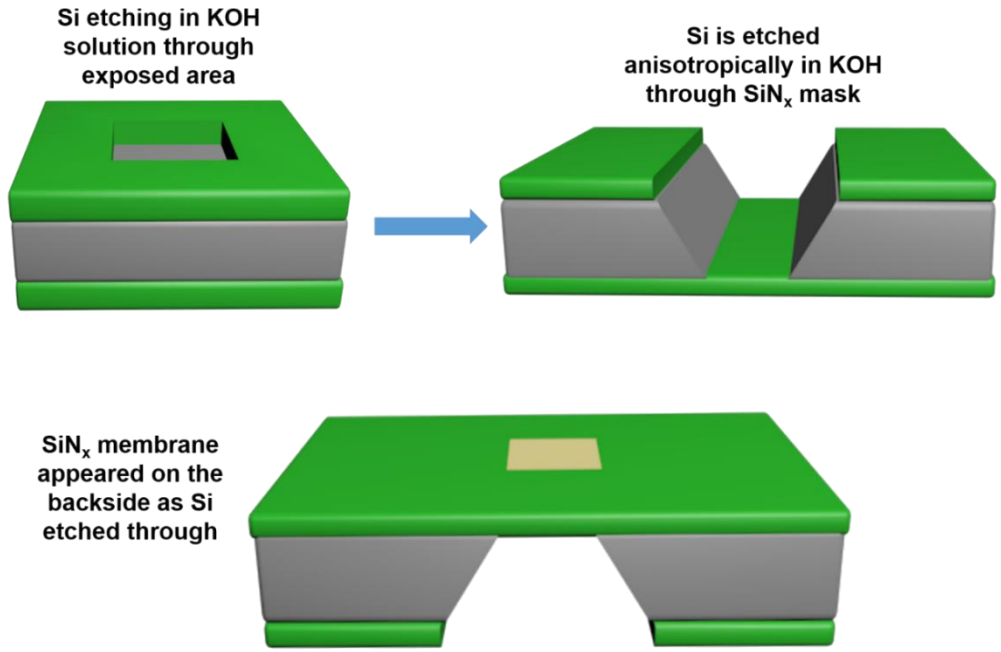

Figure 3.10: Process of etching of Si in KOH to get SiN_x membrane. Step by step procedure for making SiN_x membrane through etching of Si in KOH. Si is etched

anisotropically in KOH through SiN_x mask, it is shown in cross-section for better view. A free-standing SiN_x membrane appears on the backside.

KOH etching is the anisotropic etching and has a preferred etching rate in one or some other crystallographic orientation as a contrast to RIE which is isotropic. Silicon etching rate of alkaline etchant (KOH or NaOH) strongly depends on the crystallographic orientation (180) and has a much slower etching rate along <111> as compared to <100> and <110> direction. The difference in the etch rate along crystal orientation is due to lattice packing density in silicon and available bonds in different crystallographic orientations however the mechanism of this dependence remains inconclusive (181).

Due to the slow etching rate at the silicon <111> surface, if considering plane <111> as a non-etching plane, the final width of the membrane can be calculated as shown in figure 3.11b.

$$2\ Cotan(54.74) \approx \sqrt{2}\ Z \tag{3.3}$$

$$W_o = W_m - \sqrt{2}\,Z \tag{3.4}$$

Where W_m is the size of pattern we use to write with the laser writer and W_o is the size of the SiN_x membrane that we are getting after the KOH etching of Si. Z is the thickness of the substrate that is equal to microns and $\tan^{-1}\sqrt{2}$ is the angle between the planes <111> and <100> (figure 3.11b).

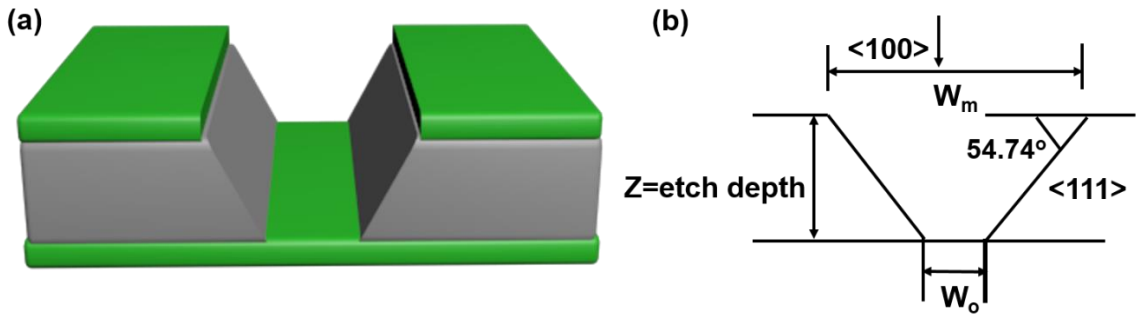

Figure 3.11: KOH wet etching of silicon along crystallographic orientation. (a) Si etching from the exposed silicon and Z, which is etch depth and is proportional to W_m. Etching goes straight through the whole Si substrate. (b) Schematic illustration of the

process along crystallographic planes. The etching stops with a sharp triangular profile.

After KOH wet etching substrate was thoroughly rinsed and cleaned with de-ionized water in repeated cycles to diminish or minimise KOH residues. 30% weight percent acetic acid in water solution can also be used to remove any left behind residue.

3.4.4 Photolithography to define a large exit aperture for nanochannels

Second photolithography is done for defining the rectangular hole (3x25 μm^2) on the SiN_x membrane. For this purpose, a rectangle of size 3x25 μm^2 is designed and exposed on the photoresist coated membrane. The photolithography is done following the same procedure described in section 3.4.1. After the photolithography step, the hole is etched through the membrane with unexposed photoresist as a mask using the same RIE recipe as in section 3.4.2. Step by step procedure of the process is shown in figure 3.12.

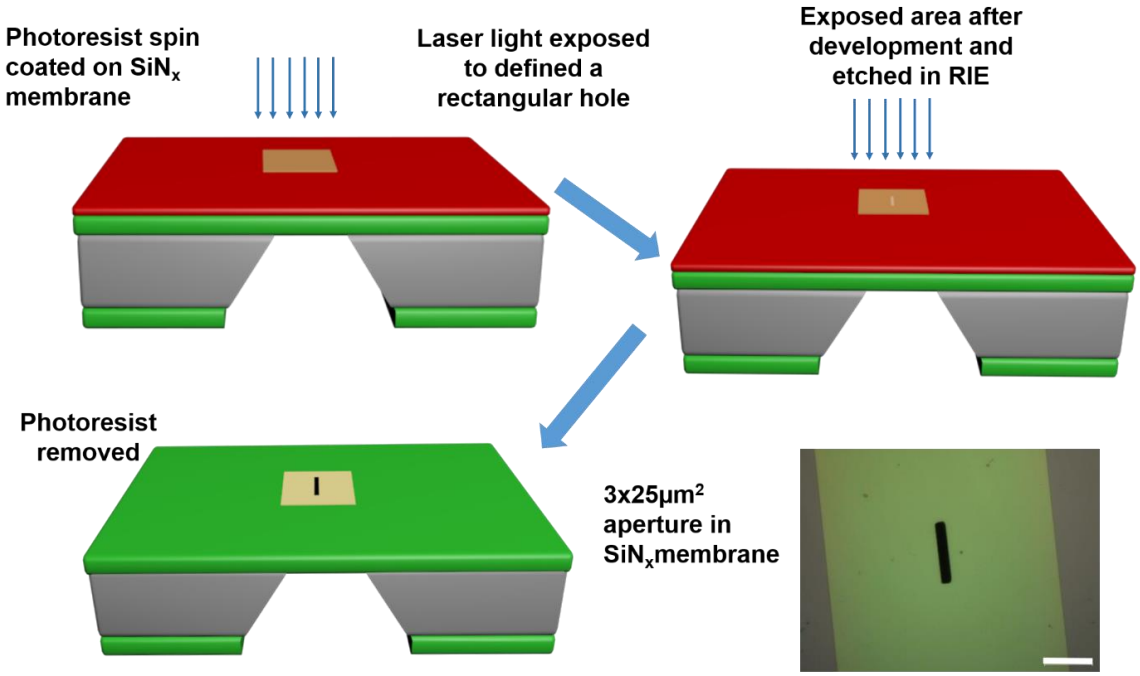

Figure 3.12: Process of defining an aperture in SiN_x membrane. A detailed step by step procedure to define an aperture (3x25 μm^2) in SiN_x membrane. Bottom right

side image is the real-time aperture in SiN_x membrane on 500nm SIN_x/Si substrate. The scale bar is equal to 20µm.

There is an uncertainty of about ±0.5 µm in the dimensions of the aperture as the lithography is done with a laser writer (optical lithography). From device to device different dimensions of the aperture were used (i.e., 2x25, 3x25, 2x50 and 3x50) depending on different applications and measured with the optical microscope with the uncertainty of ±0.5 µm.

3.5 Flake transfer

Flakes are originally prepared on SiO_2/Si wafer and to transfer it to the target substrate several transferring techniques are employed depending on the application. Flakes are lifted from the substrate with a polymer and are aligned mechanically on the target substrate with the help of a transfer machine, which is essentially a set of micro-manipulators under an optical microscope. Two different transfer techniques are used in this work which is described below, each of them has its benefits.

3.5.1 Wet transfer

Wet transfer (182, 183) involves the procedures where the flakes are in contact with some liquid, typically a polymer and finally the polymer is removed by solvents. This transfer process involves the potassium hydroxide as an etchant to etch away silicon oxide from the substrate to lift out the flake which was originally exfoliated on the SiO_2/Si substrate. A sacrificial polymer (PMMA) layer is spin-coated on the desired flake to be transferred at spin speed 3000rpm and acceleration of 1000 m/s^2 followed by hotplate baking at 130 °C for 5 minutes (figure 3.13b).

On top of the flake covered with PMMA layer, a tape is stuck which has a small cut-out window tape to visualize the flake (figure 3.13c). PMMA is scratched from the outer side of the tape to help penetrate the KOH for etching. The wafer containing the flake with spin-coated PMMA is then immersed into low concentration KOH solution (0.1mol/L) which partially etches the SiO_2 surface and releases the polymer from the substrate (figure 3.13d). PMMA membrane containing the flake is usually etched away

in four to five hours and after SiO_2 etching, the PMMA membrane floats in the water. The floated membrane is then carefully transferred to DI water and washed to remove away all KOH residue/contamination and is ready to transfer to the target substrate. The reason this method is said to be 'wet' because solvents are involved during the etching processes. (184).

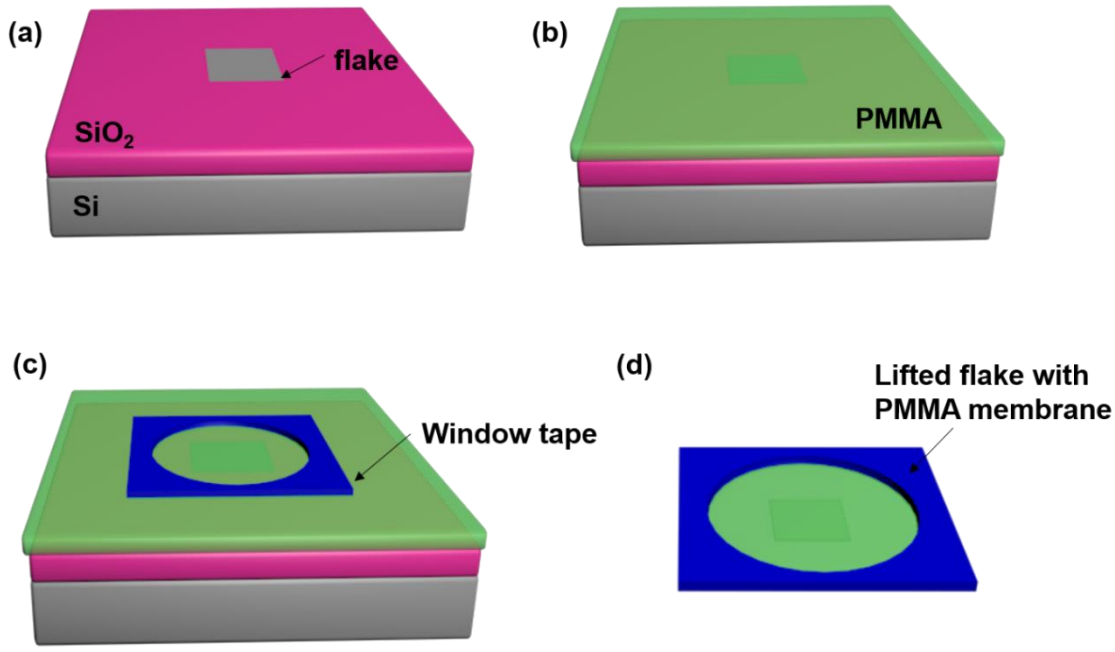

Figure 3.13: Procedure of polymer-based wet transfer. (a) Graphene flake on SiO_2/Si substrate. (b) PMMA is spun onto graphene flake. (c) Window tape is adhered to flake and PMMA is scratched from outer side of the tape. SiO_2/Si chip is immersed into KOH solution to etch SiO_2 underneath. (d) Freestanding graphene/PMMA layer attach to window tape.

As this process involves solvents, adsorbents can be trapped so annealing is done after every transfer step to minimize the contamination. Annealing is done in a H_2/Ar (10/90) atmosphere inside a furnace, which will be discussed later in the thesis.

3.5.2 Dry transfer

As the name suggests, dry transfer (185) is a technique where the flake to be transferred does not have contact with any solvent. This method uses the bilayer polymer on the substrate, similar to that described in 3.1.2. The thickness of this double layer is usually a few hundreds of nanometres. After spin coating and baking of the bilayer polymer, exfoliated 2D crystals on the adhesive tape are pressed onto double-layer polymer substrate to exfoliate thin flakes (figure 3.14b).

PMMA/PMGI double layer provides good optical contrast and acts as an extra layer to reflect light, the same way as silicon oxide(186). Contrast can be adjusted by the thicknesses of the resist layer which in turn can be adjusted and controlled by the spin speed.

Flakes are searched under the microscope which needs to be transferred afterwards. Bilayer polymer is scratched around 5 mm diameter outside the selected flake by aiming the flake in the centre under the optical microscope in the view field of 5x objective lens (figure 3.14c). Few drops of MF-319 (developer of PMGI) are added on the edges of the scratched circle to dissolve the PMGI layer leaving the PMMA layer unaffected (figure 3.14d). Flake and PMMA membrane is slipped from its place after the development of PMGI film and carefully transferred to DI water (figure 3.14e). MF-319 residue underneath PMMA can be cleaned away in DI water.

Flake/PMMA (figure 3.14f) membrane from DI water is carried on the circular metallic plectrum and transferred on the desired substrate using a transfer machine. Different concentrations of the PMMA will change the strength of the membrane due to the thickness variation of the membrane. Here, 950 K molecular weight (8% wt/v in anisole) PMMA has been used which provide stronger support during fishing and drying the membrane.

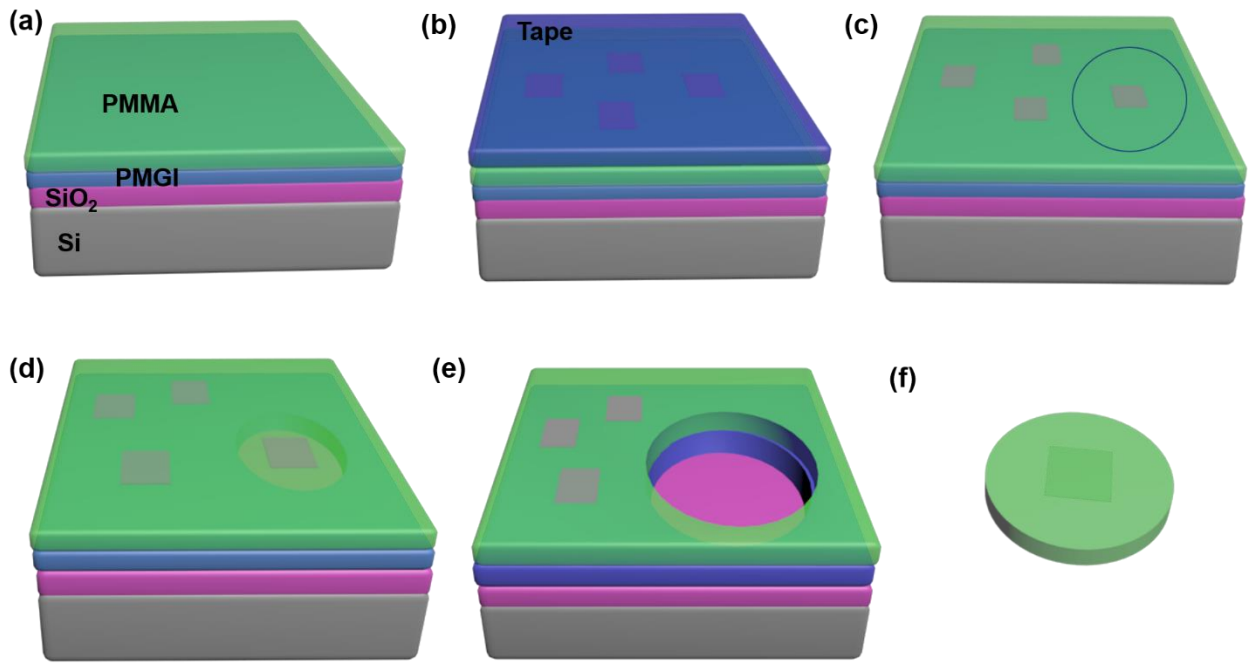

Figure 3.14: Procedures of dry transfer. (a) A double-layer PMMA/PMGI is spun on to SiO_2/Si substrate. (b)Tape with mechanically exfoliated 2D flakes (graphene, MoS_2) sticks on top of bilayer resist. After (c) Tape is removed at a low angle and flakes on PMMA. PMMA is scratched around the flake (d) PMGI under PMMA is dissolved around the scratched area with MF319 and flake is on PMMA. (e) Substrate transferred to DI water and flake with PMMA is slipped from substrate and cleaned (f) PMMA membrane with flake is ready to pick up on a plectrum for transfer with optical alignment onto the target substrate.

3.5.3 Optical alignment

The flakes on the PMMA membrane from both wet and dry transfer techniques are transferred to the target substrate with the help of a transfer machine. Flakes on the PMMA membrane are dried after taking out of DI water and carefully placed on the plectrum. The flake with a PMMA membrane is carefully stuck on to the transfer arm which allows independent motion in x, y, and z directions.

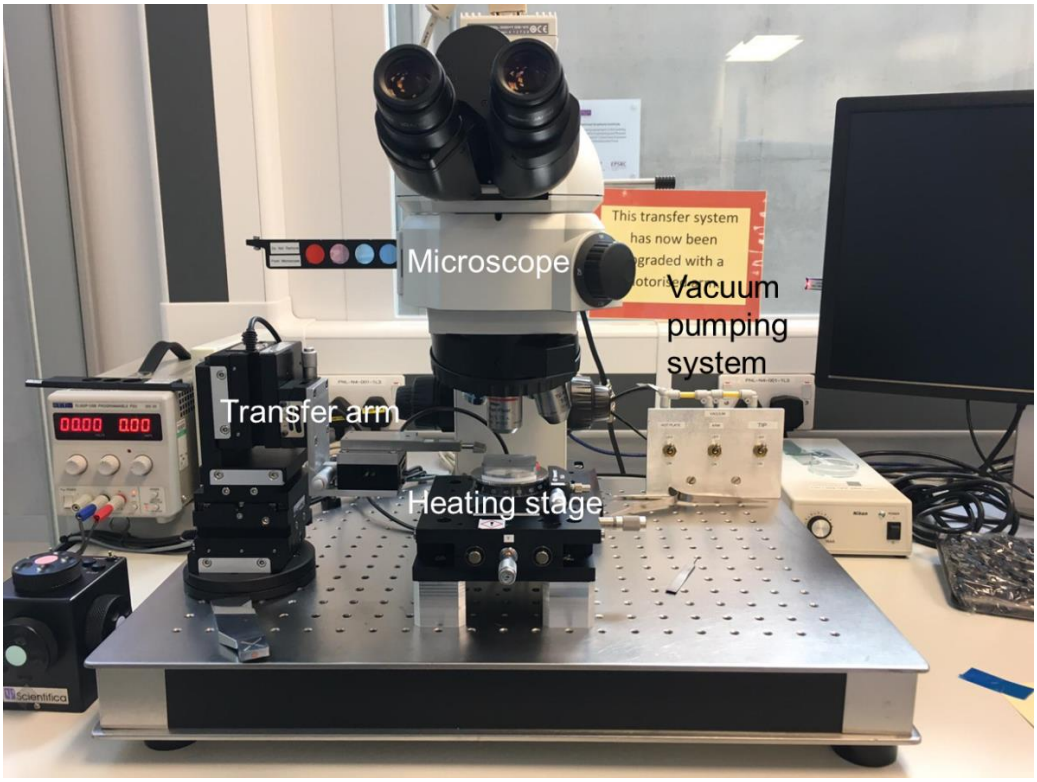

Figure 3.15: Flake transferring station. It includes an optical microscope, transfer arm, vacuum pumping system, heating stage and temperature control panel.

The custom made flake transfer station is equipped with an optical microscope (Nikon Eclipse LV100), micro-positioning heating stage with temperature controller, micro-positioning transfer arm, vacuum pump and a computer is attached to it to see the flakes during transfer (figure 3.15). The optical microscope is equipped with filters and different objective lenses which helps to improve the workability by providing better visibility and fine control on the alignment of flake position by drawing a contour. We use a vacuum to hold the plectrum containing flake, transfer arm and heating stage to avoid any misalignment. LabView PID controller is used to control the temperature of the heating stage.

The heating stage holds the substrate on which flake needs to be transferred and can move in all three directions and it can rotate as well for better alignment accuracy. Temperature control on the heating stage enables smooth uniform landing of flake without any wrinkles or folds. Increasing the temperature of the heating stage could enhance the adhesion between the membrane (containing flake) and substrate. The transfer arm has the micromanipulator to move in x, y, and z-direction. Flake is aligned

on the target (substrate placed on the heating stage) by moving the arm and stage with fine and coarse movements in all three x, y, and z directions while looking through the microscope. After this alignment, the arm holding the plectrum with PMMA membrane is moved down until PMMA and target substrate are in intimate contact. Alignment is checked in regular intervals while going down the substrate by looking at the flake and target substrate. Target substrate is heated up 75 °C which enhances the PMMA/substrate adhesion.

3.6 Electron-beam lithography (EBL)

Electron beam (E-beam) lithography is a technique for writing fine patterns in thin films of electron sensitive material by using a finely focused electron beam. E-beam lithography is done inside a scanning electron microscope (SEM), and includes a pattern generator that is Raith elphy quantum attached to SEM. An electron sensitive resist film of PMMA, 950K molecular weight (3% wt/v in anisole) is first coated on the substrate's surface and the focussed electron beam exposure modifies the resist's chemical properties. Resist developer methyl isobutyl ketone mixed in IPA (MIBK/IPA used in 1/3) remove the resist layer from irradiated/exposed part to get the desired pattern upon resist removal. The patterned films act as a mask for subsequent processes, such as etching and gold vapour deposition etc.(187).

EBL has several advantages such as high resolution, suitability for a variety of materials and the ability to expose several fine patterns with a variety of materials. The ultimate electron spatial resolution is in the range of a few nm.

The first EBL machine was developed in the 1960s and soon after polymethylmethacrylate (PMMA) was used as a resist for this technique. PMMA acts as a good e-beam resist because it has i.e., high contrast, good resolution, a continuous and homogeneous film on the surface, high-etch resistance, good thickness and high stability (188). The pattern is designed and then converted to a format that is suitable for the EBL system. The digital data paths are automatically converted and sent to the electron beam system. The electron beam scans the writing field using electric or magnetic fields and by dipping the already exposed surface into the developer the final shape pattern area is obtained.

As PMMA is a positive resist, irradiated areas can then be removed chemically using MIBK/IPA or water/IPA (cooled down to -5 ^{o}C) in (1/3) as a developer. IPA acts as a stopper for development. By dipping the e-beam exposed surface into the developer, the developer dissolve the exposed resist and the final shape of the designed pattern is obtained (189).

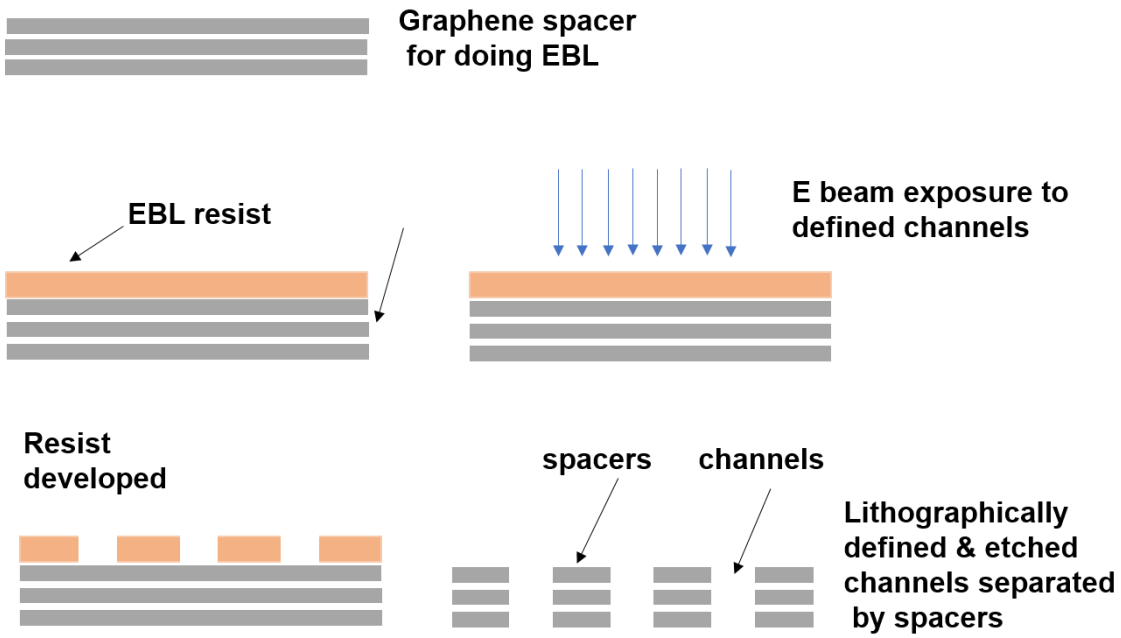

Figure 3.16: E-beam lithography and etching process to define channels. Thin graphene flake selected for making channels by E-beam lithography and etching. PMMA (E-beam resist) is spin coated on the graphene flake. The electron beam scans on the defined pattern on resist layer to change its chemical composition and wet development process to dissolve the exposed film area. Space, where graphene is etched away, is called channels (PMMA resist act as mask protection for etching). This is a cross-sectional view of spacers and channels.

To locate the desired flake on the substrate for writing with EBL, alignment marks are required. On a custom made stage coordinate system, stage coordinates are taken by assigning two marks on the horizontal corners of the substrate and the centre of these marks are set as SW (south-west) and SE (south-east). SW serves as origin and SE as an angle correction or rotational displacement correction. Flake position is recorded in the Cartesian coordinate system with reference to SW and SE. Images of SW and SE and flake coordinates could be saved for future use for writing crosses (alignment marks) in EBL. These marks (SW and SW) and flake position will be read

out and recorded in the EBL system and used for writing alignment marks (crosses) in the global of the stage coordinates (figure 3.17).

Custom made stage coordinate system is designed using a Matlab program coupled with the microscope and used for accessing the flake position. To save the coordinates of flakes as a reference to SW (origin) and SE (angle correction) exact stage position is recorded by moving the stage of the microscope to that location (figure 3.17a). Multiple flake position can be recorded on the same substrate with reference to SW and SE for writing the alignment marks later in EBL.

Atomic-scale capillaries are patterned in EBL in two steps. In the first step alignment marks (crosses) are designed and patterned (figure 3.17b) and in the second step designed lines are patterned with reference to alignment marks. Crosses are designed in such a way that it covers 1250 µm in ±X and ±Y direction and each cross is 200 µm away from the centre of each cross (figure 3.17b). It is important to note that the design is made in GDSII format so that it can be stored, and modified for subsequent patterning processes because the EBL system (Raith) read the file in GDSII format. To write the crosses dose was set to 2.2, lines step 16 nm and 150 µC/cm^2 areal dose was used. After exposure, crosses were developed for 30 sec using e-beam developer, dipped in IPA for 30 sec to stop further development and then blow dry with nitrogen gas.

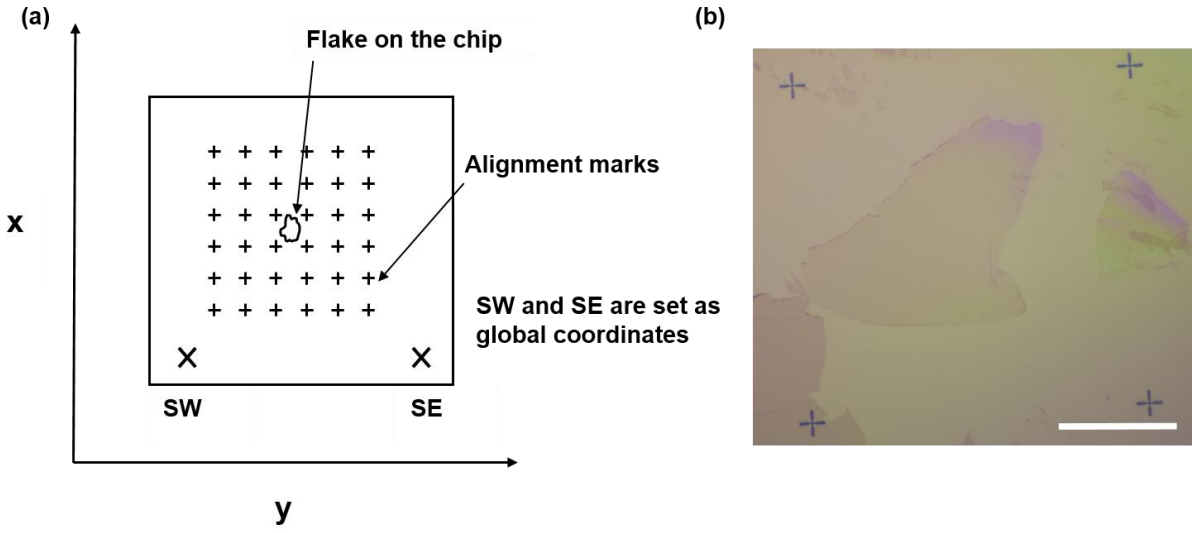

Figure 3.17: Representation of the global coordinates and alignment marks designed for EBL. (a) Schematic of global marks defined in Cartesian coordinates

system to expose alignment marks in EBL. (b) Optical image of spacer flake after exposing alignment marks in EBL. Four alignment marks which are 200 µm apart can be seen surrounding the spacers flake to write channels design. These marks are used for aligning the flake on the substrate with respect to the designed pattern feed to the EBL system. The scale bar is 25 µm.

3.6.1 Patterning process of graphene channel by nanolithography

To start patterning the channels and spacer design for making angstrom scale capillaries, flakes are searched which were exfoliated using micromechanical cleavage. Amongst flakes of different thicknesses, we chose certain layers of graphene (from monolayer to few layers) flakes to serve as a spacer (we called it spacer as this defines the space between the top and a bottom crystal. The thickness of the spacer acts as the channel height. Electron beam lithography and plasma etching were employed to pattern graphene crystal (spacer) to make parallel strips of ~110 (±10) nm spaced with a distance of 160 (±10) nm this will also refer to lines design in the next sections. An AFM image of one such spacer is shown in the figure below.

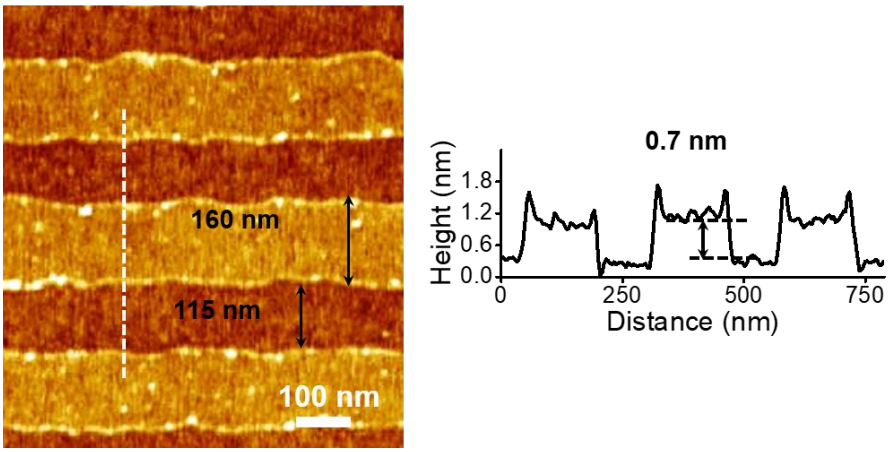

Figure 3.18: AFM image of channels design on bilayer graphene spacer. AFM image and its respective height profile of bi-layer graphene flake which act as spacer. Channels are parallel strips of e-beam lithographically defined and etched on bilayer spacer flake. Channels are 115 nm wide and spaced by 160 nm and step height is 0.7nm.

To write the design of the lines, the dose was set to 1.4, lines step 8 nm and 150 μC/cm^2 areal dose was used. While developing the line patterns, care must be taken not to exceed this development time of more than 30 sec otherwise all the lines would get merged leaving a rectangular box, or they may be overdeveloped leaving behind very wide channels after etching.

AFM checkpoints

Right after the nano-channel/lines exposure and development nano-channels are checked under the AFM to ensure that lines are exposed properly and deep enough through the resist. Through the proposed spin coating recipe PMMA thickness is 130-150 nm. AFM is done to check the exact width of lines and height of the exposed PMMA. If everything went well then the channel/spacer line width and depth of PMMA appeared to be (100/160±20) nm and 120-150nm respectively (figure 3.18).

Influence of focus and dose

In case if the beam is not focused properly, the current is not stable during exposure or the dose is not correct lines get underexposed or overexposed results in varying widths and heights of PMMA which in turn will affect the graphene nanochannel widths after etching. This step is very important because if the lines get overexposed they will result in wider channels which will sag/collapse on transfer to bottom crystal or after top transfer. Rightly exposed lines show PMMA thickness of 150 nm (figure 3.19)

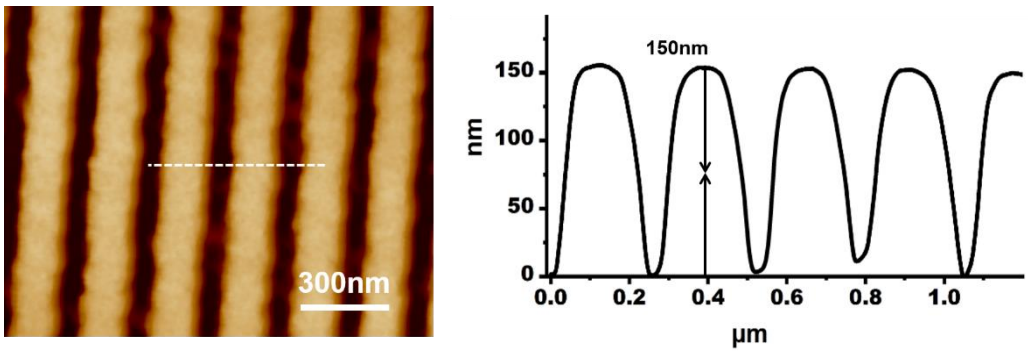

Figure 3.19: Lines design of exposed PMMA after EBL writing. AFM image of lines written on graphene flake covered with PPMA. PMMA is dissolved from the area designed and exposed in EBL depth of PMMA is 150 nm.

Etching of graphene channels

Graphene channels were etched with soft O_2/Ar plasma using a Moorefield plasma etching system. Lines were etched from the exposed region and PMMA act as a mask in the region where the flake was not exposed by the EBL. O_2 16 s.c.c.m., 20 mTorr, 2 W. recipe was used to etch graphene. The etching rate for the recipe used is usually 30 sec per graphene layer. Etching is carried out for 60-90s for 2-3 layers graphene and this was broken into a step of 20 sec to avoid crosslinking of the PMMA which in turn will not be easy to remove in the cleaning process.

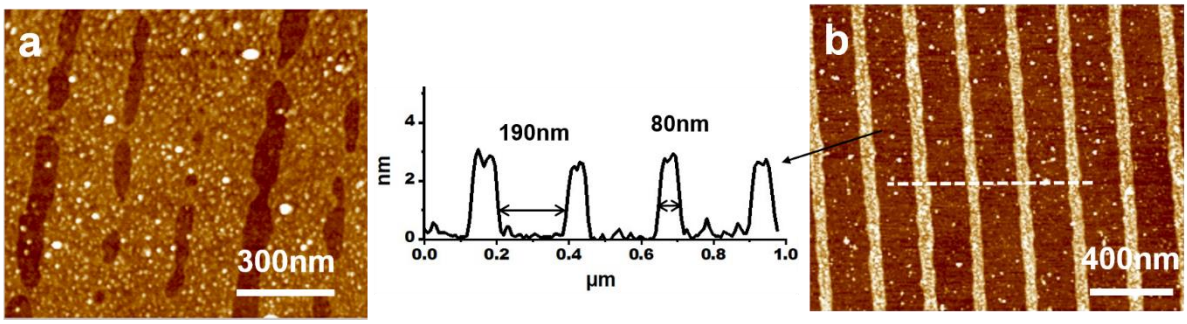

Figure 3.20: AFM images of under-etched and over-etched lines. (a) AFM image showing cross stitching that could be due to various reasons (under exposure, less etching time etc). (b) Over etching of the lines results into wider channels and narrower spacers. All the lines are of tri layer graphene.

Etching time is very critical as it can under-etch or over-etch the lines. In the case of over-etching, the channels appeared to be 180 nm and as a consequence of this widening spacer became narrower 80 nm (figure 3.20b). When the lines are underexposed/etched they are cross-stitched in between (figure 3.20a). This step is very critical as the wider channels can sag, collapse and join together while transferring or after the subsequent top transfer, under etched lines are also of no use.

Cleaning of the lines/channels

After the PMMA mask assisted etching, acetone cleaning with some mild sonication was done to remove the polymer completely from the spacer lines. The cleanliness of the lines is critical for nano-channel devices for many reasons: (i) The polymer

residues locally increase the thickness and make the channel height different (ii) Greater thickness near the channel can decrease the molecular transport and affect the conductance. Flexible polymer chains can disturb the flow of mass (water, gas and ions) or even it can clog the channels. iii) Uneven thickness due to PMMA residue sometimes leads to poor adhesion between top and spacer layer which thus leads to removal of top flake on the application of small voltage during ion flow measurements.

The cleaning protocol is divided into two parts in the first part, the polymer chains are broken by mild sonication under 10% power, 135 kHz frequency and in degas mode for 1 minute by slowly moving the substrate in and out of acetone after every 5 sec. In the second part majority of the polymer is removed with several iterations of dissolving and diluting in hot acetone at 65 °C for 1-2 hours followed by rinsing in IPA and blow-dry with nitrogen gas.

If PMMA has not been removed during this treatment completely then this two-step protocol is repeated. If PMMA residue still does not go away completely then an annealing process at temperatures 300-400 °C in an inert atmosphere (H_2/Ar) for a few (3-4) hours is carried out, in which any residual PMMA chains are thermally degraded. This is not a part of the protocol but is another treatment to remove any left out PMMA. After every cleaning procedure nano-channels are scanned under AFM to check the cleaning quality of the nano-channels.

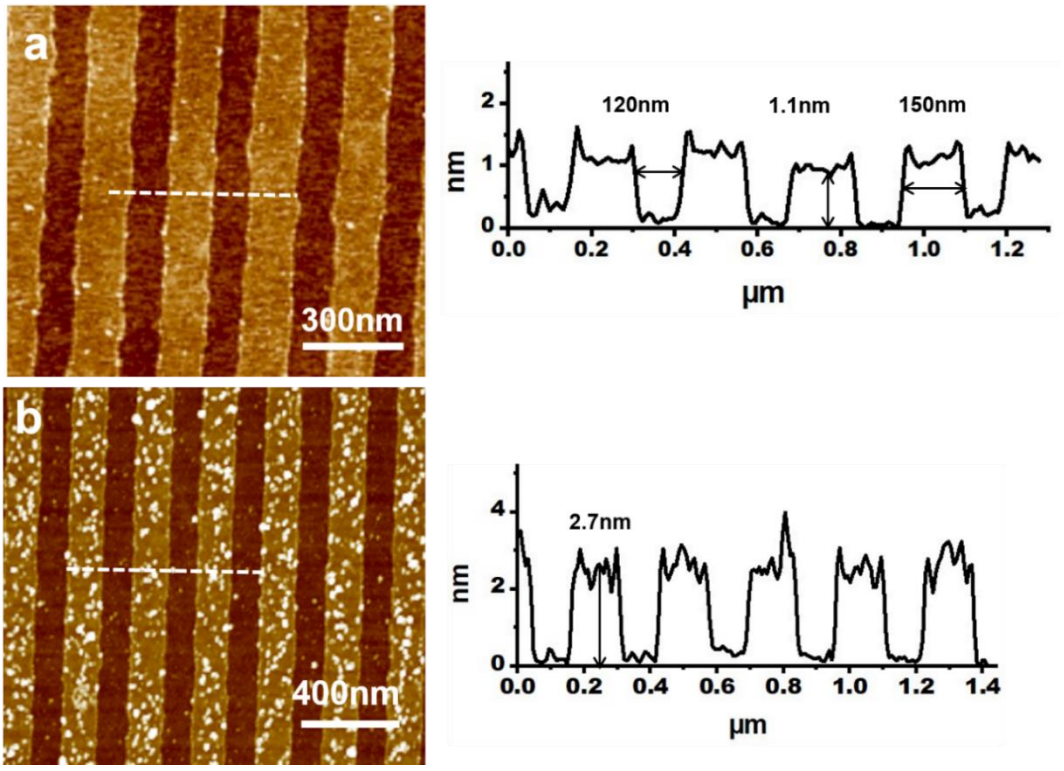

Figure 3.21: AFM images of lines after etching and cleaning with their height profile. (a) AFM image of cleaned lines with channel and spacer. (b) AFM image of uncleaned lines with PMMA residues. All the lines are of a thickness of tri layer graphene.

A comparative AFM image of cleaned and uncleaned lines with their respective height profile is presented in figure 3.21. All of the lines are made with tri-layer graphene. Cleaned lines (figure 3.21a) are giving around 1.1 nm thickness of spacer and channel/spacer width is 120/150 nm. In contrast, uncleaned lines (figure 3.21b) are more than double in thickness.

Under-etched, over-etched and uncleaned lines are not good to use as lines could merge, collapse and sag while transfer that will block the devices or give very high flux (gas, ion and water). Cross stitching and the over etched line could arise due to many reasons i.e., unstable beam current during exposure, bad focusing, astigmatism, overdose/underdose and due to long or short etching time. These all parameters need to be optimized for good quality spacers which is crucial in defining the quality of devices.

Plasma etching with masks can be well controlled using the effects of gas chemistry (190), mask selection, and plasma etching conditions (191). Control over the etch rates, selectivity, sidewall profile, and etch roughness can be optimised through tuning process parameters (192).

For a spacer width of 130 nm, wall edge roughness with ±10 nm have been seen. For the thickness as the spacer is over-etched to ensure complete removal this issue of non-uniform etching is alleviated. For instance, for a monolayer graphene spacer although it takes only 10 sec to etch a layer with the PMMA mask and narrow channels it typically takes 20 sec to etch the channels completely. Several parameters i.e., e-beam current to expose the channels, dose, development time and plasma power and etching time affect the etching so is wall edge roughness. Distribution of plasma etching does not have any impact on the height of the channels as that is defined with the number of the layers of graphene crystal used spacer is made from a different crystal and the bottom crystal is not etched. Plasma distribution only affects the width of the channels from under etching to over-etching which has been explained and shown in figure 3.20.

The number of channels designed on a spacer depends on the size of the flake selected and on the larger side of the aperture in the SiN_x membrane. Usually, the number of channels that are contributing to the flow are measured from the silicon nitride aperture size and also from the number of channel etches on the spacer crystal. Channel are etched in a parallel array on the spacer flake which is calculated with the AFM for every spacer flake after etching as shown in figures (3.18 and 3.21a). Number of channels on each device are calculated after measuring the channels and spacer width which are placed on the silicon nitride aperture. Usually, on a regular device with an aperture size 3x25 $\mu m^{2,}$ there are 200 channels but sometimes smaller or larger apertures were also used which can be calculated accordingly.

The formula for calculating the number of channels on every device is presented here in equation 3.5

$$\text{Numer of channels in a device} = 2\left[\frac{(\text{length of silicon nitride aperture})\ in\ nm}{(\text{width of spacer} + \text{width of channel})\ in\ nm}\right] \tag{3.5}$$

The length of the spacer flake on which channels are designed and etched through nanolithography must accommodate the entire nitride aperture. The top crystal is transferred on the lines with its longer edge perpendicular to the lines, and parallel to the longer side of the silicon nitride aperture as in figure 3.12. This will aid in the counting of the number of channels as described in equation 3.5.

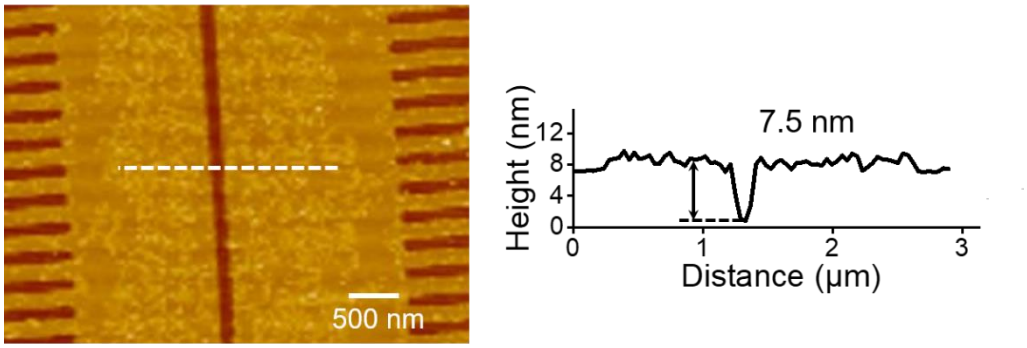

Figure 3.22: AFM image of single channel with their height profile. AFM image of single nanochannel defined in a multilayer graphene flake with the surrounding perpendicular channels to entrap hydrocarbons. Channel height is 7.5 nm.

Figure 3.22 is the AFM image of a single nanochannel defined in a 7.5 nm graphite flake. Single nanochannel is in the middle and perpendicular channels in sideways are designed to entrap any hydrocarbons to make nanochannel clean and open. Single channels are designed to check the reproducibility and quality of our fabricated channels by measuring the gas flux through single channels and comparing that with multi-channel devices.

3.7 Capillary device assembly

To construct atomic-scale capillaries with precisely controlled geometry, we need to consider how the graphene sheets would be kept at nanometre separations while they stay flat. The patterned graphene spacers need to be assembled on some substrate that is flat and support the atomic scale capillaries. Commonly used substrates like

silicon dioxide or silicon nitride have at least 1 nm surface roughness which is even more than the graphene thickness (0.35 nm). If the spacers are assembled on these surfaces they would sag into the nanochannels and take the contour of the surface they are placed on. Hence, spacers made of graphene crystal are placed on multiple layers of graphite crystal (which is called bottom) as it is far more rigid than graphene due to the added height and its surface getting flattened with thickness. For measuring the fluid flow in a constriction at the atomic scale, the capillaries are supported with the thick top crystal. The function of the top crystal is to close channels from the top and to maintain the channels opening from the side.

This assembly would make the channels as capillaries supported by top and bottom crystals. Capillaries could be blocked due to the sagging of the top graphite into wider channels, so it's important to choose the appropriate channel width and thickness of top graphite. For example, we have chosen a channel width of w ≈ 120-130 nm and we found that > 100 nm thick top layer is always flat and can prevent sagging into the channels. The channel width is chosen to obtain sufficiently narrow channels (to prevent them from collapsing) and at the same time to ensure full reproducibility using our lithography facilities. Care must be taken to ensure that top crystals have sharp edges usually thick flakes have thin edges which consequently sag and block the channels. Figure 3.23 shows SEM and STEM images for the spacer and channels illustration in the real-time device.

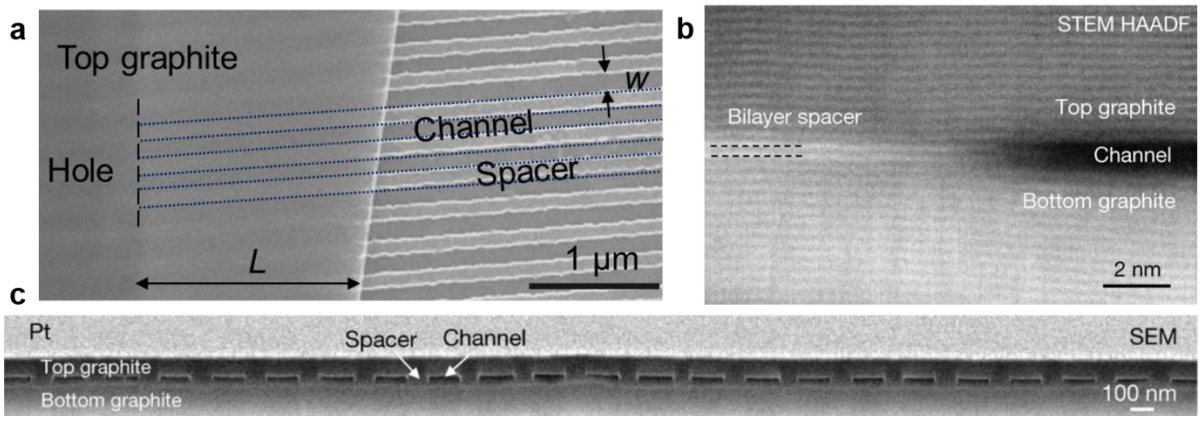

Figure 3.23: Spacers and channels illustration: (a) Top view of SEM image of the tri-layer device. Spacers are clearly seen in the area not covered by the top graphite and empty space in between spacers is channel spacer and channel are running to the hole etched in the bottom graphite. Three of the spacers are indicated by dotted lines. (b) High-angle annular dark-field (HAADF) image of the edge of the channel. (c)

Cross-sectional SEM image of a device with an array of capillaries with height $h \approx 15$ nm. Image is taken from (193).

For final device assembly, all these 2D crystals are stacked back together after exfoliating with no loss in atomic continuity in the perpendicular direction in such a way that patterned spacers are sandwiched between two flat sheets of 2D materials (figure 3.24). Spacer thickness can be selected multiples of graphene layer thickness 0.35 nm and described as the number of layers of graphene N which will determine the height (h) of the nanochannels (figure 3.23 b). After stacking the bottom and spacers on the SiN_x aperture, the assembly is etched from the backside through the hole and SiN_x as a mask to open the exit to the nanochannel before transferring the top flake (figure 3.24 c).

The top graphite is then transferred over the stack to complete the nanochannel (figure 3.24 c). All of these layers are held together with van der Waals forces.

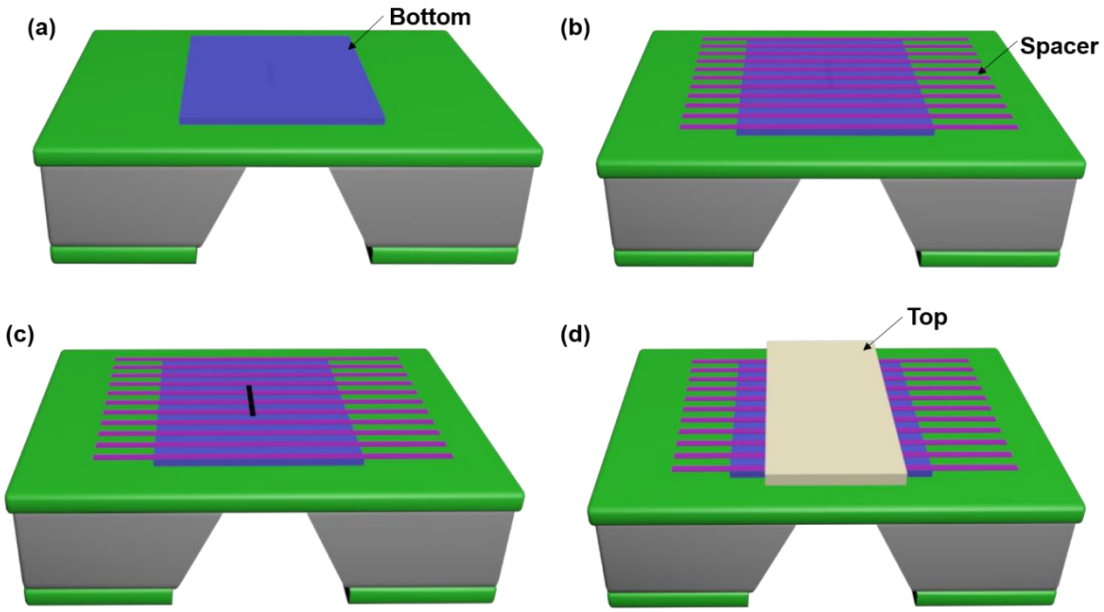

Figure 3.24: Step by step transfer of 2D layers to fabricate nanochannel device. (a) Bottom flake transferred on 3x25 μm^2 aperture on SiN_x membrane. (b) Spacer flake with EBL defined and etched channels placed on top of bottom flake. (c) The bottom and spacers are etched from the backside through-hole with SiN_x as a mask. (d) The top crystal is then transferred on top to fully cover the rectangular opening.

In general, the thick top crystal work well in stabilizing the capillaries without any blockages but there are instances of a disconnected or blocked channel that happen most likely due to the undesired thin edges of the top crystal. Step-like edges in the thick top crystal are common, and a crystal edge thinner than 20 nm can sag into the spacer and can block the channels. To solve this problem a gold patch layer above the top crystal is deposited which defines the length of the channel. Typically, the gold patch is designed in a strip on top of the aperture in the SiN_x membrane and aligned centring the aperture in middle to make the length of channels equal on both sides of the device (figure 3.25 b,c).

Gold patch serves for many purposes not only to define the channel length but also to prevent the top layer crystal from sagging into the channel, to open the channels entries and to mechanically support the device by protecting it from the structural damage when measured in the liquids.

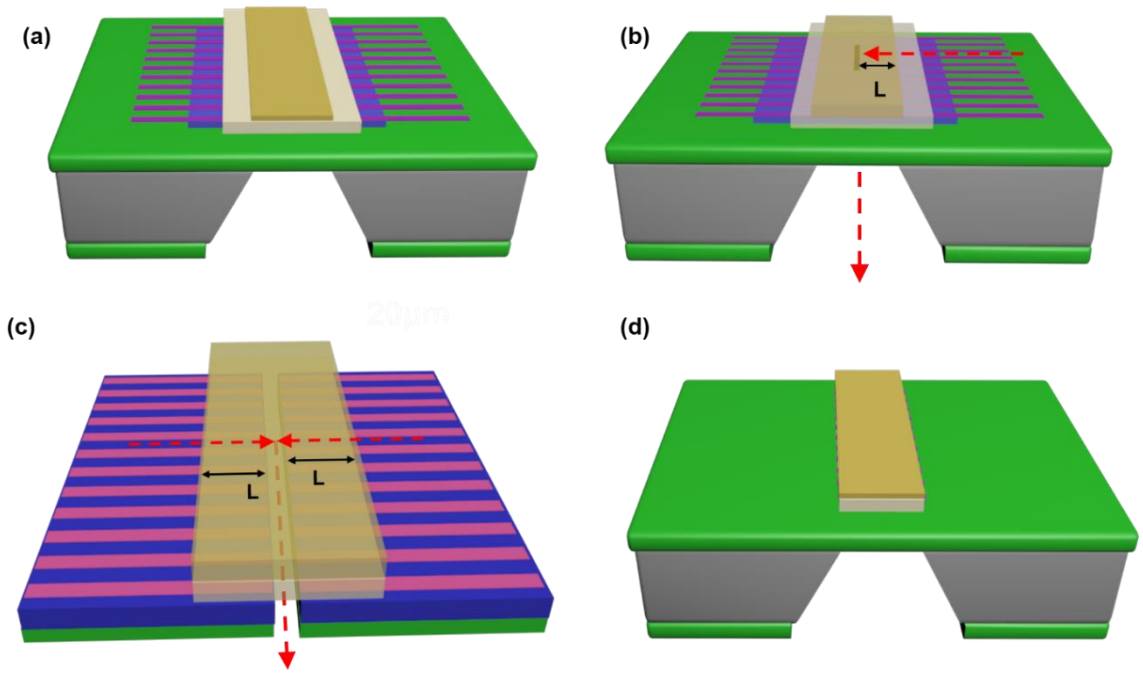

Figure 3.25: Gold Patch deposition and etching on nanochannel device to define length. (a) Schematic of a gold patch deposition on nanochannel stack of the bottom, spacer and top graphite placed on an aperture in a centimetre scale silicon nitride mount. (b) The length of the channel is represented with a gold patch on the tri-layer assembly which can be finely tuned by gold patch design variation. (c) Top graphite is

etched with a gold patch as a mask. The area around the aperture is zoomed in and the arrow in both (b) and (c) shows the direction of fluid (gas and ions) flow from inlet to outlet of the channels. For better visibility top graphite and a gold patch were made slightly transparent. (d) All crystals are etched with gold as a mask to open the channels entry.

The back of the SiN_x membrane through the aperture is the outlet to the nanochannels, while the top side of the substrate is the inlet. Fluid molecules enter from the top side, pass through the capillaries move through the aperture in the SiN_x membrane and go to the measuring system leaving behind the exit (figure 3.25 b,c).

The length of the nanochannel is the distance from the inlet i.e. the edge of the top graphite to the outlet at the aperture in the nitride membrane and denoted as L (figure 3.25 b) capillaries are stacked on either side of the aperture (figure 3.25 c) which is the zoomed-in version of the aperture containing capillaries.

The angle between the spacer and the aperture is important, which if misaligned leads to fewer channels contributing to flux. If such inadvertent misalignment happens during spacer transfer a possible number of channels are calculated geometrically. Care is taken as much as possible to optically align it perpendicular (close to 90 degrees) with the spacer guided by the edges to have the maximum flux during nanofluidic transport through the inlet to the outlet as shown in the figure (3.25 c). Channel length can also be defined even after this stage, by using a gold patch as a mask to etch away top graphite at the required length. Top graphite and the gold patch is made opaque to make the aperture in the SiN_x membrane visible underneath for a better understanding of mass flow through capillaries (figure 3.25 b,c). To open the channel entries, all crystals are etched through a gold mask (figure 3.25 d) and the direction of fluid flow is shown with a red arrow.

In most cases, post-lithography is used to define the length of the channels using a gold mask, this avoids the problem of the angle and help define the length precisely. It can be changed from 1 micron to a few microns depending on the application. The final length after etching through the gold mask is measured optically with the uncertainty of ±0.5 µm.

Devices are annealed after each transfer and etching of the top through the gold mask. Annealing is essential to maintain the cleanliness of the surfaces and to remove

contamination (e.g. hydrocarbon adsorbates from the air) or polymer residue left behind through the transfer procedures. Annealing was done at an elevated temperature in a H_2/Ar (1/9) atmosphere for a few hours. The annealing temperature is determined by the thermal stability of the selected 2D materials. For instance, we used 400 °C to anneal the devices made of graphite or h-BN crystals while the annealing temperature was decreased to 350 °C in the case of the MoS_2-based devices. For graphite and hBN devices, the annealing was performed following the recipe 300 °C for 3 hours and 400 °C for 4 hours, whereas for MoS_2-containing devices, a heat treatment recipe i.e. 300 °C for 2 hours, followed by heat treatment of 350 °C for 3 more hours was done. At this temperature, hydrogen can decompose big polymer chains to smaller hydrocarbons that escape as gases or are light enough to be flushed out in the gas stream.

The devices with graphite and hBN walls are annealed at 400 °C and MoS_2 at 350 °C showed no thermal expansion. Devices were annealed repeatedly over time and showed no unexpected higher leaks or any other changes (194). MoS_2 devices if annealed to 400 °C and showed a bulge in the flake after annealing which was due to the thermal effect. So MoS_2 devices were annealed at 350 °C.

The gold patch can be made using photolithography or e-beam lithography to write the design. The design is carefully made as it determines the place and amount of channel opening. For making gold patch design single layer or double layer resist can be used both in the case of photolithography and e-beam lithography.

Following the writing of the gold patch design, a deposition of a layer of Au/Cr (50 nm/5 nm) was employed via an electron beam evaporator or thermal evaporator. The developed gold strip, later on, can act as a mask in the RIE etching procedure to define the channel length and to open the channel entries shown in figure 3.26.

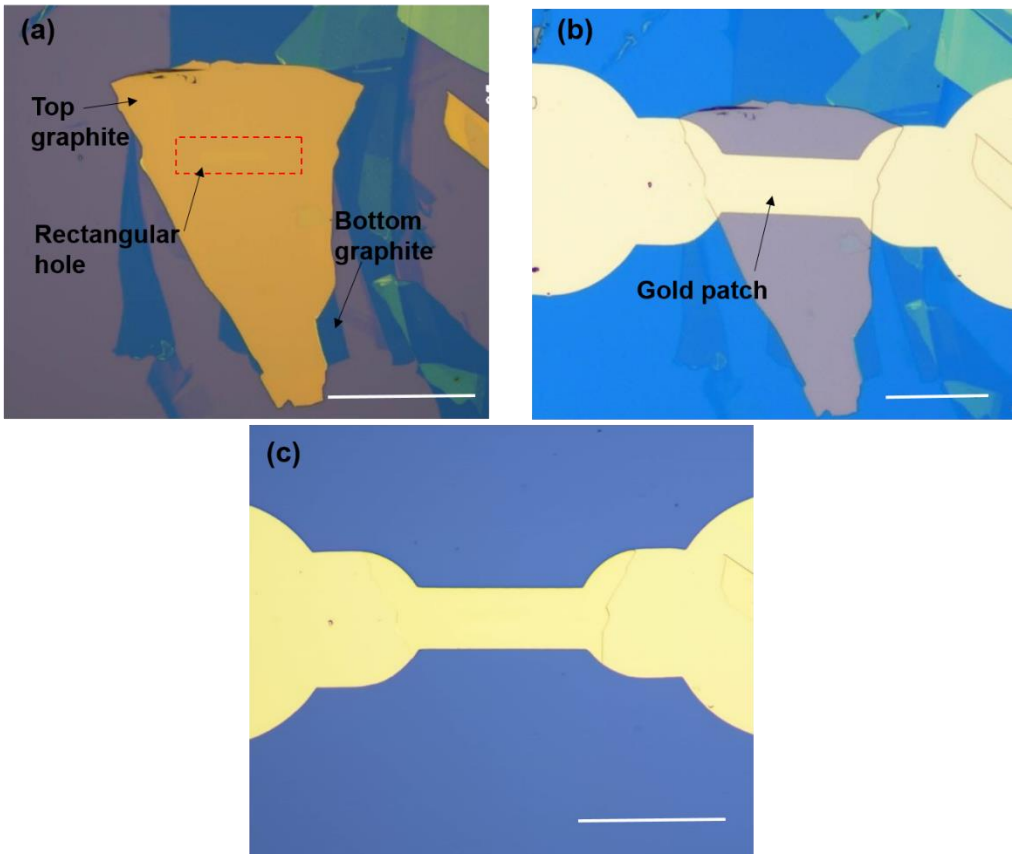

Figure 3.26: Capillary device with and without gold patch (a) Optical image of device with bottom, spacer and top flakes. Hole is inside the dotted rectangle. (b) Gold patch fabricated on the device (c) surrounding graphite etched to open the channel entries. All scale bars are equal to 25 µm.

Deposited metal on the device was lifted off in a hot acetone solution by keeping it on the hot plate (60 °C) for 2 hours. The metal lift-off process was then proceeded with blowing the substrate surface with the pipette. If all the gold is not lifted then the device was transferred to another fresh hot acetone solution (60 °C). For checking the lift-off process under microscope device is placed into an IPA filled petri dish and while transferring, an IPA wash bottle was used to wet the device surface. Metal lift-off condition (i.e., continuous Au strip with clear boundaries, no disturbed Au layer residue) under the optical microscope was closely checked with different objectives. After lift-off, a clear gold strip design will be left and the rest of the gold will be removed. Optical images of the capillary device before and after the gold patch deposition are shown in figure 3.26a and figure 3.26b respectively.

After this step, the device was etched using the reactive ion etcher. For bottom graphite, graphene spacer and top graphite device etching was done with the recipe with O_2 50 s.c.c.m., 10 mTorr, 2000 W for 1 minute. For bottom hBN, graphene spacer and top hBN device, top hBN layer was first etched with BN etch recipe using SF_6 60 s.c.c.m., O_2 15 s.c.c.m., 10 mTorr, 300W. This recipe gives an etching rate of 3 nm hBN per second. After etching top BN, graphene spacer was etched using O_2 recipe and then in the end bottom hBN was etched using BN etch recipe. To this point, device is ready (figure 3.25 c) and annealed before use under the Ar/H_2 (9/1) environment using the recipes discussed earlier in section capillary device assembly.

As graphite is hydrophobic it adsorbs hydrocarbons from the environment. Nanochannels adsorb the hydrocarbons from the air over time these hydrocarbons could even enter the nanochannels and block them. In fact, most of our channels start getting blocked within a few days, to prevent this, we store our devices in charcoal that absorbs the hydrocarbons before they reach the device and prevent our devices from clogging. Storing the devices in water also prevents clogging over a long time as water fills the channel due to the capillary effect and keep the hydrocarbons out. Annealing also desorbs the hydrocarbons and helps in opening the clogged nanochannels (194).

This method takes the advantage of self-cleansing property of van-der Waals assembly over the other nanofluidic structures. When one crystal is stacked over another by van-der Waal interaction, contamination (normally hydrocarbons) is squeezed into bubbles (195), permitting cleaner interfaces and we get atomically flat and clean channels.

To ensure the functionality of the devices few parameters i.e., channel to spacers width, the thickness of the top crystal, cleanliness of the channels are checked regularly through the fabrication process. As a check for the reproducibility of devices with atomic-scale capillaries, about 50 to 60% of devices show the measurable flow corresponding with the number of channels. Other devices did not conduct gas or showed much lower or higher gas flow. For those devices which do not show any leak or small leaks, annealing has been done and the annealing step helps conduct the gas.

3.8 Controls for 2D channels and 0D apertures

Before doing the permeation experiments through the 0D apertures and 2D channels devices control experiments were done to ensure that the nanofluidic flow is through the apertures and channels only. Silicon nitride membrane without any hole was checked with the device holder for a longer time exposure to helium to ensure there was no helium leak from the device holder or the silicon membrane. Negligible helium flow (~10^{-18} mol s^{-1} $mbar^{-1}$) below our detection limit has been detected for these membranes. A large set of bare holes (30 nm, 100 nm, 1 µm, 2 µm, 5 µm and 20µm) on the silicon nitride membranes were drilled to compare the gas leak rate with the theoretical Knudsen equation to validate our experimental values.

3.8.1 Control for 2D channels – Devices without channels

In the case of 2D channels devices, controls were designed in such a way that the top and bottom crystal is stacked on top of each other with no spacer crystal leaving no space for the fluid flow. This assembly of the top and bottom crystal with no spacer crystal between two graphite flakes create a well-sealed cross-section with no loss in atomic continuity in the perpendicular direction because of the van der wall forces amongst the two crystals. This assembly is placed on the rectangular aperture on the silicon nitride membrane to check the flow through this control device with the helium leak detector setup as of figure 4.2. All the protocols for device fabrication and annealing steps were followed for this control device. Gas flow has been tested through the helium leak detector through this control and no flow has been detected giving no leak which is also shown in figure 4.4.

3.8.2 Control for 0D apertures

As control samples for the 0D apertures devices presented in chapter 5, three different control were designed and tested to check the validity of gas flux experiments. The first control was a pristine silicon nitride membrane without any hole, the second was with a nanometre-sized hole in the silicon nitride membrane without WS_2 membrane and the third control was a non-irradiated WS_2 membrane suspended over the silicon nitride hole. The control samples were used to establish baseline flow are a different

set of membranes than those used for gas transport; however, they all come from the same fabrication procedures and chemical vapor deposition (CVD) growth. Silicon nitride membrane without any hole was checked with the device holder for a longer time exposure to confirm there was no helium leak from the device holder or the silicon membrane. A bare hole without the WS_2 layer exhibits large gas flow, as expected, and has been used as a standard leak for validation of the experimental setup (figure 4.2). A freestanding pristine WS_2 monolayer covering nine holes each with diameters of ~250 nm, without any irradiated defects, exhibited negligible helium flow below our detection limit (~10^{-18} mol s^{-1} $mbar^{-1}$). WS_2 monolayer grown by CVD methods employed in chapter five has such low intrinsic defect density that it is practically impermeable over a suspended area of a few square micrometres.

Impermeability emphasizes the excellent sealing of the WS_2 layer on the SiN_x membrane in our devices, which is even attained by repeated annealing of the samples in the H_2/Ar atmosphere at 350 °C, both right after the WS_2 monolayer transfer and also before the gas flow measurements.

Detailed gas measurements were done on the 2D capillaries and 0D aperture devices have been presented in chapter 4 and chapter 5 of this thesis.

Chapter 4

Gas transport Measurements

Gas flows in angstrom-scale constrictions are of significant importance for gas extraction and separation processes. Membranes based gas permeation and separation are well known for materials likes zeolites, carbon sieves and carbon nanotubes which provide insight into molecular separation based on size exclusion. In this chapter, I will discuss gas transport using inert helium gas molecules for the permeation of gas molecules through the capillaries. The flow rate of other gases has also been explored using a mass spectrometer to check the permeation and selectivity of these gases as compared to helium. The gases used were hydrogen, helium, deuterium, oxygen, argon, nitrogen, carbon dioxide, methane, butane, Isobutane and xenon. (H_2, He, D_2, O_2, Ar, N_2, CO_2, CH_4, C_4H_{10} and Xe).

4.1 Gas transport through atomic scale capillaries

The dynamics of gases flowing through nanostructures are significantly different from larger dimension systems. At room temperature and ambient pressure, most gases have their mean free path around 100 nm. Depending on the exact value of the mean free path and the dimension of the structure, the transport of the gas molecules could be governed by their collisions with the walls of the structure or that with each other. The flow rate (Q) of gases in conduits where the cross-sectional radius is much smaller than the mean free path (λ) of the gases lies in the molecular flow regime (196, 197). In our fabricated capillary devices height of the channel is within 5 nm, gas flux lies completely in the molecular flow regime. Molecular flow regime is attributed to the dependence of flow on the properties of the nanostructure walls, molecules are not colliding with each other but the gas wall interaction is important (196-198)., In 1909 Knudsen put forward a molecular theory to describe the mass flow rate in nanostructures (197).

$$Q = \alpha \left[A \left(\frac{M}{2\pi RT} \right)^{1/2} P \right] \qquad (4.1)$$

Where α is the transmission coefficient, *A* is the cross-sectional area of the nanochannel, *M* is the molecular mass of the gaseous molecule, *R* is the gas constant, *T* is the temperature in kelvin and *P* is the pressure. *A* is characterized as *w.h*, *w* being width and *h* is the height of the channels. For our 2D-capillary devices described in chapter 3, the width of the channel is 120 nm and the height of the channels is determined from the thickness of the chosen spacer flake. The part in the square brackets is the flow rate of molecules into the channel and *α* is the transmission coefficient of the channel that describes the fraction of molecules that pass through the channel without loss in energy and momentum. Knudsen derived this transmission coefficient for different channel geometries and assumed diffuse reflections at the channel walls. In the flow equation, the parameter related to specific gas is only the mass of the gas molecules. Channel sizes dealt with in this thesis are in a few angstroms to a few nm range, hence the flow is governed by the kinetic diameter which can physically block these molecules or lead to steric effects.

For long and narrow rectangular channels, the transmission coefficient α can be approximated by(196, 198).

$$\alpha \approx \frac{h}{L} ln\left(\frac{4w}{h}\right) \tag{4.2}$$

Helium leak detector has been used to study the helium flow rate through the channels. Capillary devices once fabricated, are checked for reliable flow rate values to ensure that the capillaries device is leak-tight and that there are no leaky paths other than the nanochannels for the discernible helium permeation.

4.2 Gas transport measurement using a leak detector

Leybold Vacuum's (INFICON UL200) helium (He) leak detector has been used for the gas transport measurements. The helium leak detector is a mass spectrometer tuned to detect the absolute leak rate of He into it. It detects the amount of gas in the connected chamber with a processing time of less than a second and act as a mass

spectrometer selective for gases up to mass 4 amu. Gases other than helium i.e. hydrogen and deuterium can also be detected with this system.

4.2.1 Helium leak detection setup

To connect the capillary device to the helium leak detector, device on the SiN_x chip is mounted on a sample holder which connects the inlet of the device to purge the gases from the top and outlet of the device to the leak detector at the bottom with help of vacuum parts.

A custom-made device holder is designed in such a way that two conical chambers having O-rings are fastened together with the nano-channel device in between. Both chambers are hollow from inside, connecting the inlet and outlet of the sample to the Helium input and leak detector respectively. The device holder is fastened with screws to keep the sample tightly in place. The sample holder is an adaptor that connects the two chambers to support the device with O-rings in place to avoid mechanical strain and breakage of the SiN_x chip as well as to pass the gas from the device to the spectrometer to detect it (figure 4.1).

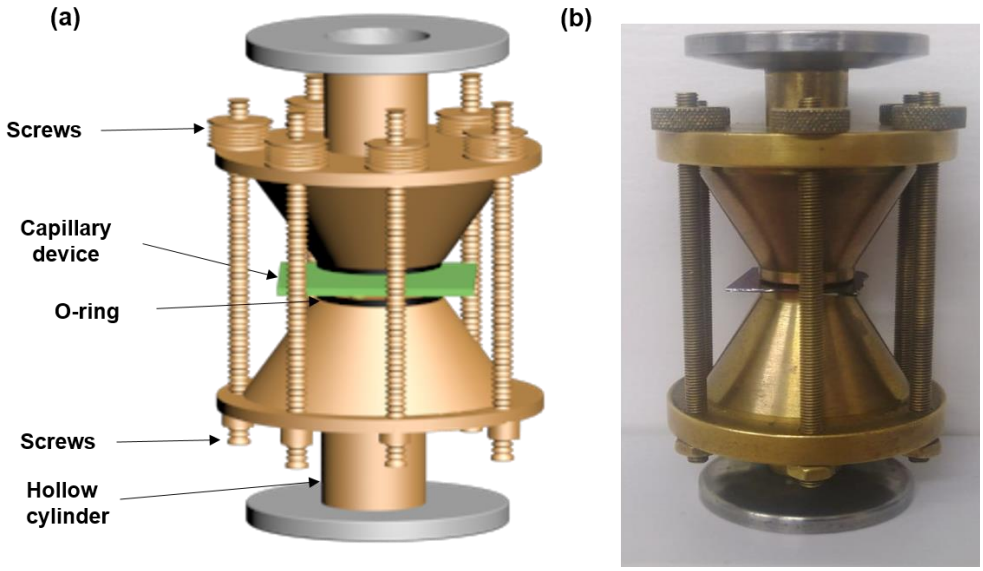

Figure 4.1: Device holder for gas flow measurements. (a) Image of the device holder that connects the input to the source of gas (balloon) and output of the device to the spectrometer to detect the amount of gas passed through the capillaries. (b) Real-time device holder used for the gas flow measurements.

Gases are introduced from the balloon connected to the upper chamber. Gases purged through the top side, entering from the inlet of the device to flow through the channels and exit from the output end below at the bottom of the setup, where it is connected to a leak detector to detect the helium leak rate. Inside the helium leak detector, helium gas flows through the turbo pump into a mass spectrometer, which has been calibrated using a known flow rate.

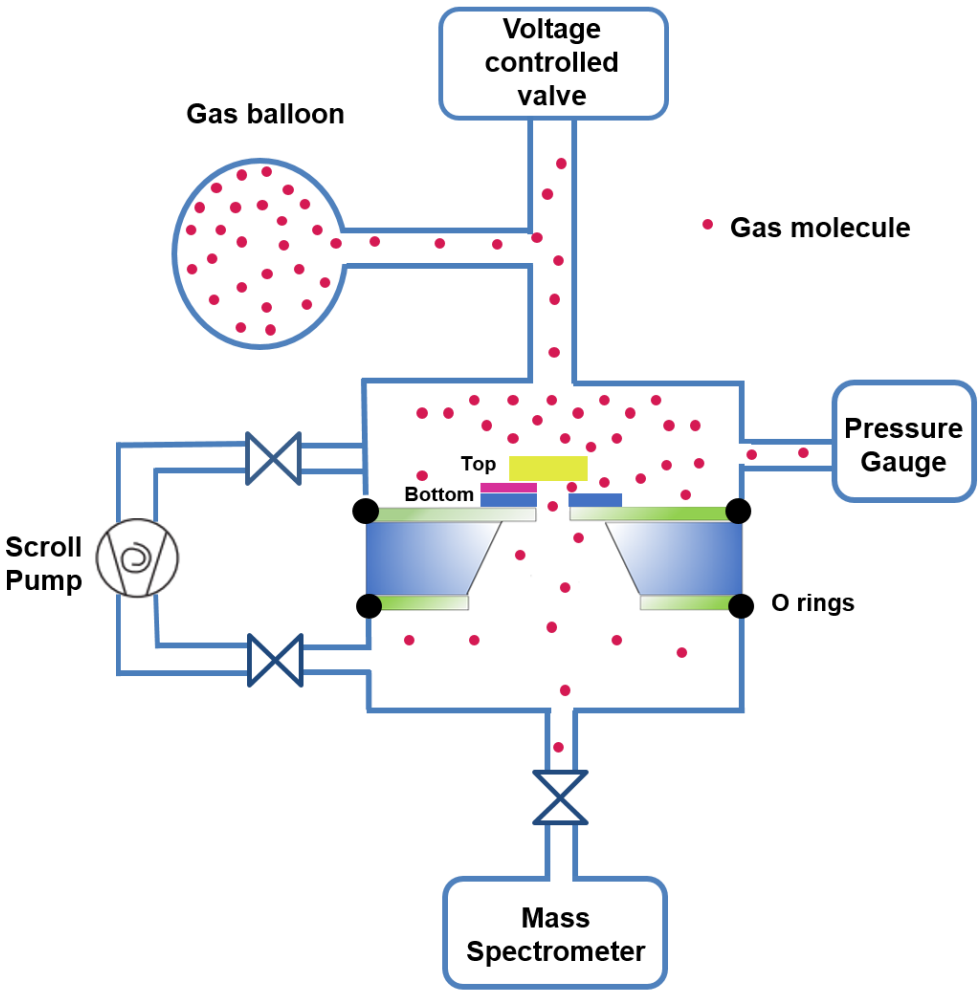

Figure 4.2: Schematic diagram of the setup used for gas flow measurements.

Before each measurement, both ends of the sample holder are connected to the vacuum pump to evacuate the setup from all other atmospheric gases. The pressure of the gases from the input is controlled by a voltage controlled valve that is connected to the input of the sample holder. The pressure in the input chamber is monitored using a pressure gauge attached to this chamber. Helium flow rate is measured through the

leak detector attached at the output end. These pressure change and leak rate values are continuously transmitted to a computer and recorded using a LabVIEW program.

Helium leak detector maintains a vacuum of the order of 10^{-3} mbar, so we apply a regulated high pressure (P) at the other end of the capillary device to cause the flow of helium atoms from the top of the device through the nanochannels into the leak detector. So, the pressure difference, $\Delta P \approx P$. The devices can withstand pressure up to 1 bar but usually flow rate is measured until 300 mbar pressure. The helium leak detector is sensitive to any small amount of gas and can detect any gas on this system in the range of 5×10^{-12} mbarL/s.

4.3 Gas permeation through capillary devices

Helium flow measurements through monolayer graphene capillaries i.e., channels made with a monolayer graphene spacer flake are shown below. Helium kinetic diameter is about 2.6 Å which is flowing here through a 3.4 Å tall 2D-slit like channel. Figure 4.3 shows the helium leak detector measurement from a capillary device with 700 graphene slit-like channels each 2 µm long, with increasing pressure difference across it.

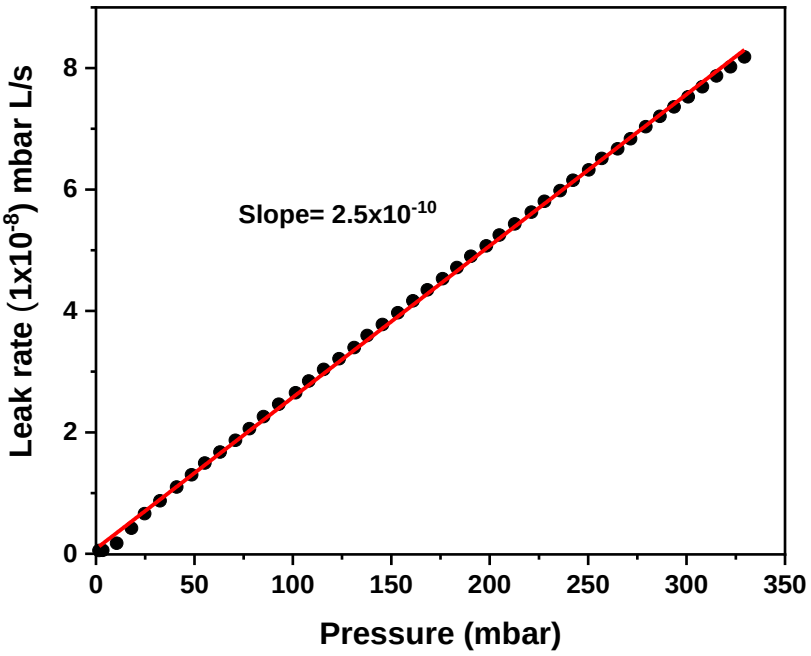

Figure 4.3: Flow rate of helium gas through monolayer capillaries. Helium gas flows through the monolayer graphene capillary device with increasing pressure difference across it. Red line represents the best fit.

For increasing pressure differences across the channels, the flow rate increases linearly. Linear fit extrapolates to zero flow for zero pressure difference. A linear flow rate with pressure indicates a flow conductance, which is independent of pressure difference. From the slope of the linear region, conductance = 2.5x10^{-10} L/s for 700 channels. This corresponds to a conductance of = 3.5x10^{-13} mbar L/s per mbar per channel. The helium leak detector measures the flow rate in mbarL/s which can be converted to molar mass or atomic flow rate using the ideal gas equation:

$$PV = nRT \tag{4.3}$$

Where P is the pressure, V is the volume, n is the number of moles and T is the temperature of the gas and R is the gas constant. To convert between flow rates from mbar L/s to mol/s, a conversion factor can be calculated as $1\,mbar.l = 1.6\text{x}10^{-4} g$ using ideal gas law for helium gas conversion.

Gas flow measurements were done through capillaries with different layers to find out the relationship of gas flow with respect to varying height (by changing layers of graphene) of the channels.

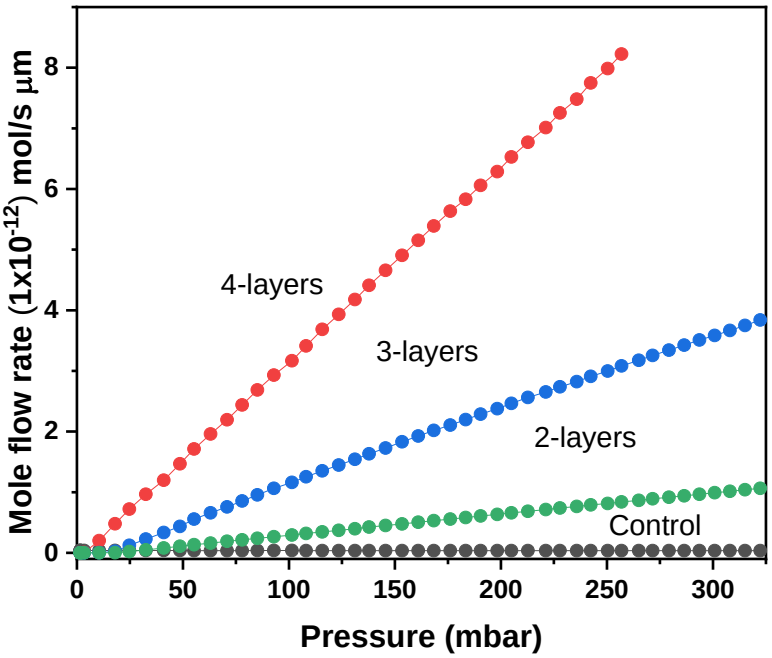

Figure 4.4: Comparison of helium gas permeation by varying height. Helium gas permeation for different capillary devices plotted with respect to channel height and a control device without graphene spacers.

Figure 4.4 plots the helium permeation through capillary devices with varying channel height. The flow rates at room temperature are normalized per single-channel and per channel length. Gas flow rate increases for increasing channels height i.e. from bilayer to 4 layers. The helium leak rate was also measured through a control device i.e., without graphene spacers. No leak rate was found for the control device which is an indication that the fabricated capillaries are the only conduits for the detectable gas flows. It also indicates that 2D layers are restacked through van der Waals heterostructures with no loss in atomic continuity.

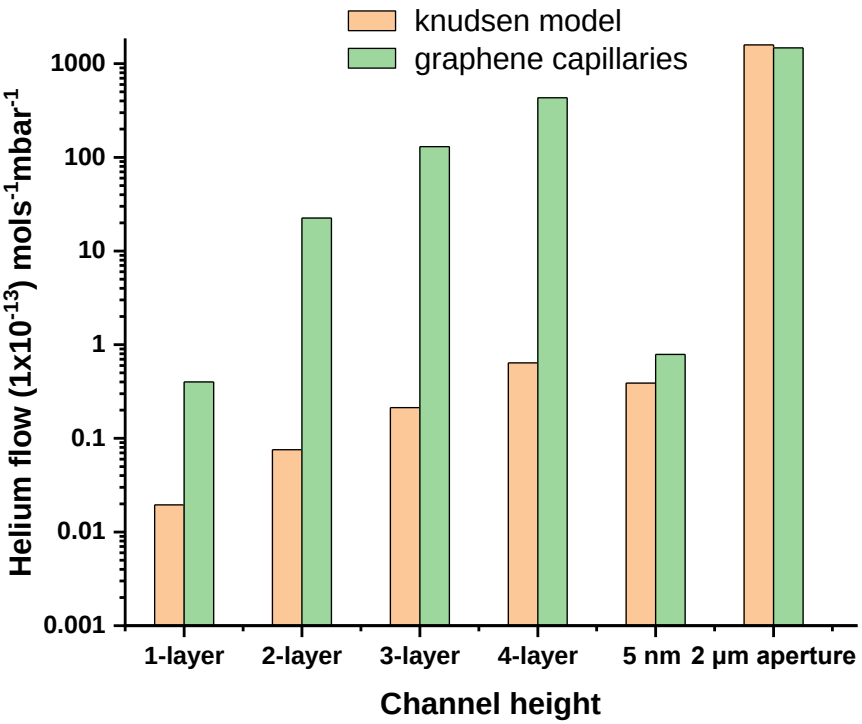

.

Figure 4.5: Enhancement of helium permeation through graphene capillaries over Knudsen theory. Helium permeation for different capillary devices plotted with respect to channel height is compared with Knudsen theory. A 2 µm aperture is also presented as a comparison.

Enhancement in flow rate is observed for graphene capillaries with the height of the channels. For graphene capillaries (1-4 layers) the enhancement is increasing from monolayer to 4 layers graphene capillary device giving maximum enhancement of more than 2 orders difference for 4 layer device. This observation is also reported in (30, 35, 80) and is attributed to the atomic smoothness of the walls. Helium molecules give specular reflections on colliding with smooth graphene surfaces and give enhanced flow rates as compared to Knudsen theory.

When the channel height is increased to a few nanometres (5 nm device i.e. capillaries made from 5 nm thick spacers) there is no enhancement and flow rates fit well with the Knudsen calculated flow thus following the standard behaviour. As a comparison, gas flow through an aperture (diameter, 2 µm) was also measured which follows the Knudsen diffusion mechanism and validates our measurement setup. The enhancement in narrow channels is attributed to the specular scattering of the helium

molecules on the atomically smooth walls of the nanochannels. For the sub-2 nm channels, self-cleansing and stronger confinement lead to polymer and hydrocarbon contamination being pushed out, whereas larger channels suffer lower confinement energy which keeps the contamination molecules within the channels (35). Thus larger channels with their relatively rough surfaces due to contamination pinning points, show the diffuse scattering as assumed in the Knudsen equation. The self-cleansing phenomenon is well known in between van der Waals crystals and is attributed to a larger van der Waals force between them than the force of interaction between the crystals and hydrocarbon residue. Due to this self-cleansing atomically clean regions are formed between van der Waals heterostructures separated by bubbles of accumulated hydrocarbon residue (121, 199) which are the reason for enhanced permeation through the graphene capillaries. These results were elaborated in the manuscript by Keerthi et al., *Nature* **558**, 420–424 (2018) where I am one of the co-authors.

4.4 Gas transport and selectivity using a residual gas analyser

To explore the transport of gases through capillaries beyond the helium mass residual gas analyser, a spectrometer capable of detecting a wide range of atomic masses was used. A residual gas analyser (RGA) is a mass spectrometer that can detect small traces of gases in high vacuum systems. The gases used were H_2, He, D_2, O_2, Ar, N_2, CO_2, CH_4, C_4H_{10} and Xe.

The RGA setup used to measure the flux of gases is similar to the leak detector setup shown in figure 4.2, except that the RGA does not have an in-built pump, and so requires an external pump to create the high vacuum. This pump maintains a pressure of 10^{-7} mbar in the lower half of the system. In this high vacuum, the RGA can detect any small traces of gas flowing in through the sample.

To achieve the selectivity of different gases the kinetic diameter of the gases should be comparable to or larger than the smallest dimension of the system which is the height of the channels in our capillary devices. The kinetic diameter of the gases used was in the range of 2.6- 5.2 Å presented in table 4.1. Kinetic diameters for selected

gases are well in the range or above the height of the monolayer graphene device i.e., 3.4 Å which is the thinnest channel we can achieve.

Gases	**Molecular weight** (g/mol)	**Kinetic diameter** (Å)
He	4	2.6
H_2	2	2.89
Co_2	44	3.3
O_2	32	3.46
N_2	28	3.64
CH_4	16	3.8
Ar	40	3.43
Xe	131	4
Butane	58	4.69
Isobutane	58	5.2

Table 4.1: Gases and their kinetic diameter. Gases used for the permeation experiment along with their molecular weight and kinetic diameter (200, 201).

Unfortunately, through various measurements performed on different devices of height 3.4 Å (monolayer graphene capillary), no detectable permeation was observed due to the flows being below the limit of detection of RGA (gas permeation system used). There could be two options to detect the gas flux to check the selectivity of different gases i) flux through the capillaries increased to surpass the detection limit of our system, few experiments could be designed to have more flux (increasing the number of channels in a device) ii) using some other more sensitive instrument.

Permeation of gases through capillary devices containing larger channel height (bilayer to 4-layers) has been measured and compared with helium for the selectivity analysis presented in figure 4.6.

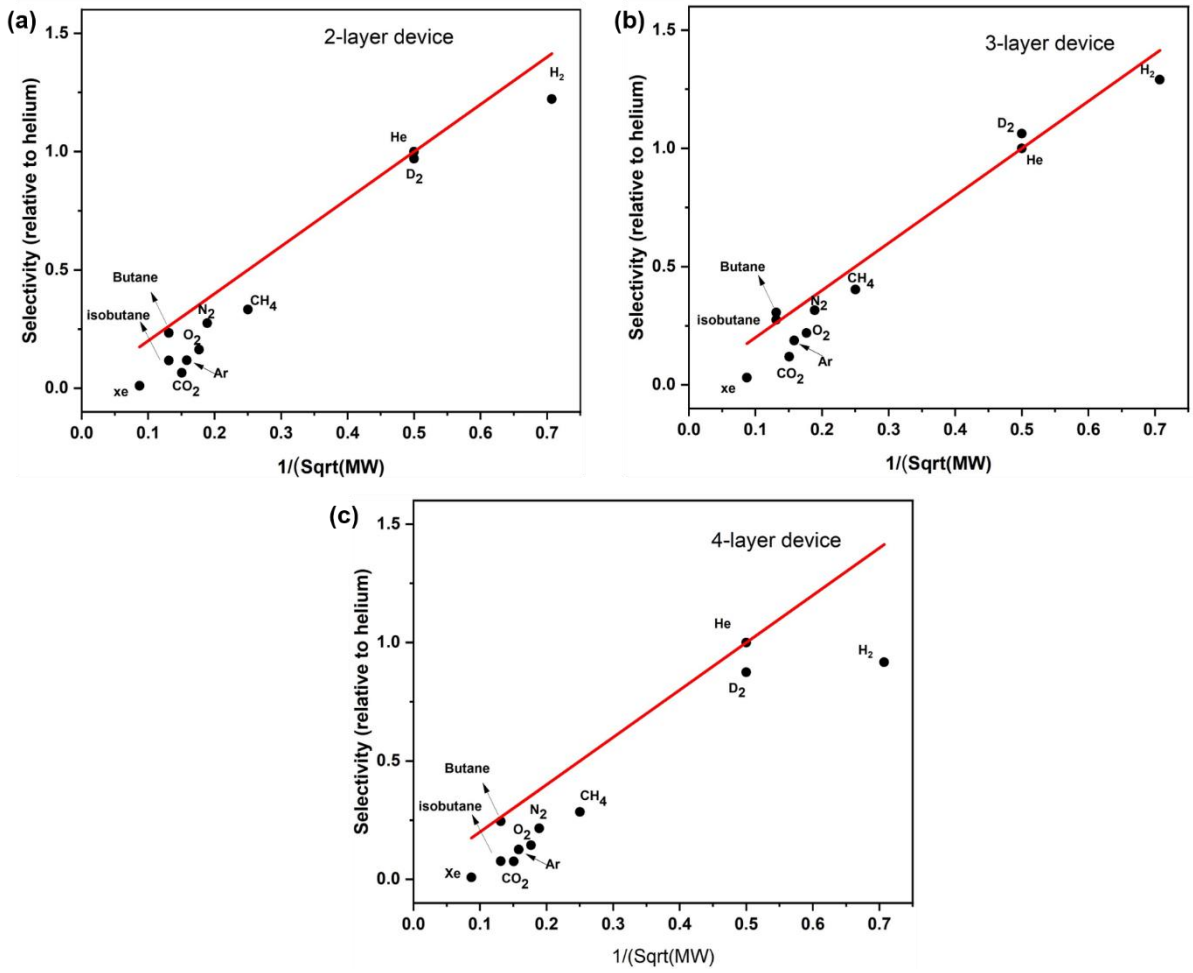

Figure 4.6: Selectivity of gases relative to helium. Selectivity of gases relative to helium for different capillary devices plotted with respect to channel height (varying with a number of graphene layers) (a) for bilayer device, (b) for tri-layer and (c) for 4 layer channel height. The red colour line is Knudsen diffusion model scaling which is presented for comparison.

For larger channel height devices (from 2-layer to 4-layer) all the gases permeated without any specific selectivity, as the Kinetic diameter of most of the gases is well below the channel height. Selectivity of the gases follows the expected inverse-square-root scaling of molecular mass (84, 202) as expected from Knudsen equation 4.1. Permeance and selectivity can depend on differences in molecule size, mass, surface adsorption, and usually permeance decreases as the kinetic diameter increases (203-206). Owing to the height of the channels being large, no direct relationship was found for gas permeation with the kinetic diameter. The permeance

of He through atomic-scale pores are measured and analysed using the same measurement setup used in this chapter 5 “Atomic-scale pores are created in WS_2 membrane knocking out the W atoms and creating atomic vacancies with a controlled localization of defect sites using FIB. The helium molecules permeated through these pores and gave fast flow, detailed results will be discussed in chapter 5.

Chapter 5

Gas flow through atomic-scale apertures

The results are from a paper published in Science Advances in 2020.

Jothi Priyanka Thiruraman, Sidra Abbas Dar, Paul Masih Das, Nasim Hassani, Mehdi Neek-Amal, Ashok Keerthi, Marija Drndić, Boya Radha, Gas flow through atomic-scale apertures. *Science Advances* **6**, eabc7927 (2020).

My contribution to the work includes the measurements of the samples and their analysis. Annealing of the samples was also done by me before any gas measurement. I also did substrate inspection of the samples in AFM and SEM to make sure the pores and membranes are intact.

Author contributions: B.R., M.D., and A.K. designed and directed the project. J.P.T. and P.M.D. grew TMD materials and fabricated and characterized the devices. Specifically, J.P.T. carried out sample fabrication, FIB irradiation, and TEM image analysis. P.M.D. conducted AC-STEM imaging and Raman/PL measurements /analysis. S.A.D., A.K., and B.R. performed the measurements and their analysis. N.H. and M.N.A. performed the DFT calculations. B.R., A.K., and M.D. wrote the manuscript with the inputs from J.P.T., P.M.D., and M.N.A. All authors contributed to discussions.

Importance of the study

The molecular permeability of helium through the atomic-scale aperture made in monolayer tungsten disulphide (WS_2) membranes is studied to validate Knudsen descriptions and to quantify the relation between atomic-scale vacancies and gas flow. Vacancies are created in a freestanding monolayer (WS_2) by focused ion beam irradiation. Gas flows through these atomic-scale vacancies proved these apertures mechanically robust and showed fast helium flow. A quantified relation amongst atomic-scale vacancies and gas flux over a large area confirming the formation of pores has been established using gas flows. Pristine monolayer WS_2 membranes proved to be atomically thin barriers to gas transport. This method proved to be simple

and robust for the quantification of pores through gas flows and can be used for molecular separation, sensing and monitoring gases.

Introduction: The rise of graphene and other atomically thin materials has opened new possibilities in membrane technology. The atomic thinness of these materials has made these membranes the thinnest possible barrier (207) to gases which has remarkable mechanical strength, chemical robustness. These membranes can sustain selective, nanometre-scale pores (68) and suggested the realization of inducing an ideal nanoporous atomically thin membrane that can be tailored to a range of applications. Membranes are widely used for gas separation and production technology. Understanding confined gas flow in membranes is the key criteria to design gas extraction techniques(92). Permeability and selectivity play a major role in designing a gas extraction technique.

The membranes exhibit a compromise between permeability and selectivity of the molecules. Separation based on size difference is common but the understanding of the pores at molecular size i.e., size of the pores, the volume of the pore and pore size distribution is desirable and key criteria for measuring the permeability and selectivity. Extremely small nanopores in thinner membranes have emerged as an ideal candidate for gases permeation with high permeation (33). The permeability and selectivity of the membranes depend on the physical and chemical characteristics of the membrane materials (208).

In such small scale pores the gas dynamics is dominated by the molecular collisions with the wall of the pore instead of collision amongst each other. The mean free path of the gas molecules is much larger than the pore size so there is very little chance of molecules interacting with each other consequently molecule wall interactions are dominated and gas dynamics are following the free molecular regime. Gas flux in the free molecular regime is due to small pore size and is characterised using the Knudsen equation(93), which is adapted and has been modified for the gas flows through various confined systems (62, 94, 95, 197).

With the recent advances in nanofluidics, various nanofluidic system has been developed for the gas flow such as nanopores (62, 69, 209) nanotubes (80, 95) and nanolaminates (33, 94, 208) etc. gas flows in such small scale lies in the free molecular regime and is governed by the Knudsen equation. There have been few systems (68,

69, 209, 210) where the Knudsen equation is not valid and these systems challenge the applicability of the Knudsen flow on the molecular scale conduits.

Atomic vacancies produced in monolayers of 2D materials are the membranes with ultimately narrow quasi–zero-dimensional (0D) apertures with atomic-scale dimensions and are best studied for gas flows and a lot of work has been done through simulation and modelling (211-214). Nanopores are not studied well experimentally and lack the connection between pores and gas flows experimentally. In this work inert gas i.e., helium flow has been investigated through atomic vacancies in freestanding monolayer tungsten disulfide (WS_2) membranes. Atomic vacancies in these membranes are produced using a focussed ion beam to knock out tungsten atoms and studied the gas flow to validate the Knudsen description in the ultimate atomic aperture limit. Because of the thinness and ultimate narrow aperture size, they provide rapid permeation of gas that can be used for separation applications.

Gas flow through atomic-scale apertures

Jothi Priyanka Thiruraman [1,2*], Sidra Abbas Dar [3,4,5*], Paul Masih Das[1], Nasim Hassani [6], Mehdi Neek-Amal [6,7], Ashok Keerthi [4,8†], Marija Drndić [1†], Boya Radha [3,4†]

[1] Department of Physics and Astronomy, University of Pennsylvania, Philadelphia, PA 19104, USA.

[2] Department of Electrical and Systems Engineering, University of Pennsylvania, Philadelphia, PA 19104, USA.

[3] Department of Physics and Astronomy, School of Natural Sciences, University of Manchester, Oxford Road, Manchester M13 9PL, UK.

[4] National Graphene Institute, University of Manchester, Manchester M13 9PL, UK.

[5] Department of Basic Sciences and Humanities, University of Engineering and Technology, New Campus, GT Road Lahore, Kala Shah Kaku, Pakistan.

[6] Department of Physics, Shahid Rajaee Teacher Training University, 16875-163 Lavizan, Tehran, Iran.

[7] Universiteit Antwerpen, Groenenborgerlaan 171, B-2020 Antwerpen, Belgium.

[8] Department of Chemistry, School of Natural Sciences, University of Manchester,

Oxford Road, Manchester M13 9PL, UK.

* These authors contributed equally to this work as co-first authors.

†Corresponding author. Email: radha.boya@manchester.ac.uk (B.R.); drndic@physics. upenn.edu (M.D.); ashok.keerthi@manchester.ac.uk (A.K.)

Gas flows are often analyzed with the theoretical descriptions formulated over a century ago and constantly challenged by the emerging architectures of narrow channels, slits, and apertures. Here, we report atomic-scale defects in two-dimensional (2D) materials as apertures for gas flows at the ultimate quasi-0D atomic limit. We establish that pristine monolayer tungsten disulfide (WS_2) membranes act as atomically thin barriers to gas transport. Atomic vacancies from missing tungsten (W) sites are made in freestanding (WS_2) monolayers by focused ion beam irradiation and characterized using aberration-corrected transmission electron microscopy. WS_2 monolayers with atomic apertures are

mechanically sturdy and showed fast helium flow. We propose a simple yet robust method for confirming the formation of atomic apertures over large areas using gas flows, an essential step for pursuing their prospective applications in various domains including molecular separation, single quantum emitters, sensing and monitoring of gases at ultralow concentrations.

INTRODUCTION Understanding confined gas flows in angstrom-scale tight spaces plays a major role not only in the design of gas extraction techniques but also in gas separation and production (1). In extremely narrow pores, the mean free path of gas is much larger than that of the dimensions of the pore itself, which leads to gas dynamics dominated by molecular collisions with walls of the pore rather than the intermolecular collisions (2). This is known as the free molecular regime, and the gas flux through these pores was comprehensively described using the Knudsen equation (2), which has been modified and adapted to explain the flows through various confined systems (3). From a theory standpoint, a pore or an aperture is a simple model system through which gas transmission is proportional to the impingement of gas molecules, i.e., the likelihood of a gas molecule encountering a pore, and the activation barrier, if any, to cross the pore. In the cases where the membrane surface can adsorb gases, the flow is a combination of direct transmission through the pore and diffusion along the membrane surface (4). Despite the emergence of many nanoscale gas flow conduits such as nanopores (5–9), nanotubes (10–12), nanochannels (11, 13–16), nanolaminates (17, 18), etc., ultimately narrow quasi–zero-dimensional (0D) apertures with atomic-scale dimensions in both the transmembrane and lateral directions, which challenge the applicability of the Knudsen equation for gas flows, have been limited (5, 8, 9, 19). Although atomic vacancies in monolayer 2D materials have been ideal candidates for theoretical simulations modelling of gas flows (4, 20–22), they have not been studied extensively in experiments (9, 14). Here, we investigate an inert gas, i.e., helium flow through atomic vacancies in freestanding monolayer tungsten disulfide (WS_2) membranes, to validate the Knudsen description in the ultimate atomic aperture limit.

RESULTS

Several studies in the past have explored various sources for atomic defect creation in 2D materials; among those, the popular techniques are oxygen plasma (*23*, *24*), thermal annealing (*25*), ion and electron beam irradiation (*26*, *27*), acid etching (*23*, *28*), and ultraviolet-induced oxidation etching (*5*). In particular, ion irradiation offers a precise method of creating atomic vacancies with a controlled localization of defect sites at comparatively high densities (>10^{11} cm^{-2}).

Recently, we have illustrated how to create highly controlled single-atom defects by focused ion beam (FIB) irradiation on a monolayer transition metal dichalcogenide (TMD) flake (*29*). In particular, TMDs provide better imaging contrast in aberration-corrected scanning transmission electron microscopy (AC-STEM) imaging and appear less prone to contamination, enabling easier characterization of the defects. We compared the effects of FIB irradiation on various suspended monolayer TMDs and established that defects with areas down to 8 $Å^2$ (single transition metal vacancy) can be produced in WS_2 with a specific low irradiation dose (increasing dose produces larger vacancies in the membrane). Therefore, we choose monolayer WS_2 as an optimal base support for hosting single-atom defects. Apart from being mechanically stable with Young's modulus of 270 GPa and a thickness of ~0.7 nm (*30*), our detailed investigation of the controlled ion irradiation mechanism minimizes the possibility of undesired damage or tears. The FIB irradiation mechanism used here allows for exclusively hosting single atomic apertures on a freestanding monolayer WS2 membrane, enabling a high density of uniform defects in the range of $9 \times 10^{11} \pm 3.5 \times 10^{10}$ cm^{-2} (see sections S1 to S3). These defect densities are comparable to those achieved in graphene membranes (*9*).

The WS_2 membranes incorporating atomic vacancies are supported on silicon chips (SiN_x/Si) with a size of 11 mm by 11 mm (Fig. 1A and fig. S1). In the centre of each chip, one or more sub-micrometre holes were drilled in a freestanding silicon nitride (SiN_x) membrane (Fig. 1B). A monolayer WS_2 flake was suspended on submicrometer holes present on these silicon chips (see fig. S1). The suspended flake was irradiated with 30-kV gallium–sourced FIB under specific precalibrated irradiation dose conditions to produce single atomic vacancies (illustration is shown in Fig. 1B). We exposed samples to an ion irradiation dose of 5.1×10^{13} ion/cm^2 and obtained a defect density of 0.08 ± 0.03%, with an average defect area of 0.12 nm^2 and a median defect

area of 0.09 nm^2. Figure 1C is a representative image of atomic-scale defects produced through this method. We observe single atomic apertures where 1W atom vacancies can be seen, as included in Fig. 1D. It is often challenging to locate S atoms in AC-STEM images because of their weaker contrast compared to heavier W atoms. The creation of atomic defects possibly leads to the reconstruction of immediate surrounding sulfurs in the monolayer lattice; hence, we see a variety of shapes of the apertures such as triangular, truncated triangular, to pseudo-spherical (see table S1 and fig. S4). On the basis of analysis of several atomic-resolution images, we estimate the total defect sites resulting from missing W atoms to be few hundreds to a few thousand per one device depending on the supported membrane area.

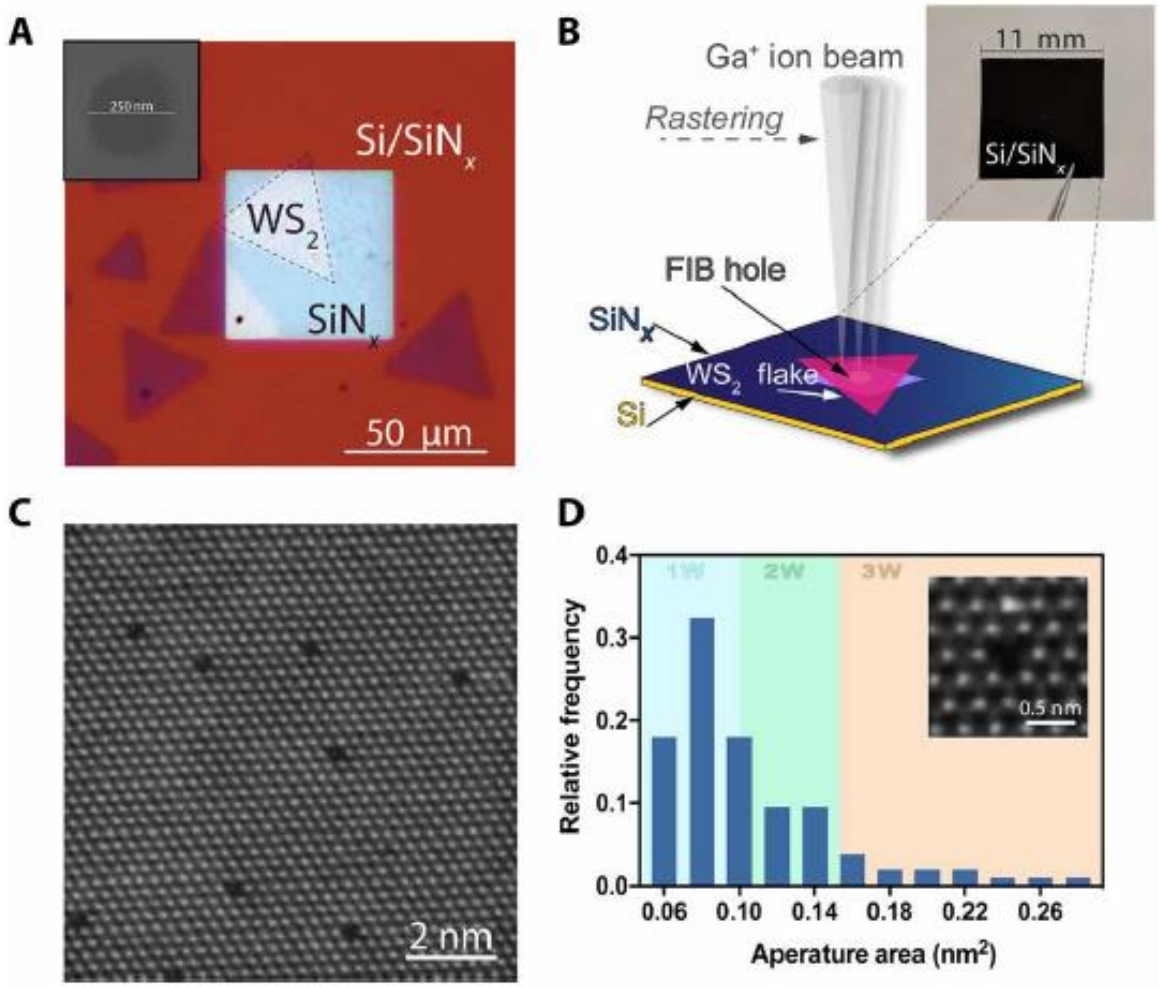

Fig. 1. Atomic apertures were fabricated using a FIB scanning technique. (**A**) Optical microscope of a monolayer WS_2 flake suspended in the centre of a silicon nitride (SiN_x) membrane (~50-nm thickness, 50 µm by 50 µm) using position-control transfer technique. The inset shows a scanning electron microscopy image of a hole of 250 nm in diameter drilled in the centre of the SiN_x membrane. (**B**) Schematics of

the irradiation technique on the suspended WS_2 flake, and the inset shows a photograph of a SiN_x/Si chip (11 mm by 11 mm). (**C**) Aberration-corrected high-angle annular dark-field (AC-HAADF) image of irradiated monolayer WS_2 flake at a dose of ~5.1 × 10^{13} ions/cm^2. Bright spots indicate W atoms. (**D**) Histogram of apertures produced with the irradiated dose used in (C). Light shading of blue, green, and orange indicate the size ranges of 1W, 2W, and 3W atomic apertures in the graph, respectively. Inset: A high-magnification AC-HAADF STEM image of one such aperture.

The relatively large number of atomic apertures (up to ~2000) in our samples enables gas flows detectable by conventional mass spectrometers, such as helium leak detector. Our membranes are mechanically robust and sustain pressure differences of up to ~1 bar.

For gas flow measurements, the experimental setup consists of mounting the silicon chips with O-rings to separate two vacuum chambers, one held at variable pressure *P* and the other in high vacuum connected to a mass spectrometer as depicted in the inset of Fig. 2A (also see fig. S5). The samples are well-sealed such that atomic apertures in the WS_2 membrane act as the only connecting paths between the two chambers where gas molecules can flow. As control samples, three replicas were done for each of the pristine silicon nitride membranes with and without holes and nonirradiated WS_2 membrane suspended over the silicon nitride hole. The control samples used to establish baseline flow are a different set of membranes than those used for gas transport; however, they all come from the same fabrication procedures and chemical vapor deposition (CVD) growth. A bare hole without WS_2 layer exhibits large gas flow, as expected, and has been used as a standard leak for validation of the experimental setup (Fig. 2).

A freestanding pristine WS_2 monolayer covering nine holes each with diameters of ~250 nm, without any irradiated defects, exhibited negligible helium flow below our detection limit (~10^{-18} mol s^{-1} $mbar^{-1}$). It is remarkable that the WS_2 monolayer grown by CVD methods (see fig. S2) has such low intrinsic defect density that it is practically impermeable over a suspended area of a few square micrometres. Let us recall the ultralow permeability, ranging from 10^{-23} mol s^{-1} $mbar^{-1}$ to only few gas molecules per hour (*31*, *32*), of intrinsic defects in 2D materials with high crystal quality such as mechanically exfoliated graphene, studied extensively with specialized device

architectures and atomic force microscopy measurements done over several days. Apart from the high crystal quality of our WS_2 monolayer, the impermeability emphasizes the excellent sealing of the WS_2 layer on the SiN_x membrane in our devices, which is achieved by repeated annealing of the samples in H_2/Ar atmosphere at 350°C, both right after the WS_2 monolayer transfer and also before the gas flow measurements (see section S3).

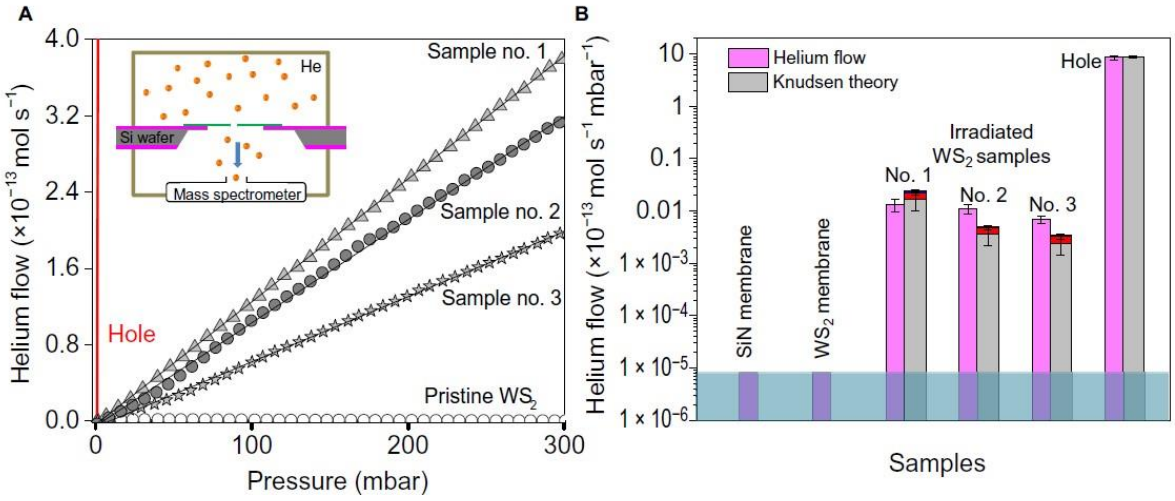

Fig. 2. Gas flow through atomic apertures. (**A**) Helium gas permeation measured through atomic apertures in WS_2 made with the same irradiation dose (5.1×10^{13} ions/cm^2) but with different WS_2 areas leading to difference in the number of defects in a given sample. The proportion of the 1W, 2W, and 3W vacancies in each sample is 69:22:9%, sample no. 1, $N \sim 2070 \pm 830$; sample no. 2, $N \sim 440 \pm 170$; sample no. 3, $N \sim 300 \pm 120$. Pristine WS2 membranes without any irradiation and large bare hole not covered with WS_2 (shown in red color) are shown alongside as controls. Solid lines running through symbols indicate best fit to the data. Inset shows a schematic of our experimental setup. (**B**) Comparison of normalized permeance per unit pressure of irradiated samples and controls, with the Knudsen estimates. The colors within the gray bars representing Knudsen estimates arise from the flow contributions due to 2W (red) and 3W (dark blue) vacancies. Horizontal light blue color bar indicates the detection limit. Error bars on the helium flow of samples are from the SD of flow values recorded over a series of helium flow measurements (measured three times) on the same sample repeated after annealing three times. For the Knudsen theory estimates, the error bars arise from the error values associated with the number of defects and with the total area of the apertures A in each sample.

Next, we did helium (He) gas flow measurements on FIB-irradiated samples containing atomic vacancy defects in suspended WS_2 membranes. Three typical irradiated samples along with controls are shown in Fig. 2A, in which sample no. 1 has WS_2 suspended on nine holes each with a diameter of ~200 nm. From our fabrication method, mainly three types of defects are possible such as 1W (~69%), 2W (~22%),

and 3W (~9%) defects, respectively. Here, the pore configuration is focused on W atoms since experimentally, the AC-STEM contrast from S atoms is weak, and hence, their locations are not identified with certainty. Unlike the geometric area given in Fig. 1D, to get the effective area (accessible pore area for He atom), the van der Waals (vdW) diameter of each atom on the aperture edge is subtracted (see section S2) (*14*). The total estimated tungsten defects is given as $N = N1 + N2 + N3$, where $N1$, $N2$, and $N3$ are estimated numbers of 1W, 2W, and 3W vacancies, respectively, from AC-STEM image analysis. In our samples, $N \sim 2070 \pm 830$ for sample no. 1; the sample no. 2 was WS_2 on a single hole with a diameter of 250 nm to yield total defects $N \sim 440 \pm 170$; the sample no. 3 was WS_2 on a 200-nm-diameter hole to give estimated defects, $N \sim 300 \pm 120$. He flow through atomic apertures increases linearly with increasing pressure and also with increasing number of defects in a sample (Fig. 2A). The gas flux is not exactly linearly correlated with the increase in N. The additional sources of error include the variation in the substrate hole area leading to an overall WS_2 suspended membrane area variation and errors in the ion irradiation dose, in total amounting to about ~40% error. At the experimental working pressure P ranges from few to 200 mbar, the mean free path of helium is >0.5 μm, and the Knudsen number for these atomic apertures in our WS_2 monolayer is $>10^3$. Here, the defects are not circular and have a well-defined atomic structure (see inset in Figs. 1D and 3), meaning that a diameter (typically used for larger circular pores) is not an optimal measure of size. We quote their geometric area, i.e., mean area $\langle A \rangle$, and the characteristic sizes in table S1. As an example, the 1W (+6S) defect has a pore with characteristic size, ~3.15 Å, and an area of 0.08 nm^2, whereas the 3W (+6S) defect has a pore size of ~5.25 Å and an area of 0.216 nm^2. To represent the size of the He, we use the kinetic diameter (~2.6 Å), which is a semiclassical notion; however, for monoatomic spherical molecules like He, this is quite close to the quantum-mechanical size of the electron cloud around the nuclei (*33*). As the aperture size is much smaller than the mean free path, the mass flow of the gas Q (moles per second) through the aperture is simply the impingement rate upon the area of the pore (see section S6), as described by Knudsen (*22*, *34*).

$$Q = PA\left(\frac{1}{2\pi M\, RT}\right)^{1/2} \quad (1)$$

where P is the inlet pressure, A is the total area of the conducting apertures, M is the atomic mass of the gas being transported (M = 4 g mol^{-1} for helium), R = 8.314 J mol^{-1} K^{-1} is the gas constant, and T is the temperature (T = 295 K in our experimental setup). In our case, A is the sum of all individual atomic aperture areas in the WS_2 membrane, which is, on average, $N1 \times A1 + N2 \times A2 + N3 \times A3$ (in our samples, N can be varied from 300 to 2000 for an individual sample by increasing the membrane area; $A1$, $A2$, and $A3$ are the accessible aperture areas for 1W, 2W, and 3W vacancies, i.e., ~0.08, ~0.13, and ~0.23 nm^2, respectively, given in table S1. In the case of control devices, i.e., large bare holes, A is the sum of individual hole areas (with diameters in the range of ~200 to ~300 nm). Taking into consideration the proportion of the various defects observed in ACSTEM images, we calculated the Knudsen estimates from all the vacancies such that 3W vacancies contribute to ~9% of the flux, whereas ~91% of the flux is contributed by 1W (+6S) and 2W vacancies together (Fig. 2B). If the pores are much narrower than the size of the molecule, then there can be a finite energy barrier, which is expressed as an exponential term in the Eq. 1, $\exp(-E/RT)$, where E is the energy barrier that substantially reduces the transmission coefficient of the gas even for small E (*14*, *22*).

The 2D membranes with atomic apertures show measurable helium flux ~10^{-16} to 10^{-15} mol s^{-1} mbar^{-1}, over two to three orders higher than the detection limit and significantly lower than the leakage rate for submicrometer holes (Fig. 2B). This corresponds to a flow of about ~10^7 to 10^8 He molecules per second per millibar pressure difference across the membrane. Theoretical simulations with such small pores in graphene have estimated a pass through frequency of 10^4 He molecules per second per defect (close to our flow values per millibar for a sample with ~2000 defects; Fig. 2), which can be likely ascribed to a low diffusion barrier for He resulting from its noninteracting nature (*14*, *20*). As a check for the reproducibility of devices with atomic apertures, we would like to point out that in a given batch of irradiated samples, about 40 to 50% samples show the measurable flow commensurate with the number of defects estimated by the irradiation dose (*29*). Other devices either did not conduct gas or showed much higher gas flow. From the He flow, we back-calculated the number of defects contributing to the flow using Eq. 1, and N matches close to the defect numbers from AC-STEM image analysis for the sample nos. 1 to 3. For high leaking samples, substituting experimental Q in Eq. 1 gave large contributing defect

area *A*, which does not correlate with the defect density statistics attained from AC-STEM, hinting that these samples might have tears or cracks in the membrane. Examination of these samples by scanning electron microscopy (SEM) on large areas indeed indicates that they are damaged samples (see tears in suspended WS_2; fig. S6).

The measured He flow values are within an order of magnitude of the values predicted by the Knudsen estimates, despite the uncertainties in our defect densities and the distribution of the type of defects. Equation 1 is based on the kinetic theory and has been applied to describe the flows through apertures using effusion mechanism in both theoretical (*4*) and experimental literature (*5*, *6*).

To more precisely validate the agreement to Eq. 1 and/or evaluate its limitations in our experiments, we would need to further decrease our experimental sources of error, including the calibration of all defect areas, which is a challenging experimental task. To verify whether there is any energy barrier, we measured gas flows by varying the temperature between ~25° to ~100°C, by using a heating tape wound around the chamber, interfaced with a temperature controller. We did not see noticeable variation in the gas flow with temperature, hinting an absence of an energy barrier (an exponential dependence is expected if an energy barrier is present). As per Eq. 1, a $T^{-1/2}$ dependence would lead to variation of flux by <10% within the temperature range tested, and this is beyond our experimental measurement error.

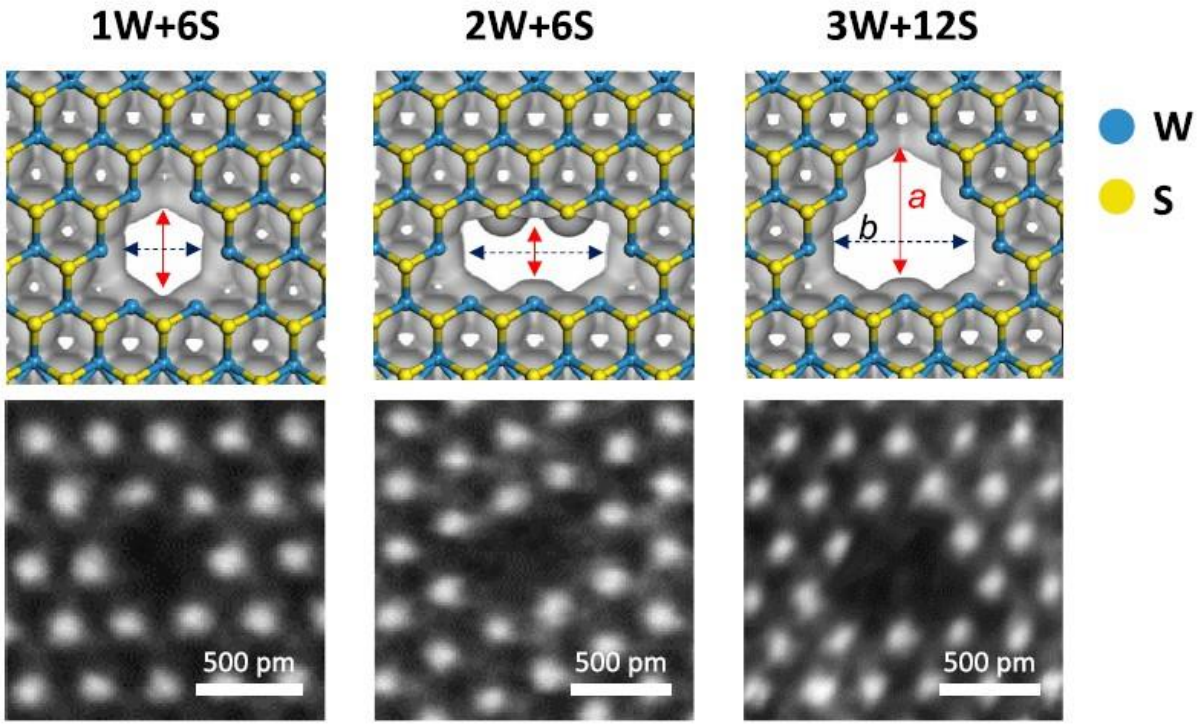

Fig. 3. Atomic apertures and electron density isosurfaces. Typical aperture sizes with the irradiation dose (~5.1 × 10^{13} ions/cm^2) are shown. The top panel shows the density functional theory (DFT) results for electron density isosurfaces of atomic apertures in a WS_2 membrane (isovalue of 0.2 *e*/Å^3). The S and W atoms are shown in yellow and blue, respectively. The blue and red arrows inside the images are the accessible dimensions in width *a* and length *b* across the pores (1W+6S, $a \approx b$ ~ 3.2 Å; 2W+6S, a ~ 2.1 Å, b ~ 6.2 Å; 3W+12S, a ~ 5.8 Å, b ~ 6.2 Å). The accessible aperture areas for helium molecules are ~0.08, ~ 0.13, ~ 0.23 nm^2, respectively. The bottom row includes the AC-STEM images of the defect, while the top row illustrates the observed atomic configuration.

From the electron density isosurface (EDI) of defects shown in Fig. 3 (and fig. S4) using first-principles density functional theory (DFT) calculations, accessible pore areas are obtained (table S1). The accessible pore areas from EDI closely match with those estimated using vdW radii (section S2). The surface transport contributions can be negligible as He does not adsorb sufficiently on the WS_2 basal plane, similar to that observed on graphene (typical adsorption layer thickness, ~4 to 6 Å) (*35*). Ideal atomic apertures with only 1W missing and with no missing sulfurs on the pore edge would likely, theoretically, be nonconducting. From the electron density isosurface (EDI) of defects shown in Fig. 3 (and fig. S4) using first-principles density functional theory (DFT) calculations, accessible pore areas are obtained (table S1).

The accessible pore areas from EDI closely match with those estimated using vdW radii (section S2). The surface transport contributions can be negligible as He does not adsorb sufficiently on the WS_2 basal plane, similar to that observed on graphene (typical adsorption layer thickness, ~4 to 6 Å) (*35*). Ideal atomic apertures with only 1W missing and with no missing sulfurs on the pore edge would likely, theoretically, be nonconducting.

On the other hand, 1W defects with six sulfur vacancies with an accessible pore diameter of ~3.2 Å, which is larger than the kinetic diameter of helium (2.6 Å), would be amenable to gas flows. As shown in Fig. 1D, the minimum area of the defects obtained from AC-STEM imaging was about 0.06 to 0.1 nm^2, which corresponds to the defects with 1W and 6S missing (~0.08 nm^2), whereas the 1W defects with no sulfurs missing would be of significantly lower area (~0.002 nm^2). As the characteristic pore size decreases, the electron overlap between He and membrane significantly increases, thereby increasing the energy barriers for the flow. However, the theoretical calculation of energy barriers might not necessarily capture all the favourable electronic interactions in real systems as there can be rearrangements in the vacancies. These discrepancies between the computed energy barriers and the experimental flows have been noted before by Wang *et al* (*8*). Specifically, our results do not imply a significant energy barrier compared to theoretical predictions (*4*, *8*, *14*, *22*), and we also note that different levels of DFT calculations (and supercell size, or equivalently, the ratio between the pore area and the simulated defect area in membrane) can give different energy barriers; thus, a separate systematic DFT study is required for carefully probing the energy barriers.

We stored our samples with atomic vacancy defects under ambient conditions. When we tested the samples after a few weeks, it was observed that they tend to get clogged with time, leading to reduced/ no He flow. As is well known, all surfaces are likely to be covered by hydrocarbons, which might cause the clogging (*15*) of atomic apertures in our case. However, upon reannealing at 350°C, He flow was regained to the previously observed value within a factor of 2. Storage of samples in activated charcoal helped extend the life span of the atomic apertures to be open for few months. Annealing with a combination of storage in charcoal has enabled us to keep the atomic apertures open for about a year. The atomic vacancy defects, once created, are quite stable and show similar helium flow with repeated annealing, indicating that the atomic

apertures do not expand or propagate rapidly. Those samples that have been irradiated but did not conduct gas remained nonconductive even after repetitive annealing. We speculate that these samples could have contained a majority of the dominant 1W defect type with one “W” atom missing but with partial or all S atoms at that site, thereby increasing the energy barrier and leading to no He flux. While the ion irradiation dose is optimized for single-atom (W) defect pores, the removal of sulfur atoms from ion irradiation and the subsequent AC-STEM imaging to precisely know the composition of sulfur vacancies at a defect site have remained a challenge. However, in the extreme limit, when there were large holes, tears, or cracks in the membrane, the flow was much higher, and the membranes themselves were not stable. In addition, we performed ion flow measurements in KCl solution on our atomic apertures as a cross-check.

Those samples that showed inconsistent and unexpectedly high gas flows showed high ionic conductance (~400 nS in 1 M KCl; see fig. S7), again indicating the presence of tears (visible in SEM; see fig. S6). The samples that showed gas flows commensurate with the Knudsen equation exhibited only a small ionic conductance, <1 nS in 0.1 M KCl for total membrane area ~0.4 to 0.6 mm^2, as shown in fig. S7. This is expected as the atomic apertures with sizes <6 Å exclude ions (*27*), but the presence of tears in the membranes leads to bulk ionic flow (see fig. S6).

These observations further emphasize that the sealing of WS_2 monolayers to the SiN_x membranes is leak proof, leaving no gaps, and hence, only irradiated defects contribute to the observed gas flow.

DISCUSSION

Let us analyze the gas flow in nano- and angstrom-scale pores from the literature, in comparison to our atomic vacancy defects presented here. It has been shown in the literature that when the pores are less than the size of the gas molecule passing through (*8*), activated transport is observed and highly sensitive energy barriers play a major role in the transport, and the barrier is usually estimated using combined theoretical and experimental efforts. In this work, since the atomic vacancy apertures are only slightly larger than the gas molecule (i.e., less than twice the size of helium molecule, 2.6 Å), the flow is governed by simple effusion (*14*). In general, effusive flow is seen as detrimental and the cause of reduction for selectivity between gases in size

exclusion. Because of this, an accurate comparison of the observed permeability and value estimated from the Knudsen description for the known size of the aperture is often overlooked. Such a comparison made for nanometer-sized holes showed the validity of the Knudsen description in graphene pores down to ~7 nm in size, where a N_2 permeance of ~0.05 mol m^{-2} s^{-1} Pa^{-1} was observed (*6*). Angstrom-size defects (size, ~0.38 to ~0.43 nm) made by ozone-induced etching in a CVD-grown graphene layer were shown to have a H_2 permeance of about 10^{-7} mol m^{-2} s^{-1} Pa^{-1} (*9*), which is only one order higher than the permeability of graphene membrane, 10^{-8} mol m^{-2} s^{-1} Pa^{-1} hosting the defects (*36*). However, the observed gas flow values for atomic defects are still much lower than that estimated from the Knudsen description for given defect densities, which might be due to the overestimation of the conducting apertures. In our WS_2 atomic aperture samples, the He gas flow obtained matches the Knudsen estimates within a factor of 2 to 3, and the gas flow normalized by the total area of defects translates to ~0.05 to 0.1 mol m^{-2} s^{-1} Pa^{-1}. From theoretical studies on graphene pores with sizes 3.6 to 4.8 Å, for defect densities up to ~10^{14} cm^{-2}, large permeance of ~0.1 mol m^{-2} s^{-1} Pa^{-1} has been predicted (*14*, *20*), which closely matches with our experimental values.

These permeance values are higher than those typically observed in silica (*37*), zeolite, and metal-organic framework membranes, graphene oxide membranes (*18*), which are in the range of ~10^{-6} to 10^{-7} mol m^{-2} s^{-1} Pa^{-1}. Large permeance values are obtained through our WS_2 apertures, even when normalized with the area of the membrane, i.e., ~10^{-4} to 10^{-5} mol m^{-2} s^{-1} Pa^{-1}, which indicates that most of the atomic apertures are in the predicted size range and hence conductive to gases.

In conclusion, we demonstrate the fast He transport through quasi-0D atomic-scale apertures (~W sites). To our knowledge, this is the first experimental observation on He gas transport in such angstrom-scale pores in WS_2/TMD monolayers where we attempt to evaluate the applicability of the Knudsen equation down to the ultimate limit. Our results indicate the necessity of future theoretical models to explore the role of sensitive variation of the energy barriers of various gas molecules and their critical dependence on the size of the aperture at this atomic limit, especially taking the electron density isosurfaces of atoms to account for the enhanced flux. In addition, this work provides a new method for corroborating atomic pore formation and their density over large areas via a simple bulk measurement technique of measuring gas flow

through them. This is analogous to using nanoholes (few hundred nanometers in size) as standard leak elements for calibration (*38*). So far, the only way to inspect and confirm the atomic pore formation in the case of atomic vacancy defects is by AC-STEM, which is limited to relatively small areas. Conventional ionic transport measurements through nanopores are mediated by Hille's equation (*27*), which yields a linear relationship between conductance and total aperture area. However, for pores that are smaller in dimensions than many common salts, ionic conductance measurements do not yield a predictable or a measurable signal, leading to the breakdown of Hille's model for atomic aperture limit (*28*). With our study, we would like to highlight that once the pore creation is confirmed and calibrated by AC-STEM locally, gas flow measurements can act as a standard to test for the presence of these pores and their density over large areas. Let us also note that the stability of pore/aperture configuration of these atomic scale defects needs further investigation (*27*, *39*) as the pores could change over time, which can be attempted in future experiments by imaging the pores over time. More advanced methods including dynamic scanning tunneling microscopy need to be devised to locate S atoms (*40*) and also any other atoms such as possible contaminants (C, O, and N) to be certain of pore compositions and sizes. Future work may involve efficient gas separation investigations using a scaled-up version of such membranes.

MATERIALS AND METHODS

Sample fabrication

CVD growth of monolayer WS_2 flakes

Monolayer WS_2 flakes were grown using CVD processes similar to previously reported methods (*27*, *29*). Solutions of 2% sodium cholate growth promoter and 15×10^{-3} M ammonium heptamolybdate (metatungstate) were spun onto piranha-cleaned silicon (Si) substrates coated with 150 nm of SiO_2, which were then loaded into the center of a tube furnace (Thermo Fisher Scientific Lindberg/Blue M). For WS_2, samples were heated in argon atmosphere [100 standard cubic centimeters per minute (sccm)] at a rate of 65 °C min^{-1} and held at 800 °C for 10 min, during which time 15 sccm of H_2 was also added. Approximately 100 mg of sulfur precursor placed 22 cm from the

substrates was kept at 180 °C during the growth procedures. Both samples were rapidly cooled to room temperature by cracking open the furnace.

Position-controlled transfer of WS_2 flakes

With WS_2 flakes grown on Si/SiO2 wafer pieces, we cut smaller pieces with areas about 3 × 3 mm^2 that contain good WS_2 flakes. Using a wet transfer technique, the TMD flake side of the SiO_2 pieces is coated with poly(methyl methacrylate) (PMMA) (MicroChem C4, 4000 rpm for 60 s). The PMMA-coated substrates are left to dry at ambient temperature for a few minutes before being floated onto the KOH etchant (8 g per 100 ml of water). Depending on the thickness of the SiO_2 wafer, the time for etching away the SiO_2 layer varies.

Last, we observe the PMMA + TMD flake floating on the KOH etchant. These PMMA + TMD flakes are then rinsed three times in clean water baths before being used to transfer them onto a SiN_x/Si chip with a hole (diameter range, 200 to 300 nm) drilled by FIB. Position transfer is practiced when the flake size and their number density are high, so that in this case, it is possible to place one PMMA + TMD flake onto the SiN_x FIB hole. This step of placing the PMMA + TMD flake over the SiN_x FIB hole is somewhat challenging since the coverage of the FIB hole depends on the number of the as-grown flakes. However, because in a given batch of CVD growth, the number of grown flakes is large, the transfer is completed within several transfer trials. In addition to this manual transfer, we have also used custom-built manipulators, with needles and tweezers to move the flake on the substrate to increase device yield. These manipulations came at a cost, since there was now a higher risk of device failure caused by the usage of additional tools, which can sometimes break the membrane. In this work, all devices were fabricated by manually “fishing” (moving) the PMMA + TMD flake onto the SiN_x FIB hole. After we transfer the flake and optically verify the coverage, the sample is then dried in ambient temperature for 30 min. Furthermore, the sample is placed into hot acetone (90°C) to remove the supporting PMMA.

Gallium ion irradiation

Monolayer TMD flakes were irradiated with a Ga^+-sourced ion beam FEI Strata Dual-Beam instrument. The acceleration voltage of the ion beam was set to 30 kV and incident normal to the surface. The beam spot size was observed to be 100 nm for a flash second at 10-pA current. To produce atomic defects, an area of 250 nm by 250

nm was irradiated with the dwell time (16 μs) and current (10 pA). Pixel resolution (1024 × 884) was kept constant. The exposure was carried out in an imaging mode, which followed a raster pattern where the beam sequentially exposed each pixel in a row. The instrument, FEI FIB Strata DB 235, has an option to “grab frame,” which takes a single scan at a set resolution; this option was used for all the scans. The dose was varied by changing the number of scans. Suspended and substrate-supported samples were exposed to FIB irradiation while sitting on holey carbon TEM grids and Si/SiO_2 substrates, respectively.

AC-STEM imaging

AC-STEM images of WS_2 samples were acquired using a C_s-corrected JEOL ARM 200CF STEM operating at 80 kV. Images were obtained using a high-angle annular dark-field (HAADF) detector with a collection angle of 54 to 220 mrad and 10-cm camera length. Probe current (22 pA), focusing time (<2 s), and electron dose (≈6.0×10^6 e^- nm^{-2}) were kept low to minimize beam-induced knock-on damage.

First-principles calculations

The DFT was performed with the generalized gradient approximations (*41*) form with exchange-correlation potential parametrization of Perdew-Burke-Ernzerhof (*42*). The calculations were carried out by the Quantum ESPRESSO package (*43*) and have been performed on the basis of the plane-wave basis sets and ultrasoft nonlocal pseudopotentials (*44*). To take the vdW contributions into account in the total energy, the Tkatchenko-Scheffler (*45*) method was used. The cutoff of kinetic energy in the plane-wave expansion and the convergence threshold for the self-consistent field calculations were chosen as 280.0 and 10^{-6} eV per atom, respectively.

The WS_2 membrane was relaxed both in plane and out of plane. Calculations were done at 0 K for a rectangular supercell shape with size 15.953 × 16.579 $Å^2$ for all considered defects consisting of 29(60), 29(54), 28(58), 28(54), 27(54), and 27(48) atoms of W (S) for 1W, 1W (+6S), 2W (+2S), 2W (+6S), 3W (+6S), and 3W (+12S) with a vacuum layer of 30 Å between periodic images in the vertical direction. We calculated the EDI using the above aforementioned functionals and energy cutoff. For the EDI images (Fig. 3 and fig. S4), the isovalue was set to be 0.2 $e/Å^3$.

REFERENCES

1. H. B. Park, J. Kamcev, L. M. Robeson, M. Elimelech, B. D. Freeman, Maximizing the right stuff: The trade-off between membrane permeability and selectivity. *Science* **356**, eaab0530 (2017).

2. M. Knudsen, Die Gesetze der Molekularstromung und der inneren Reibungsstromung der Gase durch Rohren. *Ann. Phys.* **333**, 75–130 (1909).

3. M. V. Smoluchowski, Zur kinetischen Theorie der Transpiration und Diffusion verdunnter Gase. *Ann. Phys.* **338**, 1559–1570 (1910).

4. C. Sun, M. S. H. Boutilier, H. Au, P. Poesio, B. Bai, R. Karnik, N. G. Hadjiconstantinou, Mechanisms of molecular permeation through nanoporous graphene membranes. *Langmuir* **30**, 675–682 (2014).

5. S. P. Koenig, L. Wang, J. Pellegrino, J. S. Bunch, Selective molecular sieving through porous graphene. *Nat. Nanotechnol.* **7**, 728–732 (2012).

6. K. Celebi, J. Buchheim, R. M. Wyss, A. Droudian, P. Gasser, I. Shorubalko, J.-I. Kye, C. Lee, H. G. Park, Ultimate permeation across atomically thin porous graphene. *Science* **344**, 289–292 (2014).

7. Y. Yamada, K. Murota, R. Fujita, J. Kim, A. Watanabe, M. Nakamura, S. Sato, K. Hata, P. Ercius, J. Ciston, C. Y. Song, K. Kim, W. Regan, W. Gannett, A. Zettl, Subnanometer vacancy defects introduced on graphene by oxygen gas. *J. Amer. Chem. Soc.* **136**, 2232–2235 (2014).

8. L. Wang, L. W. Drahushuk, L. Cantley, S. P. Koenig, X. Liu, J. Pellegrino, M. S. Strano, J. Scott Bunch, Molecular valves for controlling gas phase transport made from discrete angstrom-sized pores in graphene. *Nat. Nanotechnol.* **10**, 785–790 (2015).

9. J. Zhao, G. He, S. Huang, L. F. Villalobos, M. Dakhchoune, H. Bassas, K. V. Agrawal, Etching gas-sieving nanopores in single-layer graphene with an angstrom precision for high-performance gas mixture separation. *Sci. Adv.* **5**, eaav1851 (2019).

10. B. J. Hinds, N. Chopra, T. Rantell, R. Andrews, V. Gavalas, L. G. Bachas, Aligned multiwalled carbon nanotube membranes. *Science* **303**, 62–65 (2004).

11. J. K. Holt, H. G. Park, Y. Wang, M. Stadermann, A. B. Artyukhin, C. P. Grigoropoulos, A. Noy, O. Bakajin, Fast mass transport through sub-2-nanometer carbon nanotubes. *Science* **312**, 1034–1037 (2006).

12. L. Ge, A. Du, M. Hou, V. Rudolph, Z. Zhu, Enhanced hydrogen separation by vertically-aligned carbon nanotube membranes with zeolite imidazolate frameworks

as a selective layer. *RSC Adv.* **2**, 11793–11800 (2012).
13. R. W. Baker, *Membrane Technology and Applications* (John Wiley & Sons, Ltd., ed. 2, 2004).
14. L. Wang, M. S. H. Boutilier, P. R. Kidambi, D. Jang, N. G. Hadjiconstantinou, R. Karnik, Fundamental transport mechanisms, fabrication and potential applications of nanoporous atomically thin membranes. *Nat. Nanotechnol.* **12**, 509–522 (2017).
15. A. Keerthi, A. K. Geim, A. Janardanan, A. P. Rooney, A. Esfandiar, S. Hu, S. A. Dar, I. V. Grigorieva, S. J. Haigh, F. C. Wang, B. Radha, Ballistic molecular transport through two-dimensional channels. *Nature* **558**, 420–424 (2018).
16. G. Scorrano, G. Bruno, N. di Trani, M. Ferrari, A. Pimpinelli, A. Grattoni, Gas flow at the ultra-nanoscale: Universal predictive model and validation in nanochannels of angstrom-level resolution. *ACS Appl. Mater. Interfaces* **10**, 32233–32238 (2018).
17. H. W. Kim, H. W. Yoon, S.-M. Yoon, B. M. Yoo, B. K. Ahn, Y. H. Cho, H. J. Shin, H. Yang, U. Paik, S. Kwon, J.-Y. Choi, H. B. Park, Selective gas transport through few-layered graphene and graphene oxide membranes. *Science* **342**, 91–95 (2013).
18. H. Li, Z. Song, X. Zhang, Y. Huang, S. Li, Y. Mao, H. J. Ploehn, Y. Bao, M. Yu, Ultrathin, molecular-sieving graphene oxide membranes for selective hydrogen separation. *Science* **342**, 95–98 (2013).
19. M. H. Khan, M. Moradi, M. Dakhchoune, M. Rezaei, S. Huang, J. Zhao, K. V. Agrawal, Hydrogen sieving from intrinsic defects of benzene-derived single-layer graphene. *Carbon* **153**, 458–466 (2019).
20. S. Blankenburg, M. Bieri, R. Fasel, K. Mullen, C. A. Pignedoli, D. Passerone, Porous graphene as an atmospheric nanofilter. *Small* **6**, 2266–2271 (2010).
21. D.-e. Jiang, V. R. Cooper, S. Dai, Porous graphene as the ultimate membrane for gas separation. *Nano Lett.* **9**, 4019–4024 (2009).
22. L. W. Drahushuk, M. S. Strano, Mechanisms of gas permeation through single layer graphene membranes. *Langmuir* **28**, 16671–16678 (2012).
23. S. C. O'Hern, M. S. H. Boutilier, J.-C. Idrobo, Y. Song, J. Kong, T. Laoui, M. Atieh, R. Karnik, Selective ionic transport through tunable subnanometer pores in single-layer graphene membranes. *Nano Lett.* **14**, 1234–1241 (2014).
24. J. Jadwiszczak, C. O'Callaghan, Y. Zhou, D. S. Fox, E. Weitz, D. Keane, C. P. Cullen, I. O'Reilly, C. Downing, A. Shmeliov, P. Maguire, J. J. Gough, C. McGuinness, M. S. Ferreira, A. L. Bradley, J. J. Boland, G. S. Duesberg, V. Nicolosi, H. Zhang,

Oxide-mediated recovery of field-effect mobility in plasma-treated MoS_2. *Sci. Adv.* **4**, eaao5031 (2018).
25. J.-A. Ke, S. Garaj, S. Gradečak, Nanopores in 2D MoS2: Defect-mediated formation and density modulation. *ACS Appl. Mater. Interfaces* **11**, 26228–26234 (2019).
26. Z. Bai, L. Zhang, H. Li, L. Liu, Nanopore creation in graphene by ion beam irradiation: Geometry, quality, and efficiency. *ACS Appl. Mater. Interfaces* **8**, 24803–24809 (2016).
27. J. P. Thiruraman, K. Fujisawa, G. Danda, P. M. Das, T. Zhang, A. Bolotsky, N. Perea-Lopez, A. Nicolai, P. Senet, M. Terrones, M. Drndić, Angstrom-size defect creation and ionic transport through pores in single-layer MoS2. *Nano Lett.* **18**, 1651–1659 (2018).
28. P. Masih Das, J. P. Thiruraman, Y.-C. Chou, G. Danda, M. Drndić, Centimeter-scale nanoporous 2D membranes and ion transport: Porous MoS2 monolayers in a few-layer matrix. *Nano Lett.* **19**, 392–399 (2019).
29. J. P. Thiruraman, P. Masih Das, M. Drndić, Irradiation of transition metal dichalcogenides using a focused ion beam: Controlled single-atom defect creation. *Adv. Func. Mater.* **29**, 1904668 (2019).
30. K. Liu, Q. Yan, M. Chen, W. Fan, Y. Sun, J. Suh, D. Fu, S. Lee, J. Zhou, S. Tongay, J. Ji, J. B. Neaton, J. Wu, Elastic properties of chemical-vapor-deposited monolayer MoS_2, WS_2, and their bilayer heterostructures. *Nano Lett.* **14**, 5097–5103 (2014).
31. J. S. Bunch, S. S. Verbridge, J. S. Alden, A. M. van der Zande, J. M. Parpia, H. G. Craighead, P. L. McEuen, Impermeable atomic membranes from graphene sheets. *Nano Lett.* **8**, 2458–2462 (2008).
32. P. Z. Sun, Q. Yang, W. J. Kuang, Y. V. Stebunov, W. Q. Xiong, J. Yu, R. R. Nair, M. I. Katsnelson, S. J. Yuan, I. V. Grigorieva, M. Lozada-Hidalgo, F. C. Wang, A. K. Geim, Limits on gas impermeability of graphene. *Nature* **579**, 229–232 (2020).
33. N. Mehio, S. Dai, D.-e. Jiang, Quantum mechanical basis for kinetic diameters of small gaseous molecules. *J. Phys. Chem. A* **118**, 1150–1154 (2014).
34. M. Knudsen, Die Molekularstromung der Gase durch Offnungen und die Effusion. *Ann. Phys.* **333**, 999–1016 (1909).

35. Y. Tao, Q. Xue, Z. Liu, M. Shan, C. Ling, T. Wu, X. Li, Tunable hydrogen separation in porous graphene membrane: First-principle and molecular dynamic simulation. *ACS Appl. Mater. Interfaces* **6**, 8048–8058 (2014).
36. S. Huang, M. Dakhchoune, W. Luo, E. Oveisi, G. He, M. Rezaei, J. Zhao, D. T. L. Alexander, A. Zuttel, M. S. Strano, K. V. Agrawal, Single-layer graphene membranes by crack-free transfer for gas mixture separation. *Nat. Commun.* **9**, 2632 (2018).
37. R. M. de Vos, H. Verweij, High-selectivity, high-flux silica membranes for gas separation. *Science* **279**, 1710–1711 (1998).
38. V. Ierardi, U. Becker, S. Pantazis, G. Firpo, U. Valbusa, K. Jousten, Nano-holes as standard leak elements. *Measurement* **58**, 335–341 (2014).
39. S. Wang, H. Li, H. Sawada, C. S. Allen, A. I. Kirkland, J. C. Grossman, J. H. Warner, Atomic structure and formation mechanism of sub-nanometer pores in 2D monolayer MoS_2. *Nanoscale* **9**, 6417–6426 (2017).
40. Y. Wen, C. Ophus, C. S. Allen, S. Fang, J. Chen, E. Kaxiras, A. I. Kirkland, J. H. Warner, Simultaneous identification of low and high atomic number atoms in monolayer 2D materials using 4D scanning transmission electron microscopy. *Nano Lett.* **19**, 6482–6491 (2019).
41. J. P. Perdew, J. A. Chevary, S. H. Vosko, K. A. Jackson, M. R. Pederson, D. J. Singh, C. Fiolhais, Atoms, molecules, solids, and surfaces: Applications of the generalized gradient approximation for exchange and correlation. *Phys. Rev. B* **46**, 6671–6687 (1992).
42. D. Rao, R. Lu, Z. Meng, Y. Wang, Z. Lu, Y. Liu, X. Chen, E. Kan, C. Xiao, K. Deng, H. Wu, Electronic properties and hydrogen storage application of designed porous nanotubes from a polyphenylene network. *Int. J. Hydrogen Energy* **39**, 18966–18975 (2014).
43. P. Giannozzi, S. Baroni, N. Bonini, M. Calandra, R. Car, C. Cavazzoni, D. Ceresoli, G. L. Chiarotti, M. Cococcioni, I. Dabo, A. Dal Corso, S. de Gironcoli, S. Fabris, G. Fratesi, R. Gebauer, U. Gerstmann, C. Gougoussis, A. Kokalj, M. Lazzeri, L. Martin-Samos, N. Marzari, F. Mauri, R. Mazzarello, S. Paolini, A. Pasquarello, L. Paulatto, C. Sbraccia, S. Scandolo, G. Sclauzero, A. P. Seitsonen, A. Smogunov, P. Umari, R. M. Wentzcovitch, QUANTUM ESPRESSO: A modular and open-source software project for quantum simulations of materials. *J. Phys. Condens. Matter* **21**, 395502 (2009).
44. D. Vanderbilt, Soft self-consistent pseudopotentials in a generalized eigenvalue

formalism. *Phys. Rev. B* **41**, 7892–7895 (1990).
45. A. Tkatchenko, M. Scheffler, Accurate molecular van der Waals interactions from ground-state electron density and free-atom reference data. *Phys. Rev. Lett.* **102**, 073005 (2009).
46. P. K. Chow, R. B. Jacobs-Gedrim, J. Gao, T.-M. Lu, B. Yu, H. Terrones, N. Koratkar, Defect-induced photoluminescence in monolayer semiconducting transition metal dichalcogenides. *ACS Nano* **9**, 1520–1527 (2015).
47. A. Beskok, G. E. Karniadakis, W. Trimmer, Rarefaction and compressibility effects in gas microflows. *J. Fluids Eng.* **118**, 448–456 (1996).
48. T. Wu, D. Zhang, Impact of adsorption on gas transport in nanopores. *Sci. Rep.* **6**, 23629 (2016).
49. K. Wu, Z. Chen, X. Li, Real gas transport through nanopores of varying cross-section type and shape in shale gas reservoirs. *Chem. Eng. J.* **281**, 813–825 (2015).

Acknowledgments: We acknowledge assistance with AC-STEM imaging from R. Keyse of Lehigh University and D. Yates of the University of Pennsylvania. We thank J. Ford and M. Brukman of the University of Pennsylvania for help with FIB irradiation and PL/Raman spectroscopy, respectively. We also appreciate G. Danda for initial support and fabrication effort.

Funding: B.R. acknowledges the funding from EPSRC grant no. EP/R013063/1,

Royal Society fellowship and enhancement award RGF\EA\181000, and the European Union's H2020 Framework Programme/ERC Starting Grant agreement no. 852674–AngstroCAP. A.K. acknowledges the Ramsay Memorial Fellowship, the Royal Society research grant RGS\ R2\202036 and also the University of Manchester's research collaboration fund. S.A.D. was funded by a scholarship from the University of Engineering and Technology, Lahore, Pakistan. M.D. acknowledges support from the NSF through the University of Pennsylvania Materials Research Science and Engineering Center (MRSEC) (DMR- 1720530) and NSF grant EFRI 2-DARE (EFRI-1542707), NSF DMR 1905045 and NSF CCMI Advanced Manufacturing (AM) grant 2002477. This work was performed, in part, at the University of Pennsylvania's Singh Center for Nanotechnology, an NNCI member supported by NSF grant ECCS-1542153. J.P.T. acknowledges fellowship support from the Vagelos Institute of Energy Science and Technology (VIEST). N.H. was supported by the ISEF under postdoc

grant no. 2345. N.H. and M.N.-A. would like to acknowledge high-performance computing support from the Shahid Rajaee Teacher Training University.

Author contributions: B.R., M.D., and A.K. designed and directed the project. J.P.T. and P.M.D. grew TMD materials and fabricated and characterized the devices. Specifically, J.P.T. carried out sample fabrication, FIB irradiation, and TEM image analysis. P.M.D. conducted AC-STEM imaging and Raman/PL measurements/analysis. S.A.D., A.K., and B.R. performed the measurements and their analysis. N.H. and M.N.-A. performed the DFT calculations. B.R., A.K., and M.D. wrote the manuscript with the inputs from J.P.T., P.M.D., and M.N.-A. All authors contributed to discussions. **Competing interests:** The authors declare that they have no competing interests. **Data and materials availability:** All data needed to evaluate the conclusions in the paper are present in the paper and/or the Supplementary Materials. Additional data related to this paper may be requested from the authors.

Supplementary Materials

S1. Characterization of Pristine WS_2

The quality of as-grown monolayer WS_2 flakes was extensively characterized using electron and optical microscopy. Selected area electron diffraction (SAED) of suspended flakes confirmed the monocrystallinity and 2H phase of the pristine material (see Supplementary Figure S2). Atomic-resolution images were used to quantify intrinsic defect densities, which can result from imperfections and dopants during the CVD growth and/or transfer process. Multiple (> 50) AC-HAADF STEM images of monolayer WS_2 flakes transferred onto holey carbon TEM grids were sampled over to obtain an intrinsic transition metal defect density of 0.013%. During imaging, electron knock-on and radiolysis damage was minimized with a low electron acceleration voltage (80 kV) and beam current (20 pA). No discernible defect creation during STEM imaging was observed. Due to their strong optoelectronic absorption and direct visible-range band gap, monolayer TMDs can also be characterized through photoluminescence (PL) spectroscopy. Obtained PL spectra for monolayer flakes indicate spectral weight percentages that are consistent with previously reported values for high quality WS_2 (*46*).

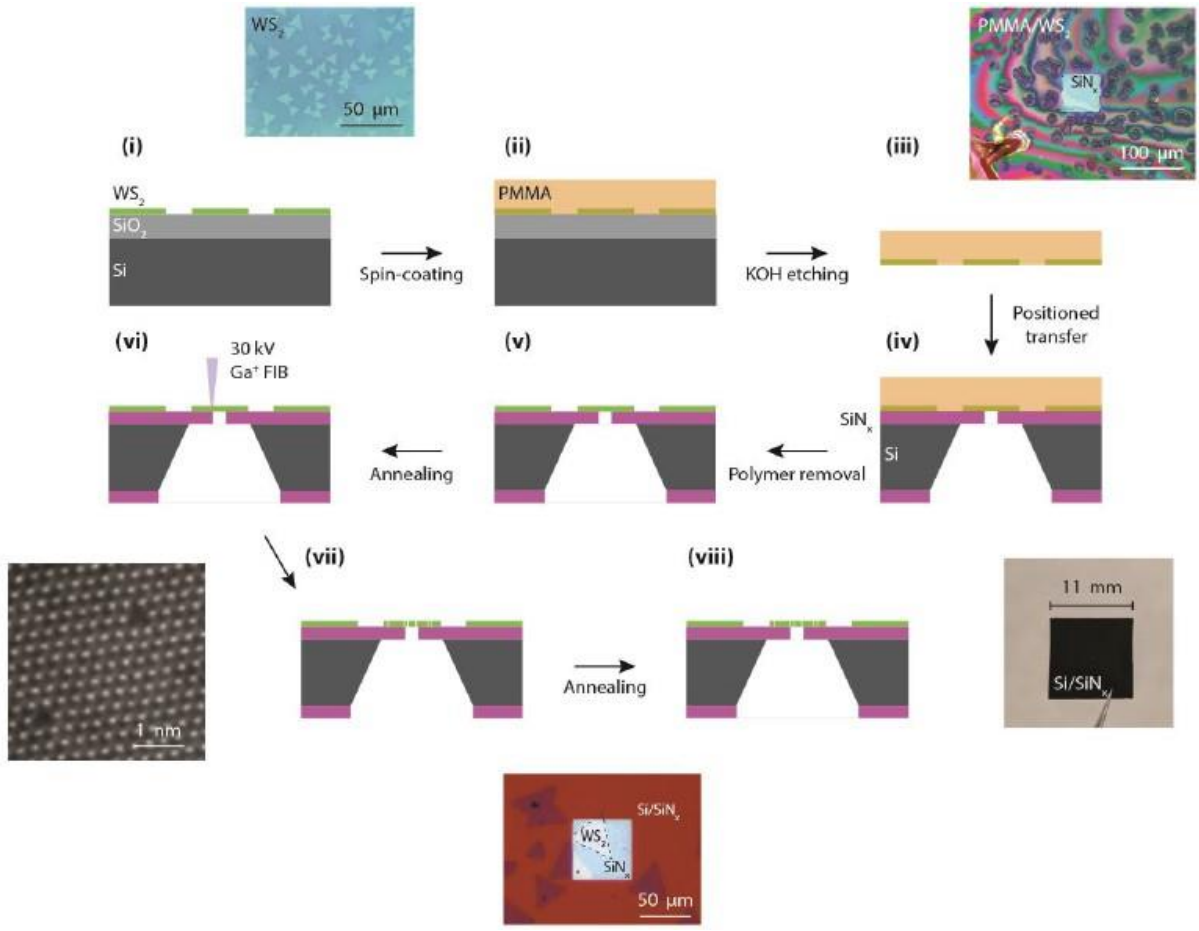

Figure S1. Schematic of fabrication process for WS_2 single atom aperture devices. (i) CVD-grown monolayer WS_2 flakes on Si/SiO_2 substrates are (ii) spin-coated with PMMA and (iii) etched in KOH solution. (iv)The PMMA/WS_2 stack is then positioned on top of a 200-300 nm diameter hole in a Si/SiN_x substrate. (v) The PMMA is subsequently removed in acetone and annealed in Ar/H_2. (vi-vii) Single atom defects in the WS_2 membrane are formed using Ga^+ FIB irradiation (Supplementary Section 1.3). (viii) Samples are annealed again prior to gas transport measurements (Supplementary Section S3). Top insets, left to right - Optical images of CVD-grown WS_2 material and a PMMA/WS_2 stack after positioning onto a sub-micron hole. Bottom insets, left to right - Atomic resolution STEM image of single atom apertures in monolayer WS_2, optical image of final FIB-irradiated WS_2 (outlined in black) on a SiN_x membrane, and optical image of the square, 11-mm-large, Si/SiN_x substrate.

S2. Characterization of Pristine and Irradiated WS_2

Monolayer WS^2 membranes were exposed to energetic 30 keV Ga^+ ions in a focused ion beam (FIB) as outlined in Supplementary Figure S1. The 30 keV energy of impinging Ga^+ ions is above the displacement threshold of W atoms (~ 20-25 eV), resulting in atomic defects. Afterwards, defects in the monolayer WS_2 flakes were characterized again using aberration-corrected STEM (AC-STEM) imaging.

Quantitative statistics for average defect size and density were obtained by averaging over multiple STEM images. For an irradiation dose of 5.07×10^{13} ions/cm^2, an average defect density of 7.9×10^{-2} % (± 2.2×10^{-2} %) and size of 1.2×10^{-1} nm^2 (± 5.5×10^{-2} nm^2) are observed. Since AC-STEM images also contain mass contrast information, the atomic configurations of various defects were analysed. Based on the contouring bright metal atoms in the image, their relative frequencies for each defect site were assessed from several TEM images for the histogram in Figure 1d. However, the accessible pore areas for transport of He atoms is expected to be much lower than pure geometric area (see below, Effective pore size calculations). Additionally, the uncertainty with TEM imaging in finding the S atoms on the defect edge would largely influence the effective area. While no changes in the Raman spectra of irradiated membranes were seen under a 532 nm excitation, photoluminescence spectroscopy revealed an increase in defect induced midgap states (X^D).

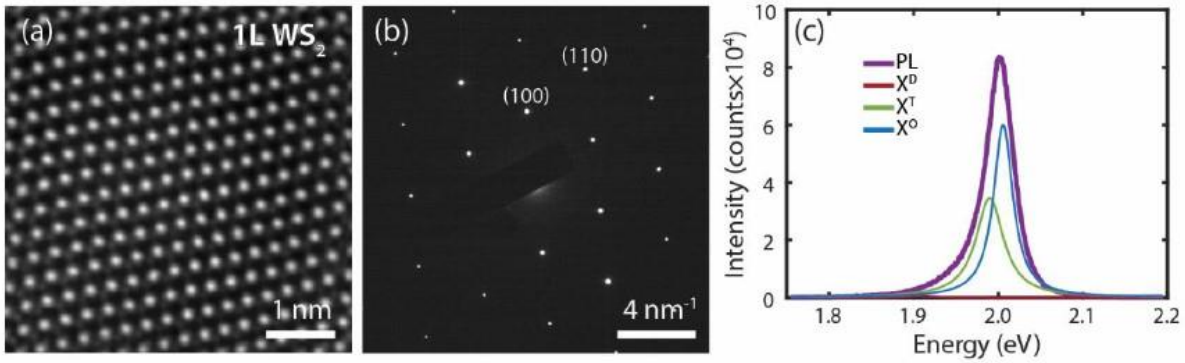

Figure S2. Characterization of CVD-grown pristine WS_2 flakes. (a) Aberration-corrected STEM image of as-grown monolayer WS_2 flakes on a holey carbon TEM grid. W and S_2 atomic sites appear as bright and dim atoms, respectively, in a trigonal prismatic (2H) coordination due to the mass-contrast behavior of high-angle annular dark-field (HAADF) imaging. Multiple atomic-resolution STEM images were sampled over to obtain quantitative defect statistics (see also Supplementary Figure S3). (b) SAED pattern of suspended monolayer WS_2. The presence of a single set of six-fold symmetric (100) and (110) diffraction spots indicates monocrystalline 2H-phase WS_2. (c) PL spectrum of a pristine flake on a 150 nm SiO_2/Si wafer taken at room temperature with a laser excitation wavelength of 532 nm (*i.e.,* green). Spectra were fit to the defect (XD), charged trion (XT), and neutral exciton (XO) peaks at 1.88, 1.96, and 2.02 eV, respectively (*46*). Pristine WS_2 was found to have XD, XT, and XO spectral weight percentages of 0.6%, 44, and 55%, respectively.

Effective pore size calculations:

The accessible effective area of the aperture for a gas molecule (in our case, He gas with kinetic diameter ~ 0.26 nm) is calculated based on the van der Waals radii of the terminal atoms on the WS_2 defect edges. For example, in 1W+6S site, the center-to-center distance between opposite W sites on the pore, $D_{w\text{-}w}$ = 0.63 nm. The van der waals diameter of W atom, d_{vdw} = 0.42 nm. The effective pore size between W atoms excluding the collision cross section is calculated using the formula (*14*)

$$D_{\mathrm{vdw}} = D_{\mathrm{W-W}} - \frac{(d_{\mathrm{vdw}})}{\sqrt{2}},$$

which gives D_{vdw} for (1W+6S) = 0.33 nm. We have also simulated electron density isosurfaces using density functional theory and calculated edge-to-edge distance between two adjacent W atoms of the aperture. Both values are almost equal and indicate that the effective area is lower than the geometric area and that the He transport is in the steric regime.

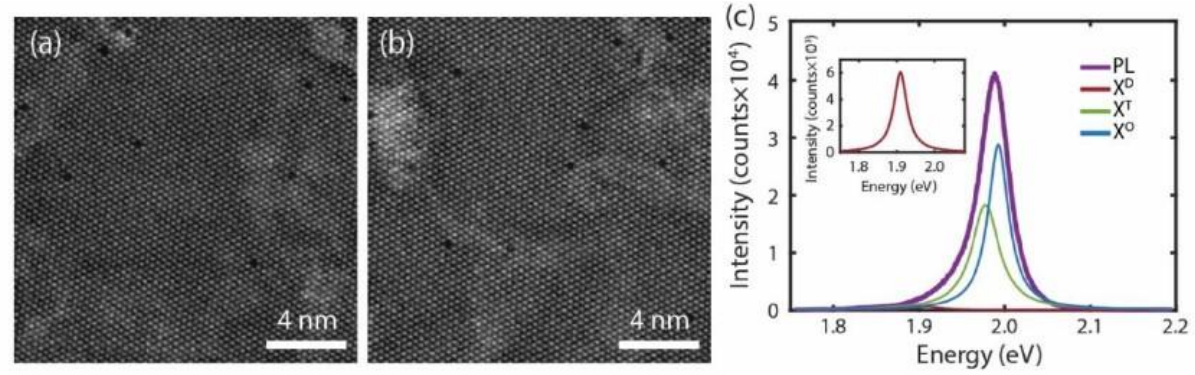

Figure S3. Characterization of FIB-irradiated WS_2 flakes. (a,b) Aberration-corrected HAADF STEM images of monolayer WS2 flakes after exposure to 5.1×10^{13} ions/cm^2 of 30 keV Ga^+ focused ion beam irradiation. Single defects appear as the absence of contrast at transition metal lattice sites. Multiple atomic-resolution STEM images were sampled over to obtain quantitative defect statistics (see also Supplementary Figure S2). (c) PL spectrum of a monolayer WS_2 flake suspended on a holey carbon film after exposure to 5.07×10^{13} ions/cm^2 of FIB irradiation. The 1.6% spectral weight percentage of the defect peak (X^D) to 1.6% suggests that FIB irradiation causes a slight increase in the PL midgap states localized at transition metal defect sites.

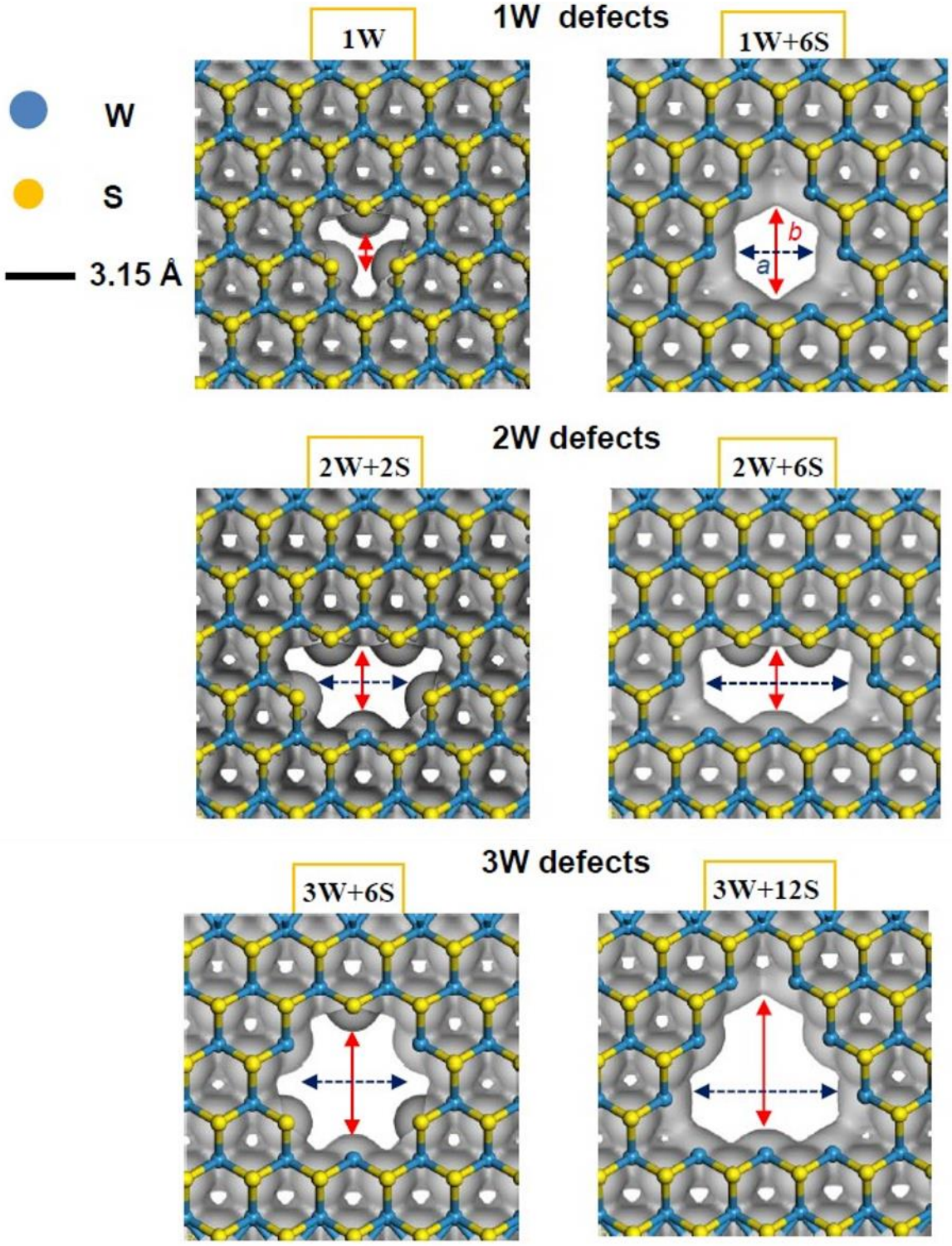

Figure S4. Atomic apertures. Typical apertures created on WS_2 monolayer upon the irradiation dose (~5.1 x 10^{13} ions/cm^2) with FIB are shown here with simulated isosurfaces. The aperture sizes were calculated using DFT based on accessible area after the electron density contours from iso-surfaces (*a* and *b* indicate the width and length of the defect respectively as depicted on images). Effective areas of the defect sites, one tungsten defect sites (1W with area, *A1** and 1W+6S with area, *A1*), two tungsten defect sites (2W+2S with area, *A2** and 2W+6S with area, *A2*), and three tungsten defect sites (3W+6S with area, *A3** and 3W+12S with area, *A3*) were

approximated based on their close match with regular shapes and values were presented in Table S1. Single W vacancy with no sulfur vacancies is likely non-conducting due to its extremely small accessible pore size (~1 Å) compared to Helium size (2.6 Å).

S3. Annealing before Gas Measurements

All the devices including controls are annealed at 350 °C for four hours in 10% H_2/ 90% Ar atmosphere. Gas measurements are performed soon after the annealing of devices. Annealing helps in unclogging of devices from atmospheric hydrocarbons and other adsorbing gases. However, this annealing step has not increased the gas flux by further widening the atomic apertures or damaging the WS_2 membranes in control samples.

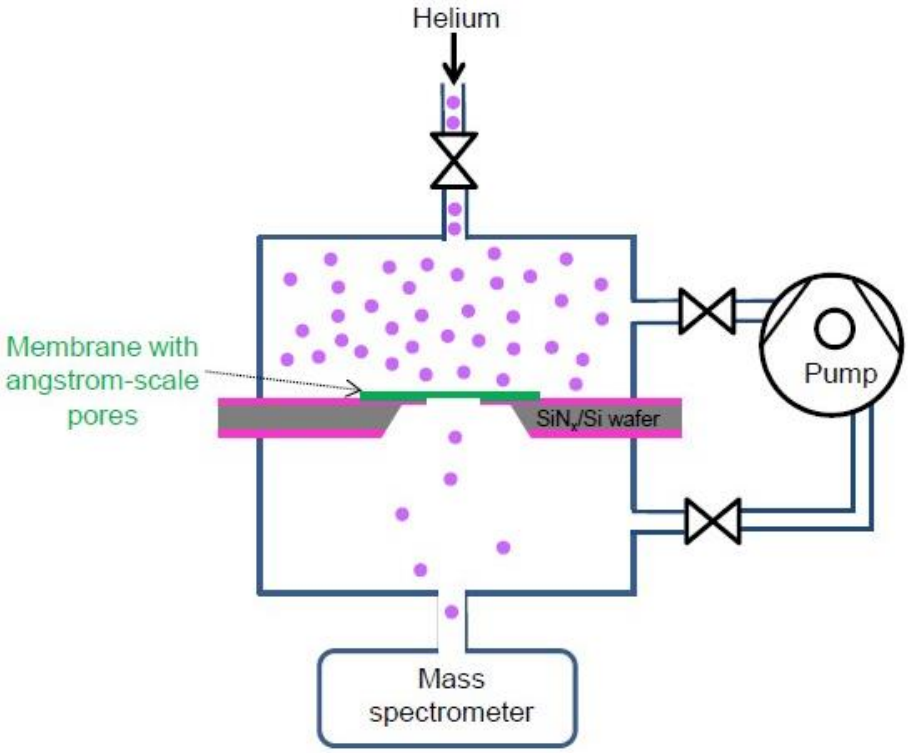

Figure S5. Helium flow measurement. Schematic representation of gas permeation measurement setup using mass spectrometer (Leybold phoenix L300i). In this setup, the only pathway between the top and bottom chambers is through the one-atom defects in WS_2 membranes i.e. atomic apertures.

S4. Gas Flow Measurements

Helium (He) gas permeation was measured using a mass spectrometer (helium-leak detector, Leybold phoenix L300i). The SiN_x/Si wafer with monolayer WS_2 membrane was clamped between O-rings (Kalrez) to separate two chambers (Figure S5). At first, both the chambers were evacuated using a bypass loop connected to a vacuum pump. Then, He gas was released into one of the chambers with controlled pressure P, and detected from the other chamber connected to the mass spectrometer as it flows through membrane with atomic defects. It was found that the gas flux detected by the mass spectrometer increased linearly with He gas pressure (main Figure 2). Since the diameter of the pores in the membrane are much smaller than the mean free path of He atoms (~140 nm at room temperature), the flux (QK) through these angstropores can be described by equation (1). For temperature variation experiments, we used a heating tape (Hemiheating AB) wound around the two chambers. A PID temperature controller (HTC-5500) interfaced with the tape, controlled the temperature with an accuracy of ± 2 ^oC. At each temperature, we waited ~5 min for stabilization before measuring the gas flow.

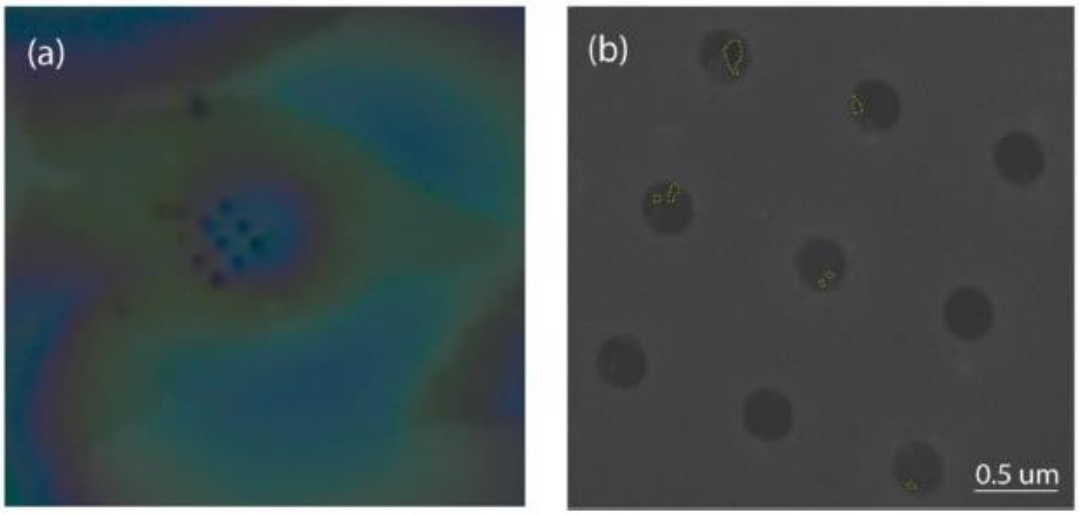

Figure S6. Tears in SEM analysis. (a) Optical image of the device after WS_2 transfer with PMMA. The image shows nine large pre-drilled holes in the centre of the chip, onto which the WS_2 monolayers are deposited. (b) Scanning Electron Microscope image of sub-micron tears within the WS_2 monolayer membranes, indicated by dashed yellow markers in five out of the nine holes.

S5. Ionic current measurements:

Ionic current measurements and experimental details are performed with parameters as in reference *(26)*. Briefly, Ag/AgCl electrodes and a patch-clamped amplifier are used to monitor ionic current as voltage is applied across the irradiated WS_2 suspended membranes. The data in this figure correspond to 0.1 M KCl and 1 M KCl solutions with a buffer (10 mM EDTA and 1 mM Tris). The pH was 8.7. Irradiated membranes were first annealed at 300 ^oC in an Ar-H_2 (10% H_2 in argon) for 90 minutes, then they were immersed in 50% water-ethanol for 30 minutes or longer to aid in wetting of membranes in KCl solutions. Wetting of sub-nm pores is a well-acknowledged problem in nanopore measurements, and therefore some pores may not contribute to ionic conductance. Maximum applied voltage was ± 0.1 V to minimize the possibility of membrane dielectric breakdown and pore enlargement during repeated measurements. We observed several faulty devices with tears in our fabrication process (Figure S6). These devices result in excessive flow (in both ionic current measurements and gas flow) and therefore are included as failed/leaky devices. Another signature of these leaky devices, after annealing, they have showed much increased flux compared to their initial flux.

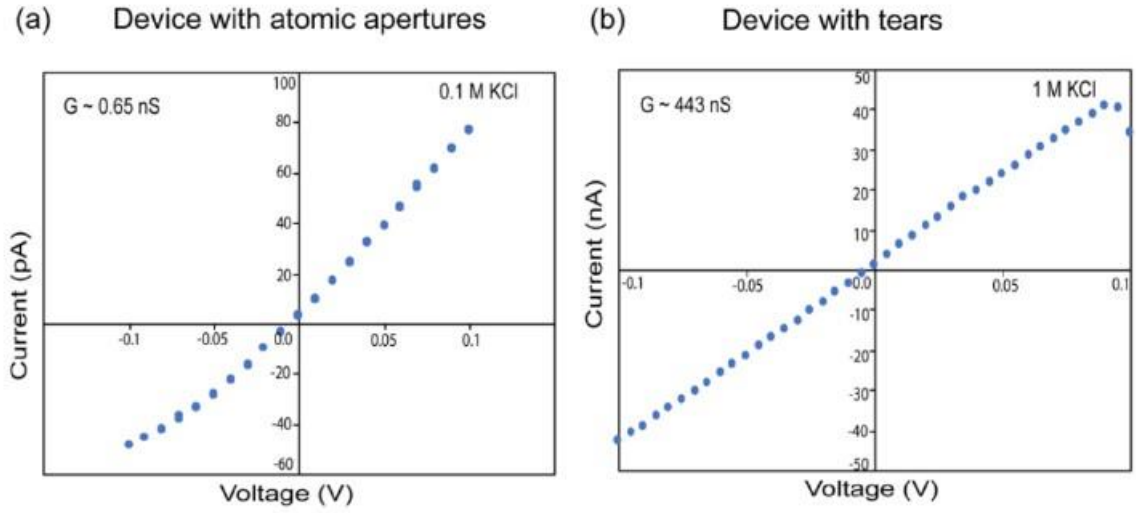

Figure S7. Current-voltage (I-V) analysis. (a) I-V of device showing negligible ionic currents (< 100 pA) up to ± 0.1 V applied voltage (conductance ~ 0.65 nS), in 0.1 M KCl. This device had nine FIB-drilled holes (with diameters in the range of 250 to 300 nm) onto which the 2D membrane was suspended. The atomic apertures were created with Ga ion irradiation dose = 5.1 x 10^{13} ions/cm^2. The defects with size of about < 0.6 nm are not expected to conduct ions based on MD simulations, and the observed small

conductance could be due to one or two pores of the size < 1 nm. One single pore of the size, ~1 nm in a TMD membrane showed a conductance of ~ 1 nS in 1 M KCl (*27*), which can further indicate upper limit on pore sizes in this sample. (b) Device showing high conductance ~ 443 nS in 1 M KCl indicative of membrane tears.

S6. Gas flow through apertures – analysis

Equation (1) is derived from the kinetic theory, and described by Knudsen as a solution for gas flow through infinitely thin apertures (*22,34*). For apertures with diameters far less than the mean free path λ, the probability of intermolecular collisions near the vicinity of the aperture goes down drastically, and the free molecular transport can be described by effusion.

There are several models (*e.g.*, BKT model, dual region model) for rarefied gas flows with Knudsen numbers $0.1 \leq K_n \leq 10$ taking the slip, adsorption of the molecules to the walls, drag *etc*., into account. Previous studies on carbon nanotubes, cylindrical, and slit-like pores with finite length, showed enhanced flow compared to Knudsen estimates, which was attributed to specular reflection of gas molecules off the atomically smooth graphite walls or pore surfaces (*47,48*). In graphene slit-pores, ballistic flow of He was observed due to specular reflections, while MoS_2 slit-pores showed diffusive reflections (*15*). However, here our atomic-scale apertures are within essentially infinitesimally thin membranes and these can be approximated as orifices, hence effusion-based mechanism seems the most suitable to describe the flow (*4-6*). The effusion mechanism depends on the impingement of gas molecule, and can be quantified as $Q = \upsilon \, \Delta n/4$, where $\upsilon = \mathrm{sqrt}(8RT/\pi M)$ is the mean velocity of the molecule, Δn is the gas number density. Combining with ideal gas law,

$$Q = P\,A\,\mathrm{sqrt}(1/2\pi MRT) \qquad (\text{eq. 1})$$

As the gas traverses through the aperture, the main hindrance to the flow is the probability of the gas hitting the aperture at a critical angle so as to be able to pass through the pore. As per Sun et al. article (*4*), the critical angle of incidence,

$\theta = \cos^{-1}(R_m/R_p)$, where radius of the helium molecule R_m = 1.3 Å and radius of the pore R_p ~1.6 Å to 3.1 Å in our case. Therefore, θ will be in the range of 35° to 65° for

1W to 3W defect pores. However, from our experiments, we observe that the He permeation/flux is within the expected estimates of equation (1) which indicates that the steric hindrance is likely not significantly reducing the flux. The steric hindrance can lead to a reduction factor of "R_p/R_m" (< 1) from ideal flux (*4*). This factor "R_p/R_m" will be >1 for 1W+6S pores and ~0.8 for 2W defects, which have pore sizes of ~3.1 Å and ~2 Å respectively. For 2W pores, there can be slight reduction of the flow, however, as the number of such pores are relatively small (~22%), the reduction of flow if any is not captured well in our measurements.

Let us note that although it is the area of the aperture that is in the equation (1), the shape of the defect is also known to influence the resulting Knudsen flux as shown by the unified model for slit-like pores with finite length (*49*). For our aperture case, we neglect the variations if any, due to the shape of the defect, as the dimensions of the aperture are quite close to the He kinetic diameter, and hence the corners of the aperture remain inaccessible. New models need to be developed in this new experimental regime to explain the shape and end effects and/or the phase transitions of the fluid while passing through such thin membranes (*48*).

For flux estimates, we have considered their area by approximating the pore as circular (1W defect) or rectangular shape (2W defects) or truncated triangular shape (3W defect). The accessible pore sizes and their effective areas are summarized in Figure S4 and Table S1.

Defect type	**Width of the pore (*a*, nm)**	**Height of the pore (*b*, nm)**	**Area (nm^2), approximated shape**
1W	0.105	0.105	0.009 (*A1**, circle)
1W+6S	0.315	0.315	0.079 (*A1*, circle)
2W+2S	0.36	0.21	0.075 (*A2**, rectangle)
2W+6S	0.62	0.21	0.129 (*A2*, rectangle)
3W+6S	0.525	0.525	0.216 (*A3**, circle)
3W+12S)	0.62	0.58	0.23(*A3*, truncated triangle

Table S1. Effective areas of atomic-scale apertures in WS_2 monolayer membrane for transport of He.

REFERENCES

1. H. B. Park, J. Kamcev, L. M. Robeson, M. Elimelech, B. D. Freeman, Maximizing the right stuff: The trade-off between membrane permeability and selectivity *Science* **356**, eaab0530 (2017).

2. M. Knudsen, Die Gesetze der Molekularströmung und der inneren Reibungsströmung der Gase durch Röhren *Ann. Phys.* **333**, 75–130 (1909).

3. M. V. Smoluchowski, Zur kinetischen Theorie der Transpiration und Diffusion verdünnter Gase. *Ann. Phys.* **338**, 1559–1570 (1910).

4. C. Sun, M. S. H. Boutilier, H. Au, P. Poesio, B. Bai, R. Karnik, N. G. Hadjiconstantinou, Mechanisms of molecular permeation through nanoporous graphene membranes *Langmuir* **30**, 675–682 (2014).

5. S. P. Koenig, L. Wang, J. Pellegrino, J. S. Bunch, Selective molecular sieving through porous graphene *Nat. Nanotechnol.* **7**, 728–732 (2012).

6. K. Celebi, J. Buchheim, R. M. Wyss, A. Droudian, P. Gasser, I. Shorubalko, J.-I. Kye, C. Lee, H. G. Park, Ultimate permeation across atomically thin porous graphene *Science* **344**, 289–292 (2014).

7. Y. Yamada, K. Murota, R. Fujita, J. Kim, A. Watanabe, M. Nakamura, S. Sato, K. Hata, P. Ercius, J. Ciston, C. Y. Song, K. Kim, W. Regan, W. Gannett, A. Zettl, Subnanometer vacancy defects introduced on graphene by oxygen gas *J. Amer. Chem. Soc.* **136**, 2232–2235 (2014).

8. L. Wang, L. W. Drahushuk, L. Cantley, S. P. Koenig, X. Liu, J. Pellegrino, M. S. Strano, J. Scott Bunch, Molecular valves for controlling gas phase transport made from discrete ångström-sized pores in graphene *Nat. Nanotechnol.* **10**, 785–790 (2015).

9. J. Zhao, G. He, S. Huang, L. F. Villalobos, M. Dakhchoune, H. Bassas, K. V. Agrawal, Etching gassieving nanopores in single-layer graphene with an angstrom precision for high-performance gas mixture separation *Sci. Adv.* **5**, eaav1851 (2019).

10. B. J. Hinds, N. Chopra, T. Rantell, R. Andrews, V. Gavalas, L. G. Bachas, Aligned multiwalled carbon nanotube membranes *Science* **303**, 62–65 (2004).

11. J. K. Holt, H. G. Park, Y. Wang, M. Stadermann, A. B. Artyukhin, C. P. Grigoropoulos, A. Noy, O. Bakajin,Fast mass transport through sub-2-nanometer carbon nanotubes *Science* **312**, 1034–1037 (2006).

12. L. Ge, A. Du, M. Hou, V. Rudolph, Z. Zhu, Enhanced hydrogen separation by vertically-aligned carbon nanotube membranes with zeolite imidazolate frameworks as a selective layer *RSC Adv.* **2**, 11793–11800 (2012).

13. R. W. Baker, *Membrane Technology and Applications* (John Wiley & Sons, Ltd., ed. 2, 2004).
14. L. Wang, M. S. H. Boutilier, P. R. Kidambi, D. Jang, N. G. Hadjiconstantinou, R. Karnik, Fundamental transport mechanisms, fabrication and potential applications of nanoporous atomically thin membranes *Nat. Nanotechnol.* **12**, 509–522 (2017).
15. A. Keerthi, A. K. Geim, A. Janardanan, A. P. Rooney, A. Esfandiar, S. Hu, S. A. Dar, I. V. Grigorieva, S. J. Haigh, F. C. Wang, B. Radha, Ballistic molecular transport through twodimensional channels *Nature* **558**, 420–424 (2018).
16. G. Scorrano, G. Bruno, N. di Trani, M. Ferrari, A. Pimpinelli, A. Grattoni, Gas flow at the ultrananoscale: Universal predictive model and validation in nanochannels of ångstrom-level resolution *ACS Appl. Mater. Interfaces* **10**, 32233–32238 (2018).
17. H. W. Kim, H. W. Yoon, S.-M. Yoon, B. M. Yoo, B. K. Ahn, Y. H. Cho, H. J. Shin, H. Yang, U. Paik, S. Kwon, J.-Y. Choi, H. B. Park, Selective gas transport through few-layered graphene and graphene oxide membranes *Science* **342**, 91–95 (2013).
18. H. Li, Z. Song, X. Zhang, Y. Huang, S. Li, Y. Mao, H. J. Ploehn, Y. Bao, M. Yu, Ultrathin, molecular-sieving graphene oxide membranes for selective hydrogen separation *Science* **342**, 95–98 (2013).
19. M. H. Khan, M. Moradi, M. Dakhchoune, M. Rezaei, S. Huang, J. Zhao, K. V. Agrawal, Hydrogen sieving from intrinsic defects of benzene-derived single-layer graphene *Carbon* **153**, 458–466 (2019).
20. S. Blankenburg, M. Bieri, R. Fasel, K. Müllen, C. A. Pignedoli, D. Passerone, Porous graphene as an atmospheric nanofilter. *Small* **6**, 2266–2271 (2010).
21. D.-e. Jiang, V. R. Cooper, S. Dai, Porous graphene as the ultimate membrane for gas separation. *Nano Lett.* **9**, 4019–4024 (2009).
22. L. W. Drahushuk, M. S. Strano, Mechanisms of gas permeation through single layer graphene membranes. *Langmuir* **28**, 16671–16678 (2012).
23. S. C. O'Hern, M. S. H. Boutilier, J.-C. Idrobo, Y. Song, J. Kong, T. Laoui, M. Atieh, R. Karnik, Selective ionic transport through tunable subnanometer pores in single-layer graphene membranes. *Nano Lett.* **14**, 1234–1241 (2014).
24. J. Jadwiszczak, C. O'Callaghan, Y. Zhou, D. S. Fox, E. Weitz, D. Keane, C. P. Cullen, I. O'Reilly, C. Downing, A. Shmeliov, P. Maguire, J. J. Gough, C. McGuinness, M. S. Ferreira, A. L. Bradley, J. J. Boland, G. S. Duesberg, V. Nicolosi, H. Zhang,

Oxide-mediated recovery of field-effect mobility in plasma-treated MoS_2. *Sci. Adv.* **4**, eaao5031 (2018).
25. J.-A. Ke, S. Garaj, S. Gradečak, Nanopores in 2D MoS2: Defect-mediated formation and density modulation. *ACS Appl. Mater. Interfaces* **11**, 26228–26234 (2019).
26. Z. Bai, L. Zhang, H. Li, L. Liu, Nanopore creation in graphene by ion beam irradiation: Geometry, quality, and efficiency. *ACS Appl. Mater. Interfaces* **8**, 24803–24809 (2016).
27. J. P. Thiruraman, K. Fujisawa, G. Danda, P. M. Das, T. Zhang, A. Bolotsky, N. Perea-López, A. Nicolaï, P. Senet, M. Terrones, M. Drndić, Angstrom-size defect creation and ionic transport through pores in single-layer MoS2. *Nano Lett.* **18**, 1651–1659 (2018).
28. P. Masih Das, J. P. Thiruraman, Y.-C. Chou, G. Danda, M. Drndić, Centimeter-scale nanoporous 2D
membranes and ion transport: Porous MoS2 monolayers in a few-layer matrix. *Nano Lett.* **19**, 392–399 (2019).
29. J. P. Thiruraman, P. Masih Das, M. Drndić, Irradiation of transition metal dichalcogenides using a focused ion beam: Controlled single-atom defect creation. *Adv. Func. Mater.* **29**, 1904668 (2019).
30. K. Liu, Q. Yan, M. Chen, W. Fan, Y. Sun, J. Suh, D. Fu, S. Lee, J. Zhou, S. Tongay, J. Ji, J. B. Neaton, J. Wu, Elastic properties of chemical-vapor-deposited monolayer MoS2, WS2, and their bilayer heterostructures. *Nano Lett.* **14**, 5097–5103 (2014).
31. J. S. Bunch, S. S. Verbridge, J. S. Alden, A. M. van der Zande, J. M. Parpia, H. G. Craighead, P. L. McEuen, Impermeable atomic membranes from graphene sheets. *Nano Lett.* **8**, 2458–2462 (2008).
32. P. Z. Sun, Q. Yang, W. J. Kuang, Y. V. Stebunov, W. Q. Xiong, J. Yu, R. R. Nair, M. I. Katsnelson, S. J. Yuan, I. V. Grigorieva, M. Lozada-Hidalgo, F. C. Wang, A. K. Geim, Limits on gas impermeability of graphene. *Nature* **579**, 229–232 (2020).
33. N. Mehio, S. Dai, D.-e. Jiang, Quantum mechanical basis for kinetic diameters of small gaseous molecules. *J. Phys. Chem. A* **118**, 1150–1154 (2014).
34. M. Knudsen, Die Molekularströmung der Gase durch Offnungen und die Effusion. *Ann. Phys.* **333**, 999–1016 (1909).

35. Y. Tao, Q. Xue, Z. Liu, M. Shan, C. Ling, T. Wu, X. Li, Tunable hydrogen separation in porous graphene membrane: First-principle and molecular dynamic simulation. *ACS Appl. Mater. Interfaces* **6**, 8048–8058 (2014).
36. S. Huang, M. Dakhchoune, W. Luo, E. Oveisi, G. He, M. Rezaei, J. Zhao, D. T. L. Alexander, A. Züttel, M. S. Strano, K. V. Agrawal, Single-layer graphene membranes by crack-free transfer for gas mixture separation. *Nat. Commun.* **9**, 2632 (2018).
37. R. M. de Vos, H. Verweij, High-selectivity, high-flux silica membranes for gas separation. *Science* **279**, 1710–1711 (1998).
38. V. Ierardi, U. Becker, S. Pantazis, G. Firpo, U. Valbusa, K. Jousten, Nano-holes as standard leak elements. *Measurement* **58**, 335–341 (2014).
39. S. Wang, H. Li, H. Sawada, C. S. Allen, A. I. Kirkland, J. C. Grossman, J. H. Warner, Atomic structure and formation mechanism of sub-nanometer pores in 2D monolayer MoS2. *Nanoscale* **9**, 6417–6426 (2017).
40. Y. Wen, C. Ophus, C. S. Allen, S. Fang, J. Chen, E. Kaxiras, A. I. Kirkland, J. H. Warner, Simultaneous identification of low and high atomic number atoms in monolayer 2D materials using 4D scanning transmission electron microscopy. *Nano Lett.* **19**, 6482–6491 (2019).
41. J. P. Perdew, J. A. Chevary, S. H. Vosko, K. A. Jackson, M. R. Pederson, D. J. Singh, C. Fiolhais, Atoms, molecules, solids, and surfaces: Applications of the generalized gradient approximation for exchange and correlation. *Phys. Rev. B* **46**, 6671–6687 (1992).
42. D. Rao, R. Lu, Z. Meng, Y. Wang, Z. Lu, Y. Liu, X. Chen, E. Kan, C. Xiao, K. Deng, H. Wu, Electronic properties and hydrogen storage application of designed porous nanotubes from a polyphenylene network. *Int. J. Hydrogen Energy* **39**, 18966–18975 (2014).
43. P. Giannozzi, S. Baroni, N. Bonini, M. Calandra, R. Car, C. Cavazzoni, D. Ceresoli, G. L. Chiarotti, M. Cococcioni, I. Dabo, A. Dal Corso, S. de Gironcoli, S. Fabris, G. Fratesi, R. Gebauer, U. Gerstmann, C. Gougoussis, A. Kokalj, M. Lazzeri, L. Martin-Samos, N. Marzari, F. Mauri, R. Mazzarello, S. Paolini, A. Pasquarello, L. Paulatto, C. Sbraccia, S. Scandolo, G. Sclauzero, A. P. Seitsonen, A. Smogunov, P. Umari, R. M. Wentzcovitch, QUANTUM ESPRESSO: A modular and open-source software project for quantum simulations of materials. *J. Phys. Condens. Matter* **21**,
395502 (2009).

44. D. Vanderbilt, Soft self-consistent pseudopotentials in a generalized eigenvalue formalism. *Phys. Rev. B* **41**, 7892–7895 (1990).
45. A. Tkatchenko, M. Scheffler, Accurate molecular van der Waals interactions from ground-state electron density and free-atom reference data. *Phys. Rev. Lett.* **102**, 073005 (2009).
46. P. K. Chow, R. B. Jacobs-Gedrim, J. Gao, T.-M. Lu, B. Yu, H. Terrones, N. Koratkar, Defectinduced photoluminescence in monolayer semiconducting transition metal dichalcogenides. *ACS Nano* **9**, 1520–1527 (2015).
47. A. Beskok, G. E. Karniadakis, W. Trimmer, Rarefaction and compressibility effects in gas microflows. *J. Fluids Eng.* **118**, 448–456 (1996).
48. T. Wu, D. Zhang, Impact of adsorption on gas transport in nanopores. *Sci. Rep.* **6**, 23629 (2016).
49. K. Wu, Z. Chen, X. Li, Real gas transport through nanopores of varying cross-section type and shape in shale gas reservoirs. *Chem. Eng. J.* **281**, 813–825 (2015).

Chapter 6

Molecular streaming and its voltage control in ångström-scale channels

The results are from a paper published in Nature in 2019.
T. Mouterde, A. Keerthi, A. R. Poggioli, S. A. Dar, A. Siria, A. K. Geim, L. Bocquet & B. Radha “Molecular streaming and voltage gated response in Angstrom scale channels”, **Nature (2019)**, 567, 87.

My contribution to the work includes device fabrication which involve flake preparation, fabrication of graphene/hBN heterostructures, patterning the graphene flake with nanolithography, AFM studies of the capillaries, gold evaporation for defining channel length. Optical lithography for making the microfluidic structure.

Author contributions: B.R., L.B. and A.S. designed and directed the project. A.K., B.R. and S.A.D. fabricated the devices. T.M. performed the measurements and their analysis. A.R.P., T.M. and L.B. provided theoretical support. T.M., L.B., B.R., A.K. and A.R.P. wrote the manuscript with inputs from A.K.G. All authors contributed to discussions.

Importance of the study

Ionic motion in confined channels is affected by direct interactions between channel walls and the hydration shells of ions. Here we demonstrate graphene channels with height down to one atomic plane with atomically smooth walls (graphite and hexagonal boron nitride) for pressure and voltage driven ionic transport to explore water and ion-interactions. Ions transport is markedly enhanced by an applied bias of fractions of volts. This gating effect observed for both wall materials but also rely on material dependent differences. Water transport strongly depends on channel wall material. Transport through these channels indicates transistor like electro hydrodynamic behavior where

small voltages induce strong responses which is similar to mechanosensitive ion channels.

Introduction: Ions and molecules are the building blocks of matter and their interaction provide more insights into the bases of physics, chemistry, materials and life sciences. Ions and molecules behave dramatically differently from bulk systems to nanoscale configurations. In confinement down to the nanoscale, the surfaces and interfaces can exert vital influence on the transport and interactive behaviours of ions and molecules.

Nanofluidics is a field studying the transport of fluids (ion and molecules of water and gas) at the nanoscale, has developed recently to a point where unexpected novel properties i.e., selective transport of ions (215, 216), ultra-rapid water transport (217)

strongly nonlinear ionic transport (218, 219), ultrafast ion sieving (37, 220) and increased ion mobility(221) are observed. These properties are expected to emerge due to water- and ion-transport (14, 222) phenomena arising from the combination of strong confinement i.e., due to high surface to volume ratios that amplifies the interaction of the interfaces, thus aggravating the van der Waals forces and electrostatic forces. The influence of surface charge and surface-induced effects occurring on the nanoscale (4) are due to exaggerated repulsive and attractive forces in nanoscales which induce anomalous ionic/molecular behaviours compared with bulk systems(223). Surface-induced effects including hydrodynamic slippage (224) and electro-kinetic (225) phenomena arise from the couplings between hydrodynamics and electrostatics.

In the case of confinement down to sub-nano (<1 nm), or even monatomic spaces, the short-range steric forces become stronger for ions/molecules. Channel surface and the hydration shells of the ions have a strong impact on the ionic motion and their interaction in such confined channels (171) and water transport has shown strong dependence on the different surfaces in this scale range (226). Under the interactions of short-range steric/hydration forces, the classical mechanics, and thermodynamic equations, such as the Navier−Stokes and Hertz−Knudsen are challenged (4, 227).

Interactions of water and ions with the confining structure and generation of electrical voltage due to phenomenon such as electrokinetics have a long history for its use and

exploration for energy conversion. Streaming current is produced in the electrolyte solution under hydrostatic pressure difference, this induces current corresponds to an electrical potential between the ends of the channels which is called streaming potential. Streaming current provides a useful technique for studying the electric properties of the solid-liquid interface as it results from the transport of ions in the electrolyte by an applied pressure gradient. Streaming currents in fluidic channels may provide a simple and effective means of converting hydrostatic pressure differences into electrical energy (228) and nanofluidic transistors (89) which appears due to electrokinetics.

There has been increasing interest in developing nanofluidic systems to manipulate ion transport to mimic the function of biological cells. The pressure-sensitive response has been observed for biological mechanosensitive ion channels (101, 102) which is very essential for understanding the cellular mechanisms which are linked to intracellular signalling and in regulating the mechanism of biochemical signalling in biological systems. Mechanically activated currents through channels (90) has been reported in protein channels which are produced due to electrical and mechanical forces and have an important role in physiology due to their impressive but complex biological ionic processes. Reproducing such an advanced response in artificial systems has not been achieved so far because of the ultra-small channel size and complex nature of forces. To observe such response in artificial channels most experimental studies done are in carbon nanotubes which have been restricted to electric forces (44, 104, 105). Carbon nanotubes with radii of ~2 nm in (106) have been explored with ionic transport in these channels using mechanical pressure and electrical voltage forces to mimic the exotic behaviour of biological channels and observed an ionic conductance that depends quadratically on applied pressure.

In the present work, we aimed at exploring the water and ion transport in atomic-scale capillaries under three different electrokinetic driving forces i.e., electrical field, concentration gradient and pressure difference along the length of the channels to come close to the sophistication of biological channels. Such a transmembrane geometry allows the detailed study of fluidic transport through the channels and their interaction with the channel wall surface. A modified continuum framework has been used to explain the material-dependent frictional interaction of water molecules, ions and the confining surfaces of channels made with different 2D materials.

Molecular streaming and its voltage control in ångström-scale channels

T. Mouterde[1,5], A. Keerthi[2,3,5], A. R. Poggioli[1], S. A. Dar[2,3,4], A. Siria[1], A. K. Geim[2,3*,] L. Bocquet[1*] & B. Radha[2,3*]

[1]Laboratoire de Physique de l'Ecole normale supérieure, ENS, Université PSL, CNRS, Sorbonne Université, Université Paris-Diderot, Sorbonne Paris Cité, Paris, France.

[2]School of Physics and Astronomy, University of Manchester, Manchester, UK.

[3]National Graphene Institute, University of Manchester, Manchester, UK.

[4]Department of Basic Sciences and Humanities, University of Engineering and Technology (KSK), Lahore, Pakistan.

Over the past decade, the ability to reduce the dimensions of fluidic devices to the nanometre scale (by using nanotubes[1–5] or nanopores[6–11], for example) has led to the discovery of unexpected water- and ion-transport phenomena[12–14]. More recently, van der Waals assembly of two-dimensional materials[15] has allowed the creation of artificial channels with ångström-scale precision[16]. Such channels push fluid confinement to the molecular scale, wherein the limits of continuum transport equations[17] are challenged. Water films on this scale can rearrange into one or two layers with strongly suppressed dielectric permittivity[18,19] or form a room-temperature ice phase[20]. Ionic motion in such confined channels[21] is affected by direct interactions between the channel walls and the hydration shells of the ions, and water transport becomes strongly dependent on the channel wall material[22]. We explore how water and ionic transport are coupled in such confinement. Here we report measurements of ionic fluid transport through molecular sized slit-like channels. The transport, driven by pressure and by an applied electric field, reveals a transistor-like electrohydrodynamic effect. An applied bias of a fraction of a volt increases the measured pressure-driven ionic transport (characterized by streaming mobilities) by up to 20 times. This gating effect is observed in both graphite and hexagonal boron nitride channels but exhibits marked material-dependent

differences. We use a modified continuum framework accounting for the material-dependent frictional interaction of water molecules, ions and the confining surfaces to explain the differences observed between channels made of graphene and hexagonal boron nitride. This highly nonlinear gating of fluid transport under molecular-scale confinement may offer new routes to control molecular and ion transport, and to explore electromechanical couplings that may have a role in recently discovered mechanosensitive ionic channels[23].

Our devices (Fig. 1) were ångström-scale channels on a Si/SiN substrate, fabricated as previously described[16,21] through van der Waals assembly of two (approximately 10 nm and 150 nm) thin crystals of graphite separated by strips of bilayer graphene. Each device had N = 200 channels of height $h_0 \approx 6.8$ Å, width w = 130 nm and length L of a few micrometres (see Methods section 'Device fabrication' and Extended Data Fig. 1). The channels were assembled on top of a micrometre opening etched in the Si/SiN wafer that served as entry to the fluidic channels, with the exit on the other side of the wafer (Fig. 1). The channels connected two macroscopic reservoirs filled with KCl solutions of concentration c and containing chlorinated Ag/AgCl electrodes for electrical current measurements. As previously reported[21], the net current I at high salt concentration is typically of the order of a few picoamps per channel for applied voltages of a few tens of millivolts and varies linearly with voltage and concentration as expected for this ultra-confined system with small surface charge[21]. In this study, we focus on the ionic current driven by the pressure drop ΔP and the effect of the additional potential difference ΔV applied along the channel. For this, ΔV was controlled by a patch-clamp amplifier (ground electrode is on the top side) with a current resolution of 0.1 pA; and pressure by a pump connected to the reservoir (Methods section 'Streaming current measurements'). We applied the pressure in both directions across the channel and found no influence on the reported results (see Extended Data Fig. 2; pressure applied from the bottom side in Fig. 1 is denoted as positive). Control experiments used similar devices but without channels and yielded no current upon application of ΔP or ΔV, confirming that our devices were structurally stable and, for example, did not delaminate under pressure (see Methods section 'Streaming current measurements' and Extended Data Fig. 3). This setup (Fig. 1) allows us to measure the pressure driven component of the ionic current, referred to as the streaming current $I_{str} = I(\Delta P, \Delta V) - I(0, \Delta V)$, which provides an indirect measure

of water flow under confinement. Figure 2 illustrates the behaviour in the absence of applied bias ($\Delta V = 0$), with Fig. 2a showing the time response of I_{str} when stepping ΔP up to 125 mbar in 25 mbar increments. Each step lasts 20 s, and the delay between successive steps is 20 s. After an initial overshoot, I_{str} rapidly reaches a steady state and, once the pressure is released, quickly returns to zero. The measured current is positive for positive applied pressures, which corresponds to a flow conveying a net positive charge that gradually increases with the pressure gradient, $\Delta P/L$. This is consistent with the reduction in chloride mobility as compared to that of potassium under strong confinement[21] (right panel of Fig. 1).

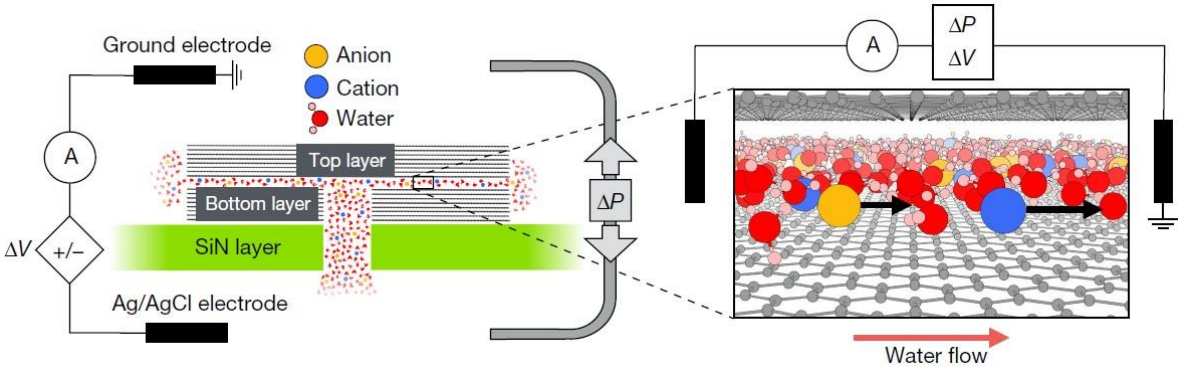

Fig. 1 | **Experimental setup for pressure- and voltage-driven current.** Schematic: ångström channels (fabricated on a Si/SiN wafer) separate two reservoirs containing KCl solutions. The entry and exit of the channel are on either side of the wafer. We set the voltage ΔV and the pressure ΔP along the channels and monitored the resulting current I. Right panel, illustration of ions moving in water under strong confinement (only one layer of top and bottom graphite walls is shown for clarity). Positive streaming currents indicate that potassium ions move faster than chloride ions inside the channel.

We find that, for concentrations between 1 mM and 300 mM, the steady-state current reached after each pressure increment (Fig. 2a) increases linearly with the driving force, that is, the pressure gradient (Fig. 2b). From the measured slopes, we calculate the streaming (electroosmotic) mobility $\mu = I_{str}/(NA\Delta P/L)$, where $A = wh_0$ is the slit cross-sectional area. The streaming mobility weakly depends on salt concentration (Fig. 2c), varying by less than 50% if c is increased by a factor of 300. However, the absolute value of μ is surprisingly high: it is of the order of 10^{-7} m^2 V^{-1} s^{-1}, which is in the range of the bulk potassium electrophoretic mobility $\mu_{K+} = 7.6 \times 10^{-8}$ m^2 V^{-1} s^{-1}

and an order of magnitude larger than streaming mobilities reported in the literature (for example, the streaming mobility for SiO_2 channels is about $0.1\mu_{K+}$).

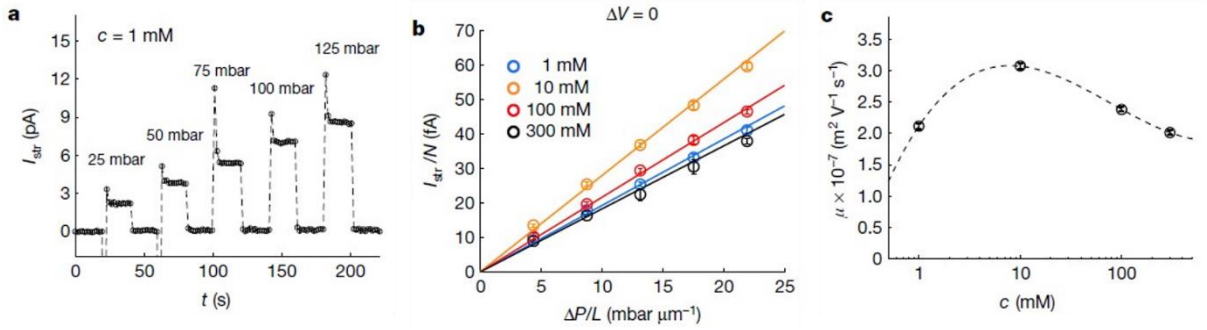

Fig. 2 | **Pressure-driven current without applying bias. a**, I_{str} as a function of time for graphite channels; c = 1 mM; L = 5.7 ± 0.1 μm. Current overshoots once the pressure is applied, and we consider only the steady-state regime in this study. **b**, Streaming current per channel, I_{str}/N, as a function of the pressure gradient $\Delta P/L$ for channels in **a**, and with different KCl concentrations c. For each c, the line corresponds to the best linear fit. **c**, Electro-osmotic mobility μ as a function of the KCl concentration (linear logarithmic coordinates; dashed line is a guide to the eye). Error bars represent: **a**, error in the currents measured during temporal evolution (± 0.1 pA); **b**, standard error; **c**, uncertainty in the fit value. Three devices were measured and showed the same behaviour.

As a comparison, we consider the measured streaming mobility in terms of the corresponding zeta potential, which has the dimension of an electrostatic potential. Using bulk water properties (viscosity η = 1 mPa s and dielectric permittivity $\varepsilon \approx 80$) gives us an apparent zeta potential, $\zeta = -\mu\eta/\varepsilon\varepsilon_0$, of roughly - 0.4 V, at least ten times the typical values in the literature[2,24,25] which are of the order of $kT/e \approx 25$ mV. Recent studies of confined water indicate that its out of-plane relative permittivity can be markedly suppressed[19] to $\varepsilon_{reduced} \approx 2$ whereas η remains close to the bulk value[16], which would translate into an even larger apparent ζ of −16 V. However, in our opinion, such a large apparent zeta potential does not reflect an anomalously high surface potential of the graphite but instead the high streaming mobility arising from the unusually fast transport of water, and hence hydrated ions, at molecular distances from the channel surfaces.

Figure 3 shows pressure-driven streaming currents measured under different applied voltage biases, allowing us to explore how the pressure- induced current couples to electric forces at these molecular scales. Figure 3a shows the time response of I_{str}

when applying pressure and Δ*V* simultaneously, revealing a considerable coupling between them in that I_{str} increases by more than 100% for Δ*V* = 50 mV as compared with its value at zero Δ*V*. As illustrated in Fig. 3b, the effects of Δ*P* and Δ*V* do not simply add: although the current always remains proportional to the pressure gradient, independent of applied bias, the slope of this linear dependence—the streaming mobility *μ*(Δ*V*)—varies with Δ*V* according to $I_{str} = \mu(\Delta V) \times A \times N \times \Delta P/L$. The linear dependence of streaming current on pressure highlights that it originates from the hydrodynamic transport of ions, while its voltage dependence indicates an unexpected interplay between mechanical and electric driving forces. To disentangle these effects further, we plot in Fig. 3d mobilities measured in graphite channels and normalized by μ_{K+} as a function of Δ*V* and *c*.

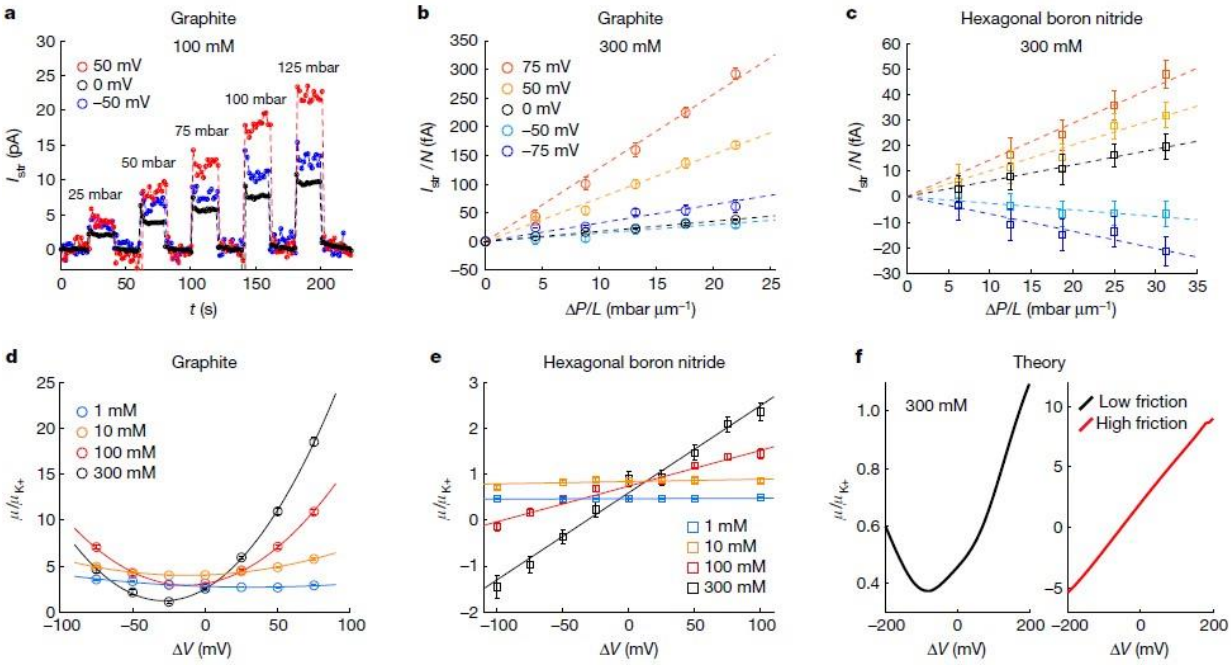

Fig. 3 | Streaming current for different biases and channel materials. a, Pressure-driven I_{str} for a graphite device at different Δ*V*. *L* = 5.7 ± 0.1 μm; KCl concentration, 100 mM. The pressure applied for 20 s intervals is gradually increased to 125 mbar in 25 mbar steps. **b**, Streaming current per channel for the same device as a function of Δ*P*/*L* (bias Δ*V* ranges from −75 to 75 mV; colour coded). **c**, Streaming current for similar devices but with hBN walls; same experiments and colour coding as in **a** and **b**. **d**, Streaming mobility (normalized by the K^+ electrophoretic mobility) as a function of Δ*V* for different KCl concentration for the graphite devices. Curves are the quadratic fits. **e**, Same as **d** but with hBN channels. Linear fits; *L* = 16 ± 0.1 μm. **f**, Extended PNP prediction for the streaming mobility using different friction coefficients between the water, ions and wall, with a factor of 100 between low and high friction. Low friction reproduces the quadratic gating observed for graphite (**d**), while high friction leads to

the linear gating observed for hBN (**e**). Detailed parameters and geometry used in the model are given in the Methods section 'Extended Poisson–Nernst–Planck theory' and Extended Data Figs. 6–10. Error bars represent: **a**–**c**, measurement uncertainty; **d**, **e**, uncertainty in the fit value.

We also compare the streaming effects in graphite channels with those of similar channels made from hexagonal boron nitride (hBN). In terms of crystal structure and atomic flatness, hBN is an analogue of graphite[26] but electrically insulating. Our hBN devices were fabricated using the same procedures as before and had the same parameters including h_0, and their behaviour was similar to that of graphite devices in that I_{str} varied linearly with ΔP (see Fig. 3c, Extended Data Figs. 2 and 4) and with a slope (streaming mobility μ) that was tuneable by applied bias. But the dependence of $\mu(\Delta V)$ differs greatly between the two materials: μ shows a quadratic response to electric bias for graphite (Fig. 3d), whereas it is essentially linear over the entire measurement range for hBN (Fig. 3e). The data can be described for graphite by

here eq 1 and 2 will come

$$\mu(\Delta V) = [1 + \alpha(\frac{\Delta V - V_{min}}{V_{ref}})^2] \quad (1)$$

and for hBN by

$$\mu(\Delta V) = \mu_0[1 + \beta\frac{\Delta V}{V_{ref}}] \quad (2)$$

where $V_{ref} = kT/e \approx 25$ mV is the thermal voltage, μ_0 is a mobility, and α and β are dimensionless parameters accounting for the voltage response. Typically, V_{min} is found to be of the order of V_{ref} and decreases with c; the voltage susceptibility α increases linearly with concentration (Extended Data Figs. 5a,b), reaching a value close to unity for high c = 300 mM. The characteristic mobility μ_0 is typically of the order of μ_{K+} for both systems. However, similar to α in graphite, the bias susceptibility β for hBN increases linearly with c (Extended Data Fig. 5c). Owing to the linear voltage coupling, the sign of the streaming current for hBN can be inverted for negative biases (Extended Data Fig. 4). For both materials, the sensitivity of I_{str} to voltage bias is very large, in contrast to other known control or gating mechanisms[27–31]. For graphite channels, a relatively small voltage ($\Delta V \approx 75$ mV) yields streaming mobilities which are up to about 20 times as large as the bulk potassium mobility, taken as a reference. This corresponds to zeta potentials up to 2 V assuming the bulk water properties, and

about 100 V if using the confined-water relative permittivity $\varepsilon_{\text{reduced}}$. Although the effect is still large for hBN, it is substantially smaller than that in graphite channels.

This observation echoes the smaller slip length for water on hBN as compared with graphite[4,22,32]. Taken together, our findings indicate that the applied bias voltage acts as a gate for pressure-driven streaming currents. Although it is tempting to rationalize this behaviour in terms of capacitive gating, as assumed, for example, for flow FET-type devices (fluidic analogues of field-effect transistors)[27], such an explanation fails to capture key experimental observations such as the contrasting voltage dependence of the gating for graphite and hBN. Any capacitive gating explanation also neglects the electrohydrodynamic coupling between ion and water transport under ångström-scale confinement, which is usually described in terms of the Poisson–Nernst–Planck–Stokes (PNPS) framework commonly used to describe ionic transport in biological or artificial channels. But this PNPS model is also unable to account for all our observations, in particular the qualitatively different bias dependence of μ seen for graphite versus hBN as summarized in equations (1) and (2). We attribute this to the strong confinement encountered in our devices, which renders the Stokes equation irrelevant when describing flow within the water/ion layer, owing to strong and direct interactions of the moving ions and water molecules with the confining walls.

We account for this effect by considering friction between water, ions and the walls, which we capture by an effective water–wall friction that depends on ion concentrations. This may be described as $\lambda_w(\rho_+,\rho_-) = \lambda_0 + h_0(\kappa_+\rho_+ + \kappa_-\rho_-)$, where λ_0 is the bare (ion-free) friction coefficient for water, $\kappa_\pm$ are coefficients characterizing the ions' contribution to the friction, and $\rho_\pm$ are the ion concentrations. (The full model for our channel geometry is detailed in the Methods section 'Extended Poisson–Nernst–Planck theory', and in Extended Data Figs. 6 to 10.) The resultant extended Poisson–Nernst–Planck (PNP) model qualitatively reproduces most of the experimental observations, leading to streaming currents that are linear in ΔP (Extended Data Fig. 7) and reproducing the large increase in streaming mobility under applied bias (Fig. 3f) that is in contrast to the standard consequences of concentration polarization. As illustrated in Fig. 3f, the model also yields different functional dependences $\mu(\Delta V)$ according to the friction behaviour of both water and ions on the different materials: low friction between water molecules and ions and the channel wall leads to a quadratic gating of the streaming mobility as observed for graphite, whereas large

friction results in an essentially linear dependence as observed for hBN. The model and underlying theory indicate that this behaviour results from a subtle and intertwined effect of concentration dependent flow and ion concentration profile across the channels in the presence of voltage. Accordingly, the different material response observed in Fig. 3 for channels made from hBN and graphite can be traced back to the difference of molecular friction of water and ions on these two materials. This is in agreement with expectations for the friction of water on these two materials[4,22,32].

A remarkable feature of this framework is that the observed nonlinear bias response thus has its roots in the fundamental nature of interactions between confining walls, water molecules and ions. For instance, the minimum mobility seen in Fig. 3d arises from the slight asymmetry in device geometry which is at the origin of different frictions (induced by the confinement) and modifies locally the transport rates of ions on each side. Although the simple model reproduced our experimental results qualitatively (Extended Data Figs. 8 to 10), it cannot account for the large amplitude of the bias voltage effect seen with graphite channels. Better agreement will require more comprehensive evaluation of the effects of strong confinement (including the suppressed dielectric constant), which are expected to modify not only water and ion dynamics but also the adsorption of the ions[33]. Furthermore, the metallicity of graphite can substantially modify ionic interactions and thereby ion concentrations. We anticipate that extending ab initio molecular simulations of water friction[22], to include the effect of ions, will provide further insight beyond the simple picture proposed here.

Our experimental system allows us to probe purely two-dimensional flow of water and ions, a configuration very different from the one-dimensional transport through nanotubes. Thanks to the lateral extension of the ångström channels, streaming currents under molecular confinement become measurable. Hence, such devices are an interesting platform in which to mimic the behaviour of biological channels in terms of stimuli responsive behaviour such as voltage gating, where ions are driven through ångström-scale confinement by coupled osmotic pressure and electric forcing. This is of relevance for gaining new insights into the electromechanical coupling at the root of the mechanosensitivity observed in recently discovered biological ionic channels[23] (TRAAK, TREK, PIEZO). Furthermore, the observed friction-based electric gating opens a new route to achieve flow-control under extreme confinement where small

voltages induce strong responses, which would constitute an important step towards building nanofluidic circuits responding to external stimuli.

References

1. Fornasiero, F. et al. Ion exclusion by sub-2-nm carbon nanotube pores. *Proc. Natl Acad. Sci. USA* **105**, 17250–17255 (2008).

2. Siria, A. et al. Giant osmotic energy conversion measured in a single transmembrane boron nitride nanotube. *Nature* **494**, 455–458 (2013).

3. Secchi, E., Niguès, A., Jubin, L., Siria, A. & Bocquet, L. Scaling behavior for ionic transport and its fluctuations in individual carbon nanotubes. *Phys. Rev. Lett*. **116**, 154501 (2016).

4. Secchi, E. et al. Massive radius-dependent flow slippage in carbon nanotubes. *Nature* **537**, 210–213 (2016).

5. Tunuguntla, R. H. et al. Enhanced water permeability and tunable ion selectivity in subnanometer carbon nanotube porins. *Science* **357**, 792–796 (2017).

6. Garaj, S. et al. Graphene as a subnanometre trans-electrode membrane. *Nature* **467**, 190–193 (2010).

7. Joshi, R. K. et al. Precise and ultrafast molecular oxide membranes. *Science* **343**, 752–754 (2014).

8. Jain, T. et al. Heterogeneous sub-continuum ionic transport in statistically isolated graphene nanopores. *Nat. Nanotechnol*. **10**, 1053–1057 (2015).

9. Feng, J. et al. Single-layer MoS2 nanopores as nanopower generators. *Nature* **536**, 197–200 (2016).

10. Hong, S. et al. Scalable graphene-based membranes for ionic sieving with ultrahigh charge selectivity. *Nano Lett*. **17**, 728–732 (2017).

11. Abraham, J. et al. Tunable sieving of ions using graphene oxide membranes. *Nat. Nanotechnol*. **12**, 546–550 (2017).

12. Eijkel, J. C. T. & van den Berg, A. Nanofluidics: what is it and what can we expect from it? *Microfluid. Nanofluidics* **1**, 249–267 (2005).

13. Schoch, R. B., Han, J. & Renaud, P. Transport phenomena in nanofluidics. *Rev. Mod. Phys*. **80**, 839–883 (2008).

14. Howorka, S. & Siwy, Z. Nanopore analytics: sensing of single molecules. *Chem. Soc. Rev*. **38**, 2360–2384 (2009).

15. Geim, A. K. & Grigorieva, I. V. Van der Waals heterostructures. *Nature* **499**, 419–425 (2013).
16. Radha, B. et al. Molecular transport through capillaries made with atomic-scale precision. *Nature* **538**, 222–225 (2016).
17. Bocquet, L. & Charlaix, E. Nanofluidics, from bulk to interfaces. *Chem. Soc. Rev*. **39**, 1073–1095 (2010).
18. Schlaich, A., Knapp, E. W. & Netz, R. R. Water dielectric effects in planar confinement. *Phys. Rev. Lett*. **117**, 048001 (2016).
19. Fumagalli, L. et al. Anomalously low dielectric constant of confined water. *Science* **360**, 1339–1342 (2018).
20. Algara-Siller, G. et al. Square ice in graphene nanocapillaries. *Nature* **519**, 443–445 (2015).
21. Esfandiar, A. et al. Size effect in ion transport through angstrom-scale slits. *Science* **358**, 511–513 (2017).
22. Tocci, G., Joly, L. & Michaelides, A. Friction of water on graphene and hexagonal boron nitride from ab initio methods: very different slippage despite very similar interface structures. *Nano Lett*. **14**, 6872–6877 (2014).
23. Coste, B. et al. Piezo proteins are pore-forming subunits of mechanically activated channels. *Nature* **483**, 176–181 (2012).
24. Sze, A., Erickson, D., Ren, L. & Li, D. Zeta-potential measurement using the Smoluchowski equation and the slope of the current–time relationship in electroosmotic flow. *J. Colloid Interface Sci*. **261**, 402–410 (2003).
25. Geismann, C., Yaroshchuk, A. & Ulbricht, M. Permeability and electrokinetic characterization of poly(ethylene terephthalate) capillary pore membranes with grafted temperature-responsive polymers. *Langmuir* **23**, 76–83 (2007).
26. Keerthi, A. et al. Ballistic molecular transport through two-dimensional channels. *Nature* **558**, 420–424 (2018).
27. Schasfoort, R. B. M., Schlautmann, S., Hendrikse, J. & van den Berg, A. Field-effect flow control for microfabricated fluidic networks. *Science* **286**, 942–945 (1999).
28. Kim, S. J., Li, L. D. & Han, J. Amplified electrokinetic response by concentration polarization near nanofluidic channel. *Langmuir* **25**, 7759–7765 (2009).
29. Jiang, Z. & Stein, D. Charge regulation in nanopore ionic field-effect transistors. *Phys. Rev. E* **83**, 031203 (2011).

30. Karnik, R. et al. Electrostatic control of ions and molecules in nanofluidic transistors. *Nano Lett*. **5**, 943–948 (2005).
31. Pang, P., He, J., Park, J. H., Krstić, P. S. & Lindsay, S. Origin of giant ionic currents in carbon nanotube channels. *ACS Nano* **5**, 7277–7283 (2011).
32. Xie, Q. et al. Fast water transport in graphene nanofluidic channels. *Nat. Nanotechnol*. **13**, 238–245 (2018).
33. Futamura, R. et al. Partial breaking of the Coulombic ordering of ionic liquids confined in carbon nanopores. *Nat. Mater*. **16**, 1225–1232 (2017).

Acknowledgements T.M. and L.B. acknowledge funding from ANR project Neptune. B.R. acknowledges a Royal Society Fellowship, a L'Oréal Fellowship for Women in Science, and EPSRC grant EP/R013063/1. A.S. acknowledges funding from the European Union's Horizon 2020 (EU H2020) Framework Programme/ERC Starting Grant agreement number 637748—NanoSOFT. L.B. acknowledges funding from the EU H2020 Framework Programme/ERC Advanced Grant agreement number 785911—Shadoks. A.R.P. acknowledges funding from the EU H2020 Framework Programme/European Training Programme 674979—NanoTRANS. S.A.D. was funded by a scholarship from the University of Engineering and Technology, Lahore Pakistan. A.K., B.R. and A.K.G. were supported by Lloyd's Register Foundation and European Research Council (ARTIMATTER). T.M. thanks S. Blin and H. Yoshida for assistance.

Reviewer information *Nature* thanks Rohit Karnik and the other anonymous reviewer(s) for their contribution to the peer review of this work.

Author contributions B.R., L.B. and A.S. designed and directed the project. A.K., B.R. and S.A.D. fabricated the devices. T.M. performed the measurements and their analysis. A.R.P., T.M. and L.B. provided theoretical support. T.M., L.B., B.R., A.K. and A.R.P. wrote the manuscript with inputs from A.K.G. All authors contributed to discussions. **Competing interests** The authors declare no competing interests.

Methods

Device fabrication. Our devices were fabricated following previously reported procedures[16,21]. In brief, a free-standing silicon nitride (SiN) membrane of around 500 nm in thickness provided mechanical support and served to separate the two

reservoirs connected by the channels. On the membrane, a rectangular hole of approximately 3 μm × 26 μm was defined by lithography and plasma etching. The channels were made by van der Waals assembly of three layers—bottom, spacer, top—of 2D crystals such as graphite or hBN. First, a bottom layer of around 10- to 50-nm-thick graphite or hBN was transferred onto the hole in the SiN membrane and etched from the back side, which projected the hole into the bottom layer. Following this, pre-patterned bilayer graphene spacers (about 6.8 Å thick) in the form of parallel ribbons about 130 nm wide and separated also by about 130 nm were transferred onto the bottom crystal and aligned perpendicular to the long axis of the rectangular hole. Finally, a thick (about 100 nm to 150 nm) top crystal of graphite or hBN was transferred onto the spacers covering the hole (Extended Data Fig. 1). The top crystal defined the length of the channels that formed on both sides of the hole.

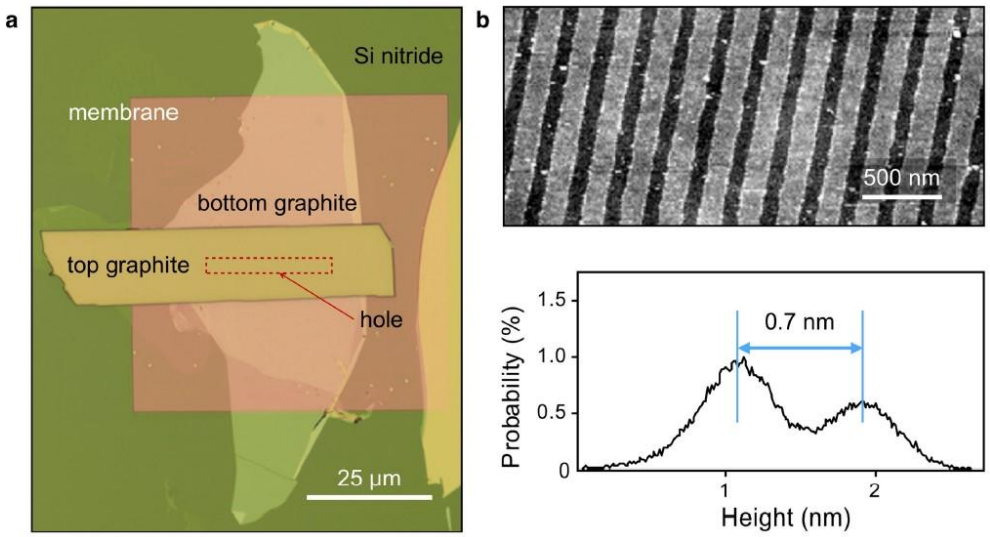

Extended Data Fig. 1 | **Ångström-scale channel devices. a**, Optical image of a device with ångström channels. The square in light pink colour is the silicon nitride membrane which has a rectangular hole shown by the red dotted line. Covering the hole, the bottom graphite layer, spacer and top graphite layer are placed. Bottom and top graphite are visible in the image in light and bright yellow colours. **b**, Atomic force microscopy (AFM) image of the bilayer graphene spacer lines on the device. The histogram of the heights (below the AFM image) shows that the spacer is about 0.7 ± 0.1 nm thick.

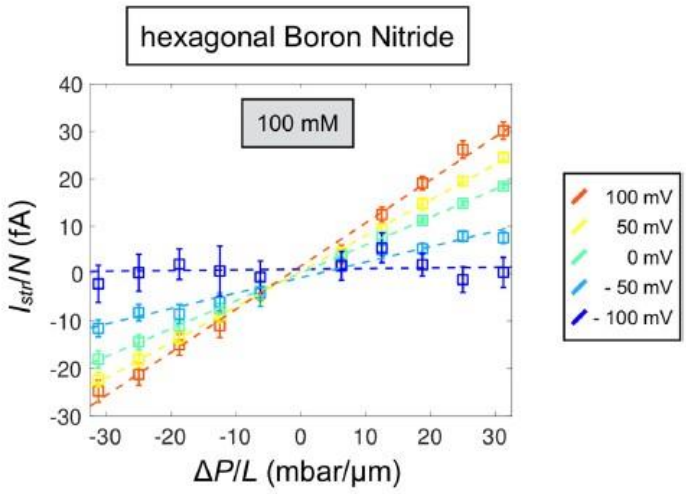

Extended Data Fig. 2 | **Gated pressure-driven current.** Streaming current per channel plotted as a function of Δ*P*/*L* with Δ*V* ranging between −100 mV and 100 mV (colour coded from blue to red with increasing voltage difference), KCl concentration of 100 mM and hBN channels of length *L* = 16 ± 0.1 µm.

Streaming current measurements. Extended Data Fig. 3a–c shows the streaming current measurements as a function of the applied pressure for a sample containing no channels (varying from 0 to 250 mbar). The pressure is applied via a pressure pump (AF1, Elveflow) (we denote a positive Δ*P* for a pressure applied through the hole on SiN) and Δ*V* is controlled via a patch-clamp amplifier (Axopatch 200B, Molecular Devices) with the ground electrode on the top side. For a sample containing no channels, we did not detect any significant current. Extended Data Fig. 3d–f compares the streaming current measured for the control sample and a graphite device containing 200 channels. In the case of graphite channels, the streaming current is four orders of magnitude larger than the noise measured in the control sample.

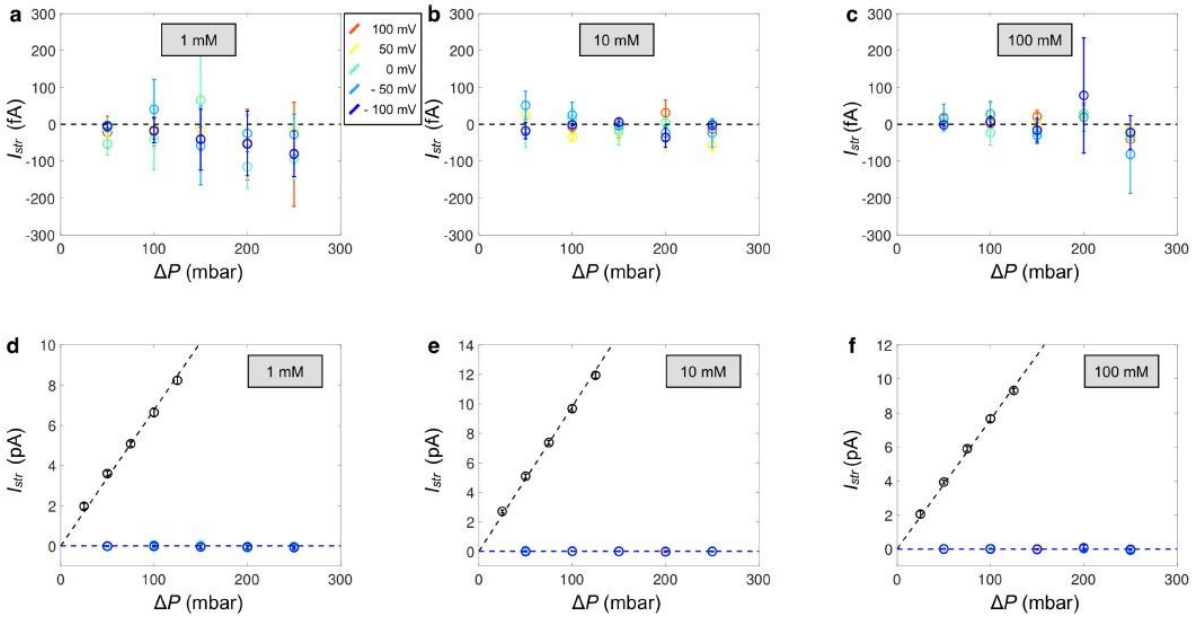

Extended Data Fig. 3 | **Control sample test. a–c**, Streaming current measured in a control sample without any channels as a function of the pressure. We varied the applied voltage from −100 to 100 mV (colour coded from blue to red). **d–f**, Same measurements as for **a–c** (coloured symbols) but compared with the streaming current measured with 200 graphite channels (black symbols). The streaming current is around 4 orders of magnitude larger, which confirms that channels remain mechanically stable and are not delaminated under pressure.

To investigate the pressure dependence of the streaming current, we performed the streaming current measurements applying the pressure successively on each side of the membrane. The inversion of the pressure gradient fully reverts the streaming current sign as presented in Extended Data Fig. 2; this confirms the linear dependence of the streaming current on the mechanical forcing. The molecular streaming current I_{str} as a function of the pressure gradient $\Delta P/L$ is shown in Extended Data Fig. 4 for both graphite and hBN devices and for different KCl concentrations and applied voltages. The streaming current varies linearly with the driving force $\Delta P/L$.

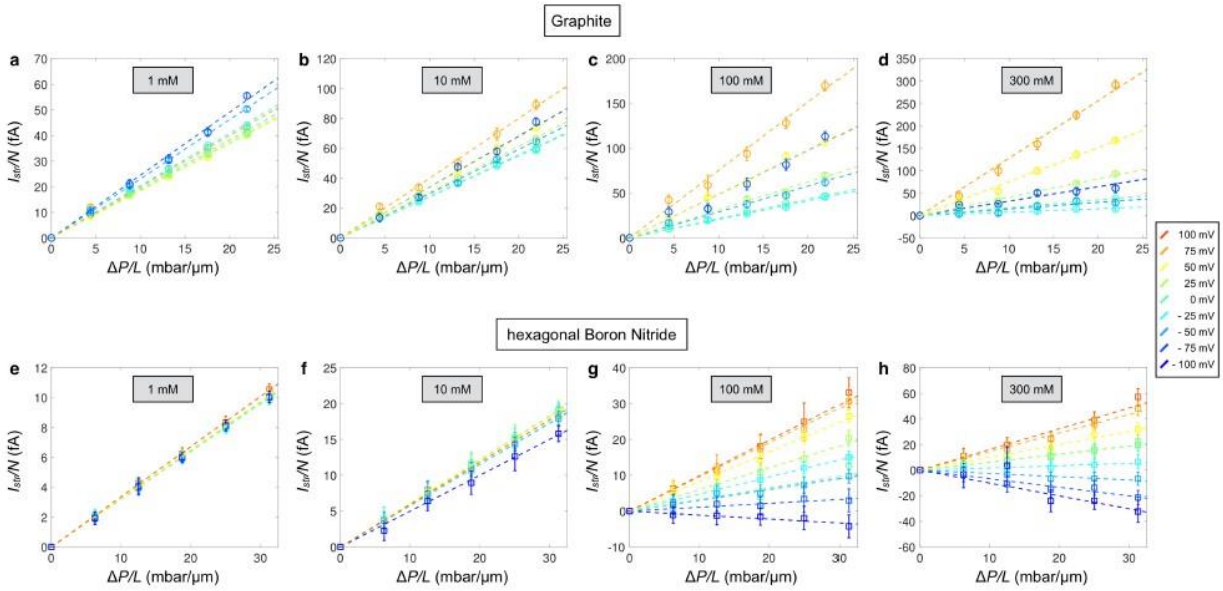

Extended Data Fig. 4 | Gated pressure-driven current and material dependency. Streaming current per channel plotted as a function of Δ*P*/*L* for a KCl concentration varying from 1 mM to 300 mM and with Δ*V* ranging between −100 mV and 100 mV (colour coded from blue to red with increasing voltage difference). **a–d**, The channel length *L* for graphite is 5.7 ± 0.1 μm. **e–h**, For hBN, *L* = 16 ± 0.1 μm.

Extended Poisson–Nernst–Planck theory. *Governing equations.* At scales greater than about 1 nm, the influence of water motion on the ionic fluxes is accounted for by (1) appending Stokes' equation for the solvent velocity to the typical PNP description of the ionic transport and (2) including an ionic drift velocity set by the balance of forces between the electric force on the individual ion and the frictional force between the ion and water in the Nernst–Planck parameterization of the solute fluxes. Both assumptions are inapplicable here owing to the extreme confinement scale of the channels considered, which approaches the diameter of the water molecules and hydrated ions themselves. In particular, application of the Stokes equation to predict the hydrodynamic velocity relies on the assumption of a spatially homogeneous and isotropic scalar viscosity, an assumption that cannot be valid when a single layer of water molecules is present. A priori, we would expect strong interaction between the ions and walls, and the water molecules and walls. The former supposition is supported by the results of ref.[21], where the chloride mobility in both graphite and hBN devices of the type examined here was observed to be reduced by approximately 65%

compared with bulk. The latter is supported by the present results when combined with the simple, first-principles model detailed below.

As noted above, the traditional ionic and hydrodynamic force balances, leading to the typical parameterization of the drift velocity and the Stokes equation, respectively, can no longer be sufficient to describe the coupled ion– water transport in one-to-two layers confinement owing to the substantial interaction with the confining material. As a simple first-principles approach, we consider the force balances on the individual ions and on a control volume of infinitesimal length along the slit containing both ions and water molecules. We include three phenomenological forces, the frictional interactions of (1) water with walls, (2) ions with walls and (3) ions with water. We emphasize that this is the simplest possible coherent approach to capture the modification in the qualitative behaviour of the ion dynamics owing to the extreme confinement. Quantifying the friction to achieve a more quantitatively accurate treatment would probably necessitate more in-depth modelling (such as ab initio molecular dynamics).

Including the ion–wall interaction, a force balance on an individual ion gives:

$$0 = \pm e\,(-\partial_x \Phi) - \xi_{\pm}\,(v_{\pm} - v_w) - \lambda_{\pm}\,v_{\pm} \tag{3}$$

where $v_{\pm}$ is the velocity of the positive or negative ion species, v_w is the water velocity and ϕ is the electrostatic potential. From left to right, the terms represent (1) the electric body force on the positive or negative ion, (2) the frictional force of the water on the ion, parameterized by friction coefficients $\xi_{\pm}$ for the cation and anion species and the frictional force of the wall on the ions, parameterized by friction coefficients $\lambda_{\pm}$ Note that we have assumed that all of the ions interact appreciably with the walls, a reasonable assumption here given the extreme confinement. We solve for the ion velocity $v_{\pm}$ to obtain:

$$v_{\pm} = \pm\,\mu_{\pm}\,(-\partial_x \Phi) - \alpha_{\pm}\,v_w \tag{4}$$

We have introduced the ionic mobilities $\mu_{\pm} \equiv e/(\xi_{\pm} + \lambda_{\pm})$and the normalized water–ion friction coefficients $\alpha_{\pm} \equiv \xi_{\pm}/(\xi_{\pm}+\lambda_{\pm}) \in (0, 1)$. The former parameters are constrained by the experimental results of ref.[21]; the latter parameters characterize how effectively

the drag of the water flow is able to overcome frictional resistance on the ions from the wall and engender ionic transport. We note that the definition of $\alpha_\pm$ may be rearranged to give $\lambda_\pm/\xi_\pm = (1-\alpha_\pm)/\alpha_\pm$. This indicates that a value $\alpha_\pm \ll 1$ corresponds to stronger ion–wall than ion–water friction, while values of $\alpha_\pm$ approaching 1 indicate relatively weaker ion–wall than ion– water interaction.

From the above definitions, we see that the sums of the ion–water and ion–wall friction coefficients are constrained by the experimentally measured mobilities reported in ref.[21], $\xi_\pm + \lambda_\pm = e\mu_\pm^{-1}$, while the relative importance of the ion–wall and ion–water interactions, characterized by the ratios $\lambda_\pm/\xi_\pm = (1-\alpha_\pm)/\alpha_\pm$, is not.

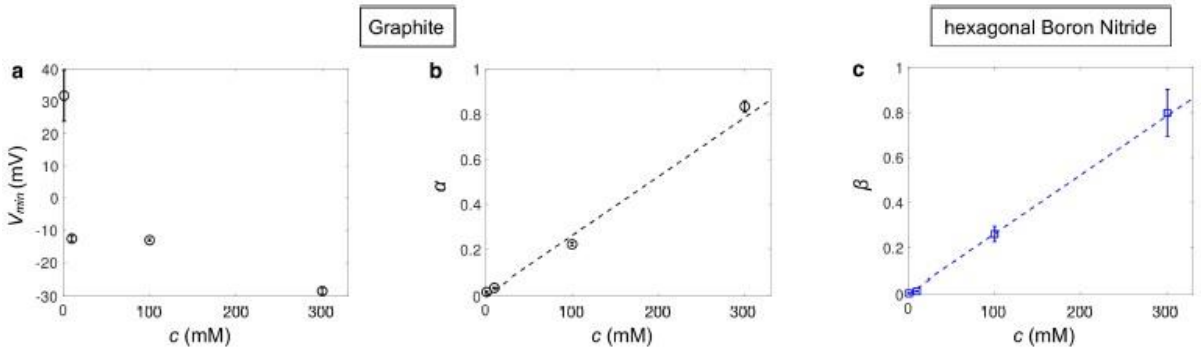

Extended Data Fig. 5 | Concentration dependence of the fit parameters of the gate-controlled mobility. We report the fitting parameters of the voltage-gated streaming current. **a**, **b**, The quadratic dependence of the gated streaming current observed in graphite channels (Fig. 3d, main text) and described by equation (1): **a**, Vmin plotted as a function of the concentration; **b**, α as a function of the concentration. **c**, We report the fitting parameter β as a function of the concentration for hBN slits: β describes the linear dependence of the streaming current observed for hBN channels (Fig. 3e, main text) as given by equation (2). The dashed lines in **b** and **c** are linear fits.

We next consider the force balance on a control volume of width and height equal to the channel width w and height h, respectively, and of infinitesimal length δ_x in the along-slit direction. The total volume of the control volume is then $\delta V \equiv wh\delta_x$. The total electric body force is given by $e(\rho_+ - \rho_-) \times (-\partial_x \phi \times \delta V$, and the net pressure force is given by $wh \times (-\partial_x P) \times \delta_x$. In the preceding, $\rho_\pm$ are the ionic densities (per unit volume) at the position x coincident with the centre of the control volume (so that in the reservoirs $\rho_\pm = N_A c$ with N_A the Avogadro number), and P is the pressure. The total frictional force due to ion–wall interactions is $-(\rho_+ \lambda_+ v_+ - \rho_- \lambda_- v_-)\, \delta V$. Finally, we

introduce a coefficient λ_0 characterizing the frictional interaction of water molecules with the walls such that $-\lambda_0 v_w$ is the force per unit wall area acting on the water molecules, and $-\lambda_0 v_w \times w\delta x$ is the total frictional force on the control volume due to water–wall interaction. The force balance on the control volume thus gives:

$$0 = e(\rho_+ - \rho_-)(-\partial_x \phi)\delta V + (-\partial_x P)\delta V - (\rho_+\lambda_+ v_+ - \rho_-\lambda_- v_-)\delta V - \frac{\lambda_0}{h} v_w \delta V \quad (5)$$

Before solving the above for the water velocity v_w, we use equation (4) and the definitions of $\mu_\pm$ and $\alpha_\pm$ to rewrite the total ion–wall friction force per unit volume δV, $\rho_+\lambda_+ v_+ - \rho_-\lambda_- v_-$, as:

$$e(\rho_+ - \rho_-)(-\partial_x \phi) - e(\alpha_+ \rho_+ - \alpha_- \rho_-)(-\partial_x \phi) + (\kappa_+\rho_+ - \kappa_-\rho_-)v_w \quad (6)$$

where we have defined $\kappa_\pm \equiv e\alpha_\pm (1-\alpha_\pm)/\mu_\pm$ and made use of the identities $\lambda_\pm\mu_\pm \equiv e(1-\alpha_\pm)$ and $\lambda_\pm\alpha_\pm \equiv \kappa_\pm$. We insert this result into equation (5) and solve for v_w to obtain:

$$v_w = K_{app}(\rho_+, \rho_-)[(-\partial_x P) + e(\alpha_+ \rho_+ - \alpha_- \rho_-)(-\partial_x \phi)] \quad (7)$$

Where $K_{app}(\rho_+, \rho_-)$ is a concentration-dependent apparent hydraulic permeance, given by:

$$K_{app}(\rho_+, \rho_-) \equiv \frac{1}{\frac{\lambda_0}{h} + \kappa_+\rho_+ + \kappa_-\rho_-} \quad (8)$$

To better interpret the significance of the parameter $\alpha_\pm$ and the non-intuitive form in which the electric field appears in equation (7), we use the above results to calculate the difference of the electric force $f_e^\pm$ and the ion–wall friction force $f^\pm_{\text{ion-wall}}$ on a given ionic species:

$$f^\pm_e - f^\pm_{ion-wall} = \pm e\alpha_\pm \rho_\pm (-\partial_x \phi) - \kappa_\pm \rho_\pm v_w \quad (9)$$

Let us discuss two extreme limits. When $\alpha_\pm = 0$, $\xi_\pm/\lambda_\pm = 0$, indicating that only ion–wall (rather than ion–water) friction is relevant. Further, from the above definition, $\kappa_\pm \propto \alpha_\pm(1-\alpha_\pm) = 0$, and the net (electric less ion–wall friction) force vanishes. Thus, in this case, all of the electric force on the given ionic species in the control volume is balanced by the strong ion–wall interaction such that the given ionic species does not communicate any electric force to the water molecules. (See equation (7) with α_+ and/or α_- set to zero.) On the other hand, when $\alpha_\pm = 1$, $\lambda_\pm/\xi_\pm = 0$, indicating that only ion–water friction is

relevant, and all of the electric force on the ions is communicated to the water molecules such that $f^{\pm}_{e}$ - $f^{\pm}_{\text{ion-wall}}$ =± $e\rho_{\pm}$ $(-\partial_x \varphi)$. (Again, $\kappa_{\pm} \propto \alpha_{\pm}$ $(1-\alpha_{\pm})$ =0.)

We emphasize that the behaviour described in equations (7) and (8) is in strong contrast to what is observed for conduits with confinement scale (radius or height) greater than about 1 nm, in which the Hagen–Poiseuille equation holds[17]. In this case, we would have a concentration-independent permeance $K_{HP}=h_0/\lambda_0$ and a net electric driving force equal to the total electric driving force $e(\rho_+ - \rho_-)$ $(-\partial_x \varphi)$. K_{HP} is recovered in the high water friction limit, $\lambda_0 / h >> \kappa_+\rho_+ + \kappa_-\rho_-$, and both K_{HP} and the total electric driving force are recovered outside of confinement where $\alpha_{\pm}=1$ (equivalent to no ion–wall friction: $\lambda_{\pm}=0$).

It is necessary to use equation (7), instead of Hagen Poiseuille, to capture the full range of qualitative behaviour observed in the experimental μ (ΔV) curves. This emphasizes the importance of the two-dimensionality of the flow, resulting in a strong frictional interaction between the channel walls, water and ions. We insert equation (7) into the general Nernst–Planck parameterization for the ionic fluxes, $j_{\pm} = D_{\pm}$ $(-\partial_x \rho_{\pm})$ + $v_{\pm}\rho_{\pm}$, to obtain:

$$j_{\pm} = \mu_{\pm}\left[\frac{k_B T}{e}(-\partial_x \rho_{\pm}) \pm \rho_{\pm}(-\partial_x \phi)\right] + \alpha_{\pm} v_w \rho_{\pm} \qquad (10)$$

where we have made use of the Einstein relation, $D_{\pm}= k_B T \mu_{\pm}/e$, $D_{\pm}$ being the diffusion coefficients.

At steady state, the conservation equations become:

$$\frac{d(hv_w)}{dx} = 0, \frac{d(hj_{\pm})}{dx} = 0 \qquad (11)$$

Finally, the electrostatic potential φ is related to the total charge density $e(\rho_+ - \rho_-)$ via the Poisson equation:

$$\partial_x\left[\varepsilon\varepsilon_0 h(-\partial_x \phi)\right] = he\,(\rho_+ ,\ \rho_-) \qquad (12)$$

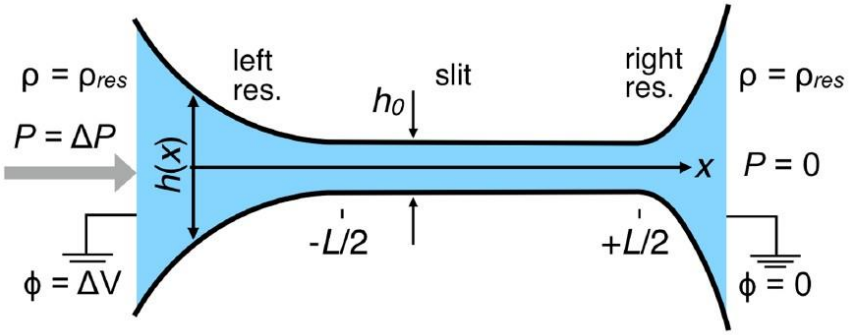

Extended Data Fig. 6 | **Geometry and effect of the asymmetry of the system.** A slit of uniform height h_0=7 Å and length L=5 μm connects two asymmetric, divergent reservoirs of variable height $h\ x$ ( ). The asymmetry in the rate of divergence of the reservoir heights qualitatively mimics the asymmetry of the experimental geometry. A voltage $\varphi = \Delta V$ and pressure $P = \Delta P$ are applied in the left reservoir (at $x = -\infty$); the voltage and pressure are held fixed at φ=0, P=0 in the right reservoir ($x = +\infty$). The density in both reservoirs is held fixed at $\rho = \rho_{res}$.

Model geometry and boundary conditions. As we are mainly interested in capturing the qualitative features of the ionic current response, we adopt a simplified one-dimensional geometry. The model geometry adopted here is sketched in Extended Data Fig. 6. A slit of uniform height h_0 = 7 Å and length L = 5 μm connects two reservoirs of divergent geometry. It is necessary to include the reservoirs in some capacity in our calculations to capture the entrance/exit effects associated with the discontinuous change in ionic mobility as the ions enter/ exit the channel. The rate of divergence of the reservoir heights is asymmetric, qualitatively mimicking the asymmetry of the experimental geometry. The height profile $h(x)$ is given by:

$$\frac{h(x)}{h_0} = \Gamma_l\left[\left(\frac{x}{L}\right)+\frac{1}{2}\right]^2 + 1, x \in \left[-\infty - \frac{L}{2}\right]$$

$$1, x \in \left[-\frac{L}{2} + \frac{L}{2}\right] \qquad (13)$$

$$\Gamma_r\left[\left(\frac{x}{L}\right)-\frac{1}{2}\right]^2 + 1, x \in \left[+\frac{L}{2} + \infty\right]$$

Γ is the rate of divergence of the confinement: the larger Γ is, the more abrupt is the transition to the open reservoir. We take $\Gamma_l = 5$ and $\Gamma_r = 20$. Although the magnitudes of Γ_l and Γ_r influence the quantitative predictions of the model, the qualitative behaviour of the mobilities is similar so long as $\Gamma_l < \Gamma_r$. We impose the reservoir conditions at $x = \pm\infty$. In the left reservoir, we apply a voltage and pressure:

$$\phi(x = -\infty) = \Delta V \tag{14}$$

$$\mathrm{P}(x = -\infty) = \Delta P \tag{15}$$

In the right reservoir, the voltage and pressures are held fixed at reference values arbitrarily set to zero:

$$\phi(x = +\infty) = 0, \ \ \mathrm{P}(x = +\infty) = 0 \tag{16}$$

The total ionic density in both reservoirs is held fixed at $\rho_{res} = 2N_A c$, and both reservoirs are assumed to be electroneutral, such that:

$$\rho_{\pm}(x = \pm\infty) = \frac{\rho_{res}}{2} \tag{17}$$

Variation of ion mobilities $\mu_\pm$ and normalized water–ion friction coefficients $\alpha_\pm$. We impose the following profiles for the ionic mobilities:

$$\mu_{\pm} = (\mu_{\pm}{}^{bulk} - \mu_{\pm}{}^{conf}) \left(1 - \frac{tanh\left(\frac{x + \frac{L}{2}}{\lambda_{adj}}\right) - tanh\left(\frac{x + \frac{L}{2}}{\lambda_{adj}}\right)}{2} \right) \pm \mu_{\pm}{}^{conf} \tag{18}$$

with an adjustment length λ_{adj}=0.3 nm. To qualitatively account for the reduction in chloride mobility, we take $\mu_-^{conf} = 0.5\ \mu_-^{bulk}$. Similarly, we impose for the normalized water–ion friction coefficients:

$$\alpha_{\pm} = (1 - \alpha_{\pm}^{conf}) \left(1 - \frac{tanh\left(\frac{x + \frac{L}{2}}{\lambda_{adj}}\right) - tanh\left(\frac{x + \frac{L}{2}}{\lambda_{adj}}\right)}{2} \right) \pm \alpha_{\pm}^{conf} \qquad (19)$$

Results. Calculations were performed using the finite element method (COMSOL). Extended Data Fig. 7a–c shows the results of the above model for low water–wall (λ_0/h_0=10^{11} kg m^{-3} s^{-1}) and water–ion ($\alpha_+ = 1 \leftrightarrow \lambda_+/\xi_+ = 0$; $\alpha_- = 0.7 \leftrightarrow \lambda_-/\xi_- \approx 0.43$) friction, and Extended Data Fig. 7d–f those for high water–wall (λ_0/h_0=10^{13} kg m^{-3} s^{-1}) and water–ion ($\alpha_+ = \alpha_- = 0.01$ equivalent to $\lambda_+/\xi_+ = \lambda_-/\xi_- = 99$) friction. We first note that in both cases we reproduce the linear dependence of the streaming current on the pressure gradient for both zero and non-zero applied voltages (Extended Data Fig. 7b, e), in agreement with experiments (Fig. 3b, c, main text).

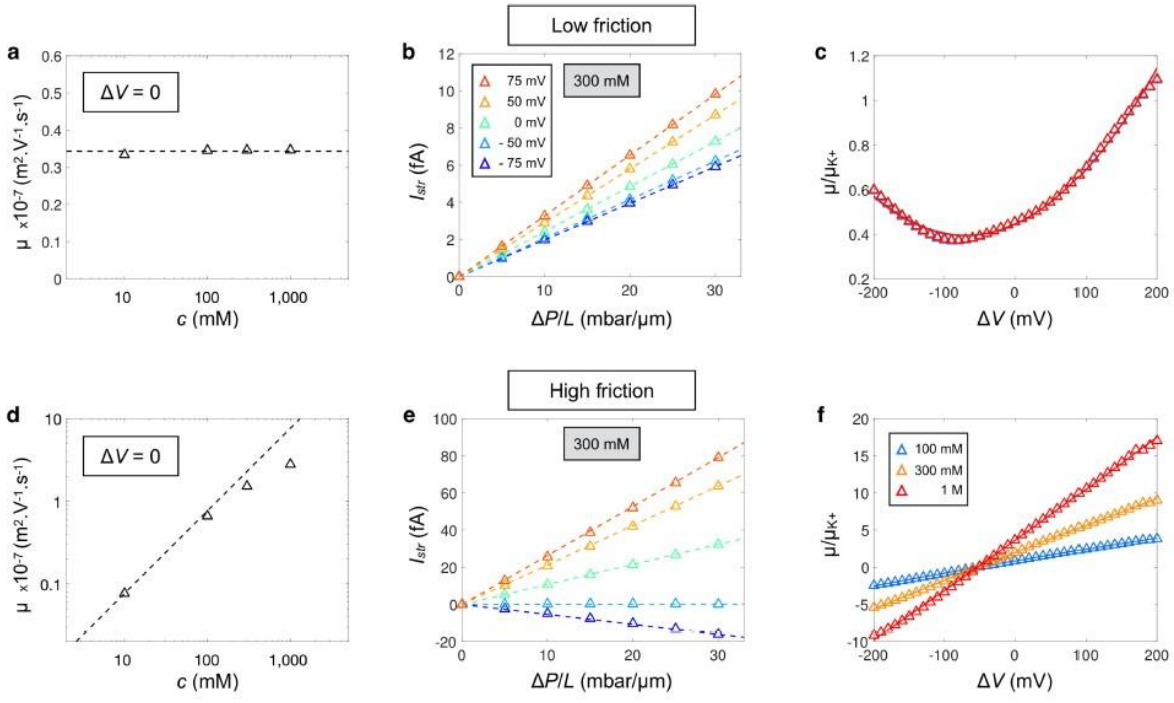

Extended Data Fig. 7 | Prediction of the streaming current from extended Poisson–Nernst–Planck modelling. a, Mobility without applied voltage as a function of KCl concentration in linear–logarithmic coordinates for low water–wall friction and $\alpha+ > \alpha-$. **b**, Streaming current per channel I_{str} for 300 mM as a function of the pressure gradient $\Delta P/L$ for ΔV varying from −75 mV (blue data) to +75 mV (red data). For each voltage, the dashed line corresponds to the linear fit of the data made to extract the

mobility. **c**, Streaming mobility μ normalized by the K+ electrophoretic mobility μK+ and plotted as a function of the applied voltage for KCl concentration varying from 100 mM (blue data) to 1 M (red data). **d**–**f**, Same as in **a**–**c** but with high water–wall friction and $\alpha+ = \alpha-$. Parameters: **a**–**c**, $\lambda_0/h_0 = 10^{11}$ kg m^{-3} s^{-1}, $\alpha+ = 1$, $\alpha- = 0.7$; **d**–**f**, $\lambda_0/h_0 = 10^{13}$ kg m^{-3} s^{-1}, $\alpha+ = 0.01$, $\alpha- = 0.01$. Dashed lines in **a** and **d** are guides to the eye corresponding to a constant value of μ and a linear variation with concentration, respectively.

The low-friction results produce a quadratic dependence of the streaming mobility on the applied voltage with a minimum mobility occurring for $\Delta V = V_{min} < 0$ (Extended Data Fig. 7c). This qualitative behaviour is in agreement with the experimental results obtained for graphite (Fig. 3d, main text). Likewise, the high-friction results reproduce the linear dependence of the streaming mobility on ΔV (Extended Data Fig. 7f) that is observed experimentally in hBN (Fig. 3e, main text). The frictional characteristics of these results are consistent with the typically much lower friction (larger slip lengths) observed on graphite than in hBN[3,22,32]. We note that, in addition to taking low to moderate values of $\lambda_\pm/\xi_\pm \approx 0$–1, it is necessary to take $\alpha_+ > \alpha_-$ to recover the qualitative behaviour of graphite. On the other hand, it is necessary to take $\alpha_+ \approx \alpha_- < \sim 0.1$ to recover the qualitative behaviour of hBN. This suggests that frictional interaction of the wall with the ions is weaker generally in graphite, and that it is stronger for chloride than potassium. In hBN, on the other hand, our results suggest that the frictional interaction of the wall with the ions is fairly strong for both species.

The numerical results presented here for the low-friction (graphite-like) configuration indicate that $\mu(\Delta V = 0)$ is independent of concentration, roughly consistent with the minimal variation observed in the experiments (Fig. 2c, main text). However, the linear dependence of the mobility on concentration for non-zero applied voltages (Fig. 3d, e, main text) is not observed in the model (Extended

Data Fig. 7c). Conversely, at higher friction (Extended Data Fig. 7d–f), $\mu(\Delta V = 0)$ varies strongly with the concentration, as well as the gated mobility (Extended Data Fig. 7f). This suggests the possibility that the concentration, applied voltage and friction are coupled in ways not accounted for in our simple model.

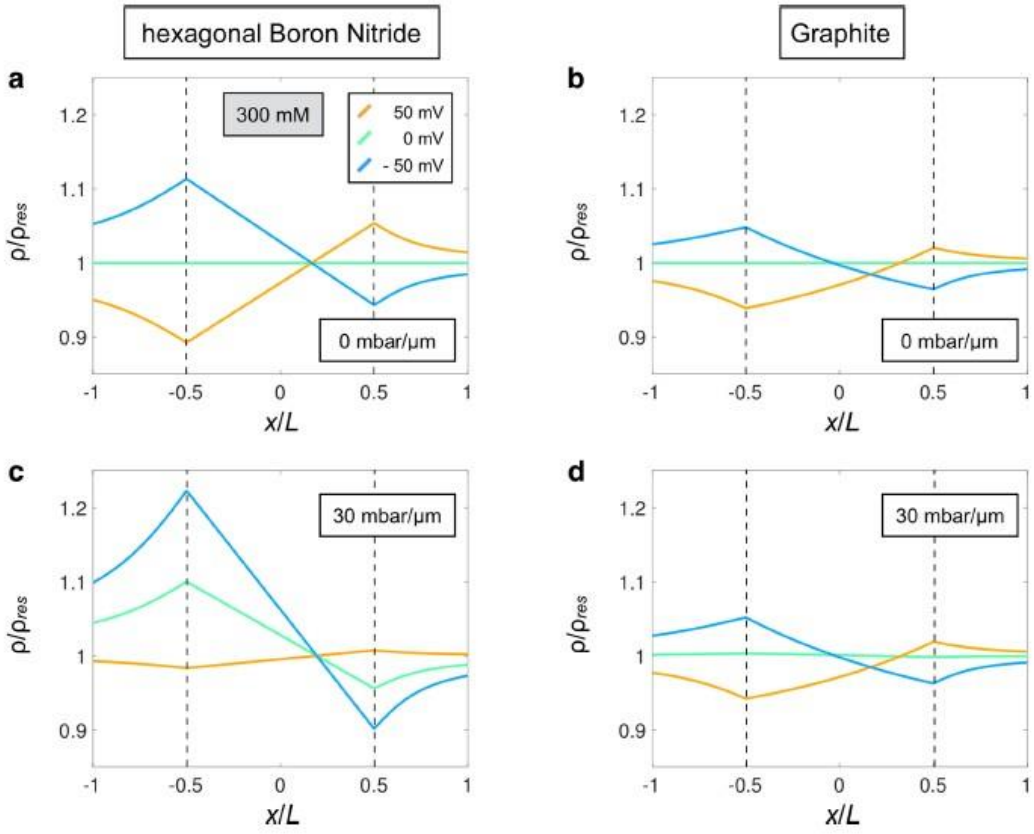

Extended Data Fig. 8 | Total ionic concentration profiles from extended Poisson-Nernst-Planck modelling. a–**d**, Total ionic concentration profiles as a function of the normalized position x/L along the channel without (**a**, **b**) and with (**c**, **d**) applied pressure for c = 300 mM. The dashed vertical lines segregate the channel interior, $x/L \in (-0.5, 0.5)$, from the left ($x/L < -0.5$) and right ($x/L > 0.5$) reservoirs. The curves are coloured according to the applied voltage from −50 mV (blue) to 50 mV (orange). **a**, The high-friction (hBN-like) configuration with $\Delta P/L = 0$. **b**, The low-friction (graphite-like) behaviour with $\Delta P/L = 0$. **c**, The high-friction (hBN-like) configuration with $\Delta P/L$ = 30 mbar μm^{-1}. **d**, The low-friction (graphite like) behaviour with $\Delta P/L$ = 30 mbar μm^{-1}.

The numerical results depend crucially on the difference in water flow characteristics between the two materials through the concentration-dependent permeance given in equation (8). However, the nature of this dependence is intricate. Our numerical results indicate that, in addition to the advective current engendered by the applied pressure, the streaming current characteristics depend crucially on the modification of the electrophoretic current $I_{ep} \propto \rho E$ (figure not shown) via the modification of the concentration and electrostatic fields by coupled voltage and pressure effects. An example of the influence of voltage on the evolution of the concentration fields in the presence of a fixed applied pressure gradient $\Delta P/L$ = 30 mbar μm^{-1} and a reservoir

concentration c = 300 mM is shown in Extended Data Fig. 8c, d. We see that both the applied pressure and voltage induce modification of the concentration profile across the channel (as well as inducing charge separation, not shown). The modification of the concentration profile due to pressure is much stronger in hBN (Extended Data Fig. 8a, c), and it is also much more sensitive to applied pressure and voltage in hBN than in graphite. This latter characteristic is consistent with the smaller streaming mobilities observed in the graphite-like configuration observed in our numerical results (Extended Data Fig. 7c, f). Additionally, we see that the evolution of the concentrations under coupled ΔP–ΔV forcing is different in the two materials; it is this difference, and the corresponding difference in the response of the advective and electrophoretic currents, that determines the difference between the two material behaviours.

There are several aspects of the observations in graphite that we are not able to reproduce: (1) the non-monotonicity of the dependence of $\mu(\Delta V = 0)$ on concentration, (2) the linear dependence of the mobility on concentration when a voltage is applied and (3) the magnitude of the mobilities measured at high concentration under an applied voltage. Indeed, the model consistently predicts mobilities in the quadratic (graphite-like) regime that are smaller than those observed in the linear (hBN-like) regime (Extended Data Fig. 7c, f). This is not an issue of the voltage range examined, as the mobilities are found to saturate or even reduce at much higher voltages. Likewise, there is much that we have not included in our model: in particular, steric effects and ionic correlations generally, as well as the ‘granular’ nature of water, which might be important at this length scale. Nonetheless, the model does reproduce much of the key qualitative behaviour, and its success depends on the strong differences in the frictional characteristics of hBN and graphite, and further on the incorporation of the retarding influence of the ions on the water transport, an effect that is exclusively two-dimensional. Thus, these results illustrate the two-dimensional character of the flow and the limit of the continuum description of matter.

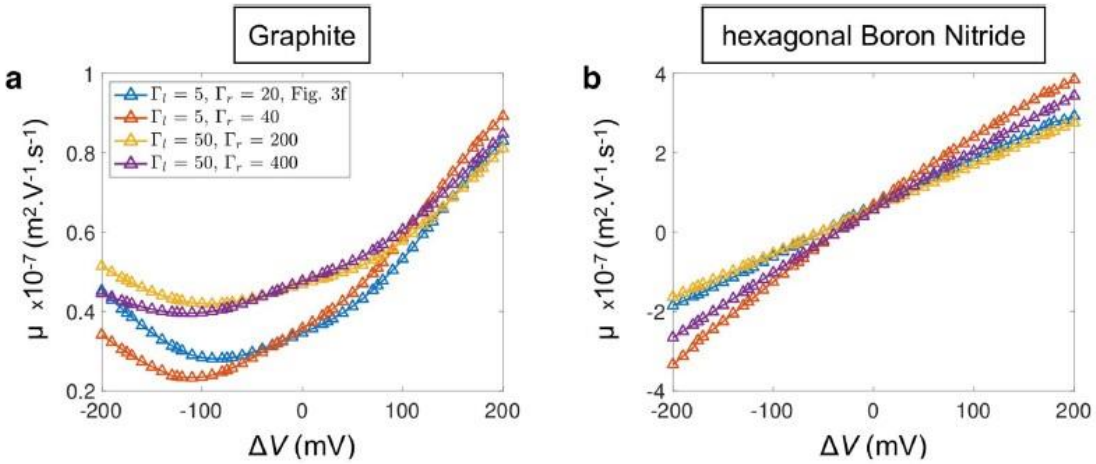

Extended Data Fig. 9 | Effect of the asymmetry of the system. a, **b**, Plots show $\mu(\Delta V)$ versus ΔV as a function of asymmetry. **a**, Low-friction (graphite-like) behaviour. In this plot we take c = 100 mM, α_+=1, α_-=0.7, μ =μ_+ + bulk, μ = . μ_- − 0.5 bulk and λ_0/h_0=10^{11} kg m^{-3} s^{-1}, as in the main text, while varying the geometric parameters Γ_l and Γ_r, as indicated in the legend. **b**, High-friction (hBN-like) behaviour, c = 100 mM, α_+=0.01, α_-=0.01, μ =μ_+ + bulk, μ = μ_- − 0.5 bulk and λ_0/h_0=10^{13} kg m^{-3} s^{-1}, as in the main text, while varying the geometric parameters Γl and Γr, as indicated in **a**.

Geometric sensitivity. The effect of the reservoir geometry on the numerical model predictions is illustrated in Extended Data Fig. 9. In this plot we show the influence of both the relative and absolute magnitudes of Γ_l and Γ_r on the predicted $\mu(\Delta V)$ responses for both the low-friction (graphite-like) and high-friction (hBN-like) configurations. Between the blue and yellow curves, we vary the absolute magnitudes of Γ_l and Γ_r by an order of magnitude while keeping the ratio Γ_l/Γ_r fixed. We see that the magnitudes of Γ_l and Γ_r have no influence on the qualitative (linear or quadratic) behaviour of the mobility curves and have only a slight quantitative influence on the graphite configuration. We also vary the ratio Γ_l/Γ_r (red and purple versus blue and yellow curves). In the graphite response, we see that the minima in the red and purple (Γ_l/Γ_r = 1/8) and the blue and yellow (Γ_l/Γ_r = 1/4) curves are coincident, even as we vary the absolute magnitudes of Γ_l and Γ_r by an order of magnitude. This indicates that in our model, for fixed values of the friction coefficients, the asymmetry determines the location of the minimum mobility in graphite. Likewise, in the hBN curves, we see that the asymmetry is the only geometric characteristic that determines the slope of the $\mu(\Delta V)$ curve.

As a final note on the model geometry, a one-dimensional model of the type that we have applied here is strictly valid only if the slope verifies $|\partial_x h| << 1$. Formally, this condition is not satisfied deep in the reservoirs. However, variations of the various profiles in the reservoir occur over length scales that are found to be at most of order the channel length L, so that $|\partial_x h| < \Gamma h_0/L$, which remains very small. Note furthermore that reservoirs are included merely to qualitatively capture the influence of (1) the device asymmetry and (2) the entrance/exit effects associated with the abrupt change in anion mobility at the entrance and exit of the slit. Previous work using this approach to include the reservoirs within a one-dimensional PNPS model was successful in capturing the nontrivial qualitative behaviour of the ionic current under applied pressures and voltages[34].

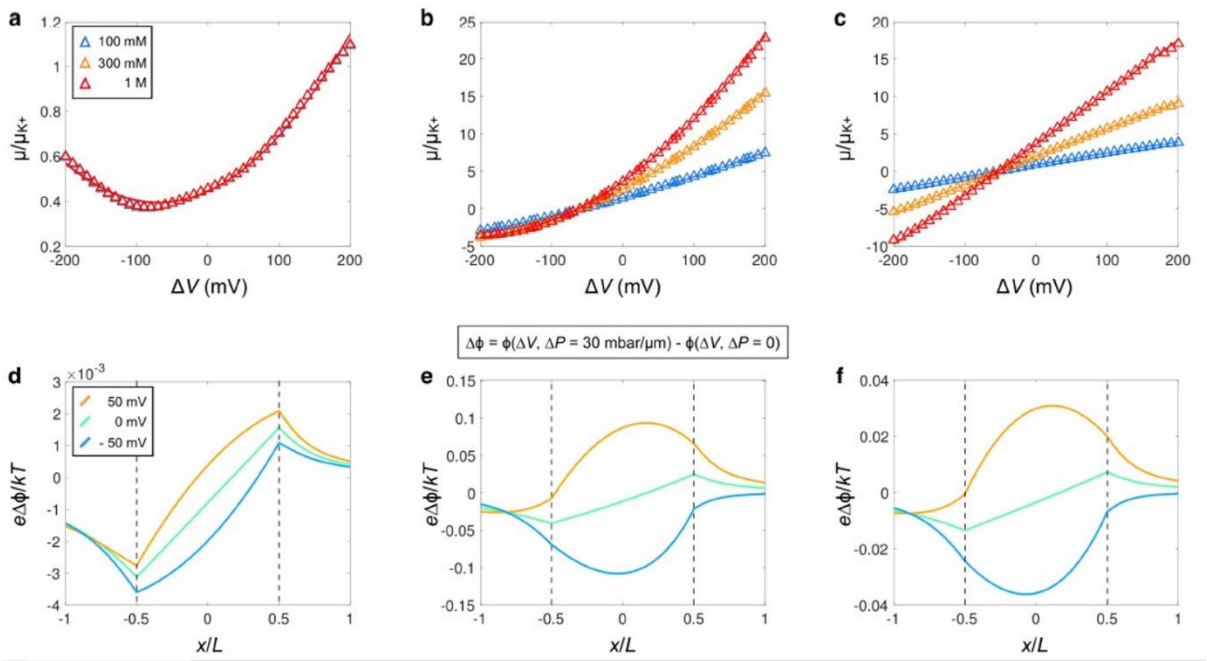

g

	a, d - Low friction (C) c = (100, 300, 1000)mM	b, e - Intermediate friction c = (100, 300, 1000)mM	c, f - High friction (hBN) c = (100, 300, 1000)mM
α_+	1	0.02	0.01
α_-	0.7	0.01	0.01
$\mu_+/\mu\kappa_+$	1	1	1
$\mu_-/\mu\kappa_+$	0.5	0.5	0.5
λ_d/h_0 (kg m^{-3} s^{-1})	10^{11}	5.10^{12}	10^{13}
$\kappa_+\rho_+$ (kg m^{-3} s^{-1})	0	(0.25, 0.75, 2.48) 10^{13}	(0.13, 0.38, 1.25) 10^{13}
$\kappa_-\rho_-$ (kg m^{-3} s^{-1})	(0.53, 1.60, 5.32) 10^{14}	(0.25, 0.75, 2.51) 10^{13}	(0.25, 0.75, 2.51) 10^{13}
λ_w/h_0 (kg m^{-3} s^{-1})	(0.53, 1.60, 5.32) 10^{14}	(1.00, 2.00, 5.49) 10^{13}	(1.38, 2.13, 4.76) 10^{13}

Extended Data Fig. 10 | Influence of the friction parameters on the model predictions. a–c, Plots show $\mu(\Delta V)$ versus ΔV for different concentrations (c = 100 mM, 300 mM and 1,000 mM) and frictional parameters. **a**, Lowfriction (graphite-like)

behaviour. In this plot, we take α_+=1, α_-=0.7, μ =μ_+ + bulk, μ = . μ_- − 0.5 bulk and λ_0/h_0=10^{11} kg m^{-3} s^{-1}. **b**, Intermediatefriction behaviour, α_+=0.02, α_-=0.01, μ =μ_+ + bulk, μ = μ_- − 0.5 bulk and λ_0/h_0=5.10^{12} kg m^{-3} s^{-1}. **c**, High-friction (hBN-like) behaviour, α = + 0.01, α−=0.01, μ =μ_+ + bulk, μ = μ_- − 0.5 bulk and λ_0/h_0=10^{13} kg m^{-3} s^{-1}. **d–f**, Pressure-induced variation of the normalized electric potential $\Delta\varphi$ = $\varphi(\Delta V, \Delta P = 30$ mbar μm$^{-1}) - \varphi(\Delta V, \Delta P = 0)$ plotted as a function of the normalized channel coordinate x/L axis for ΔV = −50 mV, 0 mV and 50 mV. The dashed vertical lines segregate the channel interior, $x/L \in (-0.5, 0.5)$, from the left (x/L < −0.5) and right (x/L > 0.5) reservoirs. The curves are coloured according to the applied voltage from −50 mV (blue) to 50 mV (orange). Panels **d**–**f** correspond to the parameters of **a**–**c**, respectively. **g**, Table of the friction parameters corresponding to the data shown in **a**–**c**. The table also shows the decomposition of $\lambda_w(c)$ into its three components for the concentrations considered here.

Transition behaviour. In Extended Data Fig. 10a–c, we show the influence of the friction parameters for high, low and intermediate friction on the gated mobilities, and in Extended Data Fig. 10d–f we show the relative pressure dependence of the normalized potential $e\Delta\varphi/kT$ along the channel axis. $\Delta\varphi$ is defined as the potential variation with an applied pressure $\Delta\varphi = \varphi(\Delta V, \Delta P = 30$ mbar μm$^{-1}) - \varphi(\Delta V, \Delta P = 0)$. The modification of the electrostatic potential, and hence the electric field, under coupled pressure–voltage forcing contributes—along with the modification of the concentration field (Extended Data Fig. 8)—to the modification of the electrophoretic current under an applied pressure. Extended Data Figs. 8 and 10 illustrate the complex interplay of competing interactions that contribute to the surprisingly simple linear streaming response observed in the model.

34. Jubin, L., Poggioli, A., Siria, A. & Bocquet, L. Dramatic pressure-sensitive ion conduction in conical nanopores. *Proc. Natl Acad. Sci. USA* **115**, 4063–4068 (2018).

Chapter 7

Conclusions and Future work

7.1 Summary

This thesis presented experimental study of molecular transport through atomic-scale apertures and capillaries made by graphene and other 2D materials using nanofabrication methods. The structure and accurate geometric control of our fabrication technique have showed great potential and proved itself a reliable technique for the fabrication of integrated micro/nanofluidic devices. Based on our 2D graphene nanofluidic capillaries, the proposed channel scheme quantitatively measure mass transport in single to multiple of graphene capillaries.

We have explored how capillary device structure can be employed to experimentally understand the physical interaction of molecules on different surfaces for gas permeation and selectivity (chapter 4). Ionic flows under such confinement has also been discovered under pressure and voltage gradient to explore ion-water coupling under such forcing (chapter 6). Gas permeation through atomic scale pores in WS_2 membranes provide a quantitative relation of pores and gas flux (chapter 5)

This final chapter provides a perspective on the implications of these properties and prospects for future work using these device structures and measurement systems. I start by discussing the heterostructures made to create atomic scale spaces with van der Waals materials, afterwards prospective future work that can build on these fundamental explorations and to conclude some technological implications of this work will be discussed.

7.2 Properties explored in atomic scale spaces in 2D materials

Van der Waals materials are known for their ability to detach into thinner layers and stacked back together with no loss in atomic continuity. We exploited this property to make ultra clean well-sealed atomic scale spaces for nanofluidic applications and took it one step ahead in already developed technology. Atomic scale spaces created using this method are like carbon nanotubes that possess similarly well-defined nanospaces however, with precise control on dimensions and channel opening during fabrication.

The fabrication process of assembling a stack of three layers with the middle layer being nanopatterned using electron beam lithography also allows for multiple duplicates of the capillaries to be built in the same stack with sub-angstrom uniformity. Micro spaces introduced in these heterostructures also have advantages over micro-spaces in other materials like silicon dioxide, as they are perfectly sealed compared to the porous and leaky nature of silicon dioxide.

In these structures helium atoms on impinging on a graphite surface reflect specularly by giving enhanced flux 2-3 orders higher (<2 nm capillaries) than expected, as demonstrated by Keerthi et al., *Nature* **558**, 420–424 (2018). Selectivity of gases relative to helium has remained unsettled.

In case of atomic vacancy defects the only way to inspect and confirm the atomic pore formation is by AC-STEM, which is limited to relatively small areas. A quick method is established to quantify the atomic vacancies created in monolayer WS_2 membranes validating the more than a century old Knudsen equation.

Ion transport under mechanical and electrical forces in atomic scale capillaries revealed transistor-like electro-hydrodynamic effect. Non-linear gating effect has been observed under such forcing with pronounced material dependence.

7.3 Future work

The idea of well-defined atomic scale capillaries produced by van der Waals heterostructure has been exploited to study several other surface properties of fluids and their interaction under such confinements (170, 171, 229). The interaction of a range of liquid and gas molecules on the surface of any 2D material can be understood. These structures come as a potential setup to study centuries old questions on properties like conductivity, capacitance, interfacial elasticity, interfacial viscosity, contact angle, slip, permeability etc. at the molecular scale.

The enhanced helium transport through atomic scale capillaries shows potential for ultrafast separation of different particles whose transport is impeded in these channels. The monolayer nanochannels with 0.35 nm high spaces are particularly interesting to check for filltration and separation applications, by size exclusion. However more careful and sensitive measurement system is needed for separating molecules. Capillary devices can be a good candidate for separation of gases i.e. volatile organic compounds (VOCs) such as cyclohexane, toluene, benzene and xylene which have the kinetic diameter above 6 Å

The angstrom scale capillaries structure provides a good device to probe the material properties further under such confinement. Properties of light waves, shock waves, magnetic fields inside these spaces and along the edges of the graphene walls can also be studied.

We expect that by engineering the fabrication methods, we can build nanofluidic circuits responding to external stimuli which will enable investigation of water transport like in biological channels such as aquaporins if more sensitive approaches of applying stimulus (*e.g.* voltage) and precise measurement methods are implemented.

References

1. Schoch RB, Han J, Renaud P. Transport phenomena in nanofluidics. Reviews of Modern Physics. 2008;80(3):839-83.

2. Eijkel JCT, Berg Avd. Nanofluidics: what is it and what can we expect from it? Microfluidics and Nanofluidics. 2005;1(3):249-67.

3. Sparreboom W, van den Berg A, Eijkel JCT. Principles and applications of nanofluidic transport. Nature Nanotechnology. 2009;4(11):713-20.

4. Bocquet L, Charlaix E. Nanofluidics, from bulk to interfaces. Chemical Society Reviews. 2010;39(3):1073-95.

5. Xu Y. Nanofluidics: A New Arena for Materials Science. Advanced Materials. 2018;30(3):1702419.

6. Duan C, Wang W, Xie Q. Review article: Fabrication of nanofluidic devices. Biomicrofluidics. 2013;7(2):026501.

7. Bocquet L, Tabeling P. Physics and technological aspects of nanofluidics. Lab on a chip. 2014;14.

8. Han J, Fu J, Schoch RB. Molecular sieving using nanofilters: Past, present and future. Lab on a Chip. 2008;8(1):23-33.

9. Kim SJ, Ko SH, Kang KH, Han J. Direct seawater desalination by ion concentration polarization. Nature Nanotechnology. 2010;5(4):297-301.

10. Cohen-Tanugi D, Grossman JC. Water Desalination across Nanoporous Graphene. Nano Letters. 2012;12(7):3602-8.

11. Clarke J, Wu H-C, Jayasinghe L, Patel A, Reid S, Bayley H. Continuous base identification for single-molecule nanopore DNA sequencing. Nature Nanotechnology. 2009;4(4):265-70.

12. Chen Z, Jiang Y, Dunphy DR, Adams DP, Hodges C, Liu N, et al. DNA translocation through an array of kinked nanopores. Nature Materials. 2010;9(8):667-75.

13. Kim SJ, Song Y-A, Han J. Nanofluidic concentration devices for biomolecules utilizing ion concentration polarization: theory, fabrication, and applications. Chemical Society Reviews. 2010;39(3):912-22.

14. Howorka S, Siwy Z. Nanopore analytics: sensing of single molecules. Chemical Society Reviews. 2009;38(8):2360-84.

15. Bonthuis DJ, Horinek D, Bocquet L, Netz RR. Electrohydraulic Power Conversion in Planar Nanochannels. Physical Review Letters. 2009;103(14):144503.

16. Daiguji H, Yang P, Szeri AJ, Majumdar A. Electrochemomechanical Energy Conversion in Nanofluidic Channels. Nano Letters. 2004;4(12):2315-21.

17. Gillespie D. High Energy Conversion Efficiency in Nanofluidic Channels. Nano Letters. 2012;12(3):1410-6.

18. Kavokine N, Netz RR, Bocquet L. Fluids at the Nanoscale: From Continuum to Subcontinuum Transport. Annual Review of Fluid Mechanics. 2021;53(1):377-410.

19. Corry B, Chung SH. Mechanisms of valence selectivity in biological ion channels. Cellular and molecular life sciences : CMLS. 2006;63:301-15.

20. Nonner W, Eisenberg R. Electrodiffusion in ionic channels of biological membranes. Journal of Molecular Liquids. 2000;87:149-62.

21. Watson H. Biological membranes. Essays in Biochemistry. 2015;59:43-69.

22. Hummer G, Rasaiah JC, Noworyta JP. Water conduction through the hydrophobic channel of a carbon nanotube. Nature. 2001;414(6860):188-90.

23. Tunuguntla RH, Henley RY, Yao Y-C, Pham TA, Wanunu M, Noy A. Enhanced water permeability and tunable ion selectivity in subnanometer carbon nanotube porins. Science. 2017;357(6353):792.

24. Guo S, Meshot ER, Kuykendall T, Cabrini S, Fornasiero F. Nanofluidic Transport through Isolated Carbon Nanotube Channels: Advances, Controversies, and Challenges. Advanced Materials. 2015;27(38):5726-37.

25. Noy A, Park HG, Fornasiero F, Holt JK, Grigoropoulos CP, Bakajin O. Nanofluidics in carbon nanotubes. Nano Today. 2007;2(6):22-9.

26. Park HG, Jung Y. Carbon nanofluidics of rapid water transport for energy applications. Chemical Society Reviews. 2014;43(2):565-76.

27. Raidongia K, Huang J. Nanofluidic Ion Transport through Reconstructed Layered Materials. Journal of the American Chemical Society. 2012;134(40):16528-31.

28. Xie Q, Xin F, Park HG, Duan C. Ion transport in graphene nanofluidic channels. Nanoscale. 2016;8(47):19527-35.

29. Hinds BJ, Chopra N, Rantell T, Andrews R, Gavalas V, Bachas LG. Aligned Multiwalled Carbon Nanotube Membranes. Science. 2004;303(5654):62.

30. Holt JK, Park HG, Wang Y, Stadermann M, Artyukhin AB, Grigoropoulos CP, et al. Fast Mass Transport Through Sub-2-Nanometer Carbon Nanotubes. Science. 2006;312(5776):1034.

31. Huang H, Song Z, Wei N, Shi L, Mao Y, Ying Y, et al. Ultrafast viscous water flow through nanostrand-channelled graphene oxide membranes. Nature Communications. 2013;4(1):2979.

32. Sun P, Liu H, Wang K, Zhong M, Wu D, Zhu H. Ultrafast liquid water transport through graphene-based nanochannels measured by isotope labelling. Chemical Communications. 2015;51(15):3251-4.

33. Kim HW, Yoon HW, Yoon S-M, Yoo BM, Ahn BK, Cho YH, et al. Selective Gas Transport Through Few-Layered Graphene and Graphene Oxide Membranes. Science. 2013;342(6154):91.

34. Li H, Song Z, Zhang X, Huang Y, Li S, Mao Y, et al. Ultrathin, Molecular-Sieving Graphene Oxide Membranes for Selective Hydrogen Separation. Science. 2013;342(6154):95.

35. Keerthi A, Geim AK, Janardanan A, Rooney AP, Esfandiar A, Hu S, et al. Ballistic molecular transport through two-dimensional channels. Nature. 2018;558(7710):420-4.

36. Wang L, Boutilier MSH, Kidambi PR, Jang D, Hadjiconstantinou NG, Karnik R. Fundamental transport mechanisms, fabrication and potential applications of nanoporous atomically thin membranes. Nature Nanotechnology. 2017;12(6):509-22.

37. Joshi RK, Carbone P, Wang FC, Kravets VG, Su Y, Grigorieva IV, et al. Precise and Ultrafast Molecular Sieving Through Graphene Oxide Membranes. Science. 2014;343(6172):752.

38. Lozada-Hidalgo M, Hu S, Marshall O, Mishchenko A, Grigorenko AN, Dryfe RAW, et al. Sieving hydrogen isotopes through two-dimensional crystals. Science. 2016;351(6268):68.

39. Nair RR, Wu HA, Jayaram PN, Grigorieva IV, Geim AK. Unimpeded Permeation of Water Through Helium-Leak–Tight Graphene-Based Membranes. Science. 2012;335(6067):442.

40. Mi B. Graphene Oxide Membranes for Ionic and Molecular Sieving. Science. 2014;343(6172):740.

41. Abraham J, Vasu KS, Williams CD, Gopinadhan K, Su Y, Cherian CT, et al. Tunable sieving of ions using graphene oxide membranes. Nature Nanotechnology. 2017;12(6):546-50.

42. Sun P, Wang K, Zhu H. Recent Developments in Graphene-Based Membranes: Structure, Mass-Transport Mechanism and Potential Applications. Advanced Materials. 2016;28(12):2287-310.

43. Chen L, Shi G, Shen J, Peng B, Zhang B, Wang Y, et al. Ion sieving in graphene oxide membranes via cationic control of interlayer spacing. Nature. 2017;550(7676):380-3.

44. Choi W, Ulissi ZW, Shimizu SFE, Bellisario DO, Ellison MD, Strano MS. Diameter-dependent ion transport through the interior of isolated single-walled carbon nanotubes. Nature Communications. 2013;4(1):2397.

45. Schneider GF, Dekker C. DNA sequencing with nanopores. Nature Biotechnology. 2012;30(4):326-8.

46. Corry B. Designing Carbon Nanotube Membranes for Efficient Water Desalination. The Journal of Physical Chemistry B. 2008;112(5):1427-34.

47. Das R, Ali ME, Hamid SBA, Ramakrishna S, Chowdhury Z. Carbon nanotube membranes for water purification: A bright future in water desalination. Desalination. 2014;336:97-109.

48. Surwade SP, Smirnov SN, Vlassiouk IV, Unocic RR, Veith GM, Dai S, et al. Water desalination using nanoporous single-layer graphene. Nature Nanotechnology. 2015;10(5):459-64.

49. Shi Z, Zhang W, Zhang F, Liu X, Wang D, Jin J, et al. Ultrafast Separation of Emulsified Oil/Water Mixtures by Ultrathin Free-Standing Single-Walled Carbon Nanotube Network Films. Advanced Materials. 2013;25(17):2422-7.

50. Wang H, Lin K-Y, Jing B, Krylova G, Sigmon GE, McGinn P, et al. Removal of oil droplets from contaminated water using magnetic carbon nanotubes. Water Research. 2013;47(12):4198-205.

51. Frackowiak E, Béguin F. Carbon materials for the electrochemical storage of energy in capacitors. Carbon. 2001;39(6):937-50.

52. Dillon AC, Jones KM, Bekkedahl TA, Kiang CH, Bethune DS, Heben MJ. Storage of hydrogen in single-walled carbon nanotubes. Nature. 1997;386(6623):377-9.

53. Liu C, Fan YY, Liu M, Cong HT, Cheng HM, Dresselhaus MS. Hydrogen Storage in Single-Walled Carbon Nanotubes at Room Temperature. Science. 1999;286(5442):1127.

54. Goral J, Panja P, Deo M, Andrew M, Linden S, Schwarz J-O, et al. Confinement Effect on Porosity and Permeability of Shales. Scientific Reports. 2020;10(1):49.

55. Kuila U, Prasad M. Specific surface area and pore-size distribution in clays and shales. Geophysical Prospecting. 2013;61(2):341-62.

56. Doyle AM, Alismaeel ZT, Albayati TM, Abbas AS. High purity FAU-type zeolite catalysts from shale rock for biodiesel production. Fuel. 2017;199:394-402.

57. https://www.youtube.com/watch?v=kNkbr_mnuRU [Online;accessed March16, 2021]. [

58. Luan X, Di B, Wei J, Zhao J, Li X. Creation of synthetic samples for physical modelling of natural shale. Geophysical Prospecting. 2016;64(4):898-914.

59. http://web.cc.iwate-u.ac.jp/~arifa/research-interest.html [Online;accessed April 16, 2021]. [

60. Duan C, Majumdar A. Anomalous ion transport in 2-nm hydrophilic nanochannels. Nature Nanotechnology. 2010;5(12):848-52.

61. Drndić M. Sequencing with graphene pores. Nature Nanotechnology. 2014;9(10):743-.

62. Celebi K, Buchheim J, Wyss RM, Droudian A, Gasser P, Shorubalko I, et al. Ultimate Permeation Across Atomically Thin Porous Graphene. Science. 2014;344(6181):289.

63. Boutilier MSH, Hadjiconstantinou NG, Karnik R. Knudsen effusion through polymer-coated three-layer porous graphene membranes. Nanotechnology. 2017;28(18):184003.

64. Boutilier MSH, Jang D, Idrobo JC, Kidambi PR, Hadjiconstantinou NG, Karnik R. Molecular Sieving Across Centimeter-Scale Single-Layer Nanoporous Graphene Membranes. ACS Nano. 2017;11(6):5726-36.

65. O'Hern SC, Boutilier MS, Idrobo JC, Song Y, Kong J, Laoui T, et al. Selective ionic transport through tunable subnanometer pores in single-layer graphene membranes. Nano Lett. 2014;14(3):1234-41.

66. Goyal G, Lee YB, Darvish A, Ahn CW, Kim MJ. Hydrophilic and size-controlled graphene nanopores for protein detection. Nanotechnology. 2016;27(49):495301.

67. Freedman KJ, Goyal G, Ahn CW, Kim MJ. Substrate Dependent Ad-Atom Migration on Graphene and the Impact on Electron-Beam Sculpting Functional Nanopores. Sensors. 2017;17(5).

68. Koenig SP, Wang L, Pellegrino J, Bunch JS. Selective molecular sieving through porous graphene. Nat Nanotechnol. 2012;7(11):728-32.

69. Zhao J, He G, Huang S, Villalobos LF, Dakhchoune M, Bassas H, et al. Etching gas-sieving nanopores in single-layer graphene with an angstrom precision for high-performance gas mixture separation. Science Advances. 2019;5(1):eaav1851.

70. Huh S, Park J, Kim YS, Kim KS, Hong BH, Nam J-M. UV/Ozone-Oxidized Large-Scale Graphene Platform with Large Chemical Enhancement in Surface-Enhanced Raman Scattering. ACS Nano. 2011;5(12):9799-806.

71. Huang S, Dakhchoune M, Luo W, Oveisi E, He G, Rezaei M, et al. Single-layer graphene membranes by crack-free transfer for gas mixture separation. Nat Commun. 2018;9(1):2632.

72. Lu N, Wang J, Floresca HC, Kim MJ. In situ studies on the shrinkage and expansion of graphene nanopores under electron beam irradiation at temperatures in the range of 400–1200°C. Carbon. 2012;50(8):2961-5.

73. Asghar W, Ilyas A, Billo JA, Iqbal SM. Shrinking of Solid-state Nanopores by Direct Thermal Heating. Nanoscale Research Letters. 2011;6(1):372.

74. Xu T, Yin K, Xie X, He L, Wang B, Sun L. Size-Dependent Evolution of Graphene Nanopores Under Thermal Excitation. Small. 2012;8(22):3422-6.

75. Kim W-g, Nair S. Membranes from nanoporous 1D and 2D materials: A review of opportunities, developments, and challenges. Chemical Engineering Science. 2013;104:908-24.

76. Patil O, Manikandan D, Nandigana VVR. A molecular dynamics simulation framework for predicting noise in solid-state nanopores. Molecular Simulation. 2020;46(13):1011-6.

77. Chogani A, Moosavi A, Rahiminejad M. Numerical Simulation of Salt Water Passing Mechanism Through Nanoporous Single-Layer Graphene Membrane. Chemical Product and Process Modeling. 2016;11(1):73-6.

78. Liu C, Jin Y, Li Z. Water transport through graphene and MoS2 nanopores. Journal of Applied Physics. 2019;126(2):024901.

79. Verweij H, Schillo MC, Li J. Fast Mass Transport Through Carbon Nanotube Membranes. Small. 2007;3(12):1996-2004.

80. Majumder M, Chopra N, Hinds BJ. Mass Transport through Carbon Nanotube Membranes in Three Different Regimes: Ionic Diffusion and Gas and Liquid Flow. ACS Nano. 2011;5(5):3867-77.

81. Whitby M, Quirke N. Fluid flow in carbon nanotubes and nanopipes. Nature Nanotechnology. 2007;2(2):87-94.

82. Cao W, Wang J, Ma M. Carbon nanostructure based mechano-nanofluidics. Journal of Micromechanics and Microengineering. 2018;28(3):033001.

83. Wang J, Lee CH, Yap YK. Recent advancements in boron nitride nanotubes. Nanoscale. 2010;2(10):2028-34.

84. Holt JK, Noy A, Huser T, Eaglesham D, Bakajin O. Fabrication of a Carbon Nanotube-Embedded Silicon Nitride Membrane for Studies of Nanometer-Scale Mass Transport. Nano Letters. 2004;4(11):2245-50.

85. Wang YY, Gupta S, Nemanich RJ, Liu ZJ, Qin LC. Hollow to bamboolike internal structure transition observed in carbon nanotube films. Journal of Applied Physics. 2005;98(1):014312.

86. https://www.zmescience.com/science/news-science/graphene-sieve-seawater [Online;accessed April 16, 2021]. [

87. Castelletto S, Boretti A. Advantages, limitations, and future suggestions in studying graphene-based desalination membranes. RSC Advances. 2021;11(14):7981-8002.

88. Liu G, Jin W, Xu N. Graphene-based membranes. Chemical Society Reviews. 2015;44(15):5016-30.

89. Schasfoort Richard BM, Schlautmann S, Hendrikse J, van den Berg A. Field-Effect Flow Control for Microfabricated Fluidic Networks. Science. 1999;286(5441):942-5.

90. Coste B, Xiao B, Santos JS, Syeda R, Grandl J, Spencer KS, et al. Piezo proteins are pore-forming subunits of mechanically activated channels. Nature. 2012;483(7388):176-81.

91. Kim HJ, Jang WK, Kim BH, Seo YH. Advancing liquid front shape control in capillary filling of microchannel via arrangement of microposts for microfluidic biomedical Sensors. International Journal of Precision Engineering and Manufacturing. 2016;17(1):59-63.

92. Park Ho B, Kamcev J, Robeson Lloyd M, Elimelech M, Freeman Benny D. Maximizing the right stuff: The trade-off between membrane permeability and selectivity. Science. 2017;356(6343):eaab0530.

93. Knudsen M. Die Gesetze der Molekularströmung und der inneren Reibungsströmung der Gase durch Röhren. Annalen der Physik. 1909;333(1):75-130.

94. Li H, Song Z, Zhang X, Huang Y, Li S, Mao Y, et al. Ultrathin, Molecular-Sieving Graphene Oxide Membranes for Selective Hydrogen Separation. Science. 2013;342(6154):95-8.

95. Ge L, Du A, Hou M, Rudolph V, Zhu Z. Enhanced hydrogen separation by vertically-aligned carbon nanotube membranes with zeolite imidazolate frameworks as a selective layer. RSC Advances. 2012;2(31):11793-800.

96. Mi W, Lin YS, Li Y. Vertically aligned carbon nanotube membranes on macroporous alumina supports. Journal of Membrane Science. 2007;304(1):1-7.

97. Yu M, Funke HH, Falconer JL, Noble RD. High Density, Vertically-Aligned Carbon Nanotube Membranes. Nano Letters. 2009;9(1):225-9.

98. Skoulidas AI, Ackerman DM, Johnson JK, Sholl DS. Rapid Transport of Gases in Carbon Nanotubes. Physical Review Letters. 2002;89(18):185901.

99. Sears K, Dumée L, Schütz J, She M, Huynh C, Hawkins S, et al. Recent Developments in Carbon Nanotube Membranes for Water Purification and Gas Separation. Materials. 2010;3(1).

100. Gruener S, Huber P. Knudsen Diffusion in Silicon Nanochannels. Physical Review Letters. 2008;100(6):064502.

101. Cox CD, Bavi N, Martinac B. Biophysical Principles of Ion-Channel-Mediated Mechanosensory Transduction. Cell Reports. 2019;29(1):1-12.

102. Anishkin A, Loukin SH, Teng J, Kung C. Feeling the hidden mechanical forces in lipid bilayer is an original sense. Proceedings of the National Academy of Sciences. 2014;111(22):7898.

103. Wu J, Lewis AH, Grandl J. Touch, Tension, and Transduction – The Function and Regulation of Piezo Ion Channels. Trends in Biochemical Sciences. 2017;42(1):57-71.

104. Yazda K, Tahir S, Michel T, Loubet B, Manghi M, Bentin J, et al. Voltage-activated transport of ions through single-walled carbon nanotubes. Nanoscale. 2017;9(33):11976-86.

105. Pang P, He J, Park JH, Krstić PS, Lindsay S. Origin of giant ionic currents in carbon nanotube channels. ACS nano. 2011;5(9):7277-83.

106. Marcotte A, Mouterde T, Niguès A, Siria A, Bocquet L. Mechanically activated ionic transport across single-digit carbon nanotubes. Nature Materials. 2020;19(10):1057-61.

107. Siria A, Poncharal P, Biance A-L, Fulcrand R, Blase X, Purcell ST, et al. Giant osmotic energy conversion measured in a single transmembrane boron nitride nanotube. Nature. 2013;494(7438):455-8.

108. Brohawn SG, Su Z, MacKinnon R. Mechanosensitivity is mediated directly by the lipid membrane in TRAAK and TREK1 K+ channels. Proceedings of the National Academy of Sciences. 2014;111(9):3614-9.

109. Castro Neto AH, Guinea F, Peres NMR, Novoselov KS, Geim AK. The electronic properties of graphene. Reviews of Modern Physics. 2009;81(1):109-62.

110. Geim AK, Novoselov KS. The rise of graphene. Nature Materials. 2007;6(3):183-91.

111. Novoselov KS, Geim AK, Morozov SV, Jiang D, Zhang Y, Dubonos SV, et al. Electric Field Effect in Atomically Thin Carbon Films. Science. 2004;306(5696):666.

112. Meyer JC, Geim AK, Katsnelson MI, Novoselov KS, Booth TJ, Roth S. The structure of suspended graphene sheets. Nature. 2007;446(7131):60-3.

113. Stankovich S, Dikin DA, Dommett GHB, Kohlhaas KM, Zimney EJ, Stach EA, et al. Graphene-based composite materials. Nature. 2006;442(7100):282-6.

114. Novoselov KS, Fal′ko VI, Colombo L, Gellert PR, Schwab MG, Kim K. A roadmap for graphene. Nature. 2012;490(7419):192-200.

115. Shore KA. Introduction to Graphene-Based Nanomaterials: From Electronic Structure to Quantum Transport, by Luis E.F. Foa Torres, Stephan Roche and Jean-Christophe Charlier. Contemporary Physics. 2014;55(4):344-5.

116. Wade. LG. Organic Chemistry. 5th edition ed: Prentice Hall; 2002.

117. Novoselov KS, Geim AK, Morozov SV, Jiang D, Katsnelson MI, Grigorieva IV, et al. Two-dimensional gas of massless Dirac fermions in graphene. Nature. 2005;438(7065):197-200.

118. Novoselov KS, Jiang D, Schedin F, Booth TJ, Khotkevich VV, Morozov SV, et al. Two-dimensional atomic crystals. Proceedings of the National Academy of Sciences of the United States of America. 2005;102(30):10451.

119. Yi M, Shen Z. A review on mechanical exfoliation for the scalable production of graphene. Journal of Materials Chemistry A. 2015;3(22):11700-15.

120. Novoselov KS, Castro Neto AH. Two-dimensional crystals-based heterostructures: materials with tailored properties. Physica Scripta. 2012;T146:014006.

121. Novoselov KS, Mishchenko A, Carvalho A, Castro Neto AH. 2D materials and van der Waals heterostructures. Science. 2016;353(6298):aac9439.

122. Frank O, Kalbac M. 2 - Chemical vapor deposition (CVD) growth of graphene films. In: Skákalová V, Kaiser AB, editors. Graphene: Woodhead Publishing; 2014. p. 27-49.

123. Chen S, Cai W, Piner RD, Suk JW, Wu Y, Ren Y, et al. Synthesis and Characterization of Large-Area Graphene and Graphite Films on Commercial Cu–Ni Alloy Foils. Nano Letters. 2011;11(9):3519-25.

124. Nandamuri G, Roumimov S, Solanki R. Chemical vapor deposition of graphene films. Nanotechnology. 2010;21(14):145604.

125. Reina A, Jia X, Ho J, Nezich D, Son H, Bulovic V, et al. Large Area, Few-Layer Graphene Films on Arbitrary Substrates by Chemical Vapor Deposition. Nano Letters. 2009;9(1):30-5.

126. Xu S, Zhang L, Wang B, Ruoff RS. Chemical vapor deposition of graphene on thin-metal films. Cell Reports Physical Science. 2021;2(3):100372.

127. Zhang Y, Zhang L, Zhou C. Review of Chemical Vapor Deposition of Graphene and Related Applications. Accounts of Chemical Research. 2013;46(10):2329-39.

128. Berger C, Song Z, Li T, Li X, Ogbazghi AY, Feng R, et al. Ultrathin Epitaxial Graphite: 2D Electron Gas Properties and a Route toward Graphene-based Nanoelectronics. The Journal of Physical Chemistry B. 2004;108(52):19912-6.

129. Mishra N, Boeckl J, Motta N, Iacopi F. Graphene growth on silicon carbide: A review. physica status solidi (a). 2016;213(9):2277-89.

130. Bae SK, Kim HK, Lee Y, Xu X, Park J, Zheng Y, et al. Roll-to-Roll Production of 30-in. Graphene Films for Transparent Electrodes. Nat Nanotechnol. 2011;5:574-8.

131. Li X, Cai W, An J, Kim S, Nah J, Yang D, et al. Large-Area Synthesis of High-Quality and Uniform Graphene Films on Copper Foils. Science. 2009;324(5932):1312.

132. Hernandez Y, Nicolosi V, Lotya M, Blighe FM, Sun Z, De S, et al. High-yield production of graphene by liquid-phase exfoliation of graphite. Nature Nanotechnology. 2008;3(9):563-8.

133. Ciesielski A, Samorì P. Graphene via sonication assisted liquid-phase exfoliation. Chemical Society Reviews. 2014;43(1):381-98.

134. Li Z, Young RJ, Backes C, Zhao W, Zhang X, Zhukov AA, et al. Mechanisms of Liquid-Phase Exfoliation for the Production of Graphene. ACS Nano. 2020;14(9):10976-85.

135. Wan X, Huang Y, Chen Y. Focusing on Energy and Optoelectronic Applications: A Journey for Graphene and Graphene Oxide at Large Scale. Accounts of Chemical Research. 2012;45(4):598-607.

136. Dong X, Su C-Y, Zhang W, Zhao J, Ling Q, Huang W, et al. Ultra-large single-layer graphene obtained from solution chemical reduction and its electrical properties. Physical Chemistry Chemical Physics. 2010;12(9):2164-9.

137. Luo J, Kim J, Huang J. Material Processing of Chemically Modified Graphene: Some Challenges and Solutions. Accounts of Chemical Research. 2013;46(10):2225-34.

138. Cheng M, Yang R, Zhang L, Shi Z, Yang W, Wang D, et al. Restoration of graphene from graphene oxide by defect repair. Carbon. 2012;50(7):2581-7.

139. PETRESCU M, BALINT M-G. STRUCTURE AND PROPERTIES MODIFICATIONS IN BORON NITRIDE. PART I: DIRECT POLYMORPHIC TRANSFORMATIONS MECHANISMS.

140. Dean CR, Young AF, Meric I, Lee C, Wang L, Sorgenfrei S, et al. Boron nitride substrates for high-quality graphene electronics. Nature Nanotechnology. 2010;5(10):722-6.

141. Wang J, Ma F, Sun M. Graphene, hexagonal boron nitride, and their heterostructures: properties and applications. RSC Advances. 2017;7(27):16801-22.

142. Majety S, Cao X, Dahal R, Pantha B, Li J, Lin J-Y, et al. Semiconducting hexagonal boron nitride for deep ultraviolet photonics. Proceedings of SPIE - The International Society for Optical Engineering. 2012;8268:70.

143. Radisavljevic B, Radenovic A, Brivio J, Giacometti V, Kis A. Single-layer MoS2 transistors. Nature Nanotechnology. 2011;6(3):147-50.

144. Wang QH, Kalantar-Zadeh K, Kis A, Coleman JN, Strano MS. Electronics and optoelectronics of two-dimensional transition metal dichalcogenides. Nature Nanotechnology. 2012;7(11):699-712.

145. Coleman JN, Lotya M, O'Neill A, Bergin SD, King PJ, Khan U, et al. Two-Dimensional Nanosheets Produced by Liquid Exfoliation of Layered Materials. Science. 2011;331(6017):568.

146. Lee Y-H, Zhang X-Q, Zhang W, Chang M-T, Lin C-T, Chang K-D, et al. Synthesis of Large-Area MoS2 Atomic Layers with Chemical Vapor Deposition. Advanced Materials. 2012;24(17):2320-5.

147. Zhan Y, Liu Z, Najmaei S, Ajayan PM, Lou J. Large-Area Vapor-Phase Growth and Characterization of MoS2 Atomic Layers on a SiO2 Substrate. Small. 2012;8(7):966-71.

148. Bana H, Travaglia E, Bignardi L, Lacovig P, Sanders CE, Dendzik M, et al. Epitaxial growth of single-orientation high-quality MoS 2 monolayers. 2D Materials. 2018;5(3):035012.

149. Liu K-K, Zhang W, Lee Y-H, Lin Y-C, Chang M-T, Su C-Y, et al. Growth of Large-Area and Highly Crystalline MoS2 Thin Layers on Insulating Substrates. Nano Letters. 2012;12(3):1538-44.

150. Thiruraman JP, Dar SA, Masih Das P, Hassani N, Neek-Amal M, Keerthi A, et al. Gas flow through atomic-scale apertures. Science Advances. 2020;6(51):eabc7927.

151. Shivananju BN, Yu W, Liu Y, Zhang Y, Lin B, Li S, et al. The Roadmap of Graphene-Based Optical Biochemical Sensors. Advanced Functional Materials. 2017;27(19):1603918.

152. Li D, Lu H, Qiu W, Dong J, Guan H, Zhu W, et al. Molybdenum disulfide nanosheets deposited on polished optical fiber for humidity sensing and human breath monitoring. Opt Express. 2017;25(23):28407-16.

153. Bernardi M, Palummo M, Grossman JC. Extraordinary Sunlight Absorption and One Nanometer Thick Photovoltaics Using Two-Dimensional Monolayer Materials. Nano Letters. 2013;13(8):3664-70.

154. Furchi MM, Höller F, Dobusch L, Polyushkin DK, Schuler S, Mueller T. Device physics of van der Waals heterojunction solar cells. npj 2D Materials and Applications. 2018;2(1):3.

155. Britnell L, Ribeiro RM, Eckmann A, Jalil R, Belle BD, Mishchenko A, et al. Strong Light-Matter Interactions in Heterostructures of Atomically Thin Films. Science. 2013;340(6138):1311.

156. Chen Y, Wang Y, Wang Z, Gu Y, Ye Y, Chai X, et al. Unipolar barrier photodetectors based on van der Waals heterostructures. Nature Electronics. 2021;4(5):357-63.

157. Choi HK, Park J, Myoung N, Kim H-J, Choi JS, Choi YK, et al. Gas molecule sensing of van der Waals tunnel field effect transistors. Nanoscale. 2017;9(47):18644-50.

158. Geim AK, Grigorieva IV. Van der Waals heterostructures. Nature. 2013;499(7459):419-25.

159. Cao Y, Mishchenko A, Yu GL, Khestanova E, Rooney AP, Prestat E, et al. Quality Heterostructures from Two-Dimensional Crystals Unstable in Air by Their Assembly in Inert Atmosphere. Nano Letters. 2015;15(8):4914-21.

160. Robinson JA. Growing Vertical in the Flatland. ACS Nano. 2016;10(1):42-5.

161. Cai Z, Liu B, Zou X, Cheng H-M. Chemical Vapor Deposition Growth and Applications of Two-Dimensional Materials and Their Heterostructures. Chemical Reviews. 2018;118(13):6091-133.

162. Liu Z, Song L, Zhao S, Huang J, Ma L, Zhang J, et al. Direct Growth of Graphene/Hexagonal Boron Nitride Stacked Layers. Nano Letters. 2011;11(5):2032-7.

163. Lin M-Y, Chang C-E, Wang C-H, Su C-F, Chen C, Lee S-C, et al. Toward epitaxially grown two-dimensional crystal hetero-structures: Single and double MoS2/graphene hetero-structures by chemical vapor depositions. Applied Physics Letters. 2014;105(7):073501.

164. Onodera M, Masubuchi S, Moriya R, Machida T. Assembly of van der Waals heterostructures: exfoliation, searching, and stacking of 2D materials. Japanese Journal of Applied Physics. 2020;59(1):010101.

165. Gong Y, Lin J, Wang X, Shi G, Lei S, Lin Z, et al. Vertical and in-plane heterostructures from WS2/MoS2 monolayers. Nature Materials. 2014;13(12):1135-42.

166. Tien DH, Park J-Y, Kim KB, Lee N, Choi T, Kim P, et al. Study of Graphene-based 2D-Heterostructure Device Fabricated by All-Dry Transfer Process. ACS Applied Materials & Interfaces. 2016;8(5):3072-8.

167. Knudsen M, Fisher WJ. The Molecular and the Frictional Flow of Gases in Tubes. Physical Review (Series I). 1910;31(5):586-8.

168. Fryer GM, Barrer RM. A theory of gas flow through capillary tubes. Proceedings of the Royal Society of London Series A Mathematical and Physical Sciences. 1966;293(1434):329-41.

169. Szymczyk A, Fievet P. Investigating transport properties of nanofiltration membranes by means of a steric, electric and dielectric exclusion model. Journal of membrane science. 2005;252(1-2):77-88.

170. Gopinadhan K, Hu S, Esfandiar A, Lozada-Hidalgo M, Wang FC, Yang Q, et al. Complete steric exclusion of ions and proton transport through confined monolayer water. Science. 2019;363(6423):145.

171. Esfandiar A, Radha B, Wang FC, Yang Q, Hu S, Garaj S, et al. Size effect in ion transport through angstrom-scale slits. Science. 2017;358(6362):511.

172. van der Heyden FHJ, Stein D, Dekker C. Streaming Currents in a Single Nanofluidic Channel. Physical Review Letters. 2005;95(11):116104.

173. Saha P, Nam C, Hickner MA, Zenyuk IV. Electrokinetic Streaming-Current Methods to Probe the Electrode–Electrolyte Interface under Applied Potentials. The Journal of Physical Chemistry C. 2019;123(32):19493-505.

174. Saha P, Zenyuk IV. Electric Double Layer at the Polycrystalline Platinum–Electrolyte Interface Probed by the Electrokinetic Streaming Current Method. The Journal of Physical Chemistry C. 2021;125(36):19706-15.

175. Blake P, Hill EW, Castro Neto AH, Novoselov KS, Jiang D, Yang R, et al. Making graphene visible. Applied Physics Letters. 2007;91(6):063124.

176. Rugar D, Hansma P. Atomic Force Microscopy. Physics Today. 1990;43(10):23-30.

177. Ni Z, Wang Y, Yu T, Shen Z. Raman spectroscopy and imaging of graphene. Nano Research. 2008;1(4):273-91.

178. Tiginyanu I, Ursaki V, Popa V. 10 - Nanoimprint lithography (NIL) and related techniques for electronics applications. In: Makhlouf ASH, Tiginyanu I, editors. Nanocoatings and Ultra-Thin Films: Woodhead Publishing; 2011. p. 280-329.

179. Jansen H, Gardeniers H, Boer Md, Elwenspoek M, Fluitman J. A survey on the reactive ion etching of silicon in microtechnology. Journal of Micromechanics and Microengineering. 1996;6(1):14-28.

180. Seidel H, Csepregi L, Heuberger A, Baumgärtel H. Anisotropic Etching of Crystalline Silicon in Alkaline Solutions: I . Orientation Dependence and Behavior of Passivation Layers. Journal of The Electrochemical Society. 1990;137(11):3612-26.

181. Orientation Dependent Etching of Silicon. In: Frühauf J, editor. Shape and Functional Elements of the Bulk Silicon Microtechnique: A Manual of Wet-Etched Silicon Structures. Berlin, Heidelberg: Springer Berlin Heidelberg; 2005. p. 17-69.

182. Reina A, Son H, Jiao L, Fan B, Dresselhaus MS, Liu Z, et al. Transferring and Identification of Single- and Few-Layer Graphene on Arbitrary Substrates. The Journal of Physical Chemistry C. 2008;112(46):17741-4.

183. Mlack JT, Masih Das P, Danda G, Chou Y-C, Naylor CH, Lin Z, et al. Transfer of monolayer TMD WS2 and Raman study of substrate effects. Scientific Reports. 2017;7(1):43037.

184. Bonaccorso F, Lombardo A, Hasan T, Sun Z, Colombo L, Ferrari AC. Production and processing of graphene and 2d crystals. Materials Today. 2012;15(12):564-89.

185. Castellanos-Gomez A, Buscema M, Molenaar R, Singh V, Janssen L, van der Zant HSJ, et al. Deterministic transfer of two-dimensional materials by all-dry viscoelastic stamping. 2D Materials. 2014;1(1):011002.

186. Zhang S, Chen W, Cheng W, Liang R, Xu J. Thickness identification of 2D hexagonal boron nitride thin flakes by optical imaging in dry transfer method. Materials Research Express. 2019;6(7):075042.

187. Groves TR. Electron beam lithography. Nanolithography: Woodhead Publishing; 2014. 80–115 p.

188. Constancias C, Landis S, Manakli S, Martin L, Pain L, Rio D. Electron Beam Lithography. Lithography2013. p. 101-82.

189. Landis S. Lithography Main techniques: John Wiley & Sons; (2011).

190. Kaspar P, Jeyaram Y, Jäckel H, Foelske A, Kötz R, Bellini S. Silicon nitride hardmask fabrication using a cyclic CHF3-based reactive ion etching process for vertical profile nanostructures. Journal of Vacuum Science & Technology B. 2010;28(6):1179-86.

191. He B, Yang Y, Yuen MF, Chen XF, Lee CS, Zhang WJ. Vertical nanostructure arrays by plasma etching for applications in biology, energy, and electronics. Nano Today. 2013;8(3):265-89.

192. Shearn M, Sun X, Henry MD, Yariv A, Scherer A. Advanced plasma processing: etching, deposition, and wafer bonding techniques for semiconductor applications. Semiconductor technologies. 2010:79-104.

193. Radha B, Esfandiar A, Wang FC, Rooney AP, Gopinadhan K, Keerthi A, et al. Molecular transport through capillaries made with atomic-scale precision. Nature. 2016;538(7624):222-5.

194. Sajja R, You Y, Qi R, Goutham S, Bhardwaj A, Rakowski A, et al. Hydrocarbon contamination in angström-scale channels. Nanoscale. 2021;13(21):9553-60.

195. Haigh SJ, Gholinia A, Jalil R, Romani S, Britnell L, Elias DC, et al. Cross-sectional imaging of individual layers and buried interfaces of graphene-based heterostructures and superlattices. Nature Materials. 2012;11(9):764-7.

196. Steckelmacher W. A review of the molecular flow conductance for systems of tubes and components and the measurement of pumping speed. Vacuum. 1966;16(11):561-84.

197. v. Smoluchowski M. Zur kinetischen Theorie der Transpiration und Diffusion verdünnter Gase. Annalen der Physik. 1910;338(16):1559-70.

198. Lafferty JM. Foundations of vacuum science and technology. New York ;: Wiley; 1998.

199. Fan S, Vu QA, Tran MD, Adhikari S, Lee YH. Transfer assembly for two-dimensional van der Waals heterostructures. 2D Materials. 2020;7(2):022005.

200. Pechar TW. Fabrication and characterization of polyimide-based mixed matrix membranes for gas separations: Virginia Tech; 2004.

201. Gehre M, Guo Z, Rothenberg G, Tanase S. Sustainable Separations of C4-Hydrocarbons by Using Microporous Materials. ChemSusChem. 2017;10(20):3947-63.

202. Kim S, Jinschek JR, Chen H, Sholl DS, Marand E. Scalable Fabrication of Carbon Nanotube/Polymer Nanocomposite Membranes for High Flux Gas Transport. Nano Letters. 2007;7(9):2806-11.

203. Hou J, Zhang H, Hu Y, Li X, Chen X, Kim S, et al. Carbon Nanotube Networks as Nanoscaffolds for Fabricating Ultrathin Carbon Molecular Sieve Membranes. ACS Applied Materials & Interfaces. 2018;10(23):20182-8.

204. Wang L, Boutilier MSH, Kidambi PR, Jang D, Hadjiconstantinou NG, Karnik R. Fundamental transport mechanisms, fabrication and potential applications of nanoporous atomically thin membranes. Nat Nanotechnol. 2017;12(6):509-22.

205. Boutilier MSH, Jang D, Idrobo J-C, Kidambi PR, Hadjiconstantinou NG, Karnik R. Molecular Sieving Across Centimeter-Scale Single-Layer Nanoporous Graphene Membranes. ACS Nano. 2017;11(6):5726-36.

206. Liu H, Chen Z, Dai S, Jiang D-e. Selectivity trend of gas separation through nanoporous graphene. Journal of Solid State Chemistry. 2015;224:2-6.

207. Bunch JS, Verbridge SS, Alden JS, van der Zande AM, Parpia JM, Craighead HG, et al. Impermeable Atomic Membranes from Graphene Sheets. Nano Letters. 2008;8(8):2458-62.

208. Alen SK, Nam S, Dastgheib SA. Recent advances in graphene oxide membranes for gas separation applications. International journal of molecular sciences. 2019;20(22):5609.

209. Wang L, Drahushuk LW, Cantley L, Koenig SP, Liu X, Pellegrino J, et al. Molecular valves for controlling gas phase transport made from discrete angstrom-sized pores in graphene. Nat Nanotechnol. 2015;10(9):785-90.

210. Khan MH, Moradi M, Dakhchoune M, Rezaei M, Huang S, Zhao J, et al. Hydrogen sieving from intrinsic defects of benzene-derived single-layer graphene. Carbon. 2019;153:458-66.

211. Sun C, Boutilier MS, Au H, Poesio P, Bai B, Karnik R, et al. Mechanisms of molecular permeation through nanoporous graphene membranes. Langmuir. 2014;30(2):675-82.

212. Blankenburg S, Bieri M, Fasel R, Müllen K, Pignedoli CA, Passerone D. Porous Graphene as an Atmospheric Nanofilter. Small. 2010;6(20):2266-71.

213. Jiang D-e, Cooper VR, Dai S. Porous Graphene as the Ultimate Membrane for Gas Separation. Nano Letters. 2009;9(12):4019-24.

214. Drahushuk LW, Strano MS. Mechanisms of Gas Permeation through Single Layer Graphene Membranes. Langmuir. 2012;28(48):16671-8.

215. Fornasiero F, Park HG, Holt JK, Stadermann M, Grigoropoulos CP, Noy A, et al. Ion exclusion by sub-2-nm carbon nanotube pores. Proceedings of the National Academy of Sciences. 2008;105(45):17250.

216. Yang Y, Hillmann R, Qi Y, Korzetz R, Biere N, Emmrich D, et al. Ultrahigh Ionic Exclusion through Carbon Nanomembranes. Advanced Materials. 2020;32(8):1907850.

217. Velioğlu S, Karahan HE, Goh K, Bae T-H, Chen Y, Chew JW. Metallicity-Dependent Ultrafast Water Transport in Carbon Nanotubes. Small. 2020;16(25):1907575.

218. Kavokine N, Marbach S, Siria A, Bocquet L. Ionic Coulomb blockade as a fractional Wien effect. Nature Nanotechnology. 2019;14(6):573-8.

219. Rezaee M, Ghassemi H. Anomalous behavior of fluid flow through thin carbon nanotubes. Theoretical and Computational Fluid Dynamics. 2020;34:177-86.

220. Wang P, Wang M, Liu F, Ding S, Wang X, Du G, et al. Ultrafast ion sieving using nanoporous polymeric membranes. Nature Communications. 2018;9(1):569.

221. Yu M, Hou Y, Song R, Xu X, Yao S. Tunable Confinement for Bridging Single-Cell Manipulation and Single-Molecule DNA Linearization. Small. 2018;14(17):1800229.

222. Eijkel JC, Van Den Berg A. Nanofluidics: what is it and what can we expect from it? Microfluidics and Nanofluidics. 2005;1(3):249-67.

223. Wang M, Hou Y, Yu L, Hou X. Anomalies of Ionic/Molecular Transport in Nano and Sub-Nano Confinement. Nano Letters. 2020;20(10):6937-46.

224. Ramos-Alvarado B, Kumar S, Peterson GP. Hydrodynamic slip length as a surface property. Physical Review E. 2016;93(2):023101.

225. Cheng L-J. Electrokinetic ion transport in nanofluidics and membranes with applications in bioanalysis and beyond. Biomicrofluidics. 2018;12(2):021502-.

226. Tocci G, Joly L, Michaelides A. Friction of Water on Graphene and Hexagonal Boron Nitride from Ab Initio Methods: Very Different Slippage Despite Very Similar Interface Structures. Nano Letters. 2014;14(12):6872-7.

227. Zhong J, Alibakhshi MA, Xie Q, Riordon J, Xu Y, Duan C, et al. Exploring Anomalous Fluid Behavior at the Nanoscale: Direct Visualization and Quantification via Nanofluidic Devices. Accounts of Chemical Research. 2020;53(2):347-57.

228. Yang J, Lu F, Kostiuk LW, Kwok DY. Electrokinetic microchannel battery by means of electrokinetic and microfluidic phenomena. Journal of Micromechanics and Microengineering. 2003;13(6):963-70.

229. Yang W, Radha B, Choudhary A, You Y, Mettela G, Geim AK, et al. Translocation of DNA through Ultrathin Nanoslits. Advanced Materials. 2021;33(11):2007682.